

Thermomechanical Analysis and  
Development of a Novel  
Monochromator First Crystal  
Using an Interference Fit

# Thermomechanical Analysis and Development of a Novel Monochromator First Crystal Using an Interference Fit

A complete redesign of first crystal assemblies from first principles

**Joshua Stimson**



**BIRMINGHAM CITY**  
University

Dissertation submitted for the degree of Philosophiae Doctor (PhD)

School of Engineering and the Built Environment  
Faculty of Computing, Engineering and the Built Environment  
Birmingham City University

In collaboration with

The Diamond Light Source

December 2018

# Contents

Glossary .....	xv
Abstract .....	1
Acknowledgments .....	2
Introduction.....	3
1. Literature Review .....	7
1.1 Introduction.....	7
1.2 History of Synchrotron Devices .....	8
1.3 Development of Current Monochromator Systems.....	12
1.4 Limitations of Current Systems .....	19
1.5 Thermomechanical Coupling.....	21
1.6 Fundamental Principles for Designing a Novel Crystal Assembly .....	23
1.7 Conclusion .....	25
2. Examining Thermal Transport through the use of Theoretical Models .....	27
2.1 Introduction.....	27
2.2 1D Analytical Model of Thermal Transport .....	32
2.3 Investigating Heat Transfer using a 1D Analytical Model.....	37
2.4 Verifying the Outputs of the 1D Analytical Model with a 3D Finite Element Model .....	39
2.5 Researching into the Temperature Dependant Properties of the Different Materials.....	48
2.6 Development of a Finite Element Model of the Full Monochromator Assembly .....	53
2.7 Conclusion .....	59

3.	Exploring Various Crystal Geometries and Heat Exchange Locations.....	62
3.1	Introduction.....	62
3.2	Isolating the Monochromator First Crystal in a 3D Model.....	64
3.3	Investigating the Benefits of Modified Crystal Designs.....	76
3.3.1	'Square' Crystal.....	76
3.3.2	'Bulk' Crystal.....	83
3.3.3	'Thin' Crystal.....	90
3.3.4	'Wafer' Crystal.....	97
3.3.5	'Cut-back' Crystal.....	104
3.4	Comparing the Results of Different Crystal Designs.....	108
3.5	Conclusion.....	111
4.	Investigating the Differing Benefits to Direct and Indirect Cooling.....	114
4.1	Introduction.....	114
4.2	Investigating the Controlling Properties of Thermal Contact.....	117
4.3	Comparing the Drawbacks and Benefits of Direct and Indirect Cooling.....	119
4.3.1	Direct Cooling.....	119
4.3.2	Indirect Cooling.....	124
4.3.2	Comparison of Direct and Indirect Cooling.....	128
4.4	Locating the Deformation Minimum with Increasing Clamping Force.....	129
4.5	Conclusion.....	132

5.	Examining the Effect of Varying Factors on Thermal Gap Conductance.....	135
5.1	Introduction.....	135
5.2	Investigating Thermal Contact Theory .....	138
5.3	Modelling Thermal Contact with Various Factors .....	141
5.4	Experimental Calculation of Thermal Gap Conductance Values.....	146
5.5	Comparing the Results of the Theoretical Models with Experimental Results.....	155
5.6	Conclusion .....	159
6.	Utilising an Interference Fit as a Clamping and Cooling System .....	162
6.1	Introduction.....	163
6.2	Modelling of an Interference Fit.....	166
6.3	Designing a New Monochromator Assembly Utilising an Interference Fit .....	175
6.4	Investigating the Performance of an Interference Fit Monochromator Assembly.....	179
6.5	Comparing the Performance of an Interference Fit to that of a Conventional Design .....	184
6.6	Conclusion .....	186
7.	Discussion .....	188
7.1	Introduction.....	188
7.2	Material Properties: Benefit or Bane .....	190
7.3	Assembly Geometry: Importance of Heat Exchange Location.....	192
7.4	Cooling Methods: Direct vs Indirect.....	194
7.5	Deformation: Optimising Thermal Induced and Stress Induced Deformation .....	196
7.6	Thermal Gap Conductance: Highly Dependent Limiting Factor .....	197
7.7	Conclusion .....	199

8. Conclusions.....	202
8.1 Overview.....	202
8.2 Limitations of the Conventional Assembly Design .....	204
8.3 Application of a Cut Back Heat Exchanger .....	205
8.4 Interference Fit Crystal Assemblies: A Novel Solution .....	206
8.5 Summary.....	208
Bibliography.....	210
Appendix A: “Analytical Model for Heat Absorption: Lessons Learned from a One Dimensional Model” – Presented at SRI 2015, published in AIP Conference Proceedings 2016 (Stimson et al., 2016). .....	215
Appendix B: “A Thermal Exploration of Different Monochromator Crystal Designs” – Presented at MEDSI 2016, published in Proceedings of MEDSI2016, 2017 (Joshua Stimson et al., 2017).....	219
Appendix C: “The Application of Interference Fits for Overcoming Limitations in Clamping Methodologies for Cryo-Cooling First Crystal Configurations in X-Ray Monochromators” – Presented at CEC-ICMC 2017, published in IOP Conference Series, 2017 (J. Stimson et al., 2017). .....	224
Appendix D: “On the Effect of Clamping Force and Interstitial Materials on Room Temperature Thermal Contact Conductance” – Under Review for Publication .....	232
Appendix E: “Application of Interference Fits on Cylindrical Monochromator Crystals to Overcome Clamping and Cooling Deformations” – Accepted, pending publication in Journal of Synchrotron Radiation.....	241

## Figures

Figure 1 – Standard synchrotron beamline from undulator to beyond double bounce crystal monochromator (Aragão et al., 2018).....	3
Figure 2 – Layout of a standard synchrotron device .....	9
Figure 3 – (Left) Indirect cooling system; coolant flows through heat exchangers, heat travels from crystal to heat exchanger to coolant. (Right) Direct cooling system; coolant flows through crystal directly, heat flows from crystal to coolant. ....	14
Figure 4 – Channel-cut monochromator crystal; beam diffracts from top of first diffraction plane, then from bottom of second diffraction plane. ....	15
Figure 5 – Synchrotron beamline from wiggler to beyond quadruple bounce crystal monochromator.....	16
Figure 6 – Demonstration of the dispersive link observed in a QBCM; a) The collimated beam diffracts from the first crystal to the second crystal, b) Thermal deformation in the first crystal leads to beam spreading, which is maintained through diffraction at the second crystal, c) Spread beam is diffracted from third crystal, exacerbating beam spreading. Beam is much more dispersed after diffraction from the fourth crystal. ....	16
Figure 7 – Silicon monochromator first crystal with cooling fins and stress relief cuts from SPring-8 (Matsushita and Hashizume, 2009).....	17
Figure 8 – Monochromator first crystal assembly currently used in I20 beamline monochromator at DLS (Docker, Alcock and Nistea, 2013).....	18
Figure 9 – CAD design of monochromator first crystal assembly currently used in I20 beamline monochromator at DLS. ....	18
Figure 10 – Heat deposited from broad-spectrum beam is transferred into heat exchanger and removed from the system by coolant .....	28
Figure 11 - Beam profile of the I20 beamline at Diamond Light Source, showing beam power as a function of x-ray wavelength. ....	35
Figure 12 - Beam penetration, showing beam power as a function of penetration depth in single crystal silicon.....	35
Figure 13 – One dimensional analytical model; temperature as a function of length for different crystal lengths L.....	36
Figure 14 – Scenario 1 analytical temperature profile: 77 K boundary temperature, $10^7$ W/m <sup>3</sup> power in, 50% power removed from each side. ....	40
Figure 15 – Scenario 2 analytical temperature profile: 77 K boundary temperature, $10^7$ W/m <sup>3</sup> power in, 100% power removed from cold side. ....	41

Figure 16 – Scenario 3 analytical temperature profile: 77 K boundary temperature, 500 W power in on right-hand boundary, 100% power removed from cold side.....	41
Figure 17 – Scenario 1 FEA temperature profile (K): 77 K boundaries temperature, $10^7$ W/m <sup>3</sup> power in throughout. ....	43
Figure 18 – Scenario 2 FEA temperature profile (K): 77 K boundary temperature, $10^7$ W/m <sup>3</sup> power in throughout. ....	44
Figure 19 – Scenario 3 FEA temperature profile (K): 77 K boundary temperature, 500 W power in at boundary .....	45
Figure 20 – Scenario 1 comparison: Analytical model on left, FEA model on right .....	46
Figure 21 – Scenario 2 comparison: Analytical model on left, FEA model on right .....	47
Figure 22 – Scenario 3 comparison: Analytical model on left, FEA model on right .....	47
Figure 23 – (Left to right) temperature dependent thermal conductivity (Glassbrener and Slack, 1964), coefficient of thermal expansion (Shah and Straumanis, 1972; Okada and Tokumaru, 1984) and specific heat (Marquardt, Le and Radebaugh, 2000) of silicon .....	49
Figure 24 – (Left to right) Temperature dependent thermal conductivity, coefficient of thermal expansion (National Institute of Standards and Technology (NIST), 1992) and specific heat (Marquardt, Le and Radebaugh, 2000) of copper. ....	51
Figure 25 – (Left to right) Temperature dependent thermal conductivity (Marquardt, Le and Radebaugh, 2000), coefficient of thermal expansion (Desai and Ho, 1978) and specific heat (Marquardt, Le and Radebaugh, 2000) of stainless steel 304 .....	52
Figure 26 – Conventional crystal assembly as used on the I20 beamline at Diamond Light Source. ....	54
Figure 27 – Mechanical boundary conditions for conventional assembly: a) bolt in copper base plate is held fully constrained; b) paired faces in mechanical contact; c) steel bolts pretensioned to 190 N .....	55
Figure 28 – Thermal boundary conditions for conventional assembly: a) internal surfaces of heat exchangers are held at 80 K; b) paired faces in thermal contact; c) all exterior faces radiate heat to an 80 K heat shield. ....	55
Figure 29 - Full conventional assembly cooling, FEA model: 3D model of assembly at 80K. Colour shows bolts remain slightly hotter than the rest of the assembly; black lines how initial assembly location (deformation increased in scale). ....	57
Figure 30 - Full conventional assembly cooling, FEA model: vertical displacement of diffracting surface. Copper heat exchanger shown to contract to a higher degree than silicon crystals. ....	58
Figure 31 – Full conventional assembly cooling, FEA model: pressure cross-section at forward steel bolt. Peak stresses observed at corners of copper heat exchanger with both silicon and steel. ....	58

Figure 32 – Design of cut-back indium foil. (Left) Indium foil covering entire silicon crystal surface with steel bolts passing through assembly. (Right) Indium foil covering most of silicon crystal surface, cut back 5 mm from diffracting surface.....	63
Figure 33 – Mechanical boundary conditions for isolated crystal: a) central point on bottom surface held fully constrained; b) line running through centre of crystal in z-direction held in x- and y-directions to prevent rotation.....	64
Figure 34 – Thermal boundary conditions for isolated crystal: a) the two long sides of the crystal held at a constant 80 K; b) all exposed surfaces modelled as radiating to an 80 K ambient temperature. ....	65
Figure 35 – Temperature plot (K) of isolated crystal at 0 (top), 0.1 (middle) and 1 (bottom) seconds after cooling begins.....	66
Figure 36 – (Top) Volume of crystal considered exposed to beam for heat deposition. (Bottom) Beam power deposition through the affected region of the crystal.....	68
Figure 37 – Isolated crystal exposed to incident beam showing surface deformation as a result of heating (K). .....	69
Figure 38 – (Top) Surface displacement of isolated crystal diffracting surface as a result of heating. (Bottom) Cross-section of sagittal plane (m), showing deformation variance of $1.02 \times 10^{-9}$ m.....	70
Figure 39 – Isolated crystal exposed to incident beam; isothermal layers mapped (K), with arrows showing movement of heat.....	72
Figure 40 – Thermal boundary conditions for isolated crystal (bottom cooled): a) bottom surface held at constant 80 K; b) all exposed surfaces radiating to an 80 K ambient temperature; c) central volume exposed to beam for heat deposition.....	73
Figure 41 - Isolated crystal exposed to incident beam and cooled on bottom surface showing more uniform surface deformation as a result of heating (K).....	74
Figure 42 - Isolated crystal exposed to incident beam and cooled on bottom surface; isothermal layers mapped (K), with arrows showing movement of heat.....	74
Figure 43 - (Top) Surface displacement of isolated crystal diffracting surface as a result of heating. (Bottom) Cross-section of sagittal plane (m), showing deformation variance of $7.58 \times 10^{-10}$ m.....	75
Figure 44 - Mechanical boundary conditions for ‘squared’ crystal: a) central point on bottom surface held fully constrained; b) line running through centre of crystal in z-direction held in x- and y-directions to prevent rotation.....	76
Figure 45 - Thermal boundary conditions for ‘squared’ crystal (side cooled): a) side surfaces of crystal held at constant 80 K; b) all exposed surfaces radiating to 80 K ambient temperature; c) central volume exposed to beam for heat deposition.....	77
Figure 46 – Temperature surface plot (K) of side cooled ‘squared’ crystal exposed to incident beam.....	78

Figure 47 – Side cooled ‘squared’ crystal exposed to incident beam; isothermal layers mapped (K), with arrows showing movement of heat. ....	78
Figure 48 - (Top) Surface displacement of side cooled ‘squared’ crystal diffracting surface as a result of heating. (Bottom) Cross-section of sagittal plane (m), showing deformation variance of $1.05 \times 10^{-9}$ m. ....	79
Figure 49 - Thermal boundary conditions for ‘squared’ crystal (bottom cooled): a) bottom surface of crystal held at constant 80 K; b) all exposed surfaces radiating to 80 K ambient temperature; c) central volume exposed to beam for heat deposition. ....	80
Figure 50 - Temperature surface plot (K) of bottom cooled ‘squared’ crystal exposed to incident beam.....	81
Figure 51 - Bottom cooled ‘squared’ crystal exposed to incident beam; isothermal layers mapped (K), with arrows showing movement of heat. ....	81
Figure 52 - (Top) Surface displacement of bottom cooled ‘squared’ crystal diffracting surface as a result of heating. (Bottom) Cross-section of sagittal plane (m), showing deformation variance of $8.70 \times 10^{-10}$ m. ....	82
Figure 53 - Mechanical boundary conditions for ‘bulk’ crystal: a) central point on bottom surface held fully constrained; b) line running through centre of crystal in z-direction held in x- and y-directions to prevent rotation.....	83
Figure 54 - Thermal boundary conditions for ‘bulk’ crystal (side cooled): a) side surfaces of crystal held at constant 80 K; b) all exposed surfaces radiating to 80 K ambient temperature; c) central volume exposed to beam for heat deposition. ....	84
Figure 55 - Temperature surface plot of side cooled ‘bulk’ crystal exposed to incident beam (K).....	85
Figure 56 - Side cooled ‘bulk’ crystal exposed to incident beam; isothermal layers mapped (K), with arrows showing movement of heat. ....	85
Figure 57 - (Top) Surface displacement of side cooled ‘bulk’ crystal diffracting surface as a result of heating. (Bottom) Cross-section of sagittal plane (m), showing deformation variance of $9.68 \times 10^{-10}$ m. ....	86
Figure 58 - Thermal boundary conditions for ‘bulk’ crystal (bottom cooled): a) bottom surface of crystal held at constant 80 K; b) all exposed surfaces radiating to 80 K ambient temperature; c) central volume exposed to beam for heat deposition.....	87
Figure 59 - Temperature surface plot of bottom cooled ‘bulk’ crystal exposed to incident beam (K).....	88
Figure 60 - Bottom cooled ‘bulk’ crystal exposed to incident beam; isothermal layers mapped (K), with arrows showing movement of heat. ....	88
Figure 61 – (Top) Surface displacement of bottom cooled ‘bulk’ crystal diffracting surface as a result of heating. (Bottom) Cross-section of sagittal plane (m), showing deformation variance of $8.63 \times 10^{-10}$ m. ....	89

Figure 62 - Mechanical boundary conditions for 'thin' crystal: a) central point on bottom surface held fully constrained; b) line running through centre of crystal in z-direction held in x- and y-directions to prevent rotation.....	90
Figure 63 - Thermal boundary conditions for 'thin' crystal (side cooled): a) side surfaces of crystal held at constant 80 K; b) all exposed surfaces radiating to 80 K ambient temperature; c) central volume exposed to beam for heat deposition.....	91
Figure 64 - Temperature surface plot of side cooled 'thin' crystal exposed to incident beam (K).....	92
Figure 65 - Side cooled 'thin' crystal exposed to incident beam; isothermal layers mapped (K), with arrows showing movement of heat. ....	92
Figure 66 – (Top) Surface displacement of side cooled 'thin' crystal diffracting surface as a result of heating. (Bottom) Cross-section of sagittal plane (m), showing deformation variance of $6.41 \times 10^{-9}$ m. ....	93
Figure 67 - Thermal boundary conditions for 'thin' crystal (bottom cooled): a) bottom surface of crystal held at constant 80 K; b) all exposed surfaces radiating to 80 K ambient temperature; c) central volume exposed to beam for heat deposition.....	94
Figure 68 - Temperature surface plot of bottom cooled 'thin' crystal exposed to incident beam (K). ....	95
Figure 69 - Bottom cooled 'thin' crystal exposed to incident beam; isothermal layers mapped (K), with arrows showing movement of heat. ....	95
Figure 70 – (Top) Surface displacement of bottom cooled 'thin' crystal diffracting surface as a result of heating. (Bottom) Cross-section of sagittal plane (m), showing deformation variance of $6.11 \times 10^{-9}$ m. ....	96
Figure 71 - Mechanical boundary conditions for 'wafer' crystal: a) central point on bottom surface held fully constrained; b) line running through centre of crystal in z-direction held in x- and y-directions to prevent rotation.....	97
Figure 72 - Thermal boundary conditions for 'wafer' crystal (side cooled): a) perimeter surfaces of crystal held at constant 80 K; b) all exposed surfaces radiating to 80 K ambient temperature; c) central volume exposed to beam for heat deposition. ....	98
Figure 73 - Temperature surface plot of side cooled 'wafer' crystal exposed to incident beam (K). ....	99
Figure 74 - Side cooled 'wafer' crystal exposed to incident beam; isothermal layers mapped (K), with arrows showing movement of heat. ....	99
Figure 75 – (Top) Surface displacement of side cooled 'wafer' crystal diffracting surface as a result of heating. (Bottom) Cross-section of sagittal plane (m), showing deformation variance of $2.90 \times 10^{-6}$ m. ....	100
Figure 76 - Thermal boundary conditions for 'wafer' crystal (bottom cooled): a) bottom surface of crystal held at constant 80 K; b) all exposed surfaces radiating to 80 K ambient temperature; c) central volume exposed to beam for heat deposition. ....	101

Figure 77 - Temperature surface plot of bottom cooled 'wafer' crystal exposed to incident beam (K). .....	102
Figure 78 - Bottom cooled 'wafer' crystal exposed to incident beam; isothermal layers mapped (K), with arrows showing movement of heat. ....	102
Figure 79 – (Top) Surface displacement of bottom cooled 'wafer' crystal diffracting surface as a result of heating. (Bottom) Cross-section of sagittal plane (m), showing deformation variance of $3.11 \times 10^{-8}$ m. ....	103
Figure 80 - Thermal boundary conditions for 'cut-back' crystal: a) long side surfaces of crystal held at constant 80 K from $z = -5$ mm down; b) all exposed surfaces radiating to 80 K ambient temperature; c) central volume exposed to beam for heat deposition. ....	104
Figure 81 – Temperature surface plot of side cooled 'cut-back' crystal exposed to incident beam (K). ....	105
Figure 82 - Side cooled 'cut-back' crystal exposed to incident beam; isothermal layers mapped (K), with arrows showing movement of heat. ....	105
Figure 83 – (Top) Surface displacement of side cooled 'cut-back' crystal diffracting surface as a result of heating. (Bottom) Cross-section of sagittal plane (m), showing deformation variance of $9.66 \times 10^{-10}$ m. ....	106
Figure 84 – Deformation variance of diffracting surface for all tested monochromator crystal designs and cooling locations; little of value can be observed due to the scale difference between the 'thin' and 'wafer' designs and the rest (note: y-axis on logarithmic scale). ....	108
Figure 85 – Deformation variance of diffracting surface for all viable monochromator crystal designs and cooling locations (note: y-axis no longer on logarithmic scale). ....	109
Figure 86 - Mechanical boundary conditions for directly cooled crystal: a) central point on bottom surface held fully constrained; b) line running through centre of crystal in z-direction held in x- and y-directions to prevent rotation; c) clamping force of 1,140 N applied on both outer faces. ....	119
Figure 87 - Thermal boundary conditions for directly cooled crystal: a) coolant channels held at constant 80 K; b) all exposed surfaces radiating to 80 K ambient temperature; c) central volume exposed to beam for heat deposition. ....	119
Figure 88 - Temperature surface plot of directly cooled crystal exposed to incident beam (K). ....	120
Figure 89 - Directly cooled crystal exposed to incident beam; isothermal layers mapped (K), with arrows showing movement of heat. ....	120
Figure 90 – (Top) Surface displacement of directly cooled crystal diffracting surface as a result of heating (m). (Bottom) Cross-section of sagittal plane (m), showing deformation variance of $8.045 \times 10^{-10}$ m. ....	121
Figure 91 - Mechanical boundary conditions for indirectly cooled crystal: a) central point on bottom surface held fully constrained; b) line running through centre of crystal in z-direction held in x- and y-directions to prevent rotation; c) clamping force of 570 N applied on both outer faces. ....	124

Figure 92 - Thermal boundary conditions for indirectly cooled crystal: a) long sides held at constant 100 K; b) all exposed surfaces radiating to 80 K ambient temperature; c) central volume exposed to beam for heat deposition.....	124
Figure 93 - Temperature surface plot of directly cooled crystal exposed to incident beam (K).....	125
Figure 94 - Directly cooled crystal exposed to incident beam; isothermal layers mapped (K), with arrows showing movement of heat. ....	125
Figure 95 – (Left) Surface displacement of directly cooled crystal diffracting surface as a result of heating. (Right) Cross-section of sagittal plane (m), showing deformation variance of $5.121 \times 10^{-8}$ m. ....	126
Figure 96 - Mechanical boundary conditions for indirectly cooled full crystal assembly: a) bolt on bottom surface held fully constrained; b) bottom surface of crystal assembly held in z-directions to prevent dropping; c) bolts pretensioned at varying clamping forces.....	129
Figure 97 – Graphs showing peak diffracting surface deformation variance of the I20 crystal assembly as a function of clamping force. ....	130
Figure 98 – (Left) Two bodies in contact without an interstitial material, showing air gaps. (Right) Two bodies in contact with an interstitial material, showing good fit. ....	138
Figure 99 – Thermal gap conductance simulation structure; two copper cylinders sandwiching a silicon cylinder. ....	141
Figure 100 - Mechanical boundary conditions for thermal gap conductance simulation: a) bottom surface held fully constrained; b) common z-axis held in x- and y-directions to prevent ejection or rotation; c) boundary load applied through top surface. ....	141
Figure 101 - Thermal boundary conditions for thermal gap conductance simulation: a) bottom surface held at constant 280 K; b) all exposed surfaces insulated thermally; c) top surface subjected to variable heat source. ....	142
Figure 102 – Difference in temperature profile between one 15 mm cooling pipe (left) and two 7.5 mm cooling pipes (right).....	143
Figure 103 – (Left) Schematic representation of thermal gap conductance experimental apparatus. Coolant loop and power supply not pictured. (Right) Force diagram of thermal gap conductance experimental apparatus.....	146
Figure 104 – Experimental data; temperature at each probe point was sampled at a rate of 10 per second. Probes are numbered 1 – 6 moving along the z-axis from the heater to the coolant.....	147
Figure 105 – Experimental data; temperature at each probe point at thermal equilibrium. Interface between two bodies was at 50 mm, visible as the end of each extrapolation. ....	147
Figure 106 – Thermal gap conductance experimental apparatus. Stress test machine is visible on the right-hand side of the picture, with copper cylinders, heater and coolant pipe in place. Note that the foil	

insulation has been removed for this image. Header tank with pumps and chiller unit are visible on the left-hand side of the picture. ....	148
Figure 107 – Experimental results: thermal gap conductance as a function of logarithmic clamping force with no interstitial material.....	149
Figure 108 – Experimental results: thermal gap conductance as a function of logarithmic clamping force for various interstitial materials.....	151
Figure 109 – Experimental results: thermal gap conductance as a function of clamping force for a new and pre-stressed piece of 500 $\mu\text{m}$ indium foil.....	152
Figure 110 – Experimental results: thermal gap conductance as a function of clamping force for a new and pre-stressed piece of 500 $\mu\text{m}$ indium foil rotated 90 °. ....	153
Figure 111 – Model of paired copper cylinders used in thermal gap conductance experiment; recess for heater at top of hot body and machined hole for coolant pipe at bottom of cold body. ....	154
Figure 112 – Mechanical boundary conditions for paired copper cylinders: a) bottom surface of cold body is held fully constrained; b) common z-axis held restrained in x- and y-directions; c) boundary load of 10 N in –z direction applied to top surface of hot body; d) paired faces in mechanical contact. ....	155
Figure 113 – Thermal boundary conditions for paired copper cylinders: a) internal surfaces of coolant pipe in cold body held at 13 °C; b) internal surfaces of heater recess in hot body subject to boundary heat source of 30 W; c) all external faces maintained as perfect insulators; d) paired faces in thermal contact with gap conductance of 1 136 W / m <sup>2</sup> K. ....	155
Figure 114 – Temperature surface plot of paired copper cylinders at thermal equilibrium. ....	156
Figure 115 – Calculated temperature throughout paired copper cylinders at thermal equilibrium.....	156
Figure 116 – Measured and calculated temperatures throughout paired copper cylinders at thermal equilibrium. ....	157
Figure 117 – Thermal interference fit; a) both components cold, shaft cannot fit in hub; b) hub heated up, shaft pushed into place; c) after hub has cooled, strong grip on shaft.....	163
Figure 118 – Pressure caused by interference fit as a function of room-temperature gap and current temperature. ....	166
Figure 119 – Model of ‘interference’ assembly; 30 $\mu\text{m}$ gap between sleeve and crystal, sleeve hollow to function as heat exchanger.. ....	168
Figure 120 – Mechanical boundary conditions for ‘interference’ assembly: a) point at bottom of crystal is held fully constrained; b) bottom surface of heat exchanger is held restrained in z-direction; c) common z-axis held restrained in x- and y-directions; d) paired faces in mechanical contact.....	168

Figure 121 – Thermal boundary conditions for ‘interference’ assembly: a) internal surfaces of heat exchanger held at 80 K; b) all external faces radiating to 80 K environment; c) paired faces in thermal contact.....	169
Figure 122 – Temperature surface plot of ‘interference’ assembly at thermal equilibrium (K).....	170
Figure 123 – Temperature surface plot of ‘I20’ assembly at thermal equilibrium (K).....	170
Figure 124 – (Top) Surface displacement of ‘interference’ assembly diffracting surface as a result of clamping. (Bottom) Cross-section of sagittal plane, showing deformation variance of $1 \times 10^{-6}$ m.....	171
Figure 125 – (Top) Surface displacement of conventional I20 crystal assembly diffracting surface as a result of clamping. (Bottom) Cross-section of sagittal plane, showing deformation variance of $17 \times 10^{-6}$ m. ....	172
Figure 126 – Complete ‘interference’ assembly; (Left) Silicon crystal inside copper heat exchanger. Brass retention peg visible at bottom left. Note that top of crystal has not been polished at this stage. (Right) Schematic view of ‘interference’ assembly, showing silicon crystal in copper heat exchanger. Brass retention pegs held on with steel bolts. Taper has been exaggerated to be easily visible.....	175
Figure 127 – ‘Interference’ assembly components disassembled; tape measure at bottom for scale. ....	176
Figure 128 – ‘Interference’ assembly held in cold finger; cold finger continues to liquid nitrogen coolant receptacle to right. ....	177
Figure 129 – ‘Interference’ assembly experimental apparatus. (Top) Vacuum vessel with clamp centred and cold finger running to liquid nitrogen receptacle on left. (Bottom) ‘Interference’ assembly located in clamp. Stress relief cut visible to left of assembly. PT-100s on rear of crystal and heat exchanger. ....	179
Figure 130 – ‘Interference’ assembly experiment: scan of diffracting surface at room temperature and vacuum. ....	180
Figure 131 – Experimental data: surface displacement of diffracting surface as a result of clamping and cooling showing diffracting surface deformation variance of 30 nm. ....	181
Figure 132 – ‘Interference’ assembly experiment: surface profile of diffracting surface as a result of clamping and cooling showing deformation at various temperatures. Note that lines on graph are in same order as series on legend.....	181
Figure 133 – ‘Interference’ assembly experimental results; graph of temperature of both silicon and copper components and calculated gap as a function of time. Note that once calculated gap becomes zero, the two components are in contact.....	182
Figure 134 – Conventional I20 assembly experiment: surface deformation of diffracting surface as a result of cooling showing diffracting surface deformation variance of 400 nm. ....	183

## Equations

Equation 1 – Bragg diffraction.....	11
Equation 2 – Equation of linear expansion.....	21
Equation 3 – Stress induced by constrained thermal expansion .....	22
Equation 4 – Equation for the absorption of a beam.....	29
Equation 5 – Beer-Lambert law .....	29
Equation 6 – Transmitted power as a function of wavelength .....	29
Equation 7 – Grey body radiation.....	30
Equation 8 – One dimensional Fourier’s Law .....	30
Equation 9 – Fourier’s law for adjacent elements.....	33
Equation 10 – Simplified conduction equation for a time dependent system .....	33
Equation 11 – Power flow over a thermal interface .....	139
Equation 12 – Simplified equation for thermal gap conductance .....	139
Equation 13 – Pressure caused by an interference fit. ....	165
Equation 14 – Force caused by linear thermal expansion.....	167

## Tables

Table 1 – Progression of synchrotron devices showing location, commissioning date and dependence of beam current on radius .....	12
Table 2 – Details of interstitial materials tested for effect on gap conductance and reason material was chosen for testing.....	150

## Glossary

CTE	Coefficient of Thermal Expansion
DBCM	Double Bounce Crystal Monochromator
DLS	Diamond Light Source; synchrotron in Oxfordshire, England
FEA	Finite Element Analysis
IM	Interstitial Material
Linac	LINear ACcelerator
QBCM	Quad Bounce Crystal Monochromator
SPring-8	Super Photon RING-8; synchrotron in Hyogo, Japan

## Abstract

Synchrotrons are particle accelerators that generate high intensity X-ray light, which is used in various disciplines including medicine (for protein sequencing), engineering (for strain analysis) and archaeology (for examination of fragile artefacts). These processes require monochromatic X-ray radiation, leading to the need for synchrotron monochromator devices. These devices are subject to demands of greater beam power and smaller footprints, such that higher resolutions can be achieved and more beamlines can be installed, as higher beam powers boost the signal to noise ratio of the experiments. This has exposed limitations in current, conventional first crystals assembly, as the heat dissipation required is very high; the first crystal receives the full beam power, and only 5-10 % is diffracted to the second crystal with the rest absorbed as heat. Through a focus on five key areas of weakness in first crystal design philosophy, a novel monochromator assembly has been constructed. The novel assembly is unconstrained at room temperature and through the use of mechanical properties is held in a firm grip at cryogenic temperatures. The deformations caused by clamping and cooling in the novel design and in a conventional design were compared experimentally; the novel design was found to exhibit surface deformations an order of magnitude lower when clamped and cooled than those observed in the conventional design due to cooling alone. The novel design had the temperature of both the crystal and heat exchanger monitored and was found to be in excellent thermal contact at cryogenic temperatures.

## Acknowledgments

Many thanks to the Diamond Light Source for funding this project, without which I could not have completed this work.

Heartfelt thanks to Michael Ward and Peter Docker, for helping me every step of the way from base principles to experimental testing, and for always having time for a (decaf) tea or coffee and a chat, and to Richard Cornish for always showing interest.

Special thanks to John Sutter, Sofia Díaz-Moreno and Jim Kay, for showing interest in my research and helping review papers, provide vital data and spend time conversing despite very busy schedules.

Also to Nitika Chadha, whose practical problems helped shift my focus and clear my mind when I was stuck.

And eternal gratitude to my father, Chris Stimson, for inspiring my scientific mind and instilling a work ethic from childhood; my mother, Sue Stimson, for always believing in me and praying for me; my brother, Connor Stimson, who always helps keep me grounded (brutally, at times); and especially my wife, Becky Stimson, who has inspired (and forced) me to work and has stood by me through the stressful times and kept me sane.

## Introduction

Synchrotron devices are particle accelerators that specialise in the production of broad-spectrum, high-intensity X-ray radiation. This is achieved through perturbing the path of relativistic electrons through the use of a series of opposing pole magnets referred to as an undulator or wiggler, such that they emit photons in rapid sequence resulting in an X-ray beam. For the vast majority of applications monochromatic X-rays are needed rather than broad-spectrum; as such, a series of crystals referred to as a monochromator are used to select a single wavelength via Bragg diffraction. A standard beamline is shown in Figure 1 below (Aragão *et al.*, 2018).

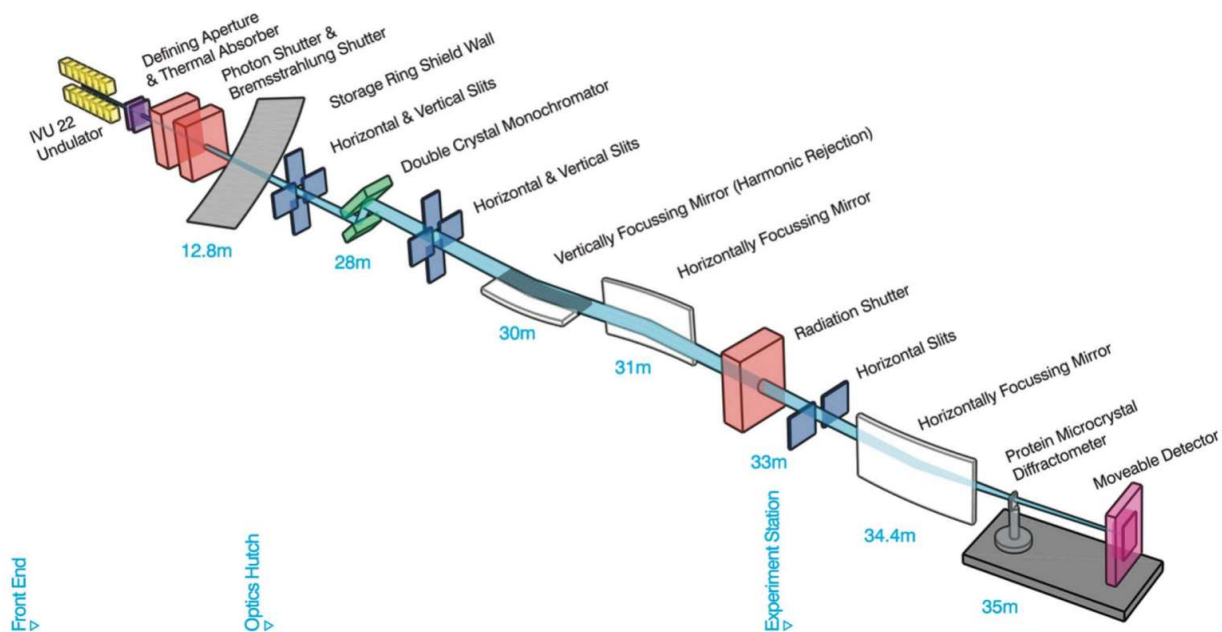


Figure 1 – Standard synchrotron beamline from undulator to beyond double bounce crystal monochromator (Aragão *et al.*, 2018).

This project aims to develop a novel monochromator first crystal in order to deal with high heat loads from next generation, high power beams. As the first crystal is exposed to the full synchrotron beam powers, of which 90 % is absorbed as heat and 10 % diffracted to the second crystal, the thermal load on the first crystal is significant and is thought to cause significant thermal deformation, impinging the monochromaticity and collimation of the diffracted beam. The novel monochromator

first crystal must be able to dissipate Megawatts of heat per cubic metre while keeping the diffracting surface flat. Many current crystals struggle with this as if the clamping forces are too high the crystal is deformed by non-uniform excess stress, while if the clamping forces are too low the crystal is deformed by non-uniform excess heat.

The first objective of the project was to understand exactly what mechanisms caused heating, heat transfer and cooling in the monochromator crystal. This gap in the background knowledge was exposed by the literature review, which found no studies of the underlying mechanisms. The power absorption was matched to the Beer-Lambert law (Beer, 1852), integrated across all wavelengths for separate absorption coefficients. It was assumed that the heat transfer within the crystals was mainly due to conventional conduction and that heat was lost through both the rear surface, by conduction to the liquid nitrogen coolant, and through the front surface, by grey body radiation (Rogers and Mayhew, 1967; Kreith, Manglik and Bohn, 2010; Venkenna, 2010).

Using these basic principles, it was possible to construct a one dimensional analytical model (Cannon, 1984). Experimentation with this model gave rise to two interesting concepts. The first of these is that if the heat loss from the front surface is increased, it is theoretically possible to drive the peak temperature of the crystal further into the bulk, reducing the thermal distortion at the surface. The second, that the thinner the crystal was the lower the peak temperature became, which is in direct contravention to the traditional approach, i.e. if the crystal is overheating, make it bigger (Stimson et al., 2016).

To ratify the one dimensional model an identical model was constructed using finite element analysis software, in this case COMSOL Multiphysics ('COMSOL Multiphysics', 2013). The FEA model matched very closely to the analytical model, and the same concepts were apparent. Further more realistic, three dimensional models of the monochromator crystal and heat exchange assembly used

in the I20 beamline at Diamond Light Source were developed. This led to interesting results showing that the different materials in the heat exchange assembly undergo thermal contraction at different rates, putting stress on and deforming the monochromator crystal before the beam even strikes it.

The next priority was to examine the beam itself in order to accurately model the complete system. In order to do this the beam spectrum was provided by Sophia Moreno-Díaz in the form of flux as a function of energy. This was converted into power as a function of wavelength, then applied in tandem with the absorption (in the form of the Beer-Lambert law, as mentioned previously). This allowed the absorbed power as a function of position to be directly input into the FEA program, generating a heat flux within the material.

Having constructed a complete, detailed model of the existing monochromator system, focus shifted to looking at new monochromator first crystal geometries that might mitigate the thermal deformation (Joshua Stimson et al., 2017).

In order to improve the accuracy of the models, material properties have been expressed as a function of temperature and included in the models. This has shed light on an interesting phenomenon, the negative coefficient of thermal expansion of silicon, having a significant effect on model designs (Shah and Straumanis, 1972).

A contact modelling technique has been explored and implemented to further increase the accuracy of the finite element analysis models against the real systems.

Experimental work has been performed to examine the variables influential on an indirect cooling system to improve the thermal contact in indirect cooling models, focusing on thermal contact conductance (Milanez, Yovanovich and Culham, 2002; Salerno and Kittel, 2003), i.e. the flow of heat between two bodies in contact. By utilising different clamping forces and interstitial materials, the

mechanisms to maximise contact conductance have been explored such that the most heat flows from the hot surface to the cold.

Two strong trends were observed from experimental work: first, that increasing the clamping force increases the gap conductance in an indirect cooling system significantly but with diminishing returns; and second, that the malleability of an interstitial material has a far greater effect than its conductivity, with a malleable insulator performing significantly better than an inflexible conductor.

In further experimental work a novel monochromator was assembled as a cylindrical silicon crystal loosely fitted in a copper heat-exchange sleeve, brought into contact as an interference fit (Moorefield, 1993; Tipler, 1999) at cryogenic temperatures to provide a uniform stress field at a pre-selected clamping force (J. Stimson et al., 2017).

This showed significant promise in the new monochromator design; between an unclamped, room temperature assembly and a clamped, cryogenic temperature assembly the deformation introduced registered only one tenth that of a conventional system between clamped, room temperature and clamped, cryogenic temperature. This new design holds potential to revolutionise the synchrotron industry, allowing far greater beam powers to be used than is currently possible.

The new design fulfils the design requirements, providing a small footprint first crystal assembly which is capable of dissipating high thermal loads comparable to next generation synchrotron device energies while maintaining a diffracting surface flatness an order of magnitude greater than that observed in conventional designs.

Each chapter below begins with a brief review of the thesis up to that point and ends with an executive summary of the chapter to make reading easier.

# 1. Literature Review

## 1.1 Introduction

This work has three key aims: first, to investigate and understand the way in which heat moves through a system; second, to use this knowledge to attain a deeper understanding of why synchrotron monochromator first crystals are struggling with higher heat loads; and finally to design, manufacture and test a novel solution, using the information learned to improve the performance of the monochromator crystal under significant thermal stress.

There is a significant quantity of literature detailing the invention and progression of synchrotron devices through the years; however, the vast majority of it deals with the core engineering, detailing what has happened and what steps have been taken but rarely delving into the why. This literature gap, once filled, should grant a deeper understanding of the problem, allowing the development of new intelligent designs such that much higher beam powers can be utilised with smaller crystals.

There are a number of core terms specific to this field. A selection of the most useful that will be frequently referred to in this work can be found here:

- Synchrotron – a particle accelerator that uses relativistic effects to produce high intensity X-rays (Gooden, Jensen and Symonds, 1947)
- Monochromator – a crystal that selects small spectrums of light from a wider-spectrum incident beam (Bonse *et al.*, 1976)
- Bragg diffraction – a system of absorption and reemission by which monochromators select their narrow spectrum (Bragg and Bragg, 1913)

## 1.2 History of Synchrotron Devices

The first synchrotron was designed as a modification to the cyclotron, a particle accelerator consisting of two magnets suspended one above the other (Veksler, 1944; Gooden, Jensen and Symonds, 1947; Wilson, 1996). The limit of power for a cyclotron was determined by the size of the magnets; as electrons were accelerated to greater and greater speeds, their circular path moved further and further towards the edge of the magnets until eventually the particle broke free. Each cyclotron required a large amount of trial and error to determine what path the particles would take. Today synchrotrons are constructed of straight lengths joined by electromagnetic beam benders (Torikoshi *et al.*, 2001) which serve to both shape the beam and function as injection devices, emitting X-rays along beamlines, in which electron beams are accelerated to and maintained at relativistic speeds.

A synchrotron consists of a series of particle accelerators as shown in Figure 2 below. Free electrons are generated at one end of the linear accelerator (or Main Injector), which are then accelerated up to high speeds. This is necessary as the annular design of a synchrotron means any device that produces free electrons would otherwise obscure the annular accelerator. The free electrons are then fired into a relatively small annular particle accelerator, known as a booster ring. This device accelerates them up to relativistic speeds through the use of electromagnetic pulses; each electron will undergo multiple circuits through the booster ring until they reach relativistic speeds (i.e. speeds a significant proportion of the speed of light), at which point they escape the magnetic fields of the booster ring into the larger, more uniform storage ring. The electrons are maintained at this energy in the larger annular ring utilising a strong, constant electromagnetic field (McMillan, 1945; Gooden, Jensen and Symonds, 1947; Wilson, 1996; Sham and Rivers, 2002). Over time, the electrons escape either by losing too much energy and falling into one of the powerful beam bending magnets or by gaining too much energy and escaping the storage ring; as such, at regular intervals

additional electron beams are accelerated through the linac and the booster ring. The period between any two such injections is known as a cycle.

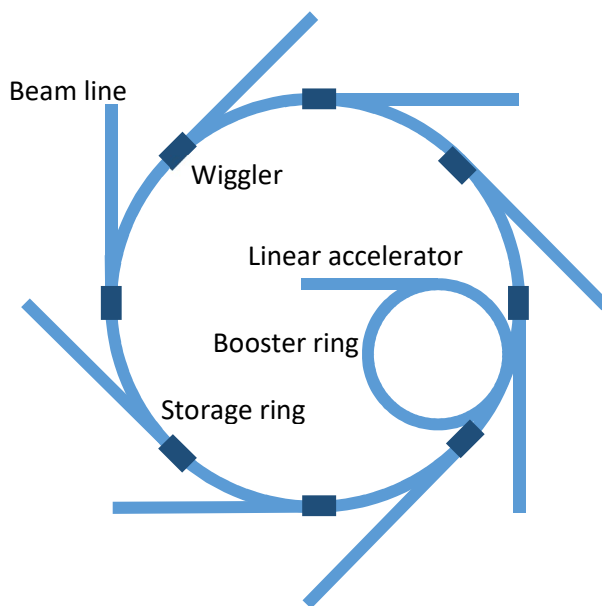


*Figure 2 – Layout of a standard synchrotron device*

These relativistic particles are then perturbed on their paths through the use of devices known as wigglers or undulators, each of which is a series of opposing pole electromagnets (Sham and Rivers, 2002). By oscillating the particles in this way broad spectrum light is generated along a tangential beam path, known as a beam line. This is due to the relativistic speeds of the electrons; as the particles move at near the speed of light, the influence of the magnetic field upon them accelerate them lateral to their direction of motion. However, due to their near-light speed, the particles cannot move faster as they are accelerated; instead the excess energy is emitted as a photon. Due to general relativity, the photon is emitted at light speed from the particle, just as though the particle were standing still (Tipler, 1999). As such, the photon has not travelled far from the electron by the time it reaches the next magnetic field, which deflects it in the opposite direction. This causes the photons emitted by the electron to form very small wavefronts, in the region of 0.01 to 10 nm, creating X-ray

radiation. The light produced by a synchrotron is brighter than that produced by any other source on Earth and consists predominately of X-rays (Wilson, 1996).

The x-ray beams generated in this way are broad spectrum, with a wide range of x-ray frequencies being generated. Most applications for x-ray radiation require a narrow spectrum, down to a single wavelength; as such the broad wavelength beam must be filtered down to one wavelength. First, the beam passes through a series of filters designed to block out non-X-ray light. After this, the beam is diffracted off of a series of regular crystals, altogether known as a monochromator. These crystals use Bragg diffraction (Bragg and Bragg, 1913) to select a single wavelength of light. Bragg diffraction is a phenomenon unique to materials that both have a regular crystal lattice and are transparent to the wavelength of light in use. As the light falls on the lattice, it is absorbed by the atoms of the crystal lattice and rapidly re-emitted. Depending on the lattice spacing of the material and the angle of incidence of the beam, as shown in equation 1 below, one frequency of the light re-emitted by the crystals experiences constructive interference while the other wavelengths interfere destructively (Beaumont and Hart, 2001), mostly being reabsorbed as heat. This results in a narrow spectrum of x-ray radiation being emitted from the crystal in a coherent beam.

Two materials are commonly used for Bragg diffraction: silicon or diamond. Diamond is commonly used for small footprint beamlines, as it is a sturdier but more expensive material; silicon is used in a wider variety of facilities. In the case of silicon, it is usually mounted such that the 111 crystal plane is parallel to the top surface of the crystal, providing a lattice spacing of 5.431 Å (Okada and Tokumaru, 1984). As the angle between the 111 and 311 plane of single crystal silicon is 29.5°, a second crystal of 311 orientation is used to select any wavelengths that would require an angle of incidence greater than this value.

$$n\lambda = 2d \sin \theta \quad [1]$$

Where  $\lambda$  is the wavelength desired

$d$  is the lattice spacing

$\theta$  is the angle of incidence.

Usually, two of these regular crystals are used in series, known as a double bounce crystal monochromator (DBCM) in order to refine the beam; as the first crystal is subject to much higher beam intensities it is likely to deform to some degree, sending more than the required wavelength on to the second crystal (Bonse *et al.*, 1976; Roessle, 2012). The second crystal then filters out the noise present in the beam, with a clean, narrow-spectrum, collimated x-ray beam being emitted in the desired direction.

The high-intensity x-ray light produced by synchrotron devices has a wide range of applications. It has been used to image protein structures, constructing a 3D map of various protein chains including the HIV virus (Zheng *et al.*, 2001; Goldstone *et al.*, 2011); it has been used in mechanical engineering, to evaluate residual stress on a number of building components (Fitzpatrick and Lodini, 2003; Hills, 2009); it has even been used by archaeologists and anthropologists, using the synchrotron to measure the relative density on ancient scrolls, too fragile to unravel, but by measuring the densities of different areas using synchrotron radiation a 3D map of the rolled scroll can be constructed and digitally unfolded (Dooryhée *et al.*, 2004; Murphy *et al.*, 2010). The limiting factor on the resolution of images generated with the synchrotron radiation is the power of the x-rays used; this has been limited to date by the performance of the monochromator crystals.

### 1.3 Development of Current Monochromator Systems

There has been a long period of innovation resulting in the powerful synchrotron devices currently in use. Table 1 below shows a list of synchrotrons both past and present, with their commission dates, radii and maximum power outputs (Boldeman, 2002; *NSLS-II Source Properties and Floor Layout*, 2010; Hill *et al.*, 2011). It is interesting to note that there is a linear relationship between commission date and energy, and between radius and power. This is expected from physics, as the energy required for a particle to escape the accelerator increases as the size of accelerator increases. Many beamlines are designed to cope with a specific intensity of x-rays, often controlled by the style of monochromator used at that facility.

*Table 1 – Progression of synchrotron devices showing location, commissioning date and dependence of beam current on radius*

Facility Name	Location	Electron Energy (GeV)	Beam Current (mA)	Radius (m)	Commissioned
<b>Birmingham Synchrotron</b>	Birmingham, UK	1	-	4.5	1953
<b>Australian Synchrotron</b>	Melbourne, Australia	3	200	216	2006
<b>Diamond Light Source</b>	Oxfordshire, UK	3	350	562	2006
<b>National Synchrotron Light Source II</b>	Brookhaven National Laboratory, USA	3	500	792	2015

When higher powers are used in synchrotron devices, primarily to increase the resolution of any generated image, more energy is absorbed by the first monochromator crystal as only a small portion of the generated spectrum is diffracted to the second crystal, with the rest being absorbed. Initially these energies were low enough that monochromators could be water cooled, but with the higher beam currents and photon energies the amount of waste heat absorbed results in a water cooling system failing due to evaporation of the water; instead, liquid nitrogen systems are used to cool with a greater efficiency (Bilderback, 1986; Bilderback *et al.*, 2000; Carpentier *et al.*, 2001); by using a colder liquid coolant, the thermal transport properties of the materials are increased and the heat

can be extracted from the system more rapidly. With the advent of these improved cooling systems, many synchrotrons optics now operate around 120 K, the practical effects of which are explored in Section 2.5.

When using any cooling system, there are two methodologies that can be applied. The body to be cooled, in this case a monochromator first crystal, can be cooled either directly, through the application of the cooling medium directly to the body, or indirectly, in which case the cooling medium is applied to a heat exchanger which is mechanically attached to the body to be cooled (Kreith, Manglik and Bohn, 2010). There is a debate in the synchrotron community as to which of these methodologies is better (Marion, Zhang and Goirand, 2006) – while direct cooling is more efficient than indirect cooling, it is also harder on the components of the systems and tends to have a limitation on the number of thermal cycles possible before components need replacing. To form a gas-tight seal against the silicon, indium gaskets are inserted between the crystal and the coolant manifold. As the system undergoes thermal cycling, these gaskets are subject to increased stress causing increased fatigue and damaging the seal. Examples of indirect and direct cooling are shown in Figure 3 below. This dichotomy is examined further in Chapter 4.

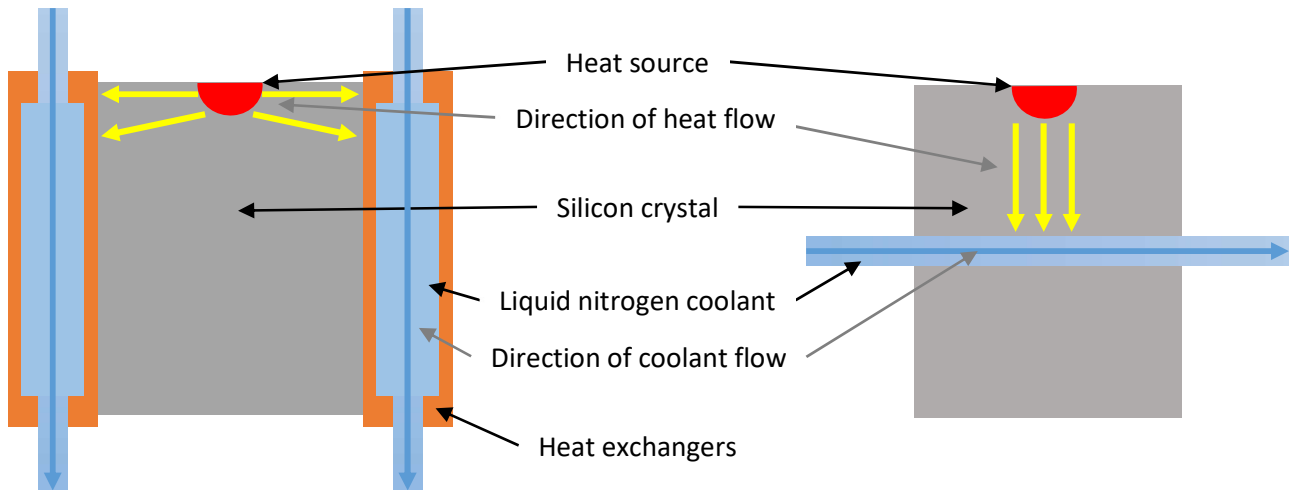
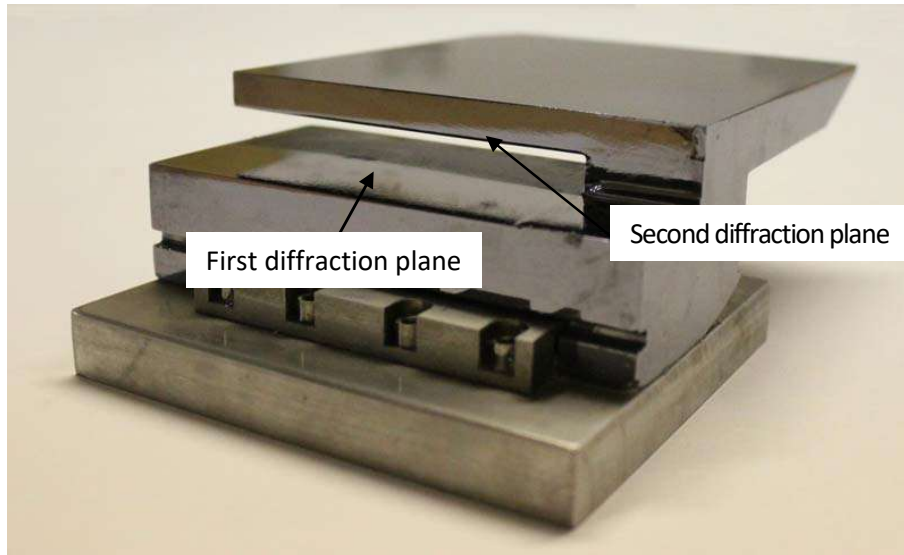


Figure 3 – (Left) Indirect cooling system; coolant flows through heat exchangers, heat travels from crystal to heat exchanger to coolant.

(Right) Direct cooling system; coolant flows through crystal directly, heat flows from crystal to coolant.

In order to improve the alignment of the monochromator system, channel cut crystals have been designed as shown in Figure 4 below (*Crystal Scientific, 2011*). These crystals feature a trench machined into the silicon, such that the two opposing faces are used as the first and second crystals. This maintains the separation and alignment of the monochromators, while also ensuring the lattice planes in the two diffracting surface are parallel. However, the narrow gap limits the ability to polish the diffracting surfaces, leading to a higher chance of optical aberrations, and the interconnected crystals removes the ability to scan the beam over a sample without changing the wavelength of x-rays used.



*Figure 4 – Channel-cut monochromator crystal; beam diffracts from top of first diffraction plane, then from bottom of second diffraction plane.*

One suggested solution to perform energy and spatial scans is a quad bounce crystal monochromator (QBCM) as shown in Figure 5 (Mosselmans, 2018), wherein four crystals are used (Collins, Wagner and Rau, 2010; Wagner *et al.*, 2013). Although this allows a greater control over the scanning function of the system, a QBCM is more susceptible to deformation of the first crystal as the middle two crystals are in a dispersive alignment (Huang *et al.*, 2012). In a standard DBCM setup, any beam spreading caused by deformation induced in the first crystal is maintained through the second crystal; as such, thermal deformations are allowable if they are not too severe. However, in a QBCM setup, any beam spreading from the first crystal is maintained through the second crystal but is then magnified in the link between the second and third crystals, as shown in Figure 6 below, before being maintained past the fourth and final crystal. In order to perform energy scans, in which multiple X-ray wavelengths are passed through a specified point, or spatial scans, in which one X-ray wavelength is passed through a range of locations, the optimal solution would therefore be a QBCM with minimised deformation of the first crystal.

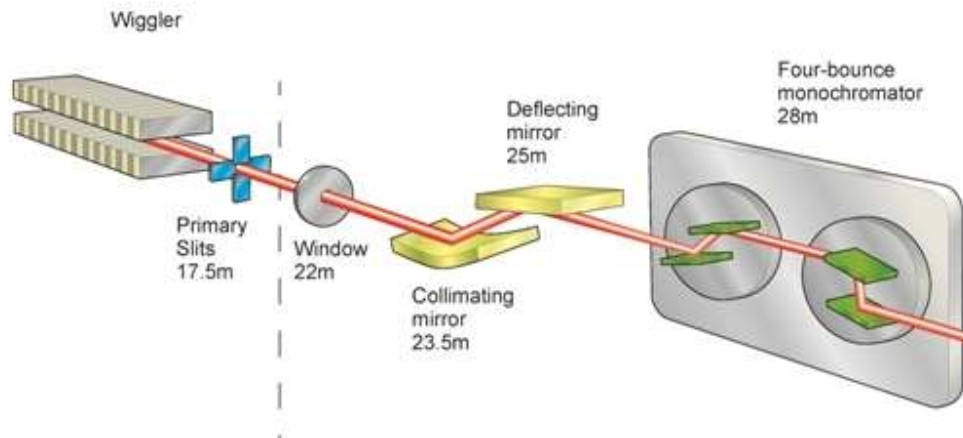


Figure 5 – Synchrotron beamline from wiggler to beyond quadruple bounce crystal monochromator

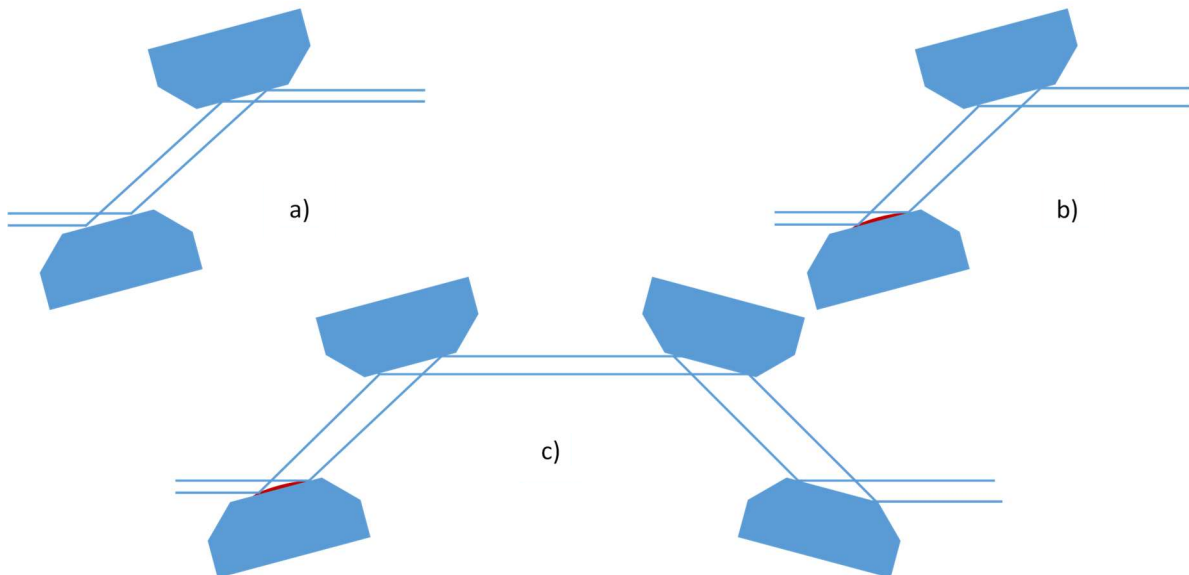
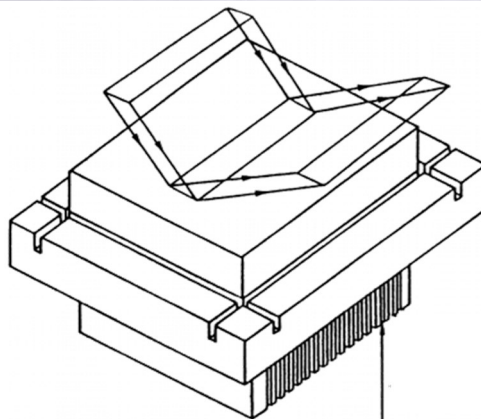


Figure 6 – Demonstration of the dispersive link observed in a QBCM; a) The collimated beam diffracts from the first crystal to the second crystal, b) Thermal deformation in the first crystal leads to beam spreading, which is maintained through diffraction at the second crystal, c) Spread beam is diffracted from third crystal, exacerbating beam spreading. Beam is much more dispersed after diffraction from the fourth crystal.

Different beamlines use a wide variety of different crystal geometries. The most basic geometries are large, cuboid pieces of silicon bolted between two pieces of copper, while more complex designs feature stress relief cuts, cooling fins and use of negative space to allow x-rays to pass through. A few examples of silicon monochromator crystals are given in Figure 7 and Figure 8 below, with a CAD

file of Figure 8 presented in Figure 9. Due to the semi-competitive nature of different synchrotron facilities, very little comparative work has been done between different crystal designs.



*Figure 7 – Silicon monochromator first crystal with cooling fins and stress relief cuts from SPring-8 (Matsushita and Hashizume, 2009).*

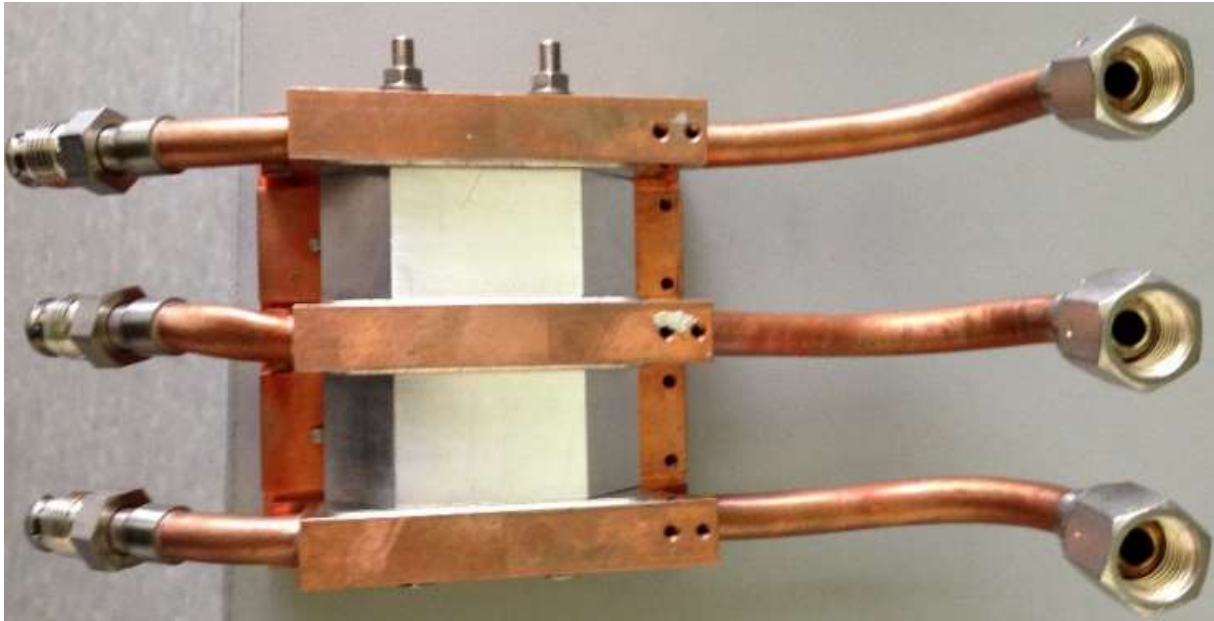


Figure 8 – Monochromator first crystal assembly currently used in I20 beamline monochromator at DLS (Docker, Alcock and Nistea, 2013).

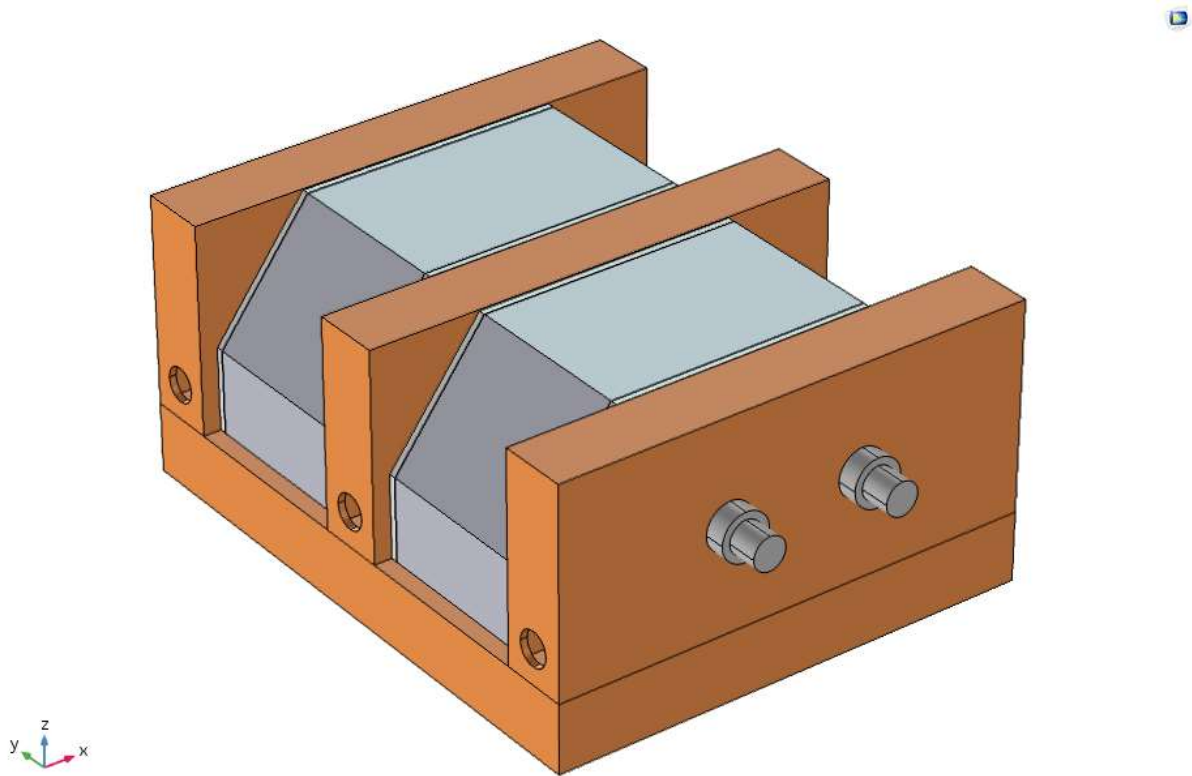


Figure 9 – CAD design of monochromator first crystal assembly currently used in I20 beamline monochromator at DLS.

## 1.4 Limitations of Current Systems

Current system designs are sufficient for current power requirements and resolutions; however, along with the constant push to increase the powers used in the synchrotron devices to increase resolution, there is also a recent move to develop more ‘spur’ beamlines, in which two or more beamlines share the output from a single wiggler or undulator. While the power and quantity of x-rays produced is sufficient for this design, the limitation of the physical space requires smaller monochromator crystals. The current design philosophy is to use a crystal significantly larger than the beam footprint, in order to allow the worst thermal deformation, which occurs at the edges of the crystal, to remain outside of the diffracting area. With the new move towards crystals of similar size to beam footprints, this area of greater deformation is being forced into the diffracting region. In addition, improving indirect cooling efficiency has largely been achieved through applying additional clamping force to hold heat exchangers to crystals, an approach which is limited by the introduction of mechanical deformation into the crystal (Bilderback *et al.*, 2000).

A large number of works have been performed detailing the performance of individual monochromators; however, these works tend to be theoretical, exclusively making use of FEA software or similar models (Marion, Zhang and Goirand, 2006; Zhang *et al.*, 2013). While FEA is a powerful tool, it is limited by the user’s understanding of the initial and boundary conditions, resolution of the free elements, and accuracy of geometry. If the data input into an FEA model is perfect, then its output will be perfect; however, with each inaccuracy the output of the model deviates further and further from correct. As such, theoretical works should be considered as part of a solution but not an entirety unto themselves unless supported by experimental results.

Many of these works also treat thermal deformation as something to be worked into the design of the monochromator crystals, rather than as a problem to be resolved (Marion, Zhang and Goirand,

2006; Zhang *et al.*, 2013). While this approach does produce novel solutions regarding heat management and stress relief, it discounts the possibility of removing the root of the thermal deformation which would improve the performance of the Bragg diffraction.

An aspect that is underexplored in the literature is the development of deformation caused by clamping and cooling monochromator assemblies. As higher and higher clamping forces are used, either to improve the thermal conductance in indirectly cooled systems or to form a seal in directly cooled systems, these forces are usually effective upon the body of the crystal itself (Tipler, 1999). This can give rise to structural deformations at many points in the assembly of a monochromator, including the initial assembly, application of clamping forces, attachment of coolant lines and even during cooling itself. Effectively in order to reduce thermal stresses in the system many solutions instead introduce mechanical stresses. It is important to isolate these two sources of deformation and examine them, with the goal of using the two deformations against one another to minimise deterioration of the diffracting surface. This concept is developed upon in Section 4.4.

Deformation of the crystal diffracting surface causes the angle of incidence of the beam and the lattice spacing of the crystal to become non-uniform; this affects the Bragg diffraction at the crystal surface, selecting a wider range of X-ray wavelengths than desired, as well as affecting the collimation of a diffracted beam, as diffracted X-rays will travel at an angle equal to the angle of incidence. These two issues, combined with the presence of at least one additional monochromator crystal, causes only some sections of the beam to be present at the end of the monochromator; this masked beam is not suitable for testing. The acceptable surface roughness of a monochromator crystal is  $< 10 \text{ \AA}$  root mean square, so any deformation significantly greater than this would render a crystal unsuitable for usage.

## 1.5 Thermomechanical Coupling

One aspect to be considered is the interaction between thermal effects and mechanical effects, particularly in regards to how stresses and deformations are affected by temperature. Unlike with other stress factors temperature does not couple directly into stress factors; instead the varying of temperature causes the material properties of components to change, altering how the material interact and respond to altering forces. This concept is expanded upon in Section 2.5.

Changes in temperature do cause materials to change in size. This size change can exert a significant force if obstructed, whether the material is extracting or contracting. For any given material, in any given direction, the expansion (or contraction) due to a change in temperature is defined by equation 2 below (Tipler, 1999).

$$\Delta L = L\alpha_L\Delta T \quad [2]$$

Where  $\Delta L$  is the change in length.

$L$  is the initial length.

$\alpha_L$  is the linear expansion coefficient.

$\Delta T$  is the change in temperature.

Where this expansion is constrained, i.e. the material is prevented from expanding or contracting, a strain is induced in the material. This strain can reach significant amounts over small temperature changes; given monochromator first crystals range between 300 K and 80 K, the thermal strain must be considered as a major influence on the system. The thermal strain is calculated using equation 3 below (Stronger and To, 1991).

$$\sigma = E\alpha_L\Delta T \quad [3]$$

Where  $\sigma$  is the thermal stress.

$E$  is the Young's modulus of elasticity.

$\alpha_L$  is the linear expansion coefficient.

$\Delta T$  is the change in temperature.

## 1.6 Fundamental Principles for Designing a Novel Crystal Assembly

In order to develop a new and improved monochromator assembly, the first priority is to understand the mechanisms of thermal transport through the system. Thermal transport itself is a well-researched field, with many works and textbooks existing on thermal transport covering energy absorption (Lambert, 1760; Beer, 1852; IUPAC, 2006), conduction (Tipler, 1999; Kreith, Manglik and Bohn, 2010) and radiation (Holman, 1997; Tipler, 1999; Kreith, Manglik and Bohn, 2010), as well as various works on mechanical properties and their relation to heat, but very little of these works are tied to or even cited in monochromator crystal design. A theoretical examination of thermal transport in the system is established in Chapter 2, and a published paper on the subject (Stimson *et al.*, 2016) is included in Appendix A.

As there are so many different styles of monochromator crystal it will be useful to explore how differing crystal designs affect thermal and mechanical deformations. The development of cooling fins, stress relief cuts and bolting surfaces have resulted in a wide range of crystal designs, but no overarching work has been completed to compare the efficiency of the different approaches. This concept is developed further in Chapter 3, and a published paper on the subject (Joshua Stimson *et al.*, 2017) is included as Appendix B.

The next aspect that needs to be better understood to develop a novel solution is the potential benefits and drawbacks to both direct and indirect cooling. Some work has been compiled on the matter (Marion, Zhang and Goirand, 2006) but further research is necessary to conclusively state whether the benefits of direct cooling outweigh its drawbacks. This work is presented in Chapter 4.

One aspect of indirect cooling that requires more in depth examination is how the thermal interface can be modified, potentially to improve the efficiency. A number of works have looked at how clamping forces and interstitial materials affect heat flow across a gap (Snaith, O'Callaghan and

Probert, 1984; Milanez, Yovanovich and Culham, 2002; Salerno and Kittel, 2003; Madhusudana, 2014), but due to the complex nature of thermal contact conductance it will be necessary to examine this aspect as a potential method to improve the efficiency of indirect cooling. This work is detailed in Chapter 5 and Appendix D.

The final aspect to consider is whether a novel first crystal assembly can be designed using the information gained in the preceding Chapters. By identifying the limitations in each of these fields, the novel design can be engineered from base principles to give the best possible thermal and mechanical performance. This work is detailed in Chapter 6 and Appendix E.

## 1.7 Conclusion

Overall, the development of synchrotron monochromators has been well documented in literature, with each new synchrotron and beamline spawning at least one paper detailing how its monochromator will work. However, each of these papers addresses how the system has been designed and built, with very little investigation into the why. This literature gap, if filled, could improve the performance of monochromators drastically as utilising the underlying theory will allow new monochromators to be designed intelligently, using details on the effects of geometry and the performance of different cooling methods to determine the ideal shape, clamping and cooling of each crystal.

Existing systems have been built to work with the current beam energies and to fit within the existing optics hutches. However, the desire for higher beam powers and intensities, as well as retrofitting additional beamlines, are therefore difficult to meet. It is possible to design a new assembly such that it is both small enough to fit with an existing beamline and sturdy enough to cope with a higher power load, allowing current synchrotrons to upgrade and expand without needing to rebuild the linac, booster ring or storage ring; this would allow the cost of such upgrades to be drastically reduced, while allowing more beamlines utilising higher powers.

The deformation in the crystals is currently widely treated as purely thermal, with allowances made in the design phase to minimise the mechanical deformation and clamping and cooling prioritising the elimination of thermal deformations, with very little consideration of how this may introduce structural deformation. However, the lack of theoretical works limits confidence in this assumption; therefore, the potential role of structural deformation needs to be explored and examined to see if this is an alternative consideration needed to improve the performance of synchrotron devices.

Arguments have been made for both direct and indirect cooling. While direct cooling is very well understood, and to some extent much simpler than indirect, it has significant drawbacks. It is necessary to examine how direct cooling improves the performance of the system, and using that understanding and taking into account the limitations of direct cooling to determine whether the priority should be to improve the performance of indirect cooling as much as is possible, or to move to direct cooling and embrace the drawbacks to improve the efficiency of the overall system.

With these factors taken into consideration and a firm grasp on the base principles it will be possible to design a new monochromator assembly configuration that will allow crystals near the size of the beam footprint to be used to take energy loads up to and greater than those currently used in synchrotron devices. This new design has been modelled, manufactured and tested, and its performance compared to existing assembly configurations. For this work, the crystal assembly currently in use at the Diamond Light Source (DLS) I20 beamline has been used as a baseline, as it is a secondary beamline with little room for optics and high power.

### [Executive Summary of Chapter 1](#)

Literature has been reviewed around the design and building of existing beamlines, monochromators and crystals. However there is a literature gap in why these devices have been designed the way they have, as well as a lack of research including mechanical deformation. These aspects are the focus of the rest of this work, understanding the base principles and identifying the issues at hand in order to address them in the novel interference fit monochromator design.

## 2. Examining Thermal Transport through the use of Theoretical Models

### Review of the Thesis up to Chapter 2

The Literature Review has shown that there is a lack of research into the underlying causes of deformation in the diffracting surface of monochromator first crystals; instead, most literature focuses on mitigating this deformation. In addition, a current need for increased synchrotron beam powers and more beamlines per storage ring facility requires a redesign of monochromator first crystals, as they will ideally have a smaller footprint and be able to dissipate more heat for future demands.

### 2.1 Introduction

The most basic concept underlying a monochromator assembly is that of thermal transport. As energy is deposited into the first crystal from the x-ray beam, the vast majority is absorbed and converted into heat within a short depth beneath the beam footprint; in the I20 beamline the first crystal is subject to beam powers of up to 500 W, while the second crystal is only subject to a beam power of 15 W. This is why the first crystal is the focus of this work. The heat then dissipates through the crystal. Once it reaches the boundaries, it is transferred into the heat exchanger. The heat travels through the heat exchanger to the coolant channels, where it is conducted away to be disposed of. This transport mechanism is shown in Figure 10 below.

Ideally, the crystal would be at a uniform temperature throughout; with a uniform crystal temperature, there would be no difference in thermal deformation throughout the crystal, giving a more uniform diffracting surface. However, as the heat travels different lengths to reach the heat exchanger, higher temperatures are present around the beam footprint compared to the rest of the crystal. When one part of the crystal is a different temperature to another, the crystal deforms thermally; the energy imparted into the lattice of the crystal causes the bond length between

molecules to vary in size. This deformation is what compromises the collimation (on a macro scale) and monochromaticity (on a micro scale) of the diffracted beam. In order to remove the thermal deformation, the first step is to understand how the heat moves through the system.

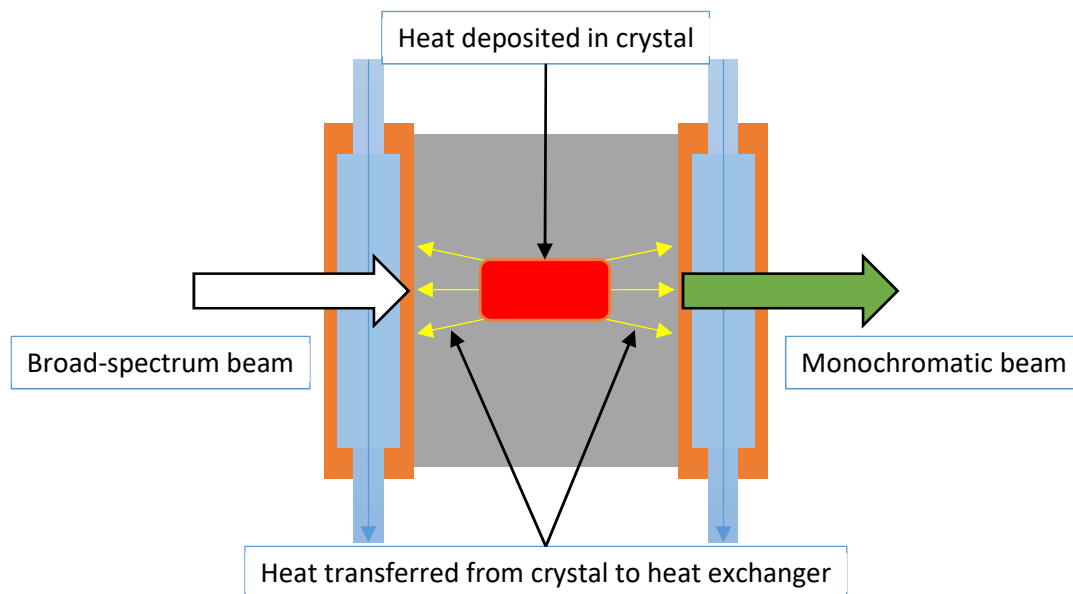


*Figure 10 – Heat deposited from broad-spectrum beam is transferred into heat exchanger and removed from the system by coolant*

By developing a one dimensional, analytical model the thermal transport mechanisms were examined from fundamental principles. This allows an understanding of the mechanisms at work to be developed and explored, and by modifying the individual model parameters the dominant thermal mechanisms can be identified. The simple nature of a one dimensional model also provides an easy entry point to the systems, simplifying the underlying equations and interdependencies and facilitating understanding of thermal transport. The model features a length of material. At one end of the length, absorption was modelled as a beam absorbed (equation 4) and transmitted (equation 6) through the crystal using the Beer-Lambert law (equation 5), and radiation was modelled using grey-body radiation (Kaviany, 2002) shown in equation 7 below. At the other end, cooling was

modelled by fixing the temperature of the material at 80 K, or  $-173\text{ }^{\circ}\text{C}$ . Throughout the model conduction was modelled using Fourier's law (Fourier, 1822) as shown in equation 8 below.

$$P(x) = \mu I_0 e^{-\mu x} \quad [4]$$

Where  $P(x)$  is the beam power at depth  $x$ .

$\mu$  is the absorption coefficient of the material.

$I_0$  is the beam intensity at the surface of the material.

$$T = e^{-\mu l} \quad [5]$$

Where  $T$  is the proportion of the transmitted beam.

$\mu$  is the absorption coefficient of the material.

$l$  is the distance the beam passes through the material.

$$T(\lambda) = P(\lambda) e^{-\mu(\lambda)l} \quad [6]$$

Where  $T$  is the transmitted beam power at wavelength  $\lambda$ .

$P(\lambda)$  is the incident beam power at wavelength  $\lambda$ .

$\mu(\lambda)$  is the absorption coefficient of the material at wavelength  $\lambda$ .

$l$  is the distance the beam passes through the material.

$$R = \epsilon\sigma(T_h^4 - T_c^4)A \quad [7]$$

Where  $R$  is the power lost to radiation.

$\epsilon$  is the emissivity of the material.

$\sigma$  is the Stefan-Boltzmann constant.

$T_h$  is the temperature of the hot body.

$T_c$  is the temperature of the cold body.

$A$  is the radiating area.

$$Q = -k \frac{dT}{dx} \quad [8]$$

Where  $Q$  is the local heat flux.

$k$  is the thermal conductivity of the material.

$\frac{dT}{dx}$  is the temperature gradient.

This simulated a length of material with a beam depositing energy on an exposed end, perfect insulation along its length and a high efficiency cooling system at the other end. The analytical model ran in a time loop, updating at constant time periods. Once the program reached its end, the thermal equilibrium the system has settled into was recorded. By examining how the temperature travels through the system a solid understanding was achieved on how the different thermal processes affected the equilibrium state.

Once the one dimensional model had provided an understanding of the thermal processes in the system, a new model was developed in three dimensions in a Finite Element Analysis (FEA) program. The FEA modelling software used was COMSOL MultiPhysics, a widely used system that specialises in

applying multiple sets of physics principles at once; in this instance, combining thermal mechanics with structural mechanics to model both the way heat moves through the system and how the bodies deform and are stressed. To ensure correct modelling of the problem, and to gain confidence that the FEA software is accurate, the programs executed in the one dimensional analytical model were replicated with the FEA software. As the results agreed, a degree of confidence was achieved that both models are accurate and that the system is properly understood. This confidence carried over into the results generated by the FEA. Caution was required, however, as FEA packages are very strongly dependant on initial conditions; many of the underlying equations and interactions are provided as part of FEA packages, but if incorrect boundary conditions were entered the model would not have generated accurate results.

Having ascertained the abilities of the FEA software, we began by modelling the crystal in isolation. The boundary conditions were as accurate as possible for the simplified design. The behaviour of the system was examined as various boundary conditions were adjusted to note their effect. Once completed, the entire monochromator assembly in use at the I20 beamline at the Diamond Light Source was modelled using observations from the isolated crystal model. The effective boundary conditions at the crystal were adjusted by modifying the assembly. With this model fully realised the thermal transport properties of the current system were investigated, and any weak points or unforeseen issues with the design were identified and corrected. Taking the result of this exercise, various alternate designs were modelled in order to identify a novel design that can perform better than the conventional design.

## 2.2 1D Analytical Model of Thermal Transport

The first aspect of the one dimensional model addressed was the beam absorption. As the x-ray beam falls on the crystal, the majority of the energy is absorbed as heat; depending on the wavelength selected by the Bragg diffraction, only around 10% is diffracted and the remaining 90% is absorbed by the first crystal. In practice, while most of the x-ray beam is absorbed by the first few microns of the material, the high penetration of x-ray radiation results in some portion of the beam permeating beneath the surface and being absorbed across the first couple of millimetres. To model this, the Beer-Lambert law was implemented as shown in equations 5 & 6. The Beer-Lambert law governs transmitted power through a medium; as the beam passes through subsequent layers of the crystal, the power falls in proportion to the distance travelled and the absorption coefficient of the crystal, which in turn is dependent on the wavelength of light as shown in equation 6. This transmitted beam is then subject to the same absorption and transmittance, until all of the energy has been absorbed or the remaining beam is emitted from the far side of the crystal.

The second mechanism to consider at the diffracting surface of the crystal is radiation. As the crystal heats up, it will radiate heat to its environment. Though this is an ineffective method of heat transfer when compared to conduction and convection, it is not negligible and must be considered. In practice, the crystal is mounted in vacuum with a heat shield a short distance from the diffracting surface; in this instance, the heat shield is a piece of metal cooled to approximately 80 K by liquid nitrogen. This information allows us to model the radiation as grey body. Grey body radiation refers to an object radiating power to its environment, and is a modified version of black body radiation (in which the object is in thermal equilibrium with its environment) as shown in equation 7.

Once the temperature of the surface element has been calculated, taking into account absorption and radiation, the next consideration is how power is conducted into the next element. Conduction

is governed by Fourier's law (equation 8) and is directly dependent on the difference in temperature between the two elements. Conduction is considered in both directions from each element at each time step, i.e. showing the heat flowing into and out of the unit cell in each direction per time step; this allows heat to flow in either direction depending on where the hottest element of the model lies as shown in equation 9. As we are considering a uniform material in a time dependent system, we can simplify Fourier's law into equation 10.

$$Q(x) = \frac{d}{dx} \left[ -k(T(x)) \frac{dT(x)}{dx} \right] \quad [9]$$

Where  $Q$  is the local heat flux at position  $x$ .

$k$  is the thermal conductivity of the material.

$T(x)$  is the temperature at position  $x$ .

$$Q(x, t) = \frac{d^2T(x, t)}{dx^2} \quad [10]$$

Where  $Q(x, t)$  is the local heat flux at position  $x$  at time  $t$ .

$T(x, t)$  is the temperature of element  $x$  at time  $t$ .

In order to get meaningful results from the model accurate boundary conditions were needed. To model the beam, a power-wavelength spectrum was used as provided by Diamond Light Source, a graph of which is shown in Figure 11 below. The graph shows a peak around 0.75 nm, which has been chosen for the I20 beamline; this peak can be moved through the use of different strengths of magnets in the undulators or wigglers. The sharp features visible on the graph come from filters used to remove other spectra of light from the beam, which are not completely transparent in the X-ray regime.

This has been combined with values for the absorption coefficient of silicon (Seltzer and Hubbell, 1995) to calculate how the material is heated by the beam, shown in Figure 12. To model the heat shield, the cold body temperature was set at 100 K for the grey body radiation equation; this is to match the temperature observed in use at the I20 beamline at the Diamond Light Source, as the heat shield is cooled by a secondary loop from the liquid nitrogen cooling system. To model the heat exchanger, the temperature of the cold surface of the model was fixed at 80 K, to simulate a perfect thermal contact with a liquid nitrogen cooled heat exchanger. The model was run with eleven different lengths of material, the results of which are shown in Figure 13 below. The major trend observed was that the shorter the length of a given crystal, the lower the peak temperature observed.

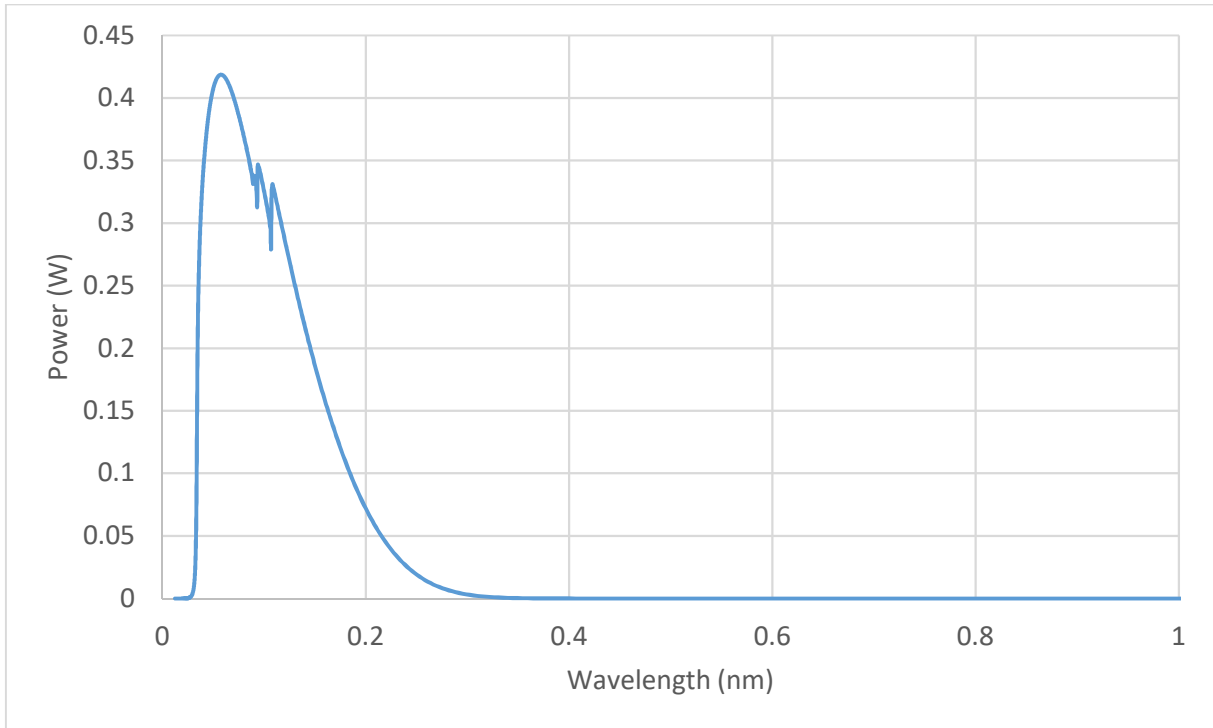


Figure 11 - Beam profile of the I20 beamline at Diamond Light Source, showing beam power as a function of x-ray wavelength.

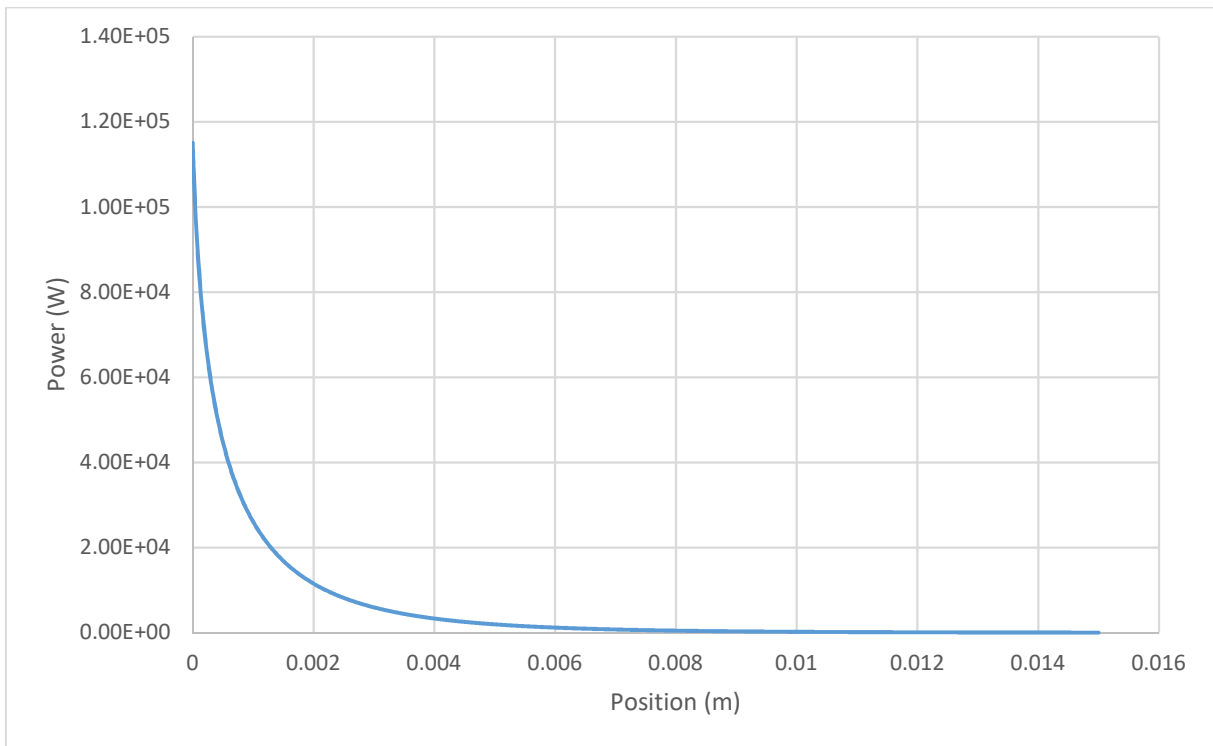


Figure 12 - Beam penetration, showing beam power as a function of penetration depth in single crystal silicon.

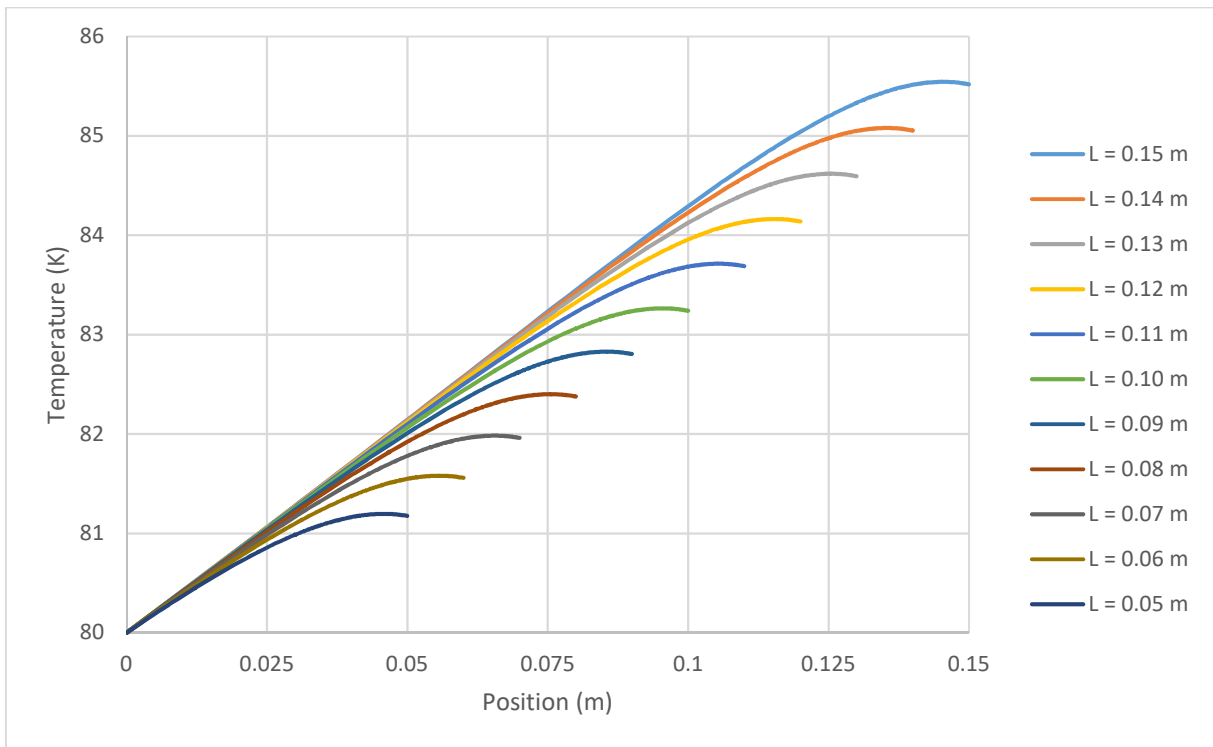


Figure 13 – One dimensional analytical model; temperature as a function of length for different crystal lengths  $L$ .

### 2.3 Investigating Heat Transfer using a 1D Analytical Model

Another major result noted from Figure 13 is that the temperature gradient is constant through most of the material. This is due to the conduction term being linear; in regions without absorption or radiation we therefore have a linear temperature change. This indicates that, with constant beam power and a fixed temperature cold side, the thicker the piece of material is the higher the surface temperature will reach. It is worth noting that the thickness of material represented by the one dimensional model would translate to the distance from the beam footprint to the heat exchanger in a 3D model, not necessarily the thickness of the crystal.

This result suggests that one way to minimise the temperature of the diffracting region is to minimise the distance to the heat exchanger, or the thermal transport length. This runs somewhat counter to the design philosophy as standard, which leans towards utilising larger crystals to spread the deformation across a larger area in order to locate the diffracting region in the deformed crystal's flattest area. As the temperature of a point appears to be directly proportional to the thermal transport length, another option may be to attempt to make this distance uniform for the diffracting surface; this would give rise to a bowl-shaped or bottom-cooled crystal, such that all regions of the diffracting surface are the same distance from a cooled point, ensuring a uniform temperature across the diffracting surface. However, as in reality the angle of the crystal is adjusted to select a different wavelength, this would result in the shaped crystal being suitable for a very narrow spectrum.

A final observation from Figure 13 is that in each case the peak temperature is slightly beneath the surface of the material. This is likely somewhat exaggerated due to the size of the elements. This means the power absorbed by the sub-surface elements will likely be slightly high. However, it does give rise to an interesting concept – if the surface of the crystal is cooled, even slightly, the peak temperature point can be buried beneath the surface. This restrains the thermal deformation to a

degree, presenting a more uniform diffracting surface. This may prove very difficult in practice, as attempting to remove heat from in and around the diffracting surface is likely to affect the lattice structure and vary the thermal path length, leading to a less uniform temperature; any attempt to cool the diffracting surface would require machining of the surface on some level, and this would destroy the lattice in the areas that have been machined.

## 2.4 Verifying the Outputs of the 1D Analytical Model with a 3D Finite Element Model

In order to develop a more physical model, the next step was to move from one dimension to three. To build a three dimensional analytical model from scratch would be prohibitively expensive and time consuming, so instead COMSOL MultiPhysics was used. COMSOL is a Finite Element Analysis (FEA) program, specifically designed to simulate physical models with multiple sets of physical rules, by breaking the model into a number of small, tetrahedral elements, solving the physics for each element and then ensuring the boundaries between the elements are consistent. In order to gain confidence with COMSOL, results from our one dimensional analytical model were compared to those generated by an identical model run in COMSOL. As the two sets of results matched, this shows that both systems are consistent – due to the difference in approach it is unlikely both systems were wrong in the same way, so another degree of confidence was gained.

To test the two models against one another, a set of ‘hot rod’ experiments were designed as detailed in Section 2.2. Three models were compared; in all models, a cuboid prism of length 10 cm and height and width 1 cm was used as the body to be examined. Heat was conducted through the body in accordance with Fourier’s Law.

In scenario one, a constant, uniform power of  $10^7 \text{ W / m}^3$  was applied throughout the system, and both ends of the sample were maintained at 77 K to simulate liquid nitrogen cooling. The temperature gradient at the rear surface was set such that half of the power was removed from each end of the sample. The temperature profile produced is shown in Figure 14 below.

The second scenario was similar, although in this case only the rear end of the crystal was maintained at 77 K and the temperature gradient was set such that all of the power was removed from the rear end of the crystal. The temperature profile produced is shown in Figure 15 below.

The third scenario was more physical; 500 W was supplied as an exponential decay in accordance with the Beer-Lambert law, with the beam being incident on the front edge of the crystal. Again, the rear surface was maintained at 77 K and the temperature gradient was set such that all of the power was extracted through the rear of the crystal. In order to keep the fine detail at the heated edge visible, this scenario was modelled with a depth of just one millimetre rather than the 10 cm used in the other scenarios. The temperature profile produced is shown in Figure 16 below.

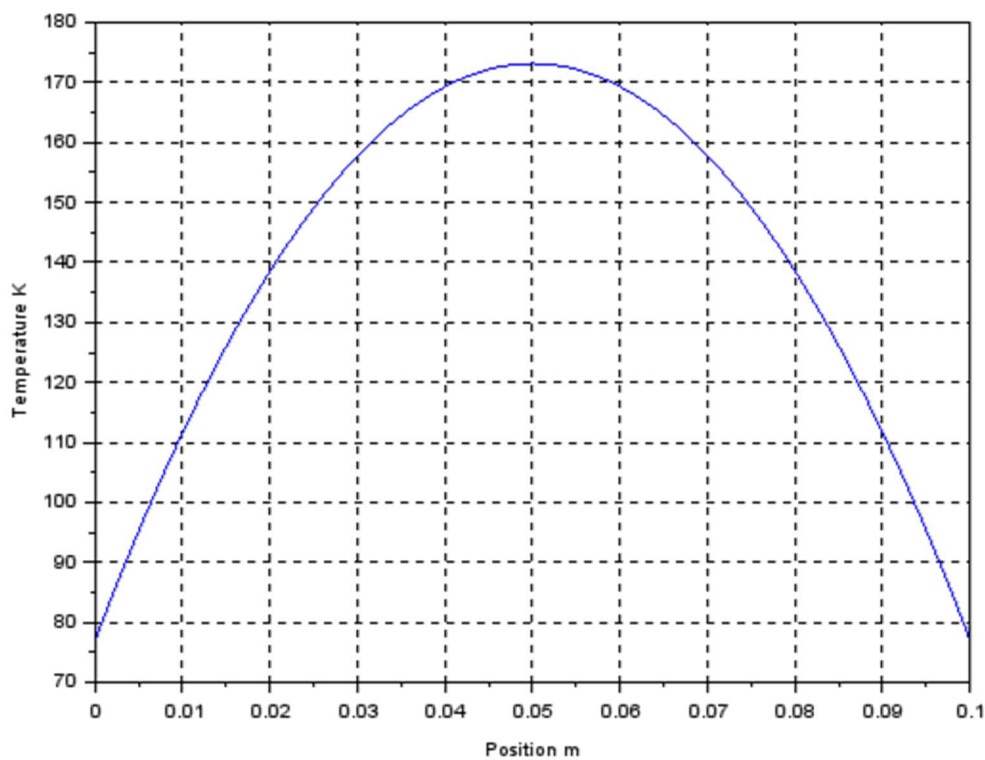


Figure 14 – Scenario 1 analytical temperature profile: 77 K boundary temperature,  $10^7$  W/m<sup>3</sup> power in, 50% power removed from each side.

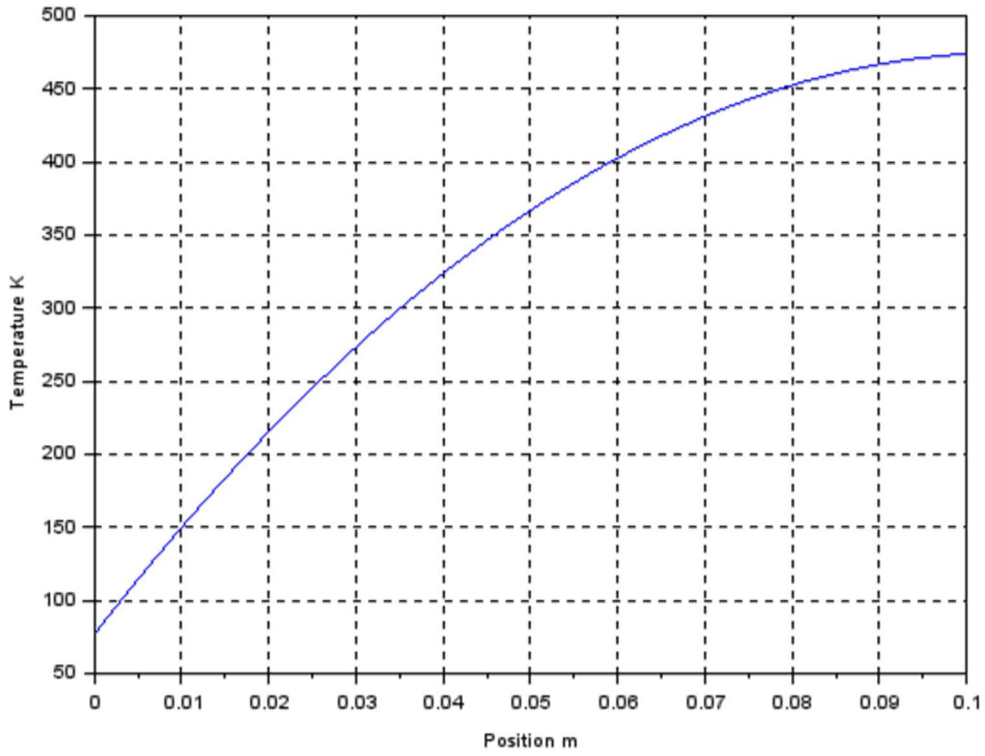


Figure 15 – Scenario 2 analytical temperature profile: 77 K boundary temperature,  $10^7$  W/m<sup>3</sup> power in, 100% power removed from cold side.

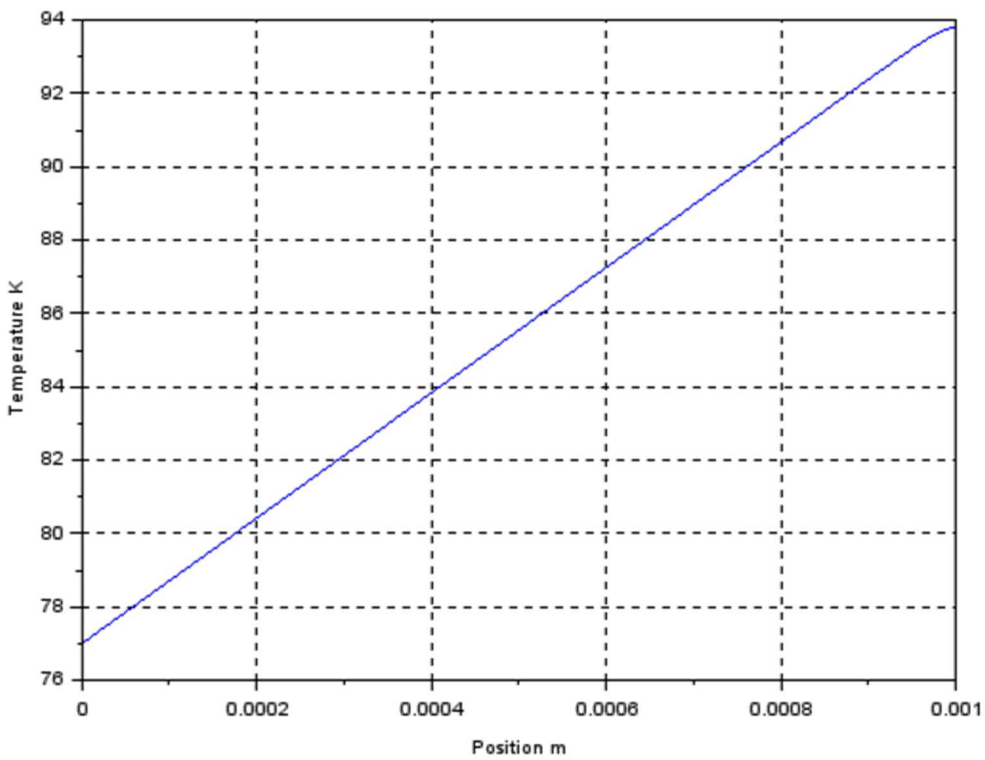


Figure 16 – Scenario 3 analytical temperature profile: 77 K boundary temperature, 500 W power in on right-hand boundary, 100% power removed from cold side.

To compare to the scenarios described above, a three dimensional model was assembled in COMSOL to emulate each scenario. In each case the cold surface was fixed at 77 K, and all four surrounding faces were set as thermal insulators.

In scenario one, a body power source of  $10^7 \text{ W/m}^3$  was applied throughout the system, and both ends of the sample were set as constant temperature at 77 K to simulate liquid nitrogen cooling. The temperature profile produced and a surface graph of temperature over the simulation is shown in Figure 17 below.

The second scenario was similar, although in this case only the rear end of the crystal was set as constant temperature at 77 K. The temperature profile produced and a surface graph of temperature over the simulation is shown in Figure 18 below.

The third scenario consisted of a single cooled boundary on the left at 77 K and a boundary heat source of 500 W on the right. Again the model was shortened to one millimetre to be comparable to previous models. The temperature profile and surface temperature plot produced are shown in Figure 19 below.

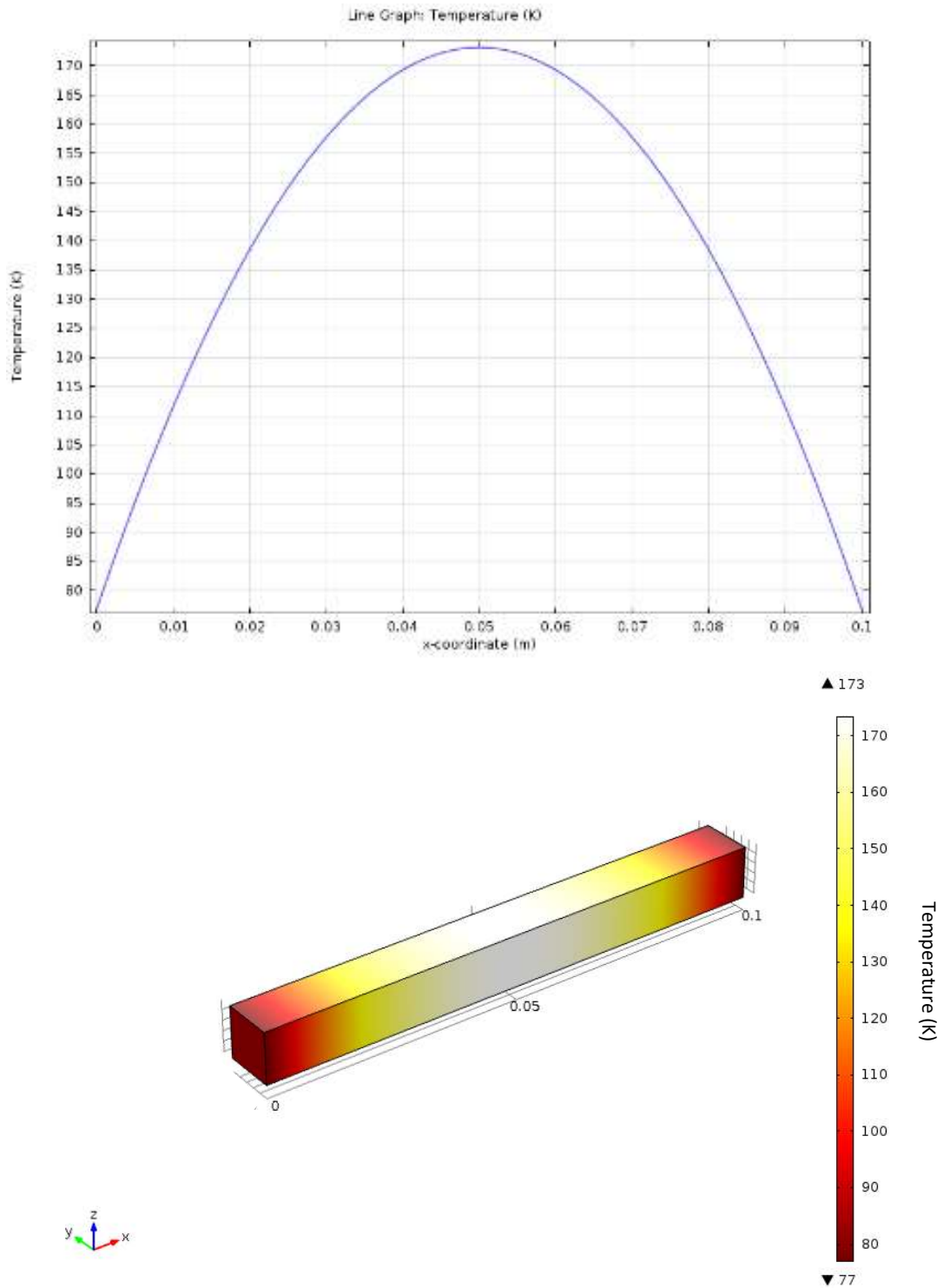


Figure 17 – Scenario 1 FEA temperature profile (K): 77 K boundaries temperature,  $10^7 \text{ W/m}^3$  power in throughout.

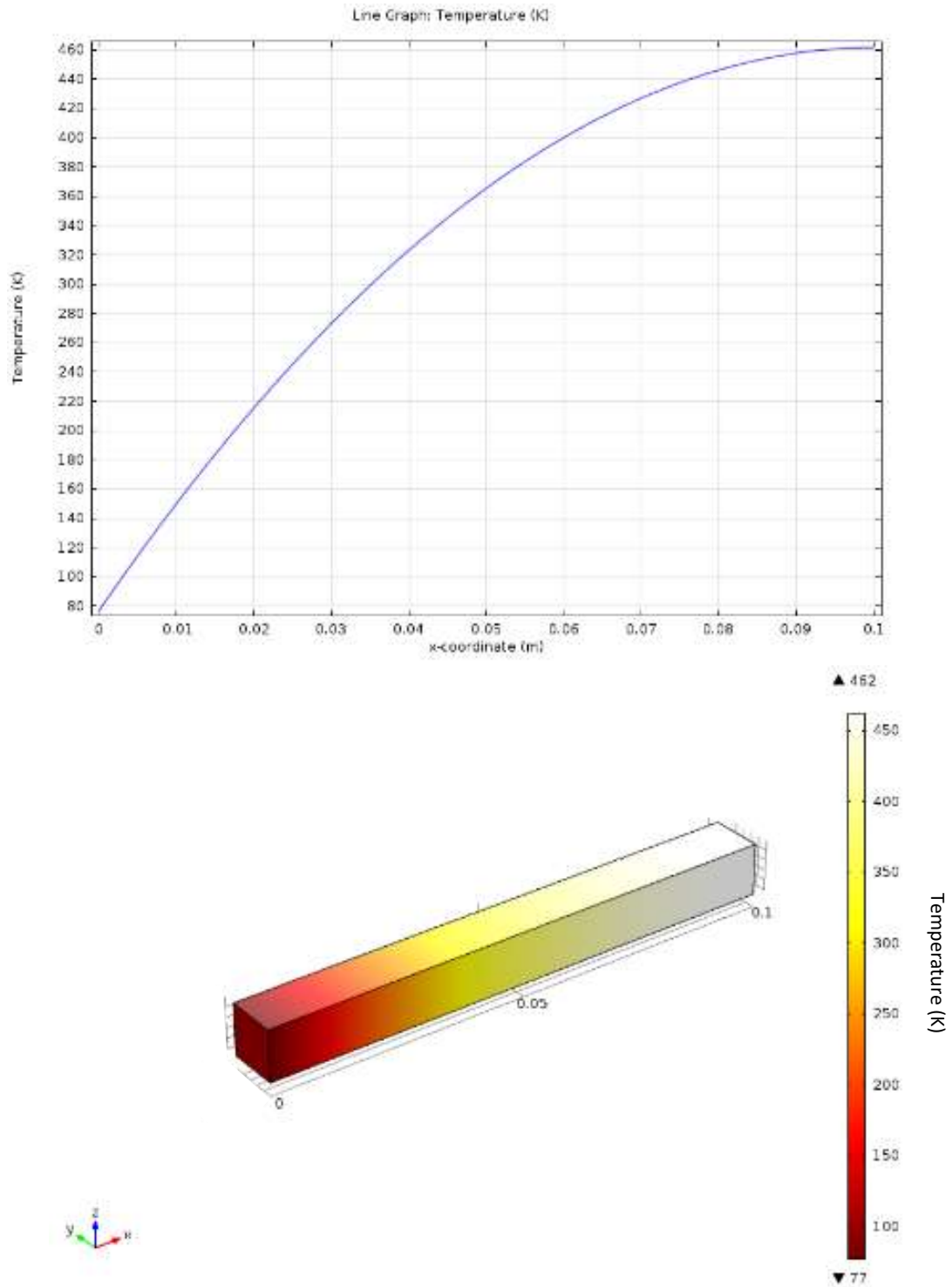


Figure 18 – Scenario 2 FEA temperature profile (K): 77 K boundary temperature,  $10^7$  W/m<sup>3</sup> power in throughout.

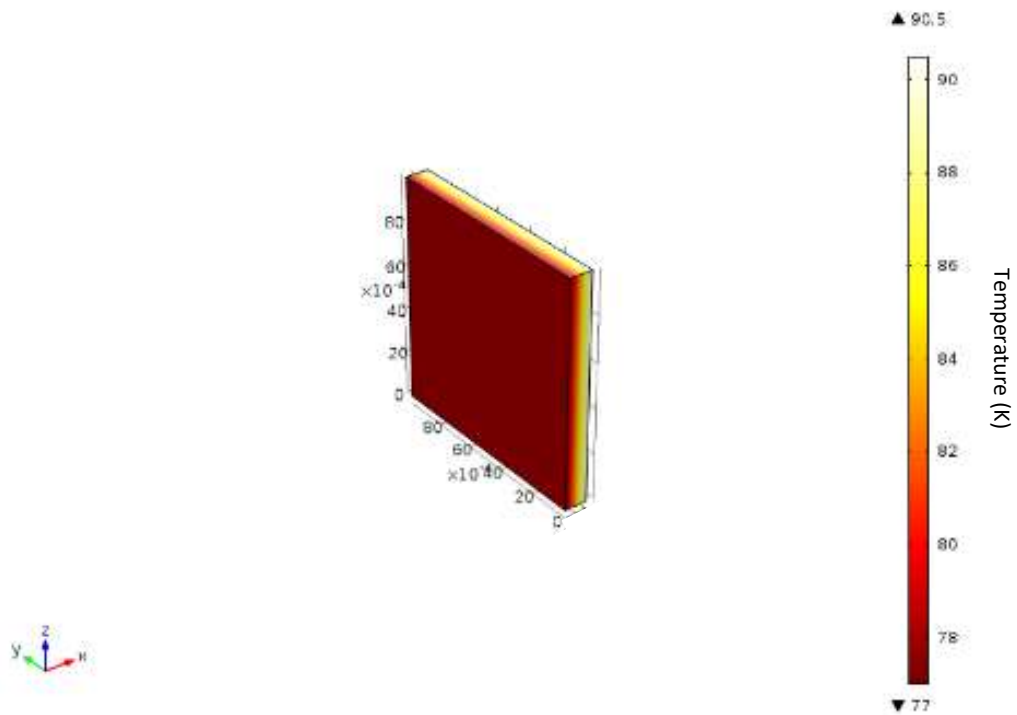
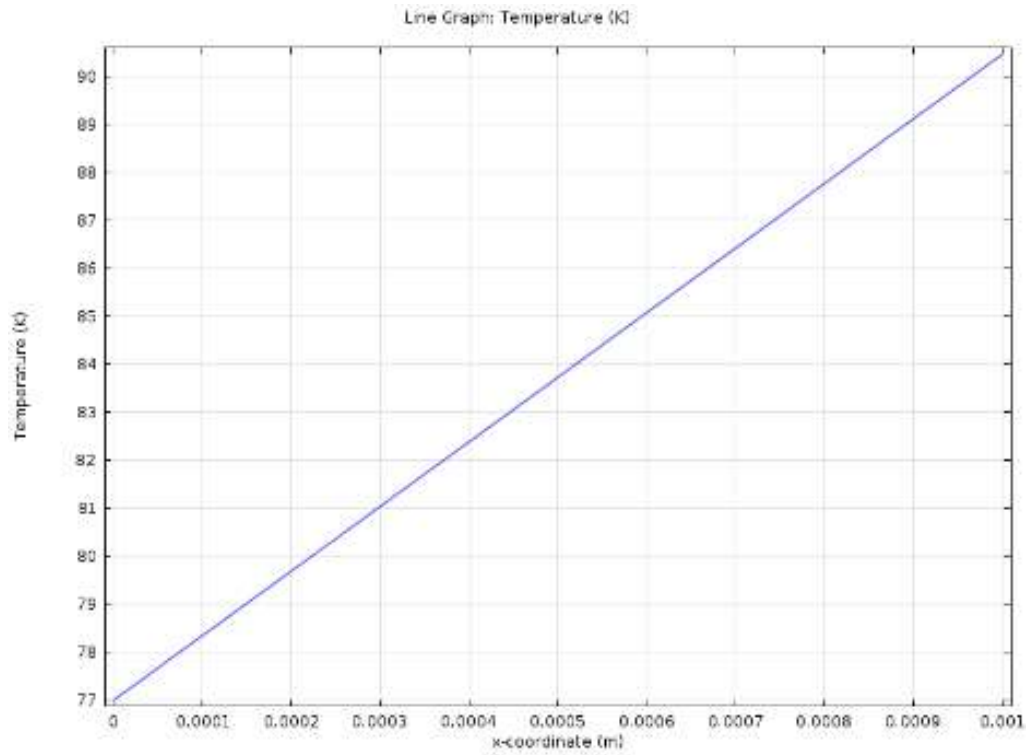


Figure 19 – Scenario 3 FEA temperature profile (K): 77 K boundary temperature, 500 W power in at boundary

For the first two of the three scenarios the FEA results were found to strongly agree with those produced by the analytical model as shown in Figure 20 and Figure 21 below; both peak temperatures and temperature gradients were found to be very strong matches. The third model did not agree perfectly as shown in Figure 22; this is due to the element size being too large in the analytical model, but decreasing the size caused the model to fail due to excessive runtime. Despite this technical limitation, the results show that it is very likely both models work; if there were an error introduced, it would be unlikely for these errors to be the same in both unrelated models. With this confidence gained, both in understanding of the system and in the performance of COMSOL, it was decided to move forward using the FEA software confident that with the correct input information we will receive accurate results.

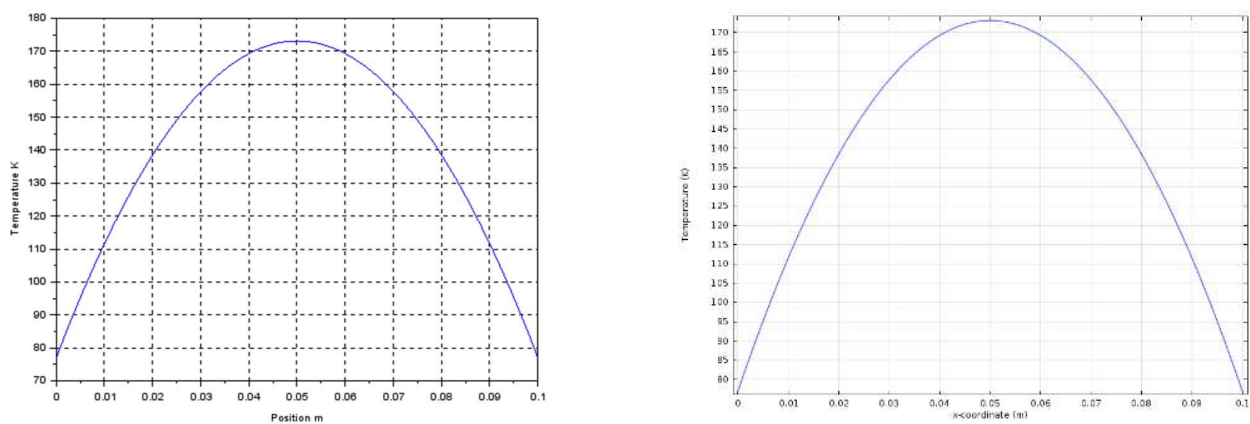


Figure 20 – Scenario 1 comparison: Analytical model on left, FEA model on right

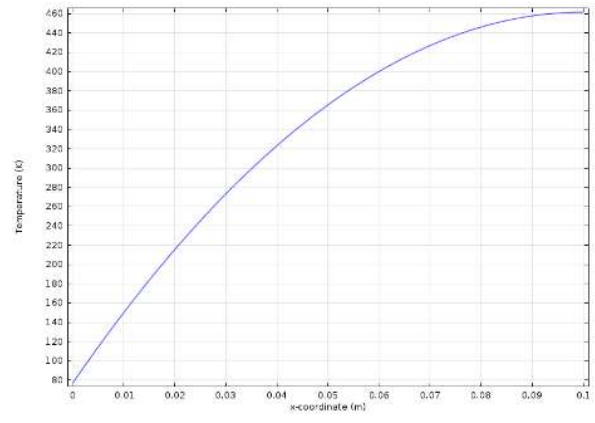
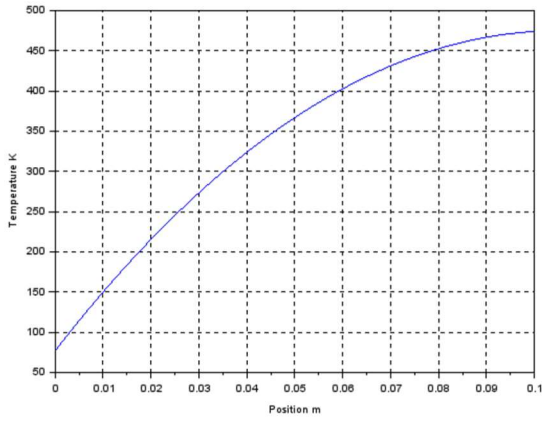


Figure 21 – Scenario 2 comparison: Analytical model on left, FEA model on right

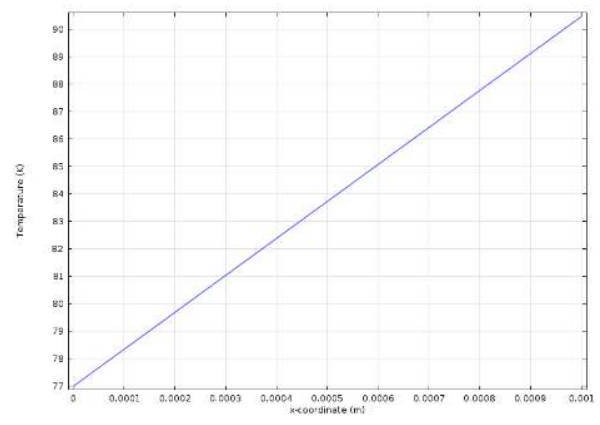
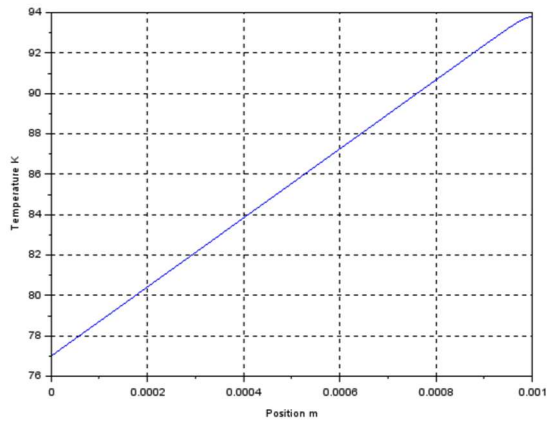


Figure 22 – Scenario 3 comparison: Analytical model on left, FEA model on right

## 2.5 Researching into the Temperature Dependant Properties of the Different Materials

In the examples given so far, used the room temperature values of the material properties have been used: thermal conductivity, the coefficient of thermal expansion and the heat capacity. However, in reality these values are all temperature dependant; i.e. they vary not only from material to material but also with the temperature of the system. This is due to temperature contributing to how the molecules move within the material; as the molecules become more or less active, this has an effect on the properties of the material. For each of the different materials used in the conventional system, how the thermal conductivity, coefficient of thermal expansion and heat capacity vary with temperature was found from literature, as described below. This was deemed necessary due to the large temperature range over which the models will be operating; for many applications with a smaller temperature range, it is a reasonable approximation to set the material properties as constant, but as the models begin at 300 K, cool down to 77 K and then heat back up to anywhere around 120 K the properties of the materials vary widely.

The thermal conductivity (Glassbrener and Slack, 1964), coefficient of thermal expansion (Shah and Straumanis, 1972; Okada and Tokumaru, 1984) and heat capacity (Marquardt, Le and Radebaugh, 2000) of silicon are given in Figure 23 below.

The thermal conductivity of silicon contains no surprises; silicon has its highest conductivity at 37.5 K, and conducts less at both lower and higher temperatures. At diffracting temperature, around 120 K, we find a thermal conductivity of 9 W / cm K.

The coefficient of thermal expansion of silicon does contain something of a surprise; below 120 K the coefficient becomes negative. This means that as the silicon is heated it shrinks, and as the silicon is cooled it swells. This is an interesting phenomenon caused by low entropy modes in the lattice structure of silicon (Shah and Straumanis, 1972); usually, as a material is heated this additional energy

is stored as kinetic and elastic potential energy within molecular bonds, and this increase in kinetic and potential energy causes the molecules to move apart from one another, causing the material to expand. However, as silicon drops below 120 K, this additional energy allows the crystal lattice to adopt a tighter structure by overcoming repulsive forces between the component particles; supplying additional thermal energy allows the molecules to adopt closer positions, resulting in the material compressing. In practice, this means that at operating temperatures silicon will vary between a positive and negative expansion coefficient. This may be of benefit as it will average to a near-zero expansion.

The specific heat of silicon is again fairly regular. As the temperature falls, the specific heat lowers; this will lead to the material heating up more with less energy. This means that as the crystal is warmed by the beam it will heat up at a slower rate from a uniform beam power, reaching equilibrium at a lower temperature than a material with a higher specific heat.

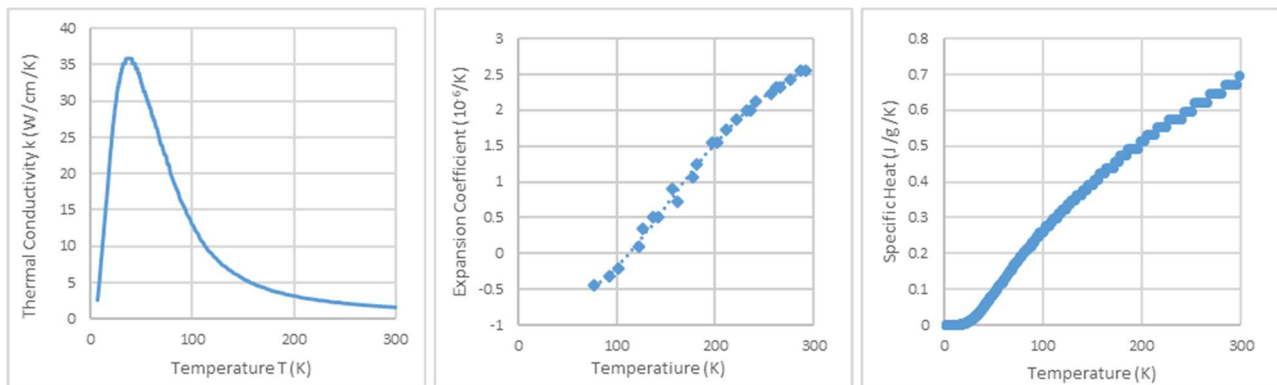


Figure 23 – (Left to right) temperature dependent thermal conductivity (Glassbrener and Slack, 1964), coefficient of thermal expansion (Shah and Straumanis, 1972; Okada and Tokumaru, 1984) and specific heat (Marquardt, Le and Radebaugh, 2000) of silicon

The thermal conductivity, coefficient of thermal expansion and heat capacity of copper (National Institute of Standards and Technology (NIST), 1992; Marquardt, Le and Radebaugh, 2000) are given in Figure 24 below.

Compared to that of silicon, the thermal conductivity of copper is higher at room temperature but significantly lower at cryogenic temperatures. This means the silicon will be the limiting factor for thermal transport at room temperature, but once the temperature drops below 150 K the copper will become the limiting factor. As such, we will want to limit the thickness of copper proportional to the silicon in order to prevent creating a thermal bottleneck and slowing the heat transfer.

The expansion coefficient of copper is ten times higher than that of silicon at room temperature and, although it falls with temperature, does not come close to a zero point. This will cause the copper to shrink faster than the silicon when cooled, which can introduce mechanical stress and strain into the system before a heat source is ever applied.

The heat capacity of copper is approximately half that of silicon, both at room temperature and at cryogenic temperatures. This will cause the copper to hold less heat than the silicon, allowing it to reach higher temperatures with the same amount of energy. This could cause the copper to become hotter than the silicon as energy flows across the boundary; as heat flows from a hotter body to a cooler one, this would again cause a thermal barrier as heat cannot be removed from the system – as each joule of energy flowing from the silicon to the copper heats the copper more than it cools the silicon, if the copper is too thick the boundary between the silicon and the copper will reach thermal equilibrium at a much higher temperature than would be possible with a thinner copper wall.

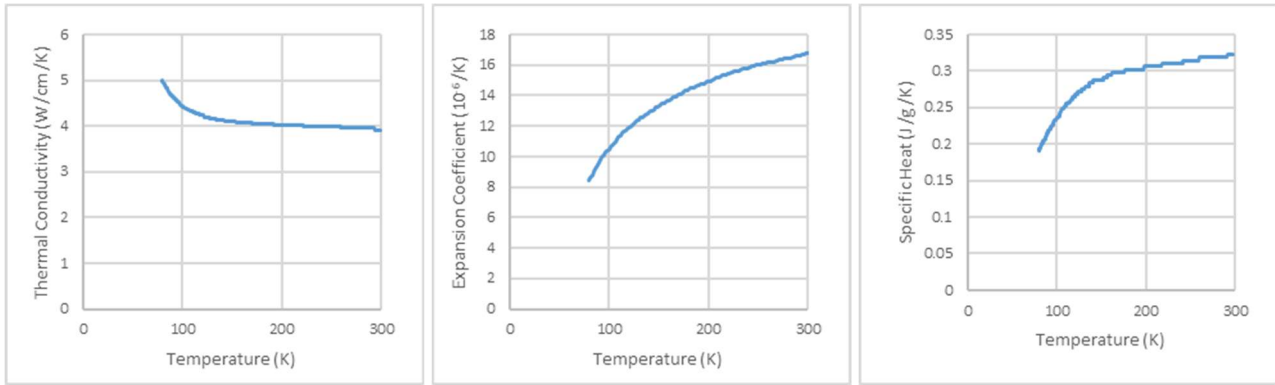


Figure 24 – (Left to right) Temperature dependent thermal conductivity, coefficient of thermal expansion (National Institute of Standards and Technology (NIST), 1992) and specific heat (Marquardt, Le and Radebaugh, 2000) of copper.

The thermal conductivity, coefficient of thermal expansion and heat capacity of 304 stainless steel (Desai and Ho, 1978; Marquardt, Le and Radebaugh, 2000) (the alloy commonly used at Diamond Light Source) are given in Figure 25 below.

Stainless steel 304 has a very low thermal conductivity, only 0.15 W / cm K at room temperature and falling from there. As its conductivity is so much lower than that of the silicon and the copper, it is a reasonable approximation that negligible amounts of heat flow through the steel bolts.

The alloy of stainless steel used has a comparable expansion coefficient to copper; as the two metals have much higher expansion coefficients than the silicon they will contract to a much greater extent than the silicon will during cooling.

The heat capacity of the steel lies between that of copper and silicon, meaning it takes more energy to heat than the silicon but less than the copper. As the thermal conductivity will prevent much heat passing through the steel it is likely to reach equilibrium with the copper and silicon without having a strong bearing on the state of the system.

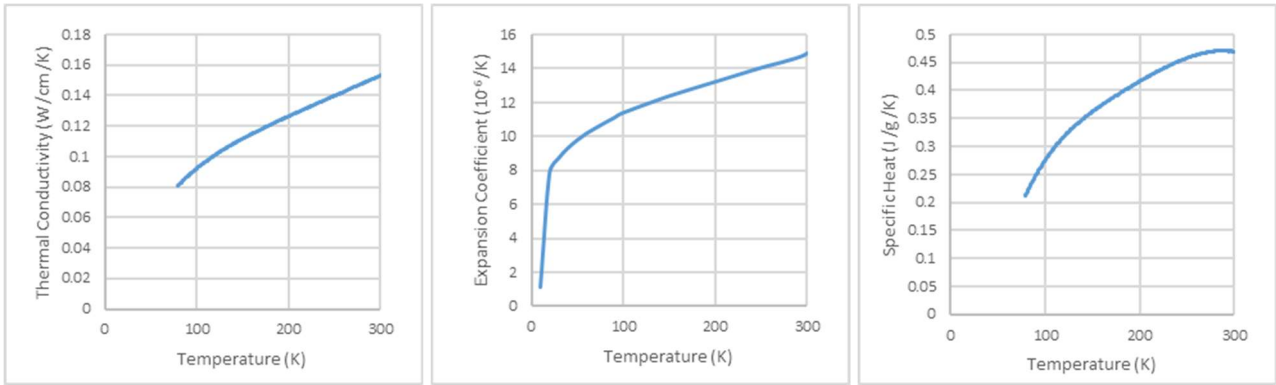


Figure 25 – (Left to right) Temperature dependent thermal conductivity (Marquardt, Le and Radebaugh, 2000), coefficient of thermal expansion (Desai and Ho, 1978) and specific heat (Marquardt, Le and Radebaugh, 2000) of stainless steel 304

## 2.6 Development of a Finite Element Model of the Full Monochromator Assembly

Having a firm grasp on both the underlying mechanisms of thermal transport and the effect of temperature on material properties, the next step was to model the conventional crystal in COMSOL in order to examine how heat moves through the assembly. The Diamond Light Source provided a schematic of the crystal and assembly which was replicated in CAD software as shown in Figure 26. The shape of the crystal is designed to accommodate the cramped confines of the I20 optics hutch; the removed 'shoulders' of the crystal are to allow the second crystal to sit very close to the first crystal without catching or being limited in angle. The conventional assembly consists of two trimmed crystals, one machined such that the 111 lattice plane is parallel to the diffracting surface and the other machined such that the 311 lattice plane is parallel to the diffracting surface to reduce the necessary angle of rotation, as explained on page 10 in Section 1.2.

The two crystals are leaved within three copper heat exchangers, each of which has a through-flow of liquid nitrogen. These heat exchangers are secured to a copper base plate which holds the assembly in place and is used to angle the assembly in the optics hutch.

A thin foil of high purity indium is sandwiched between each piece of silicon and the adjacent heat exchanger; the indium foil is malleable even at liquid nitrogen temperatures, which allows it to freely deform and mitigate the stresses and strains induced in the assembly. It is also intended to improve the thermal gap conductance between the different components, filling in micro-scale gaps and improving the contact between the surfaces.

The entire assembly is held together through two steel bolts, threaded through the vertical centre of the crystals and heat exchangers, one forward of the diffracting surface and one behind. These bolts are secured by nuts on the ends, pretensioned to 190 N of clamping force.

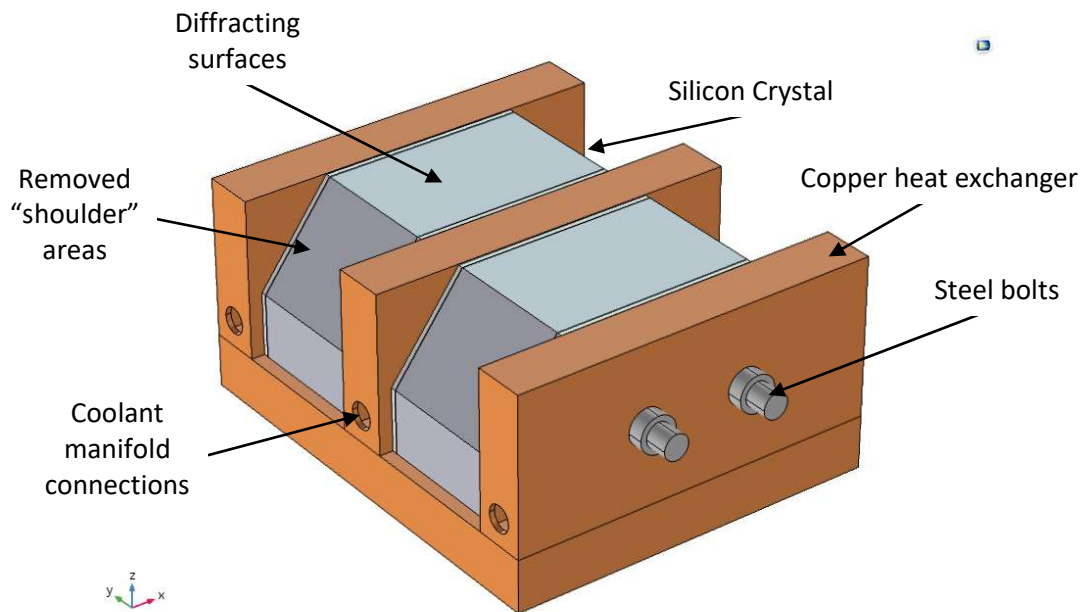


Figure 26 – Conventional crystal assembly as used on the I20 beamline at Diamond Light Source.

Within COMSOL MultiPhysics a combined thermomechanical problem is considered using both the Heat Transfer and the Solid Mechanics physical constraint sets. The two sets of physical rules combine, with the heat causing thermal deformation which is in turn used to calculate stress and strain. For each set of physics boundary conditions were required to restrain the initial status of the simulation; the simulation then ran over a time loop, updating the temperature, stress and strain throughout the components on each time step. The initial mechanical boundary conditions are shown in Figure 27, and the initial thermal boundary conditions are shown in Figure 28.

Mechanically, the location of the bolt in the copper baseplate is held fully constrained; for the purpose of this simulation, the bolt cannot be deformed or displaced in any way. This is a best approximation; the FEA model requires an absolute reference point to constrain the model, and as this is the point by which the actual assembly is held it was the logical selection. In addition, all paired surfaces are in contact with each other; they are restricted from moving through each other and friction is taken into account with a coefficient of friction of 0.2 (Mishina and Buckley, 1984). The two steel bolts are pretensioned to 190 N to hold the components together.

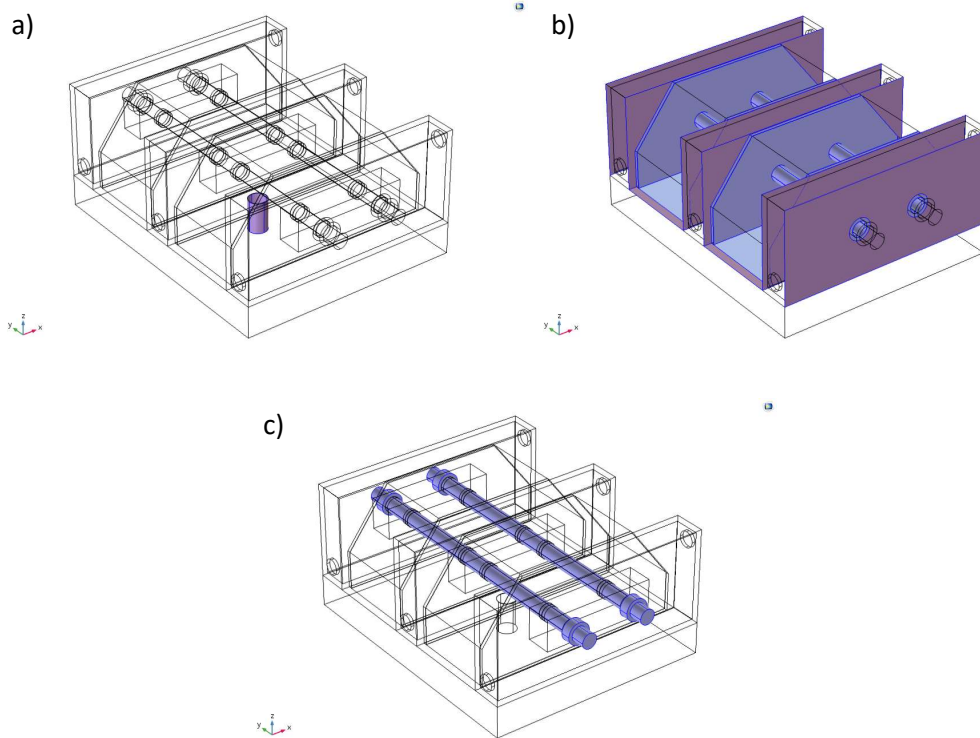


Figure 27 – Mechanical boundary conditions for conventional assembly: a) bolt in copper base plate is held fully constrained; b) paired faces in mechanical contact; c) steel bolts pretensioned to 190 N

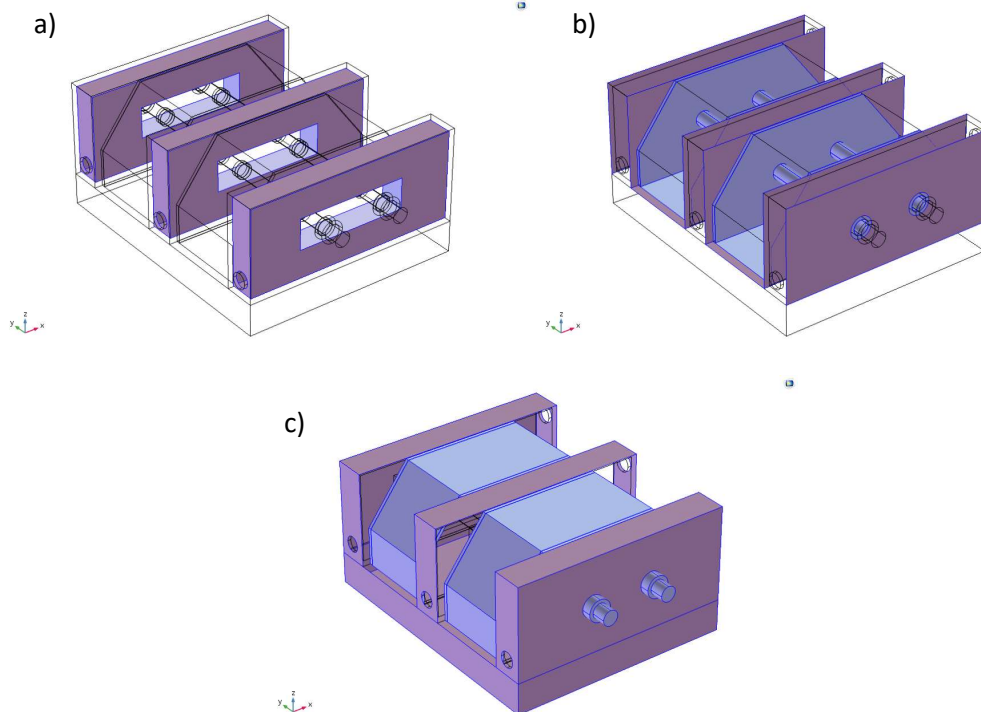


Figure 28 – Thermal boundary conditions for conventional assembly: a) internal surfaces of heat exchangers are held at 80 K; b) paired faces in thermal contact; c) all exterior faces radiate heat to an 80 K heat shield.

The inside faces of each heat exchanger are set at a constant temperature of 80 K; this is to simulate their through-flow of liquid nitrogen. Again, all contacting surfaces are modelled in contact; this allows thermal gap conductance dependent on the force holding the faces together in order to simulate heat flow between adjacent surfaces. All of the surface faces are set to radiate heat to an 80 K heat shield.

Additionally, the anisotropic nature of silicon was taken into account – as silicon is composed of a lattice structure that is not completely rotationally symmetrical, the material properties of silicon differ in different directions. As such all FEA models presented in this work have been oriented such that the 111 crystal orientation is normal to the z-direction, such that the results are accurate to the crystal in Figure 26.

Before even running the simulation one concern becomes apparent; in order to properly align the silicon crystals in the optics hutch, the bolts are loosened slightly and a laser is used to find the angle of reflection from each silicon crystal. This angle is adjusted by making slight changes to the angle of the crystal; once the reflected beam is travelling in the desired direction, the bolts are tightened to hold the crystal in place. However, as the system is cooled, the difference in thermal expansion coefficients will cause the copper and steel components to shrink faster than the silicon. This potentially releases the silicon crystals from their clamping force, allowing them to settle with gravity and undoing the alignment. This would cause alignment drift errors, something observed with some frequency at the I20 beamline.

The results of the simulation are shown below; first, in Figure 29, the temperature profile across the entire surface of the assembly; then in Figure 30 a surface plot showing the deformation present in the diffracting surface itself; and finally in Figure 31 as a cross-section of pressure through the forward steel restraining bolt. It is readily apparent that cooling the system has caused it to deform

significantly, whereas the conventional philosophy is that most, if not all, deformation is caused by the heat of the incident x-ray beam. The key issue at work appears to be the differences in expansion coefficients; as the copper has contracted at a faster rate and to a greater extent than the silicon, and as the silicon is strong enough to resist the subsequent motion of the iron bolts as they are dragged down by the copper, the bolts take on a bowed, m-like shape. This causes significant deformation in the silicon, resulting in a much deviated diffracting surface before the beam is even switched on.

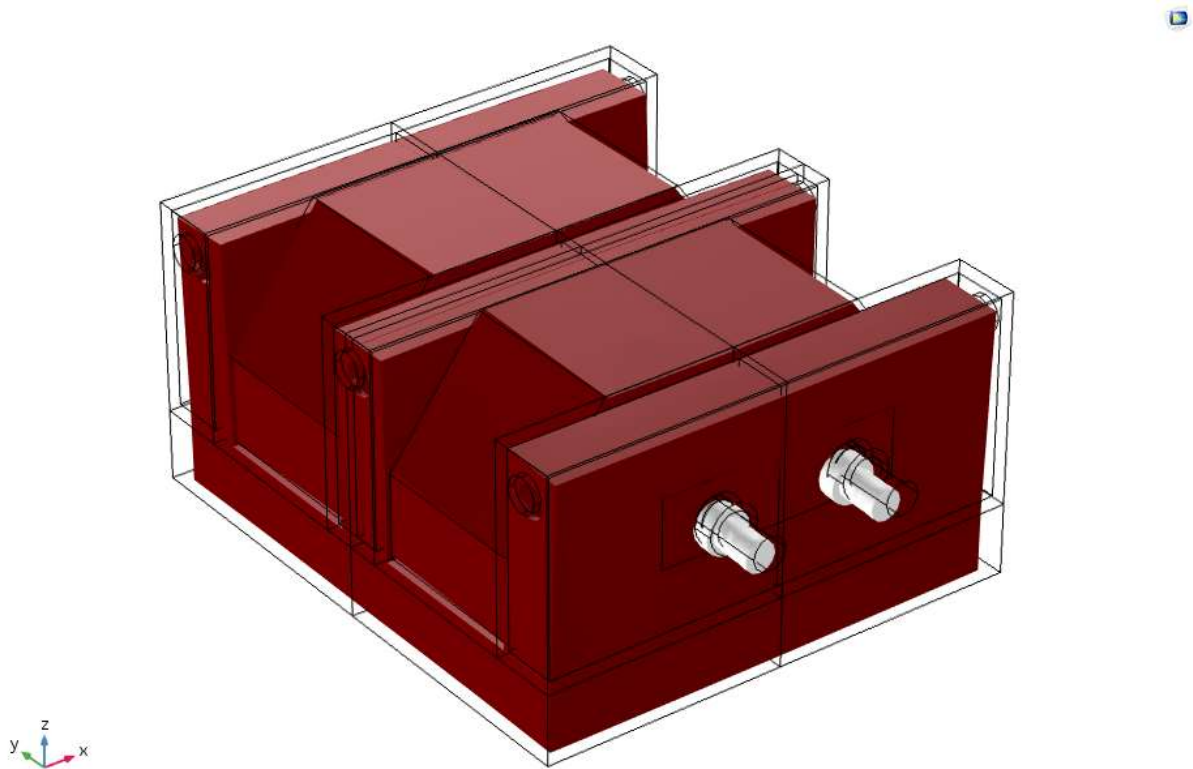


*Figure 29 - Full conventional assembly cooling, FEA model: 3D model of assembly at 80K. Colour shows bolts remain slightly hotter than the rest of the assembly; black lines how initial assembly location (deformation increased in scale).*

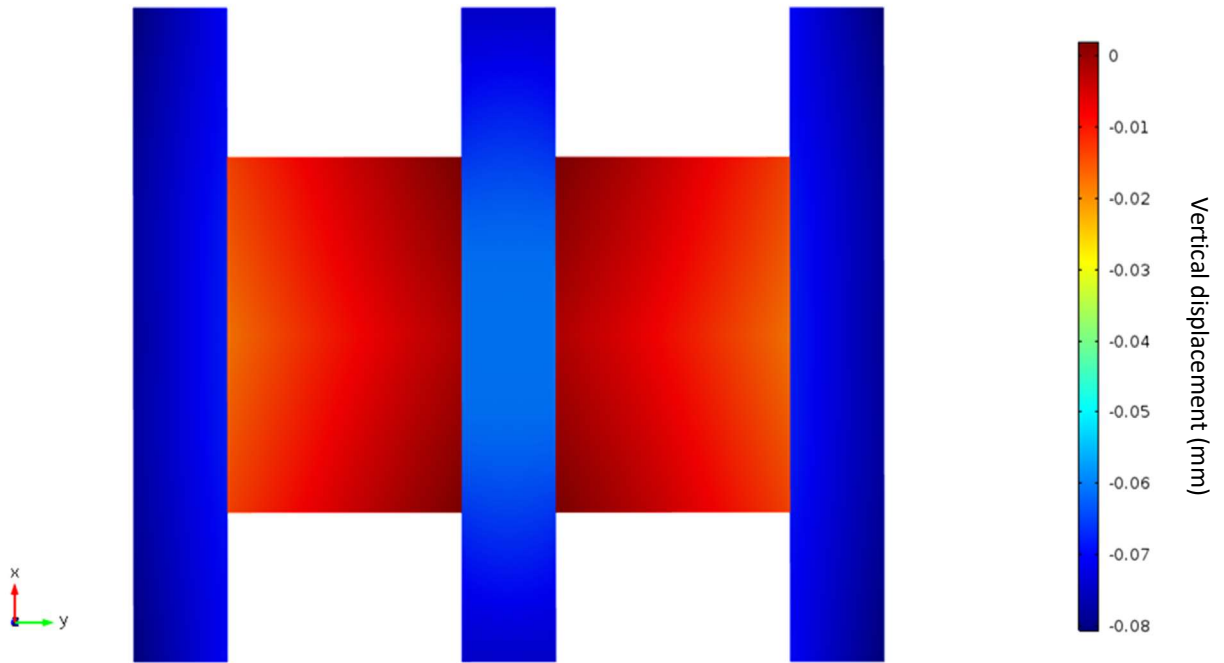


Figure 30 - Full conventional assembly cooling, FEA model: vertical displacement of diffracting surface. Copper heat exchanger shown to contract to a higher degree than silicon crystals.

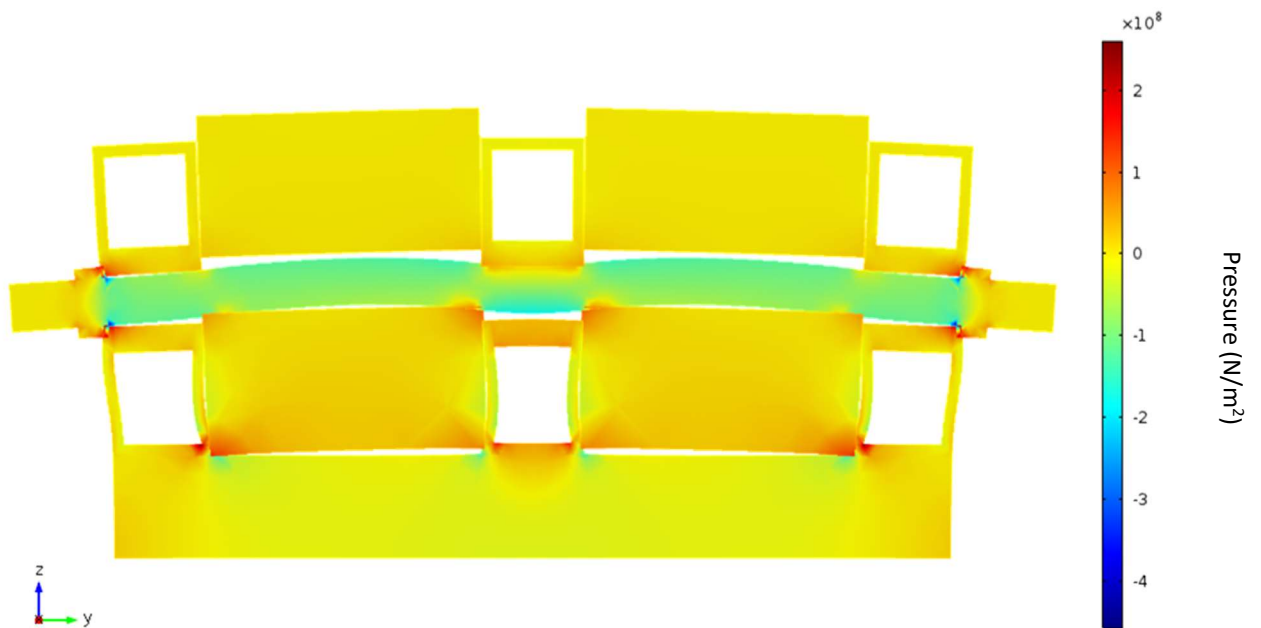


Figure 31 – Full conventional assembly cooling, FEA model: pressure cross-section at forward steel bolt. Peak stresses observed at corners of copper heat exchanger with both silicon and steel.

## 2.7 Conclusion

By comparing the results of the COMSOL 'hot rod' simulations to those generated by the one dimensional analytical model, a high level of confidence was attained in both simulations; it is unlikely any error would have been generated identically in both systems. As such, the base principles of thermal transport used in the simulation accurately represent those within the system, and the more complex FEA simulations. This gives us a great deal of confidence that the results of said simulations are accurate.

The severity of the mechanical deformation introduced by the cooling rather than through the heat of an incident beam is something unexpected from the literature and current design philosophies; much work is put into minimising conflicting forces when the assembly is assembled, but to date no work has gone into detail examining the deformation caused during the cooling of the crystal assembly. This introduces more deformation before the beam is ever switched on; even minor deviations in the flatness of the diffracting surface can cause an entirely different wavelength of x-rays to be selected by the Bragg diffraction, and if this deformation varies across the diffracting surface the collimation and monochromaticity of the beam are impinged. This gives rise to a new aspect to focus on; rather than looking to mitigate the build-up of heat within the crystal, minimising the deformation to the crystal during the cooling process should instead be a priority.

Another interesting result that comes out of this is that as the dominant deformation is due to the cooling of the crystal, high efficiency cooling is less important than expected; some of the cooling efficiency can be sacrificed, increasing the temperature of the crystal as a whole, to instead improve the uniformity of the cooling, decreasing the temperature variance throughout the crystal. This is because it is the temperature variance that causes varying thermal deformation and introduces surface distortion; in summary, a uniformly bad cooling system will introduce less of a surface

distortion and produce a higher quality beam than a non-uniform, higher efficiency cooling system. This is a departure from the conventional design philosophy, and is used in the design of the novel, interference fit monochromator in Chapter 6.

Overall it is apparent that the primary cause of diffracting surface distortion is the opposing material properties acting in counterpoint to one another. The copper and silicon oppose one another vertically; if both were unconstrained, the copper would contract to a much greater degree than the silicon but the steel bolts cause the two materials to act against one another. Horizontally the steel opposes the silicon; again, if both were unconstrained the steel would contract to a greater degree than the silicon, causing the two disparate materials to exert a strain on one another. These opposing forces introduce unnecessary stress and strain into the system, causing rotational deformations that distort the diffracting surface and ruin the monochromatic beam we are hoping to generate. Furthermore, the scale of this mechanical deformation greatly exceeds that of the thermal deformation caused by the incident beam. This changes the scope of the issue; rather than looking to improve the thermal transport in the system in order to reduce the build-up of heat in the monochromator crystal, we instead need to focus on minimising the temperature variation within the crystal and limit the amount of opposing forces introduced into the system.

### [Executive Summary of Chapter 2](#)

Heat transfer through the system is governed by three processes: absorption, conduction and radiation. These three processes taken together formed a one-dimensional model, which was shown to agree fully with three-dimensional FEA software.

The three different materials used each exhibit different mechanical properties when heated and cooled; in fact, it was ascertained that the majority of the deformation observed in the first crystal assembly was due to the disparate materials straining against one another.

The conventional monochromator design has too many materials interacting, causing mechanical deformations during cooling.

### 3. Exploring Various Crystal Geometries and Heat Exchange Locations

#### Review of the Thesis up to Chapter 3

Chapter 1, Literature Review, showed a lack of research into underlying causes of deformation in monochromator first crystals, with most literature focusing on mitigating said deformation. As increased synchrotron beam powers are demanded in concert with more beamlines per storage ring facility, a redesign of monochromator first crystals is required.

Chapter 2, Examining Thermal Transport through the use of Theoretical Models, has shown that with suitable boundary conditions FEA modelling is suitable to examine varying crystal designs. In addition, the presence of three contrasting sets of material properties gives rise to excessive stresses in the crystal assembly before the synchrotron beam is even incident, degrading the quality of the diffracted beam. This is a major factor and will need to be addressed in the novel design presented in this work.

#### 3.1 Introduction

Having examined the assembly in its entirety and identified the drawbacks inherent in it, the next step was to examine the existing crystal in isolation. By isolating the crystal deformations on a smaller scale can be observed without the deformation of the rest of the assembly overpowering that of the crystal. This identified what variables were dominant in the deformation of the crystal, rather than the current assembly, and from there a new assembly was designed to optimise these variables. There were some challenges associated with this - constraining the crystal in isolation is a difficult task, needing to approximate the thermal and mechanical coupling to a non-existent heat exchanger.

Once the crystal was isolated and the boundary conditions accurate to a decent approximation, new crystal designs were modelled and tested. This allowed new concepts to be explored; do the removed shoulders on the conventional crystal design have a significant effect on thermal

performance? Can the cooling of the crystal be improved by thinning it such that the bulk of waste X-ray radiation passes through the crystal, rather than being absorbed as heat? What effect does increasing the size of the crystal have? The answer to these questions informed the design of the novel, interference fit crystal.

The final aspect investigated by isolating the crystal was to identify the optimal position for the heat exchangers. In the conventional crystal used at the I20 beamline the heat exchangers are fastened to the sides of the crystal, covering the entirety of both long sides. However, anecdotal evidence suggests that cutting back the indium foil between the silicon crystal and the copper heat exchanger decreased the deformation of the diffracting surface as shown in Figure 32; as such this was identified as a potential interest to see if this was the case and whether it was caused by a mechanical or a thermal effect. It was also decided to push this to the logical extreme by testing a bottom-cooled design with the heat exchanger attached opposite the diffracting surface rather than to one of the parallel sides.

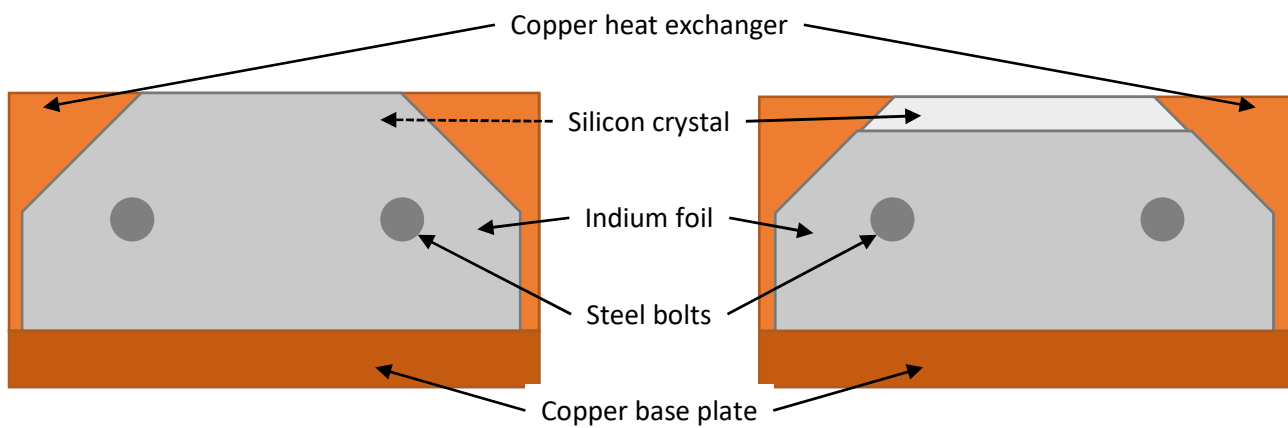


*Figure 32 – Design of cut-back indium foil. (Left) Indium foil covering entire silicon crystal surface with steel bolts passing through assembly. (Right) Indium foil covering most of silicon crystal surface, cut back 5 mm from diffracting surface.*

### 3.2 Isolating the Monochromator First Crystal in a 3D Model

To examine the crystal in isolation in COMSOL required two steps: first, to reproduce the crystal geometry in isolation; then, to accurately model the boundary conditions to properly constrain and support the silicon crystal without the surrounding components. The first step was simple, as the dimensions of the crystal were already known and had already been produced in COMSOL as part of the full finite element model. The latter however required some consideration; without the heat exchangers boundary conditions were needed to emulate both the thermal and mechanical interactions within the system.

The crystal was held in place through the use of a fixed point, located at the centre of the bottom face of the crystal; to prevent the crystal rotating around this point while still allowing free deformation otherwise, a line from this point to the centre of the diffracting surface was considered fixed in the x- and y-directions, as shown in Figure 33.

The two long sides of the crystal were maintained at 80 K to simulate perfect thermal contact. Omitting the two long sides and the bottom surface, the rest of the crystal faces were modelled as radiating to an 80 K environment, as shown in Figure 34. The crystal was modelled as starting at 300 K, so the change in dimensions from cooling could be observed.

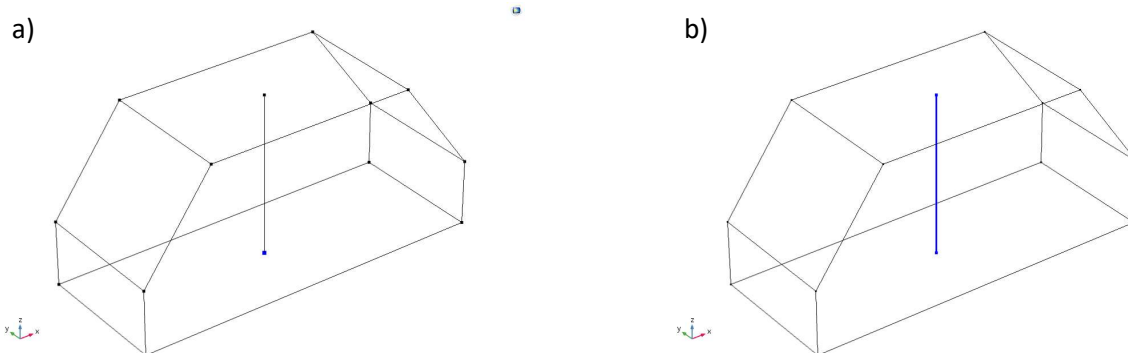


Figure 33 – Mechanical boundary conditions for isolated crystal: a) central point on bottom surface held fully constrained; b) line running through centre of crystal in z-direction held in x- and y-directions to prevent rotation.

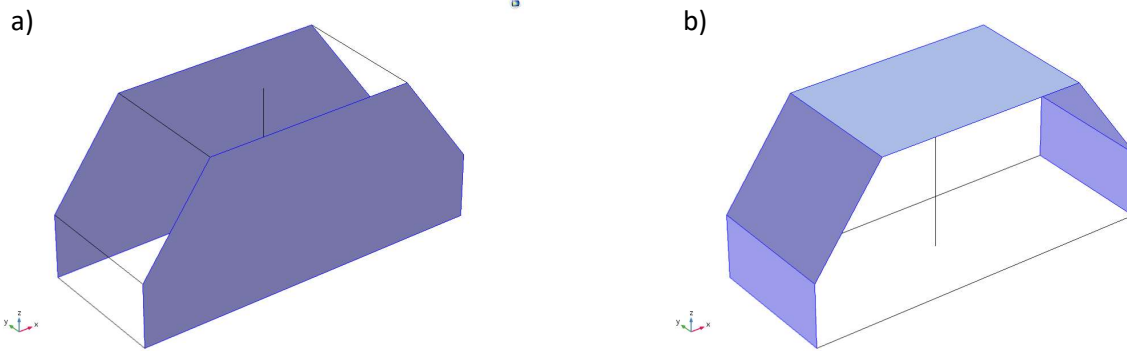


Figure 34 – Thermal boundary conditions for isolated crystal: a) the two long sides of the crystal held at a constant 80 K; b) all exposed surfaces modelled as radiating to an 80 K ambient temperature.

As the silicon crystal was cooled down from room temperature, the long sides shrink first and fastest. This is due to them being modelled at a fixed temperature of 80 K. Over time the rest of the crystal approaches thermal equilibrium, heat flowing to the cold surfaces where it would be conducted away into the heat exchangers. As the temperature of the crystal drops below 120 K, the coefficient of thermal expansion becomes negative and the crystal begins to grow, rather than shrink. Due to the loose boundary conditions, by the time the crystal has thermalized there is negligible stress within the crystal as the thermal deformation is uniform. The crystal is smaller at 80 K than it was at 300 K, but has grown since passing the 120 K mark. This regime change, expanding below 120 K, will cause a build-up of pressure in any assembly when cooling past this temperature. Images of the crystal at 0, 0.1 and 1 seconds are shown in Figure 35 below.

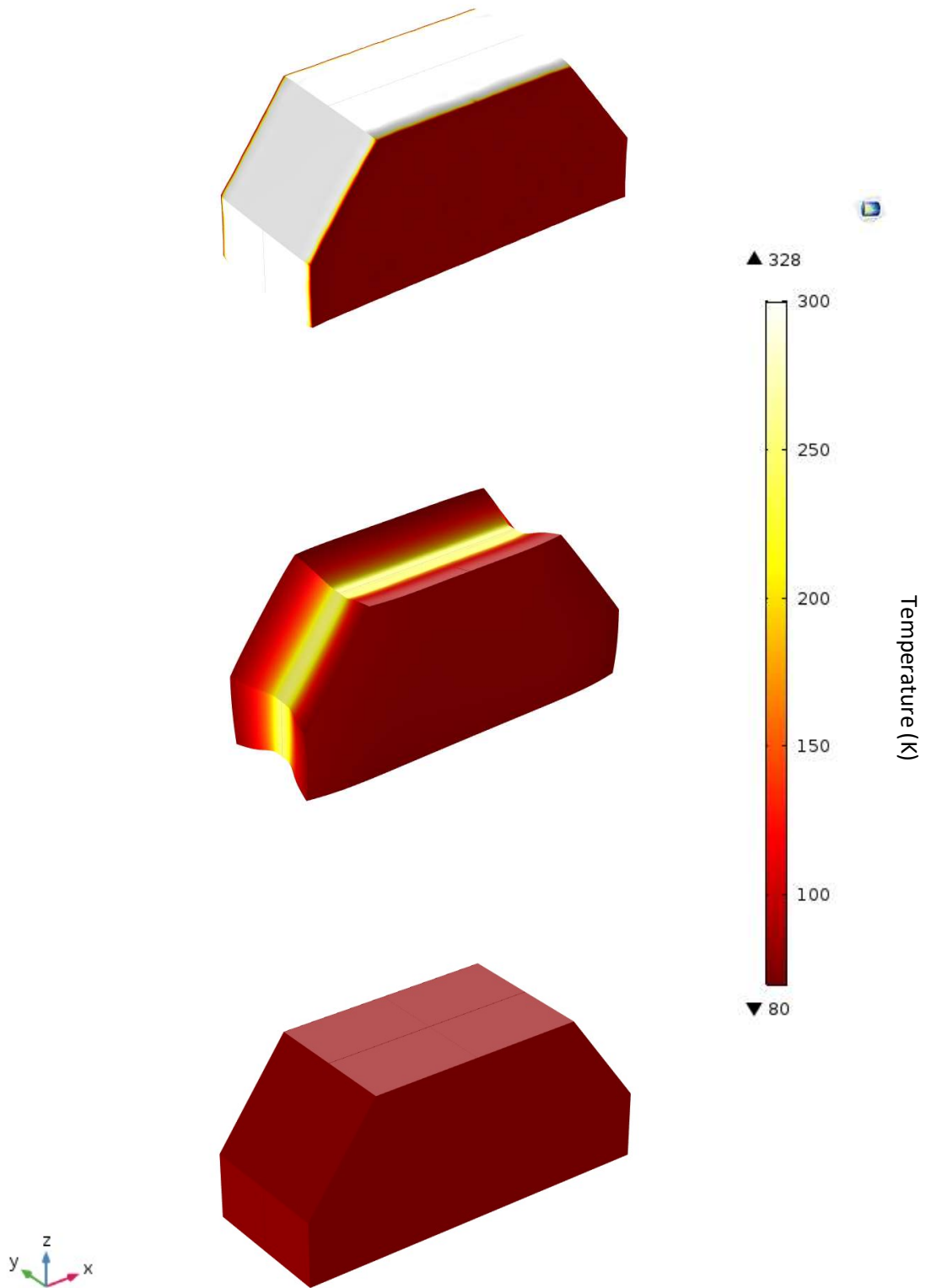


Figure 35 – Temperature plot (K) of isolated crystal at 0 (top), 0.1 (middle) and 1 (bottom) seconds after cooling begins

Having modelled the crystal cooling in isolation, the next step was to model an incident beam on the diffracting surface of the crystal. To do this, the flux of the I20 beamline at Diamond Light Source as a function of wavelength was combined with the absorption coefficient of silicon at different wavelengths to create a graph of power as a function of penetration depth, as shown in Figure 12 in Section 2.2. This was modelled in COMSOL as a heat source applied throughout a rectangular section of the crystal as a function of the z-co-ordinate, such that the beam footprint is considered incident on the diffracting surface; this added boundary condition and a surface plot of beam power throughout the crystal is shown in Figure 36 to illustrate the intensity of deposited power throughout the crystal.

The model was run until it reached thermal equilibrium using the boundary conditions in Figure 34 above; once thermal equilibrium had been reached, heat was deposited in the region shown in Figure 36 as though the beam was incident on the crystal. The resultant temperature is shown in Figure 37.

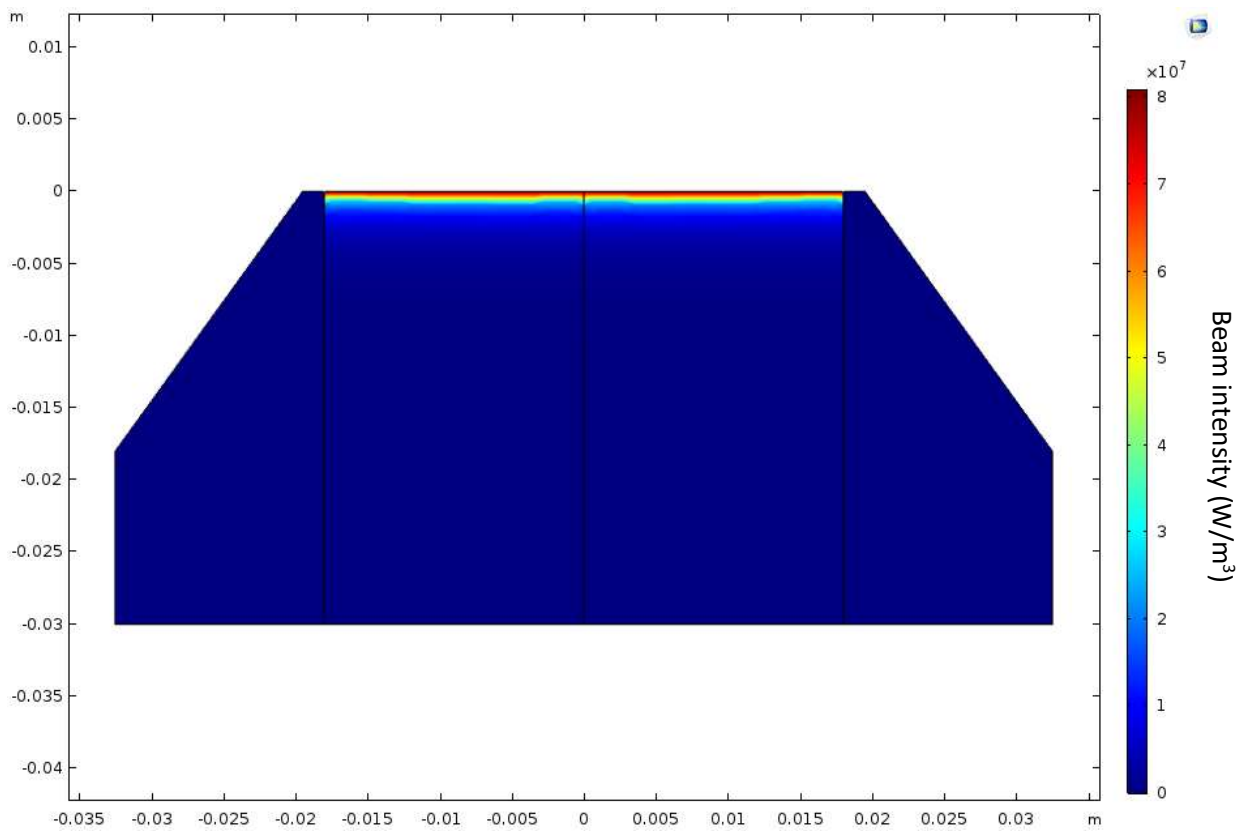
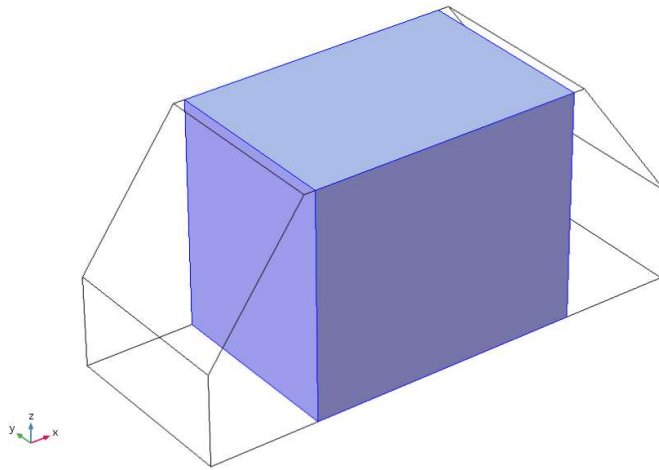


Figure 36 – (Top) Volume of crystal considered exposed to beam for heat deposition.  
 (Bottom) Beam power deposition through the affected region of the crystal.

As the diffracting surface heats, it contracts due to the negative coefficient of thermal expansion of silicon below 120 K. This contraction of the diffracting surface is opposed by the cooled, long sides of the crystal maintaining a constant size due to their fixed temperature. These contrasting effects cause the sides to bow inwards as the diffracting surface dips in the centre, causing a difference in

deformation across the diffracting surface of  $1.02 \times 10^{-9}$  m, as shown in Figure 38. The deformation variance in the sagittal plane (YZ) has been used to test the performance of monochromator designs henceforth and defined as the difference in surface deformation measured in the sagittal plane. This has been decided as the deformation deviance will directly change the wavelength of x-ray radiation selected by the monochromator; in most tests, it has been observed that the deformation in the sagittal plane is equal to or greater than that in the transverse plane (XZ).

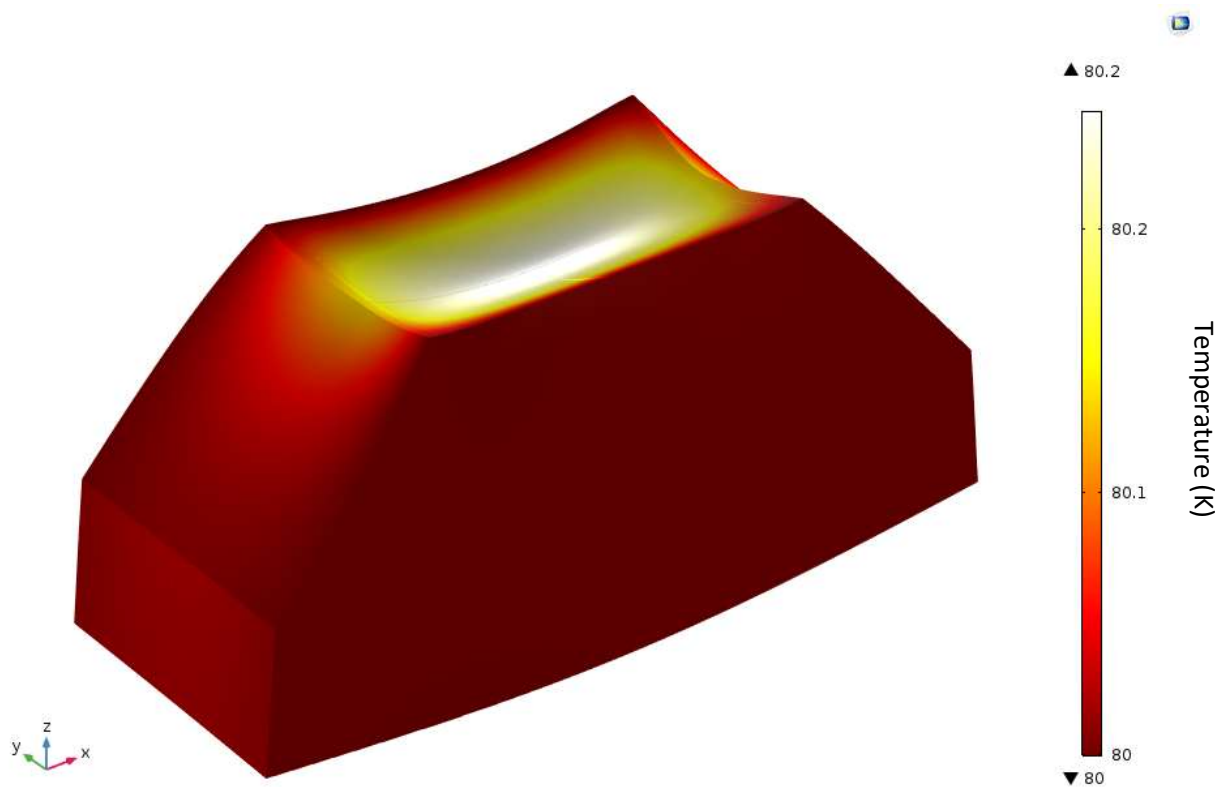


Figure 37 – Isolated crystal exposed to incident beam showing surface deformation as a result of heating (K).

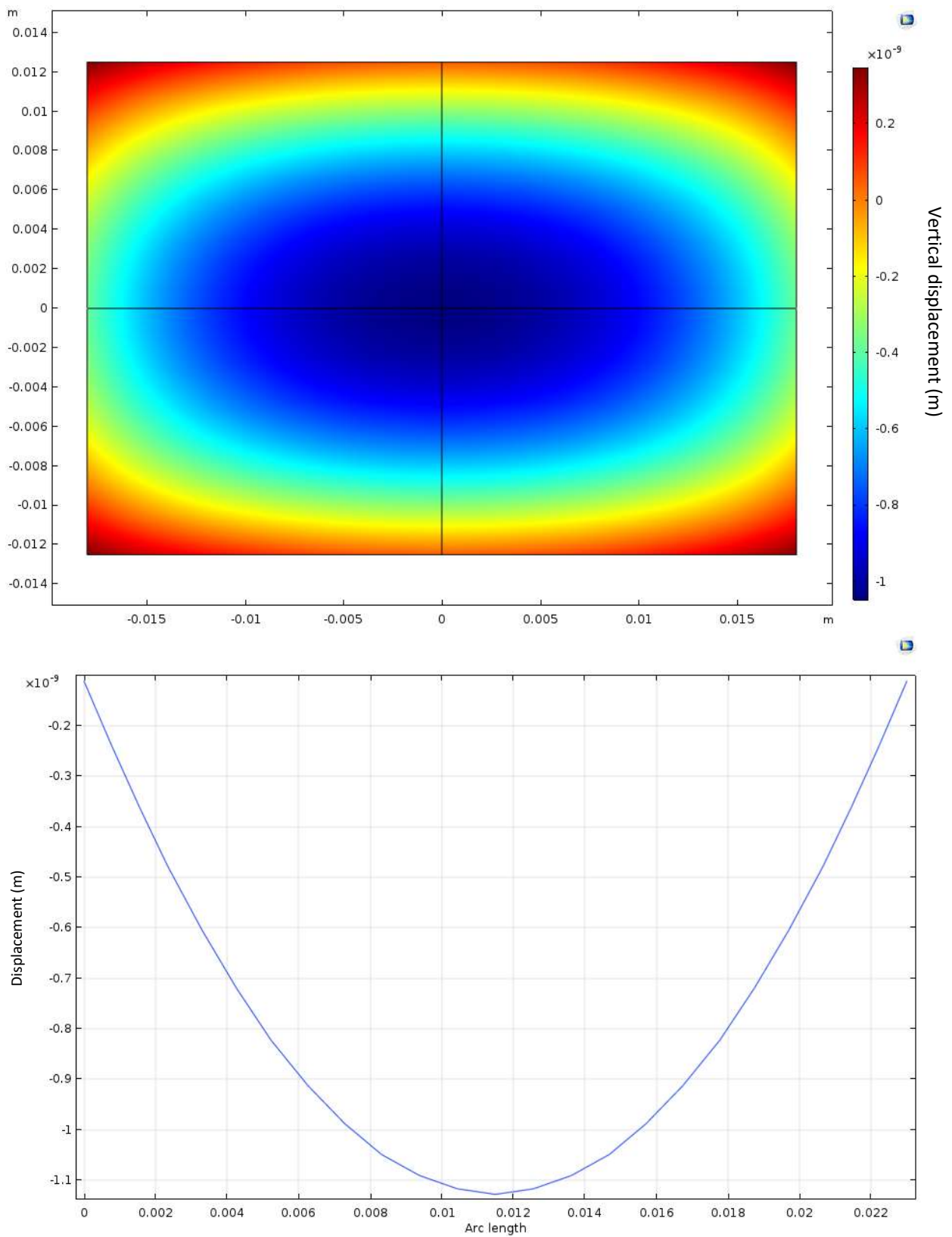
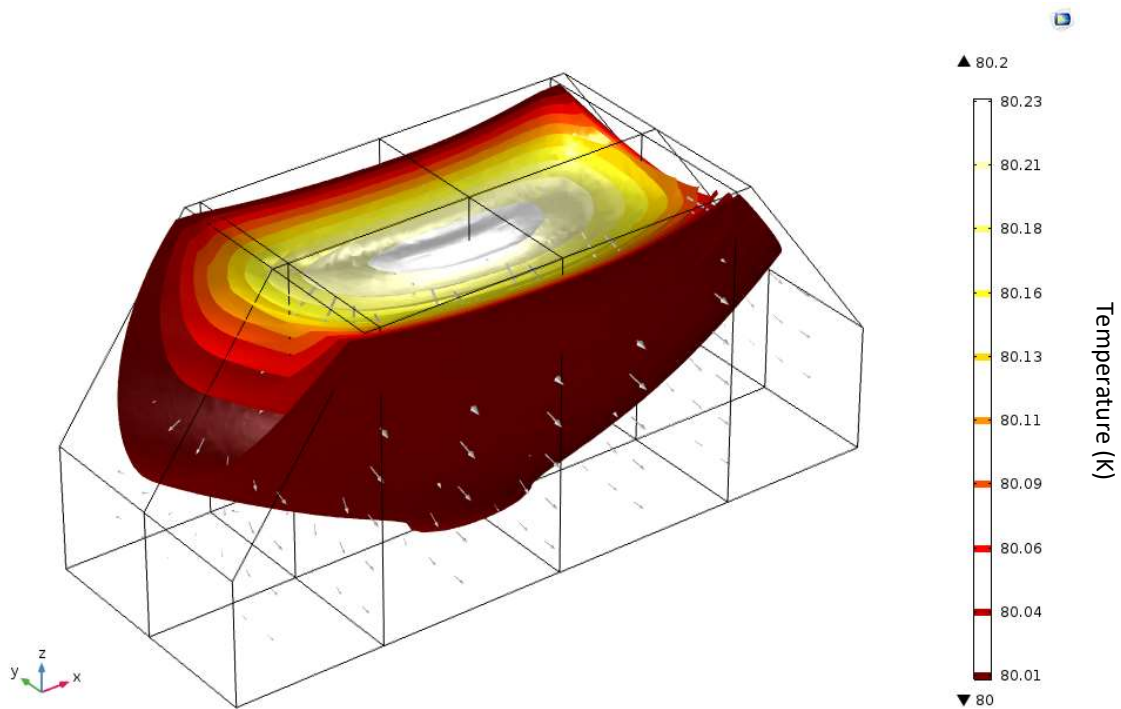


Figure 38 – (Top) Surface displacement of isolated crystal diffracting surface as a result of heating. (Bottom) Cross-section of sagittal plane (m), showing deformation variance of  $1.02 \times 10^{-9}$  m.

By isolating the crystal we have been able to observe the deformation on a smaller scale, giving us greater understanding of the system. In addition to the deformation caused by the mismatched materials cooling at different rates, as observed in Chapter 2, Figure 39 below shows that the heat deposited by the beam travels a variable distance to get to the cooled surfaces. This variable heat path causes a temperature gradient to form in the crystal; as shown in Section 2.2, the greater the distance between the absorption point of the heat and the cooling area, the higher the temperature reached. Therefore areas with a longer distance for heat to travel, hereafter referred to as a 'thermal pathway', will reach a higher temperature than areas with a shorter thermal pathway. As this creates areas of different temperatures the crystal experiences non-uniform thermal deformation.

There are two ways we can approach this issue to try and minimise the deformation: first, we could try to normalise the thermal path length by shaping the crystal such that contact with the heat exchanger followed the shape of the isothermal surfaces shown in Figure 39. This would result in constant temperature across the crystal. However, as the angle of the crystal is changed to select different wavelengths of X-ray radiation, the heated area changes size – this would change the thermal path lengths needed on a minute-to-minute basis, and so disqualifies this as a possibility.



*Figure 39 – Isolated crystal exposed to incident beam; isothermal layers mapped (K), with arrows showing movement of heat.*

The other approach modelled was to increase the distance between the diffracting surface and the heat exchanger, to allow the temperature to normalise across the diffracting surface. To investigate this possibility, a bottom-cooled crystal was considered. A bottom cooled crystal is likely to result in a higher temperature throughout the crystal, as the mean thermal pathway will be increased comparative to a side-cooled crystal; however, as the thermal pathways are all of similar length, the temperature throughout the crystal should be far more uniform. In order to test this hypothesis, the I20 beamline crystal was modelled in isolation with the bottom surface cooled, rather than the sides. The mechanical boundary conditions match those given in Figure 33, while the thermal boundary conditions are shown in Figure 40 and the resultant temperature profile is shown in Figure 41. As hypothesised, the diffracting surface is showing a higher but more uniform temperature. Figure 42 shows the isothermal layers in the crystal, which are also much more uniform. The heat is visibly moving down the crystal, rather than out the sides, resulting in smooth,

flat isothermals. Figure 43 shows the deformation across the diffracting surface to vary by  $7.58 \times 10^{-10}$  m, which is half that shown in Figure 38. This shows that bottom cooling could be an improvement for the I20 crystal, so it has been considered as a possibility for other crystal designs.

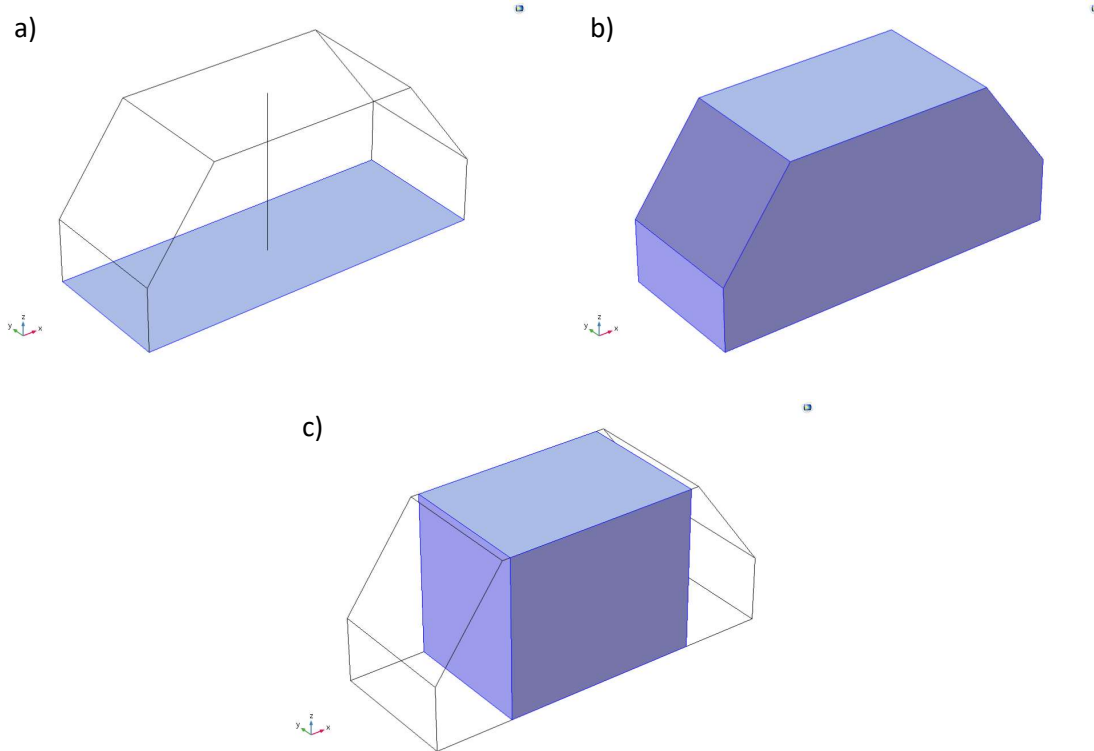


*Figure 40 – Thermal boundary conditions for isolated crystal (bottom cooled): a) bottom surface held at constant 80 K; b) all exposed surfaces radiating to an 80 K ambient temperature; c) central volume exposed to beam for heat deposition.*

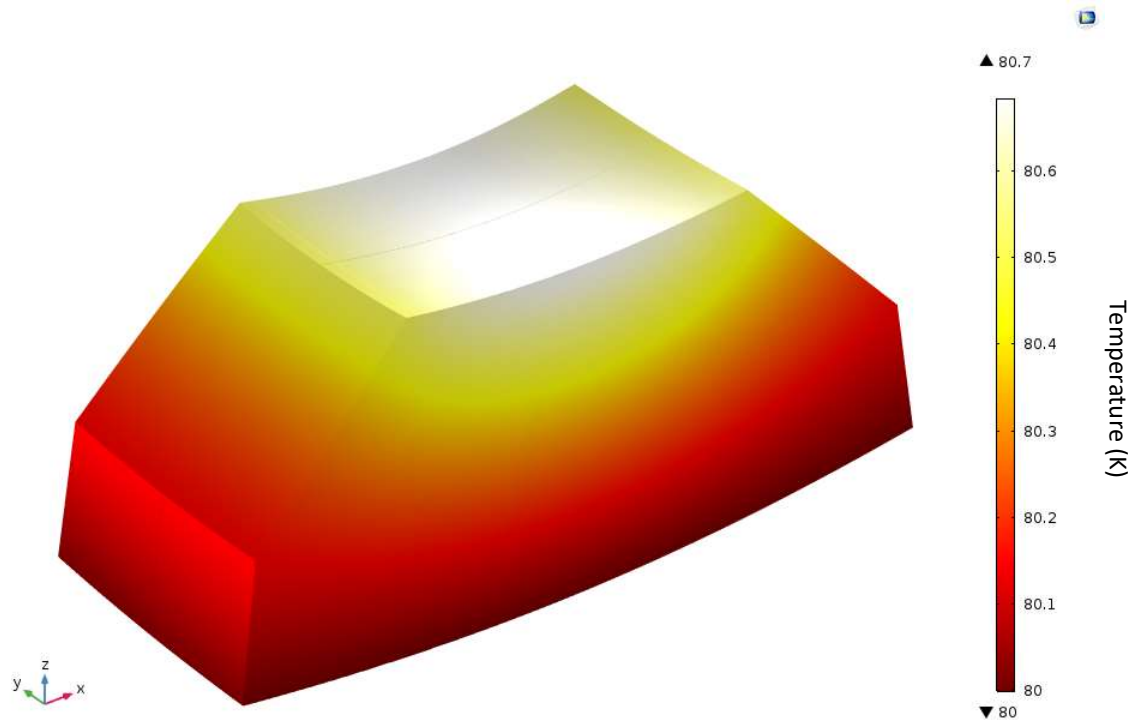


Figure 41 - Isolated crystal exposed to incident beam and cooled on bottom surface showing more uniform surface deformation as a result of heating (K).

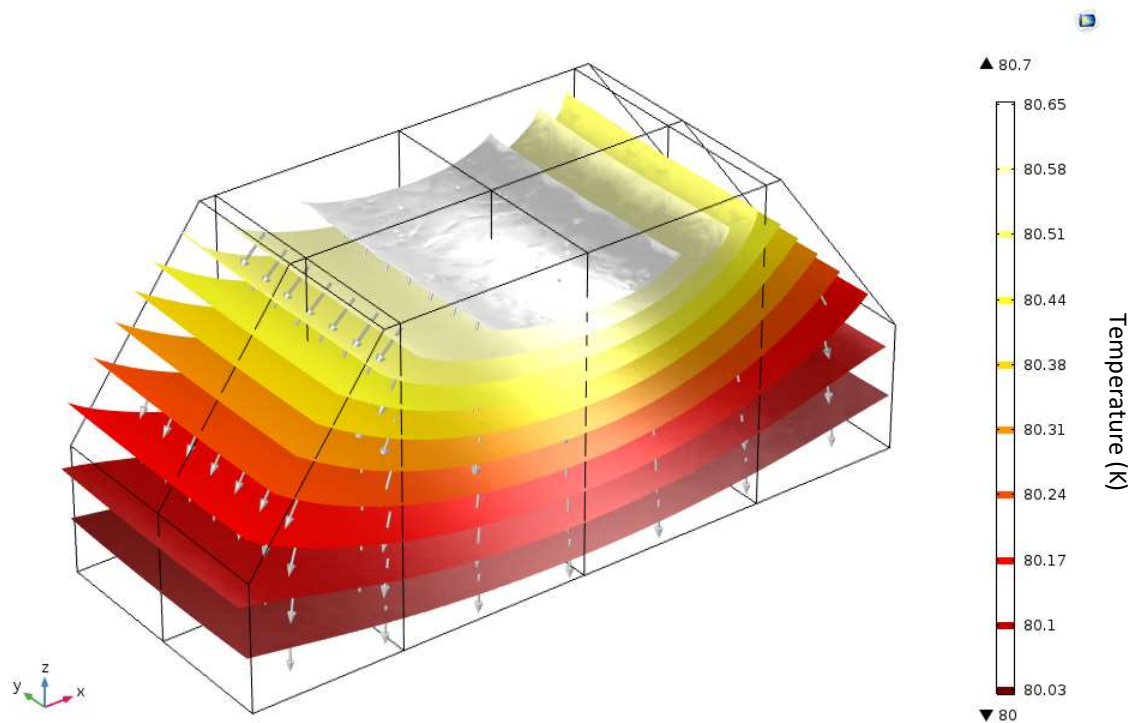


Figure 42 - Isolated crystal exposed to incident beam and cooled on bottom surface; isothermal layers mapped (K), with arrows showing movement of heat.

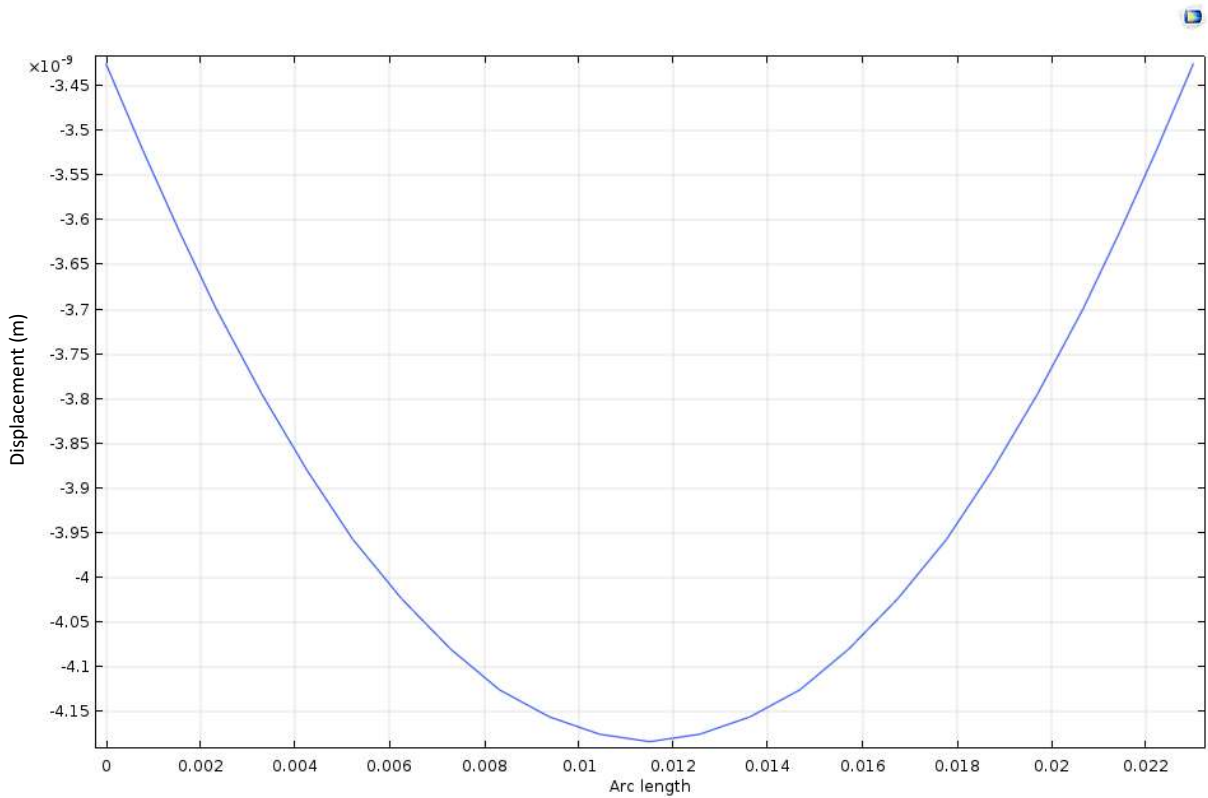
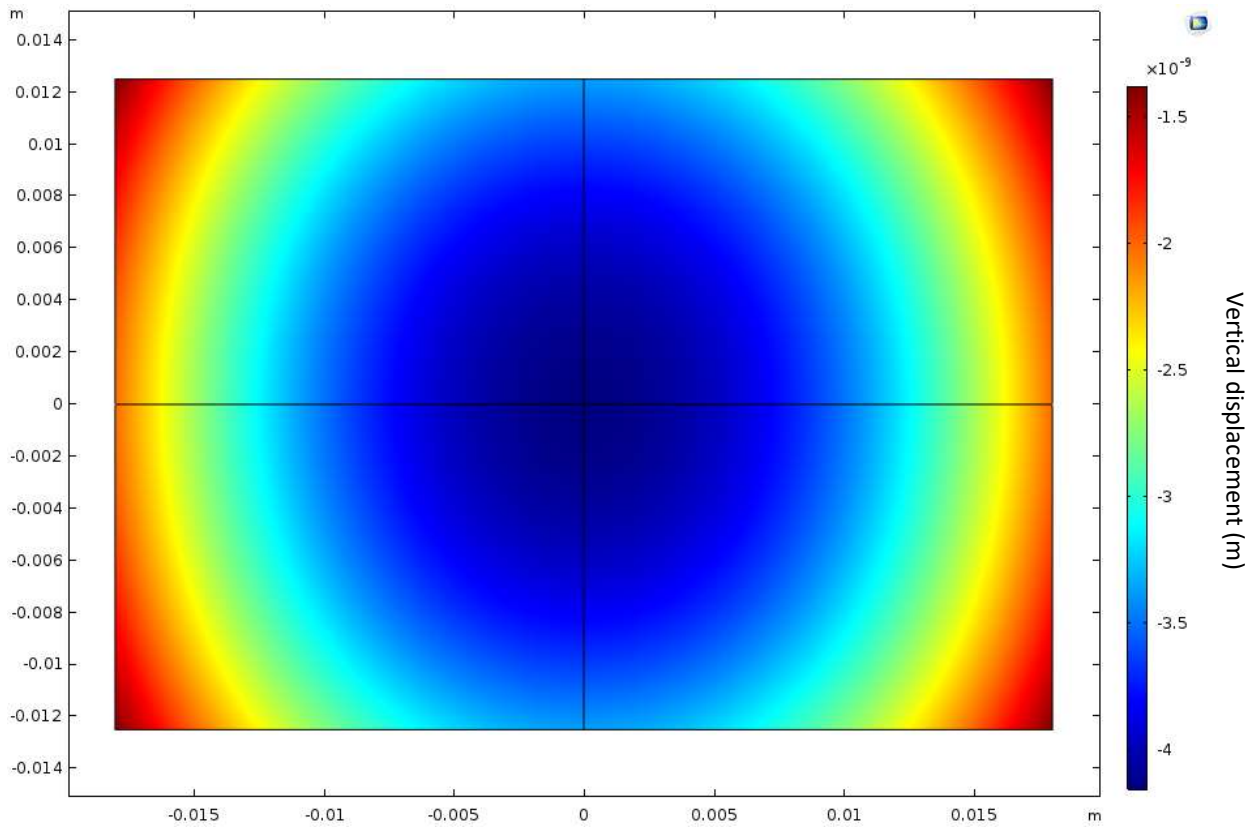


Figure 43 - (Top) Surface displacement of isolated crystal diffracting surface as a result of heating.

(Bottom) Cross-section of sagittal plane (m), showing deformation variance of  $7.58 \times 10^{-10}$  m.

### 3.3 Investigating the Benefits of Modified Crystal Designs

Having gained a thorough understanding of how heat is transferred through the crystal, along with the factors that control deformation at the diffracting surface, the next step was to model a number of different crystal designs. Beyond modelling boundary conditions for free thermal expansion, at this point how these crystals would be held was not considered; while cooled sides and fixed points were defined, no form of assembly was modelled that would provide these boundaries as the priority was to examine how different crystal designs would affect the thermal deformation introduced into the crystals. Each crystal design was given one or more surfaces fixed at 80 K, and exposed to a beam footprint of 23 mm x 36 mm to simulate the I20 beam at maximum angle of incidence.

#### 3.3.1 'Square' Crystal

The first modification to the design was to remove the 'shoulder' sections from the existing I20 crystal, creating a smaller, cuboid crystal, hereafter referred to as the 'squared' crystal, measuring 38 mm x 26 mm x 30 mm. This was modelled in two ways: first, with side cooling, and second with bottom cooling. The mechanical boundary conditions consisted of a fixed point at the centre of the bottom surface of the crystal, along with a vertical line prescribed from moving in the x- or y-direction as shown in Figure 44; the thermal boundary conditions are detailed below.

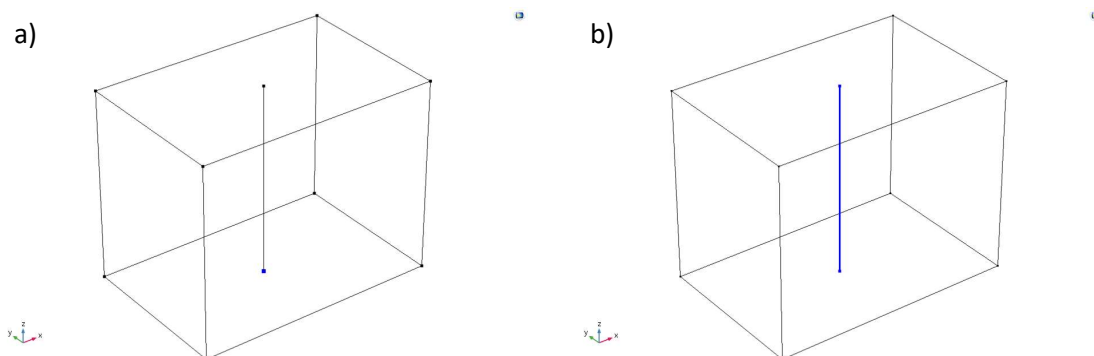


Figure 44 - Mechanical boundary conditions for 'squared' crystal: a) central point on bottom surface held fully constrained; b) line running through centre of crystal in z-direction held in x- and y-directions to prevent rotation.

### 3.3.1.1 Side cooling

Considering first the side-cooled crystal, the thermal boundary conditions consisted of a fixed temperature along the two long side faces, a diffuse surface on all the non-contact faces and a general heat source applied throughout the crystal as described in Section 3.2; these boundary conditions are shown in Figure 45.

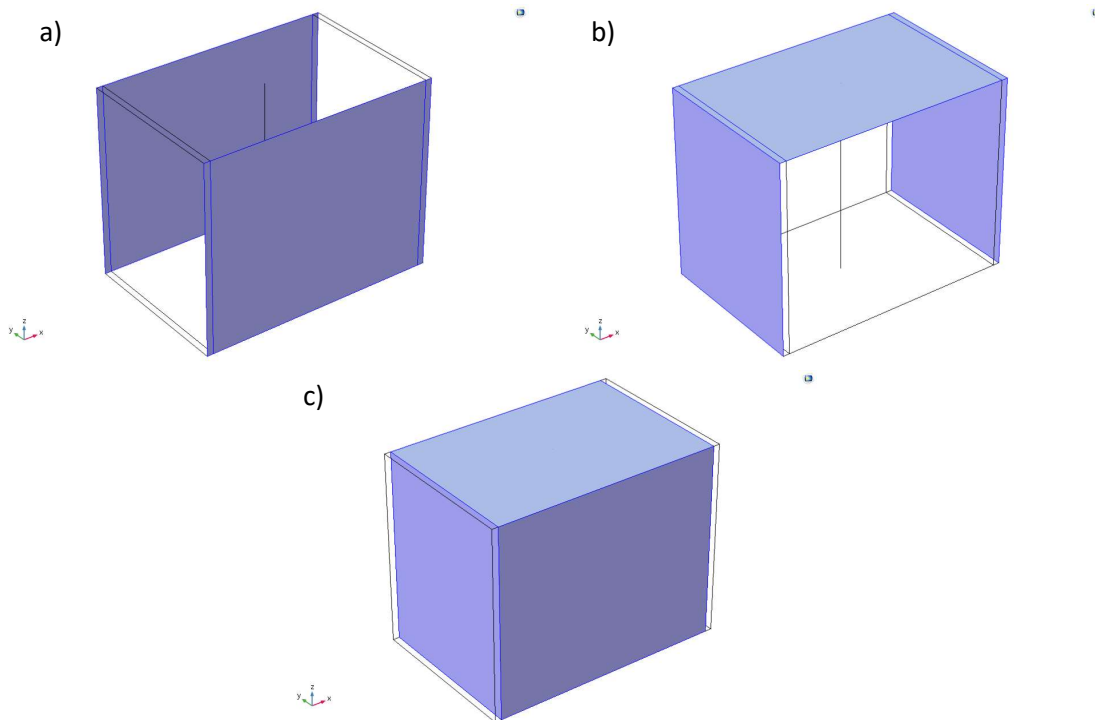


Figure 45 - Thermal boundary conditions for 'squared' crystal (side cooled): a) side surfaces of crystal held at constant 80 K; b) all exposed surfaces radiating to 80 K ambient temperature; c) central volume exposed to beam for heat deposition.

The temperature throughout the crystal is shown in Figure 46, with an isothermal layer plot shown in Figure 47 and a surface plot of deformation of the diffracting surface shown in Figure 48. The surface deformation is found to have a variance of  $1.05 \times 10^{-9}$  m, showing a comparable diffracting surface to the conventional, side-cooled crystal. Removing the shoulders of the conventional crystal has improved the uniformity of the thermal pathways, reducing surface deformation variance, but not by any significant degree.

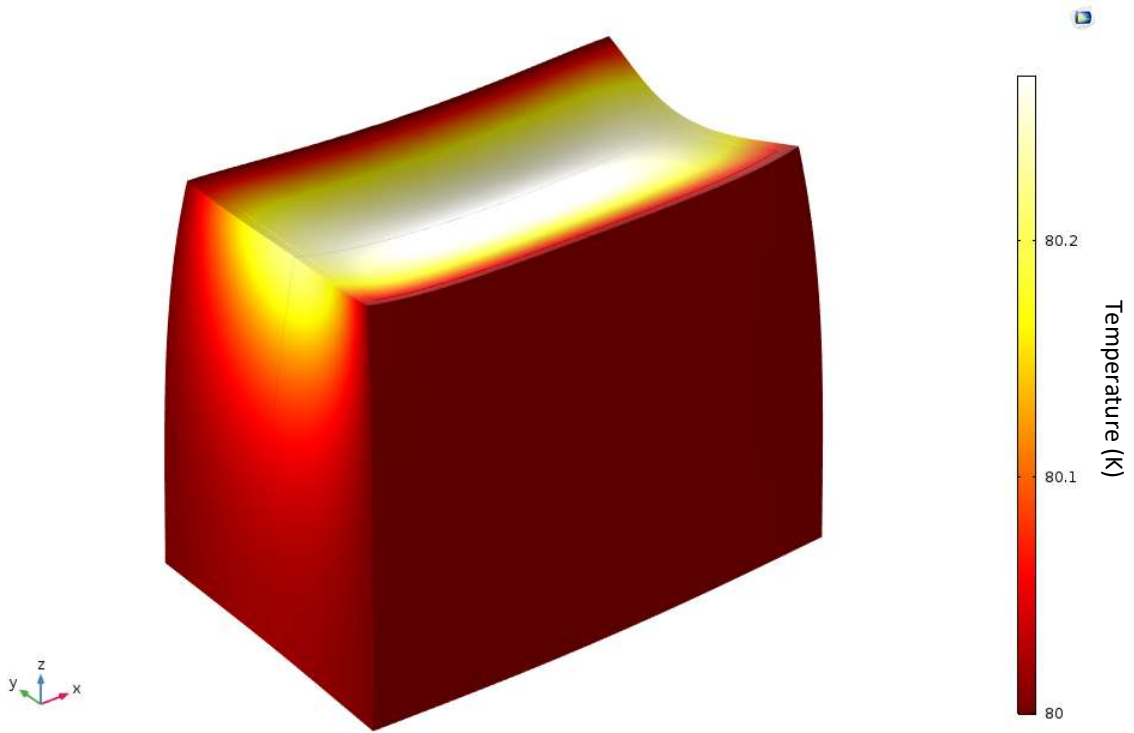


Figure 46 – Temperature surface plot (K) of side cooled ‘squared’ crystal exposed to incident beam.

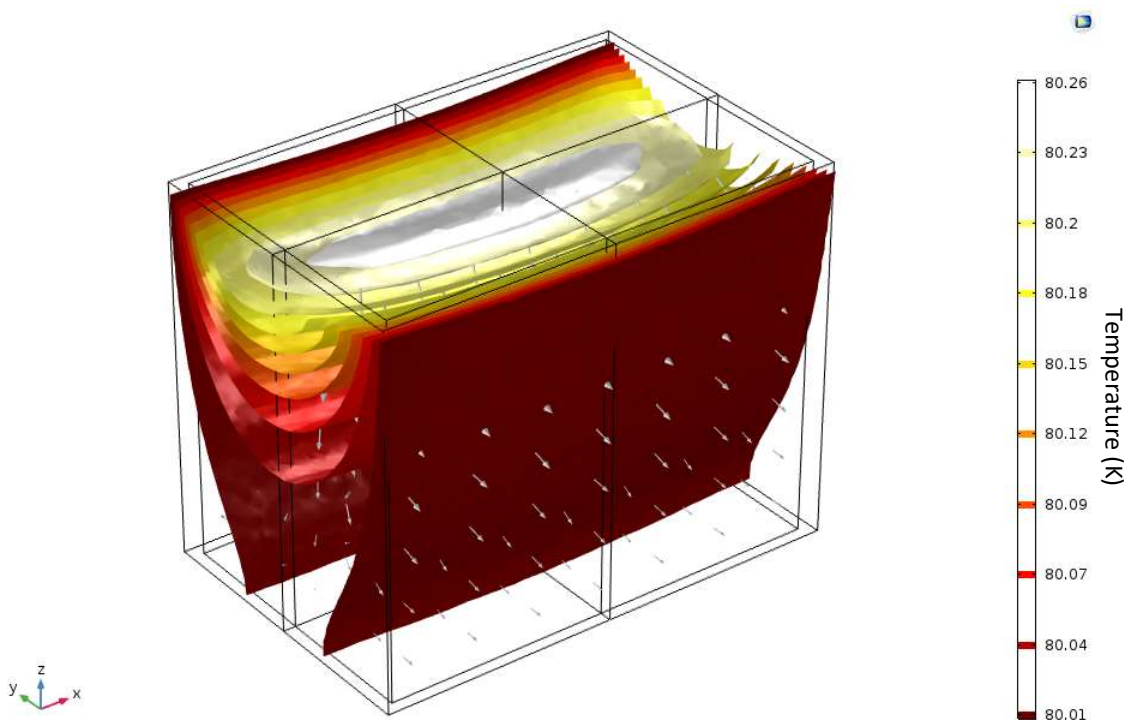


Figure 47 – Side cooled ‘squared’ crystal exposed to incident beam; isothermal layers mapped (K), with arrows showing movement of heat.

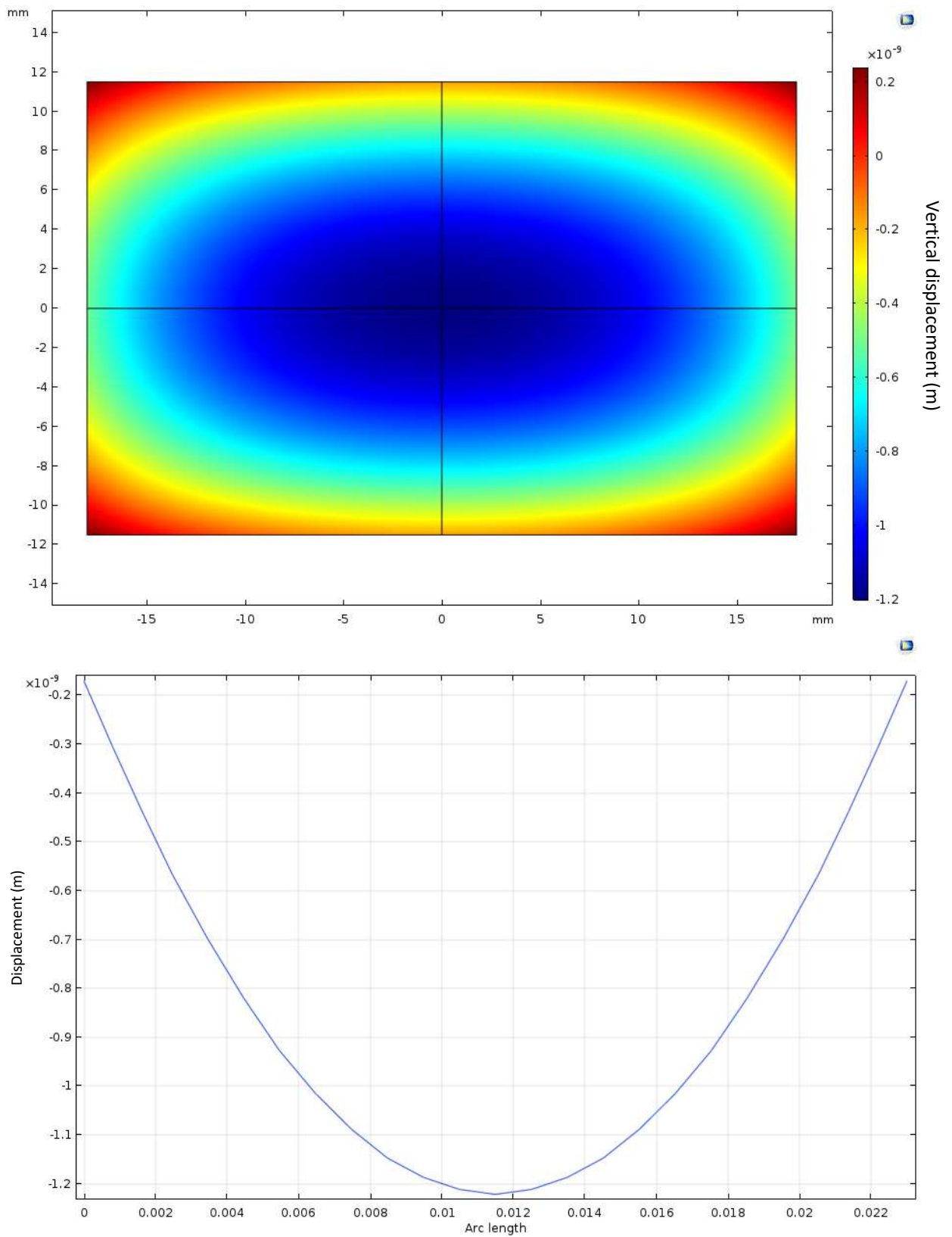
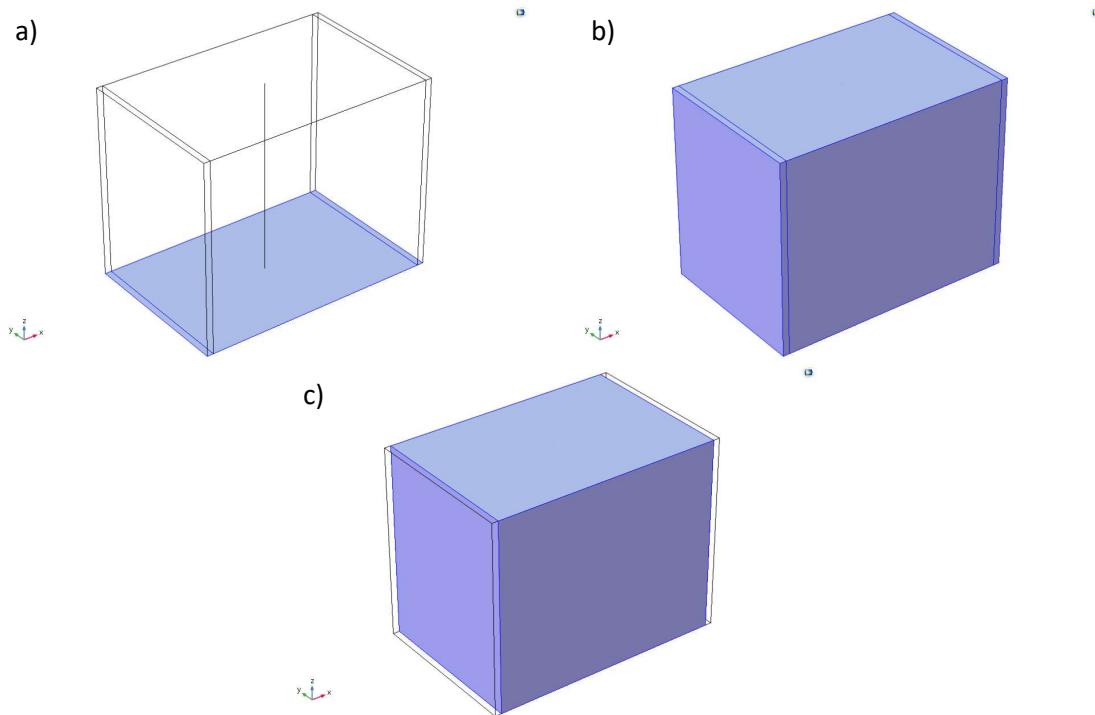


Figure 48 - (Top) Surface displacement of side cooled 'squared' crystal diffracting surface as a result of heating.

(Bottom) Cross-section of sagittal plane (m), showing deformation variance of  $1.05 \times 10^{-9}$  m.

### 3.3.1.2 Bottom cooling

Considering the bottom-cooled crystal, the thermal boundary conditions consisted of a fixed temperature along the bottom side face, a diffuse surface on all the non-contact faces and a general heat source applied throughout the crystal as described in Section 3.2; these boundary conditions are shown in Figure 49.



*Figure 49 - Thermal boundary conditions for 'squared' crystal (bottom cooled): a) bottom surface of crystal held at constant 80 K; b) all exposed surfaces radiating to 80 K ambient temperature; c) central volume exposed to beam for heat deposition.*

The temperature throughout is shown in Figure 50, an isothermal layer plot in Figure 51 and the diffraction surface deformation in Figure 52, showing a variation of  $8.70 \times 10^{-10}$  m. Once again, cooling the crystal from the bottom has led to a higher peak temperature, but an overall slight reduction in the difference in deformation across the diffracting surface, resulting in a more uniform surface and therefore improving the quality of a reflected beam. Moving from the I20 crystal to the 'square' crystal has had a similarly insignificant effect on the bottom-cooled crystal.

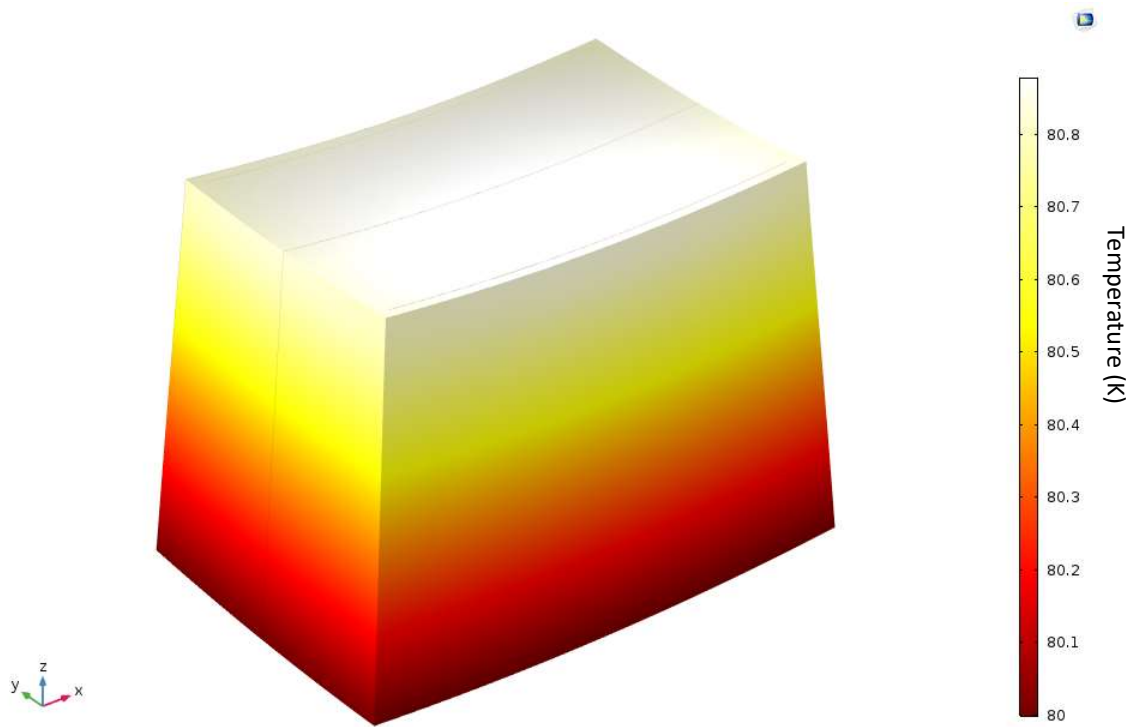


Figure 50 - Temperature surface plot (K) of bottom cooled 'squared' crystal exposed to incident beam.

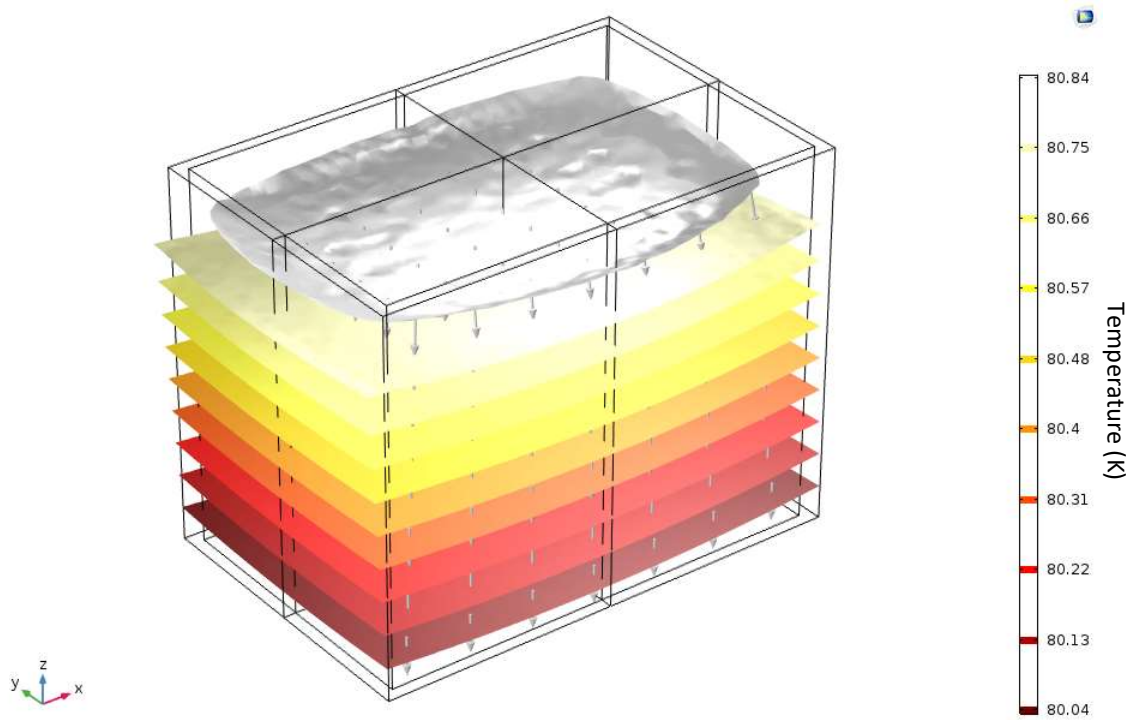


Figure 51 - Bottom cooled 'squared' crystal exposed to incident beam; isothermal layers mapped (K), with arrows showing movement of heat.

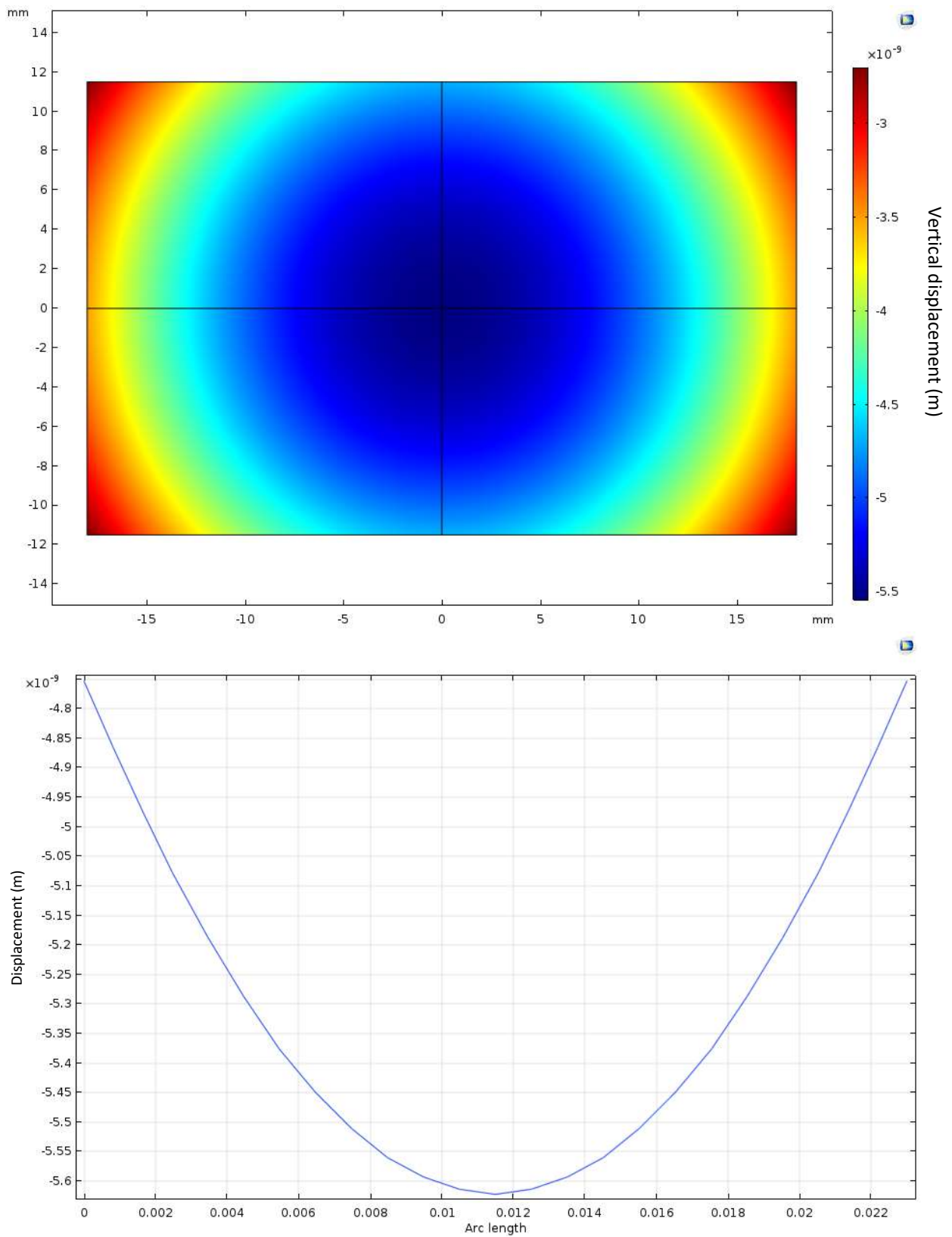
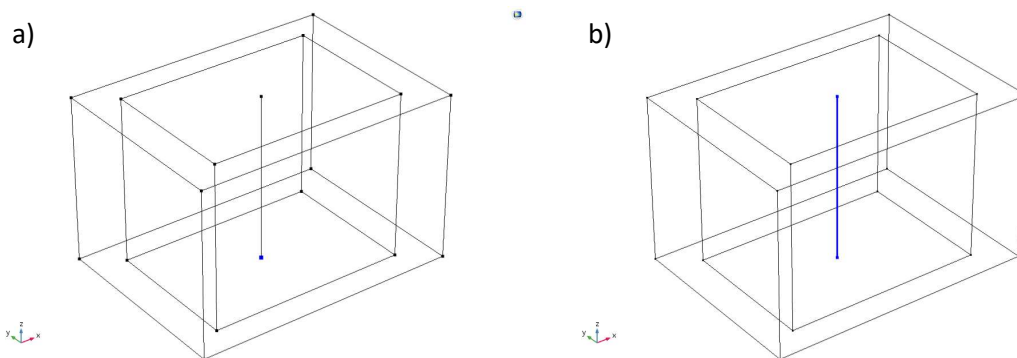


Figure 52 - (Top) Surface displacement of bottom cooled 'squared' crystal diffracting surface as a result of heating.

(Bottom) Cross-section of sagittal plane (m), showing deformation variance of  $8.70 \times 10^{-10}$  m.

### 3.3.2 'Bulk' Crystal

The next design modelled was intended to investigate the industry standard design philosophy, that of increasing the size of the crystals in order to dissipate the heat and maintain a more uniform shape across the diffracting region, rather than being concerned with the entire crystal. This solution, should it get significant results, is not ideal as it greatly increases the size of the beamline optics and therefore reduces the number of beamlines we can install around each storage ring. Regardless, it is worth investigation as the industry standard. To simulate this approach, the 'squared' crystal was expanded 10 mm in both the x- and y-directions, creating a larger 'buffer area' around the diffracting region and hereafter referred to as the 'bulk' crystal, the new crystal measuring 48 mm x 36 mm x 30 mm. The mechanical boundaries are the same as those used previously and are shown in Figure 53, as are the thermal boundaries as shown in the sections below.



*Figure 53 - Mechanical boundary conditions for 'bulk' crystal: a) central point on bottom surface held fully constrained; b) line running through centre of crystal in z-direction held in x- and y-directions to prevent rotation.*

### 3.3.2.1 Side cooling

Considering first the side cooled crystal, similar thermal boundary conditions have been used as in the previous section and as shown in Figure 54 below.

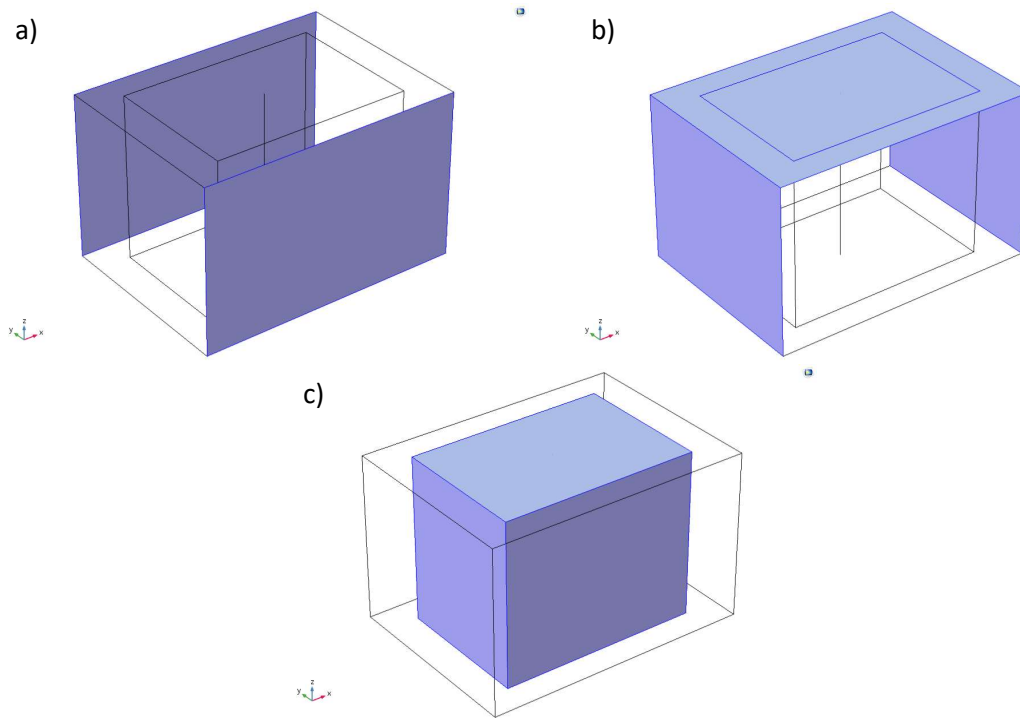


*Figure 54 - Thermal boundary conditions for 'bulk' crystal (side cooled): a) side surfaces of crystal held at constant 80 K; b) all exposed surfaces radiating to 80 K ambient temperature; c) central volume exposed to beam for heat deposition.*

The temperature is comparable to that of previous crystals cooled through the long sides, as shown in Figure 55, and the heat again travels through the crystal along pathways of variable length as shown in Figure 56. The diffracting surface deformation is shown in Figure 57 and is found to have a variance of  $9.68 \times 10^{-10}$  m, a result which is a marked improvement over that observed in both the squared and I20 crystal designs.

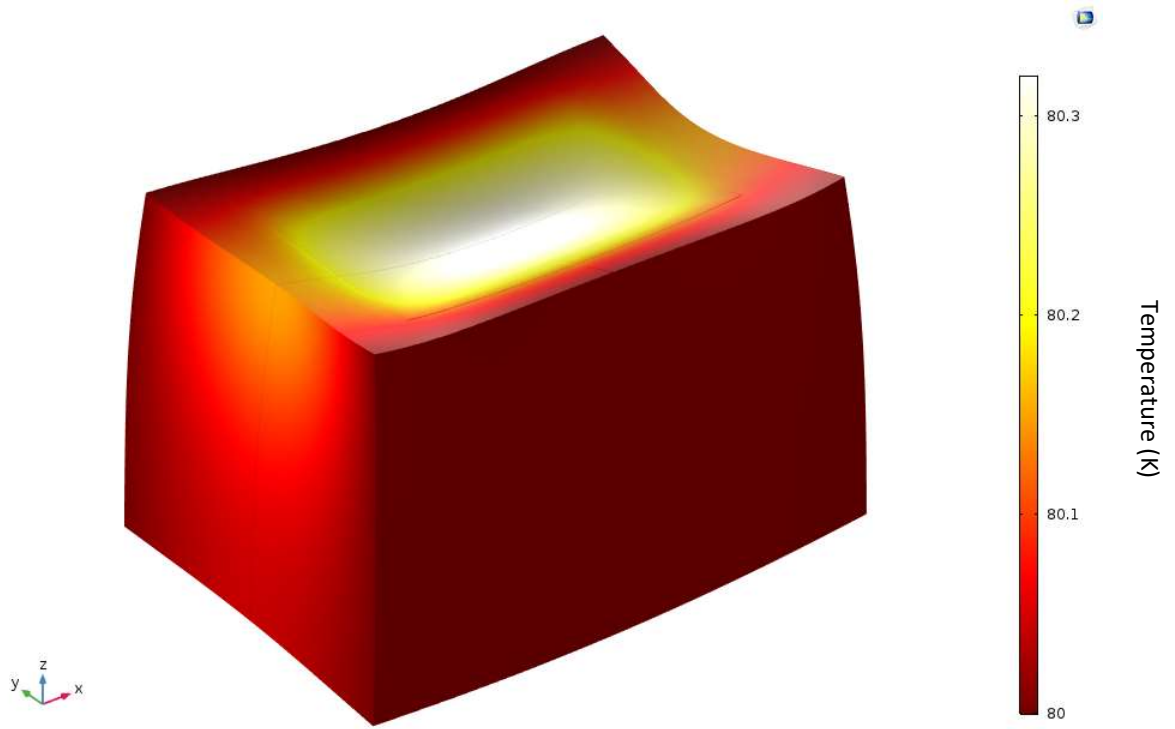


Figure 55 - Temperature surface plot of side cooled 'bulk' crystal exposed to incident beam (K).

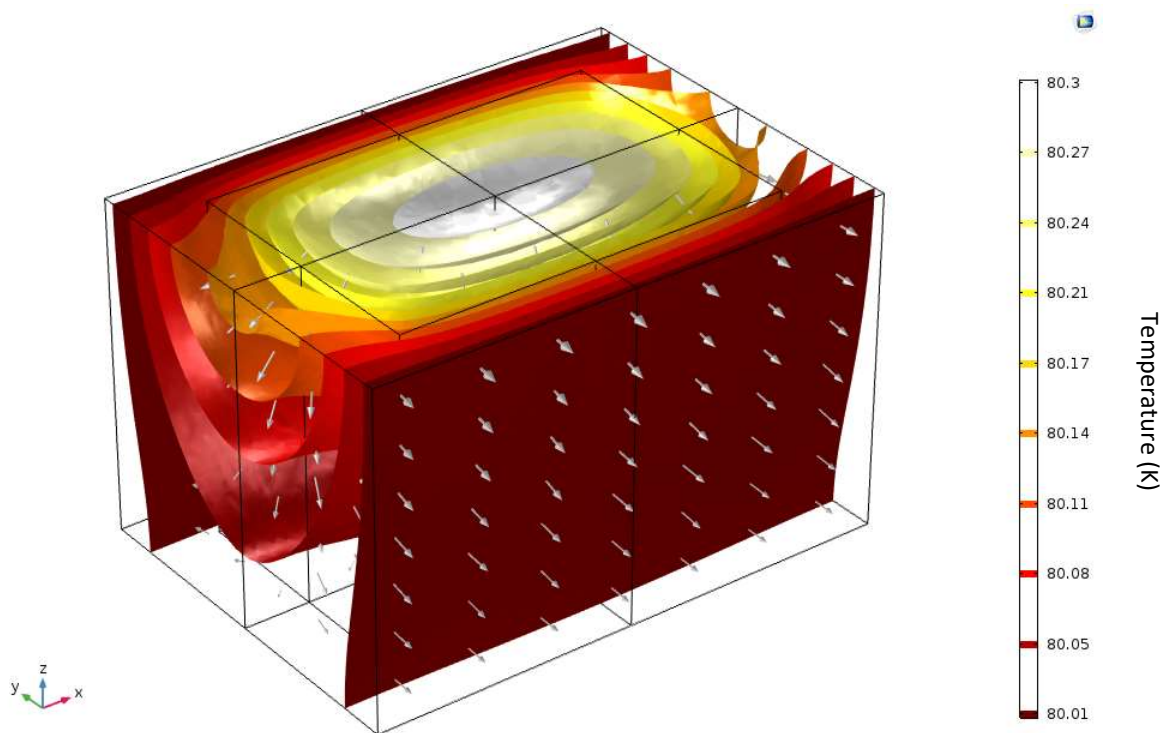


Figure 56 - Side cooled 'bulk' crystal exposed to incident beam; isothermal layers mapped (K), with arrows showing movement of heat.

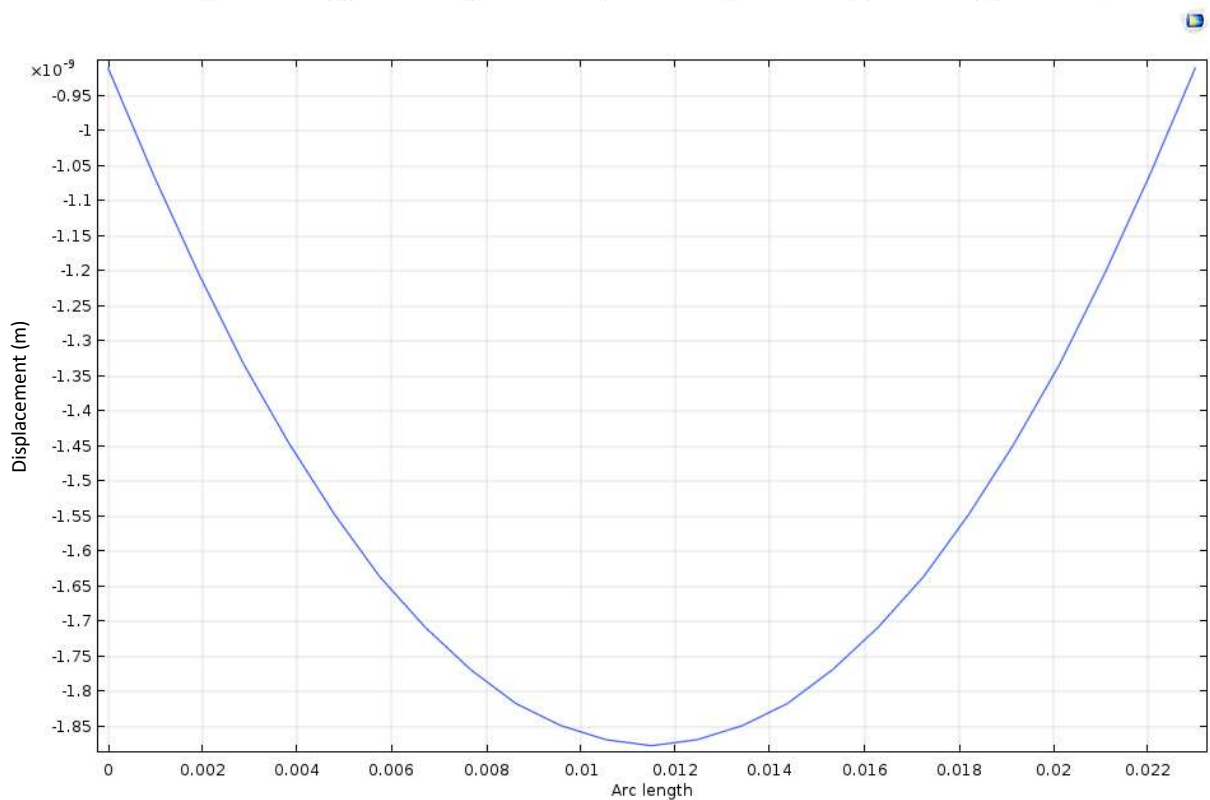
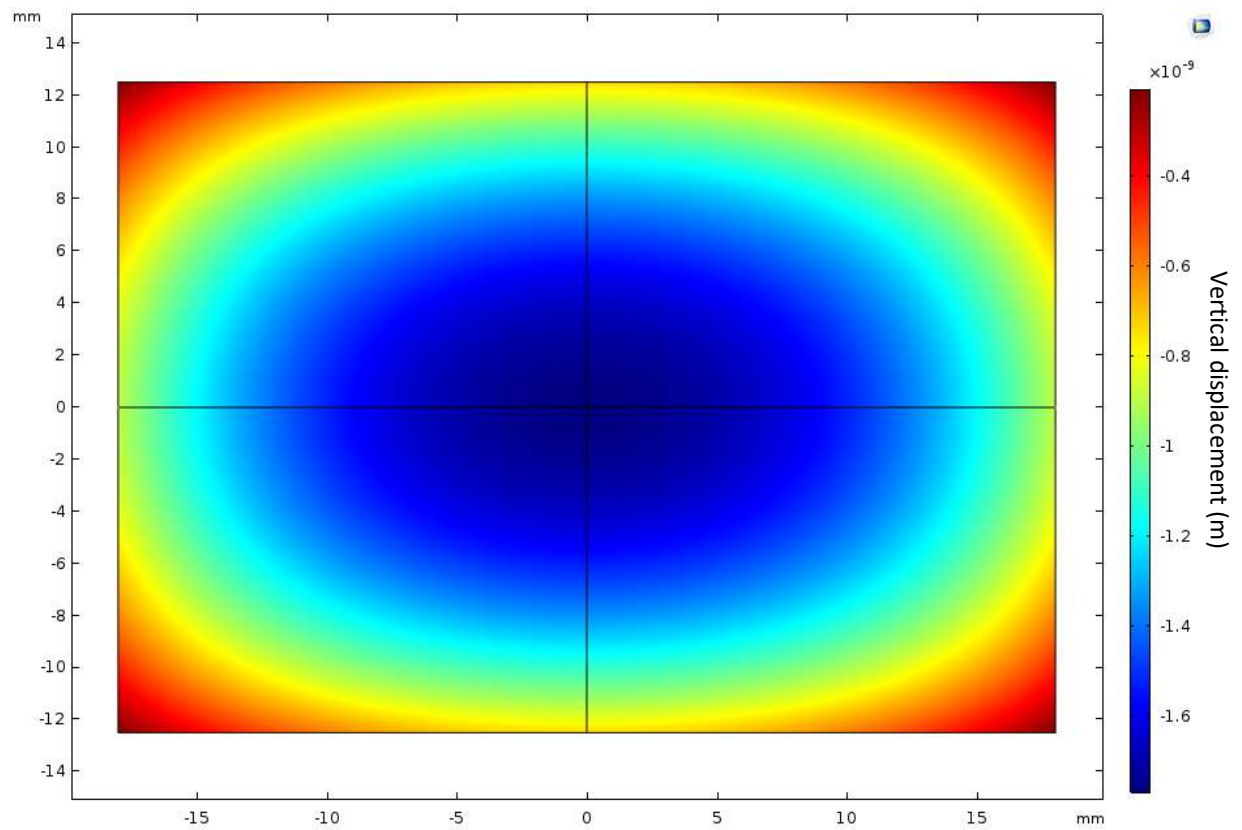


Figure 57 - (Top) Surface displacement of side cooled 'bulk' crystal diffracting surface as a result of heating. (Bottom) Cross-section of sagittal plane (m), showing deformation variance of  $9.68 \times 10^{-10}$  m.

### 3.3.2.2 Bottom cooling

Considering the bottom cooled crystal, similar boundary conditions have been used as in the previous bottom cooled sections and as shown in Figure 58 below.

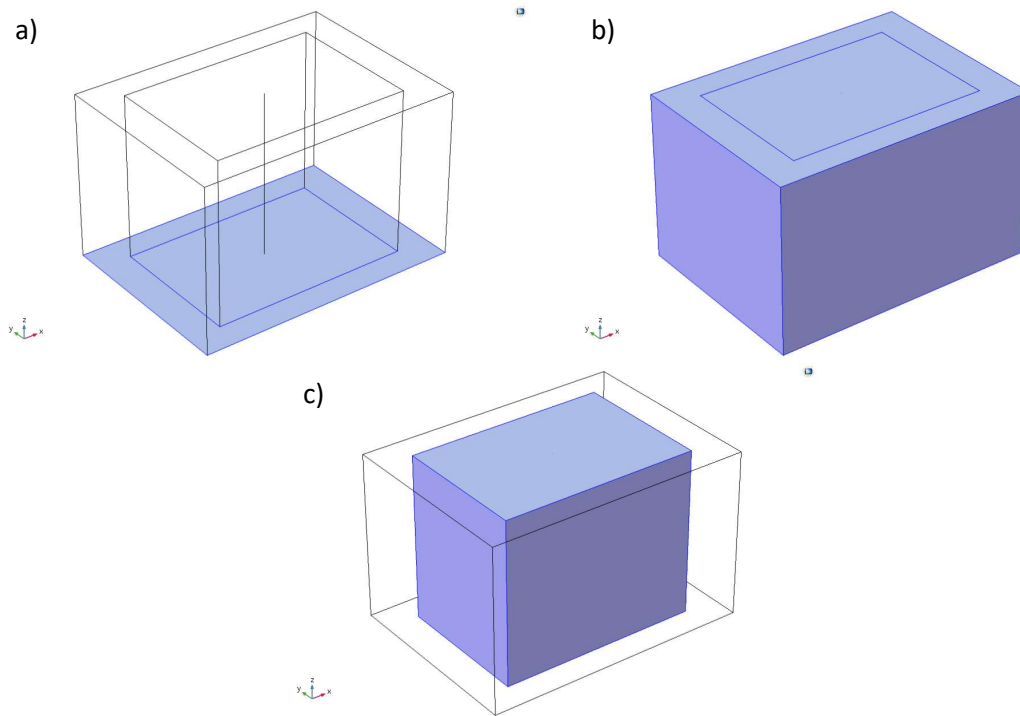


Figure 58 - Thermal boundary conditions for 'bulk' crystal (bottom cooled): a) bottom surface of crystal held at constant 80 K; b) all exposed surfaces radiating to 80 K ambient temperature; c) central volume exposed to beam for heat deposition.

The crystal has not reached as high a temperature as in previous crystal designs as shown in Figure 59; however, the isothermal surfaces are less uniform, showing a curved shape as shown in Figure 60 due to the large conducting area outside the absorbing region. The diffracting surface has a deformation variance of  $8.63 \times 10^{-10}$  m, as shown in Figure 61 – this is comparable to any other bottom cooled crystal design so far, but is not a significant improvement over the side cooled 'bulk' crystal. This supports the theory that the performance of the crystals is improved by increasing the distance between the heated area and the cooled surfaces as the trends in both temperature and surface deformation variance are the same in both bottom-cooling and bulk design.

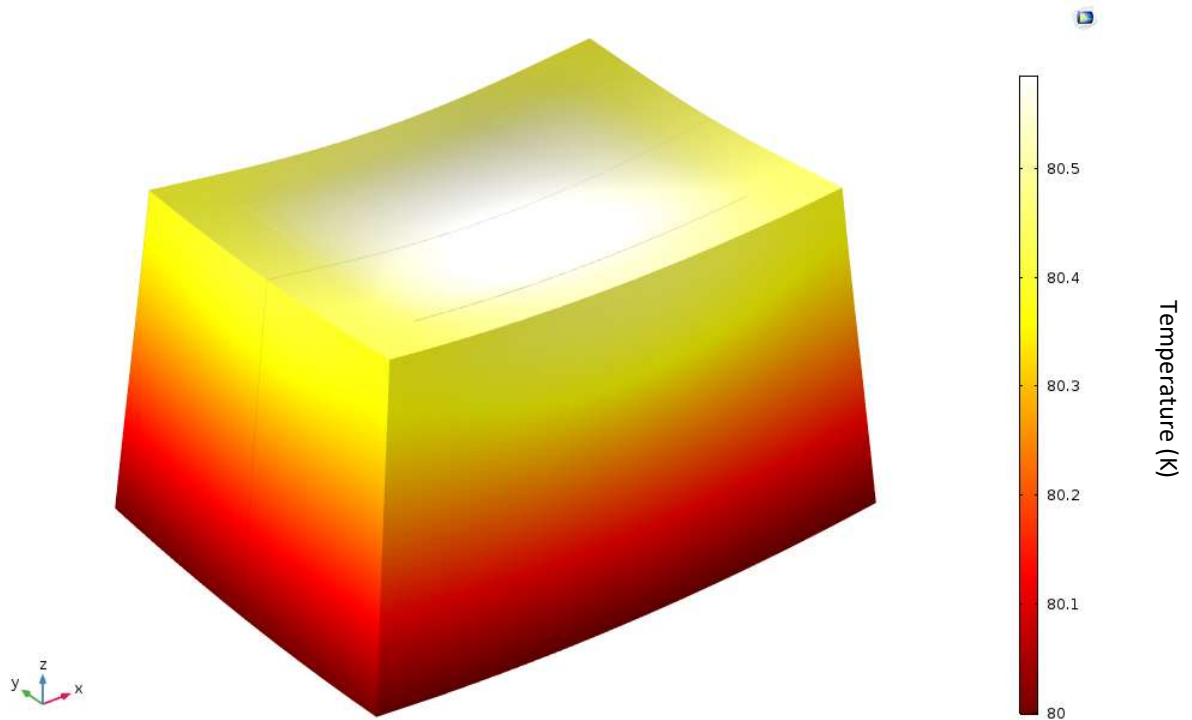


Figure 59 - Temperature surface plot of bottom cooled 'bulk' crystal exposed to incident beam (K).

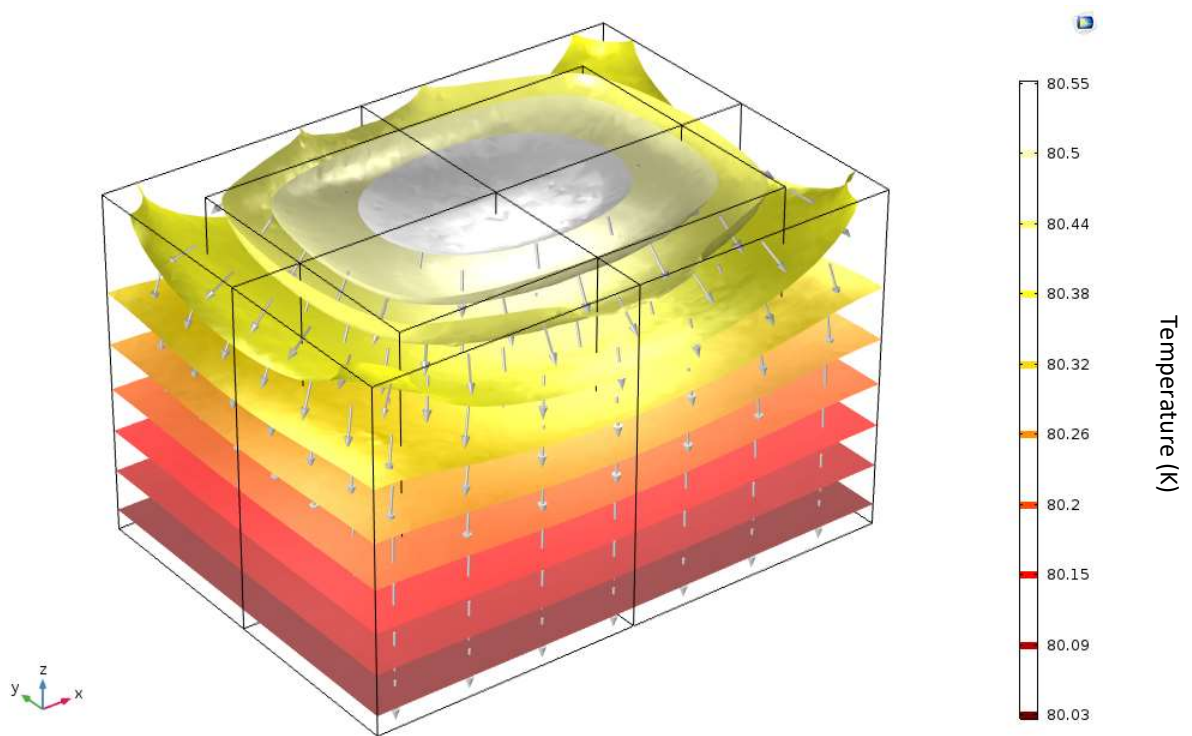


Figure 60 - Bottom cooled 'bulk' crystal exposed to incident beam; isothermal layers mapped (K), with arrows showing movement of heat.

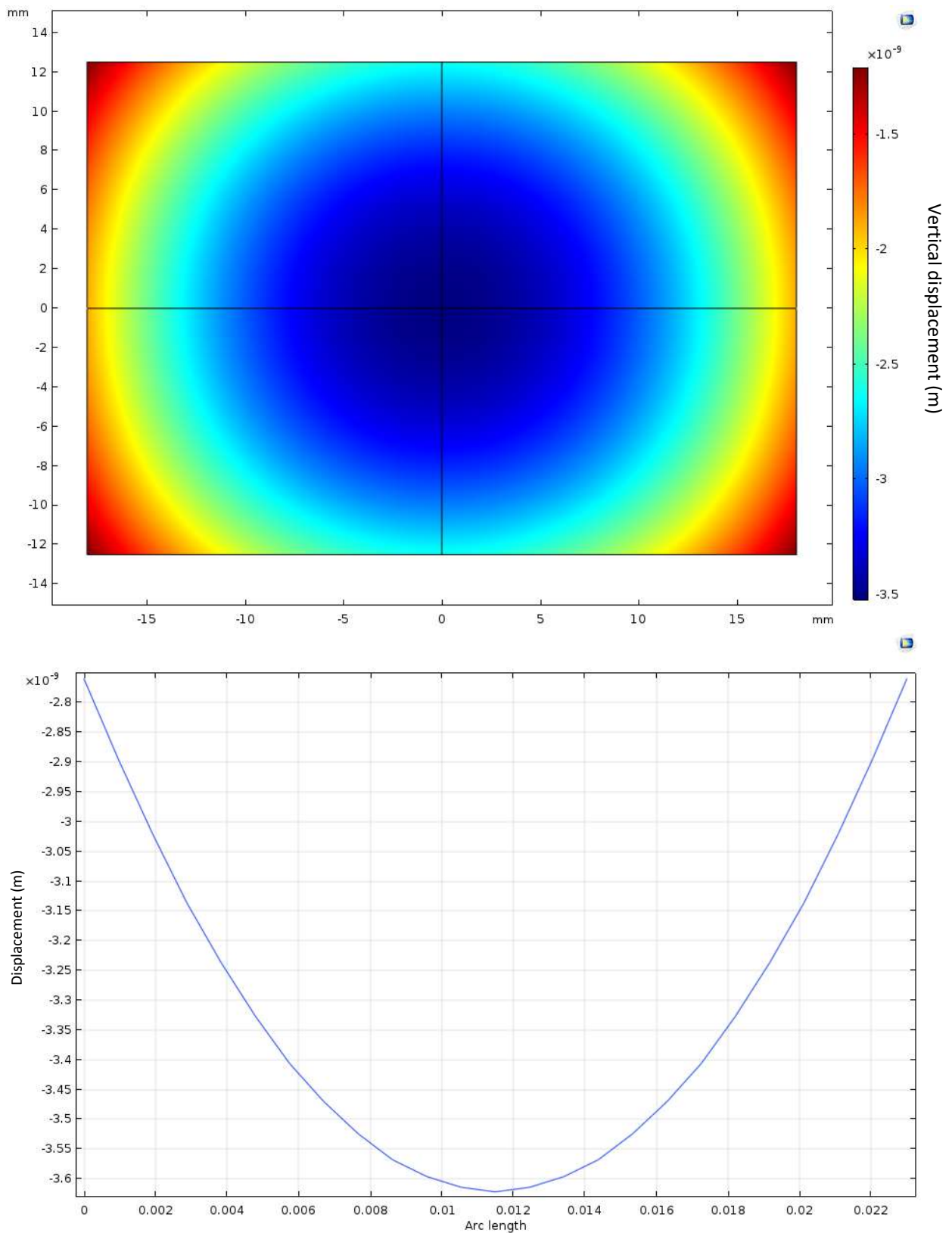
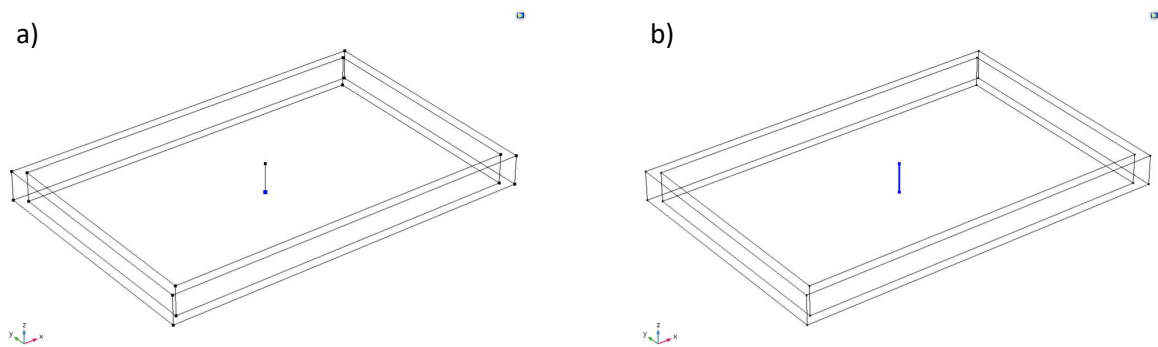


Figure 61 – (Top) Surface displacement of bottom cooled ‘bulk’ crystal diffracting surface as a result of heating.

(Bottom) Cross-section of sagittal plane (m), showing deformation variance of  $8.63 \times 10^{-10}$  m.

### 3.3.3 'Thin' Crystal

The penultimate design considered was the same footprint as the 'squared' crystal, i.e. 38 mm x 26 mm, but thinned down to a thickness of just 3 mm (hereafter referred to as the 'thin' crystal). This design was tested after observing the graph of beam power as a function of penetration depth (Figure 12), which shows 90% of the beam power is absorbed after the beam has penetrated 3 mm. By thinning the crystal, it was hoped to allow some of the incident beam power to pass through while still providing enough bulk crystal to perform the Bragg diffraction. The mechanical boundaries are identical to those used in previous tests scaled down to the new crystal (shown in Figure 62), as are the thermal boundary conditions.



*Figure 62 - Mechanical boundary conditions for 'thin' crystal: a) central point on bottom surface held fully constrained; b) line running through centre of crystal in z-direction held in x- and y-directions to prevent rotation.*

### 3.3.3.1 Side cooling

Considering first the side cooled crystal, similar thermal boundary conditions have been used as in the previous sections and as shown in Figure 63 below.

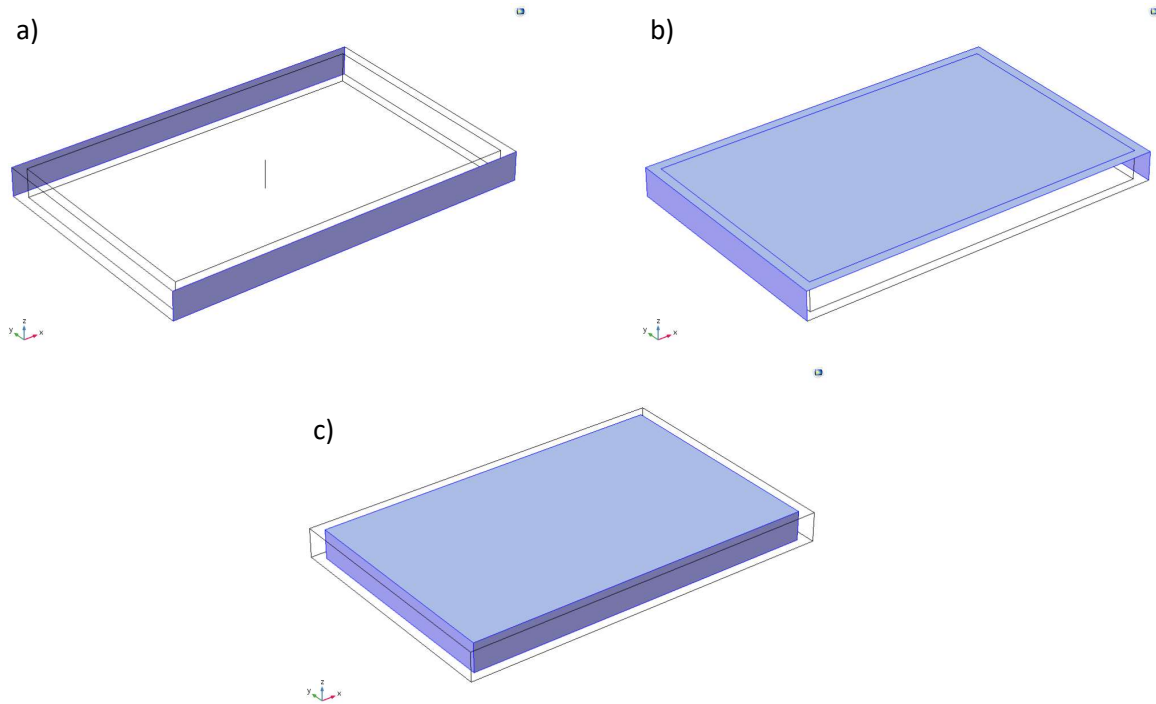


*Figure 63 - Thermal boundary conditions for 'thin' crystal (side cooled): a) side surfaces of crystal held at constant 80 K; b) all exposed surfaces radiating to 80 K ambient temperature; c) central volume exposed to beam for heat deposition.*

Due to the smaller cooling surfaces the crystal reaches a higher peak temperature as shown in Figure 64. The isothermal surfaces show significantly shorter thermal pathways as the vast majority of the heat travels lateral to the diffracting surface, as shown in Figure 65. However, the thermal deformation is too high for this improved thermal transport to offset, and coupled with the increased flexibility caused by a thinner crystal the diffracting surface variance is significantly higher than any other observed, peaking at  $6.41 \times 10^{-9}$  m as shown in Figure 66.

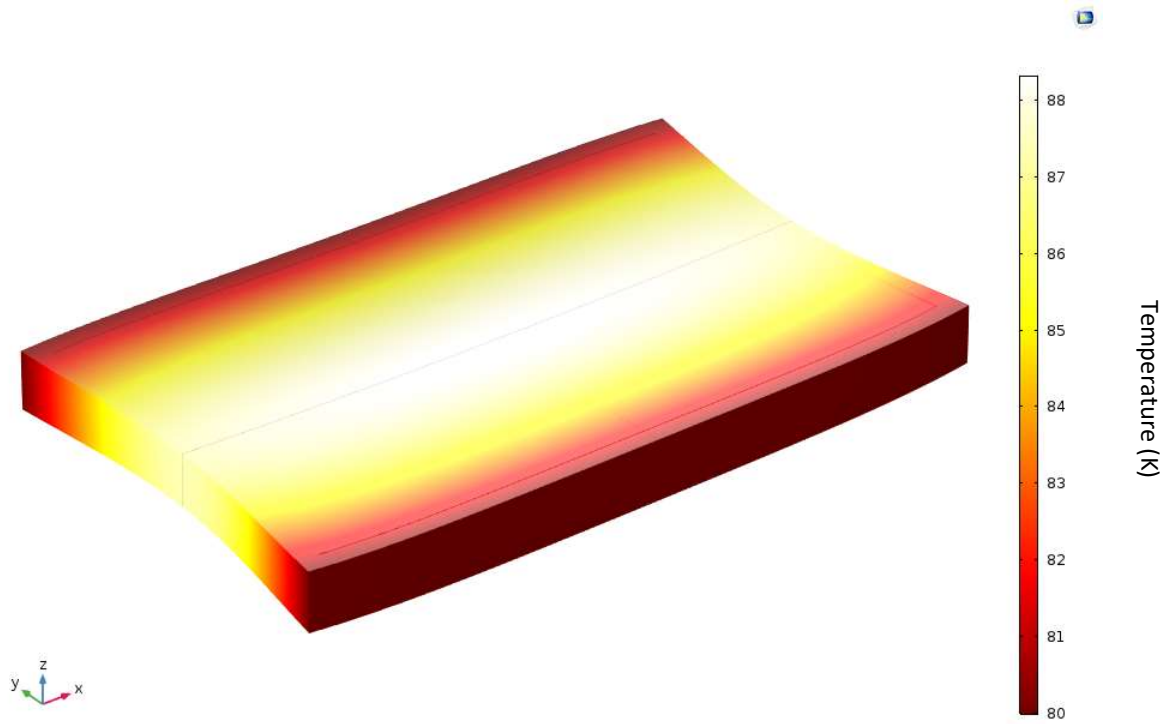


Figure 64 - Temperature surface plot of side cooled 'thin' crystal exposed to incident beam (K).

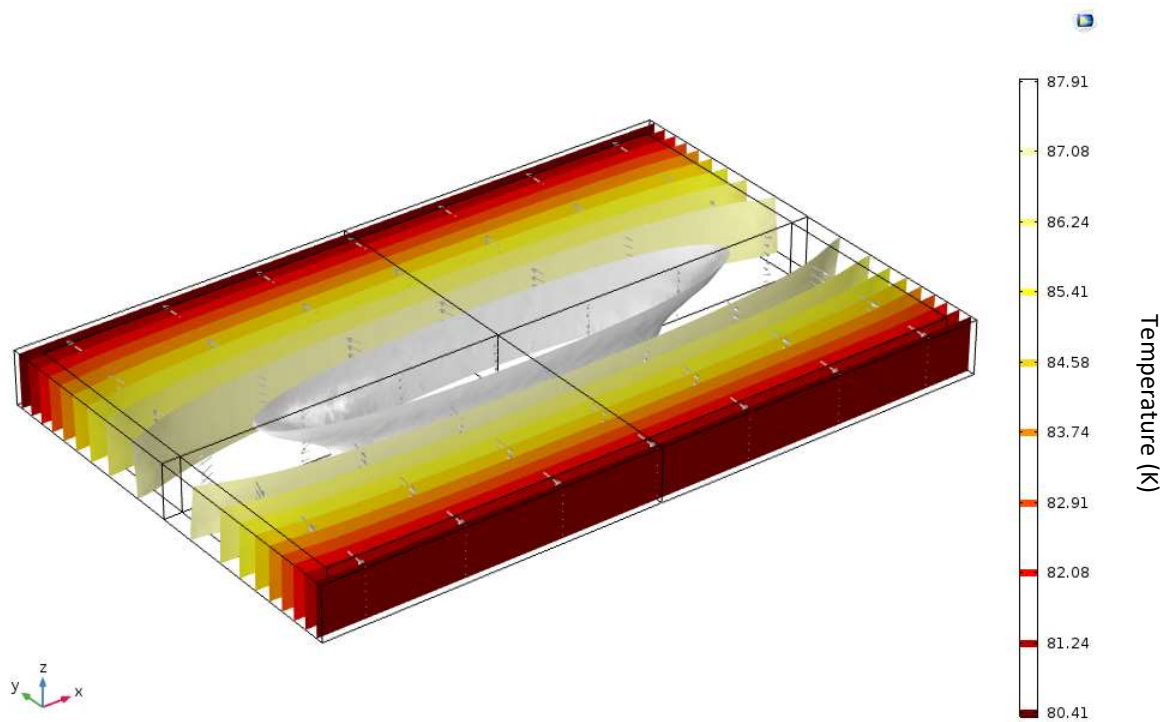


Figure 65 - Side cooled 'thin' crystal exposed to incident beam; isothermal layers mapped (K), with arrows showing movement of heat.

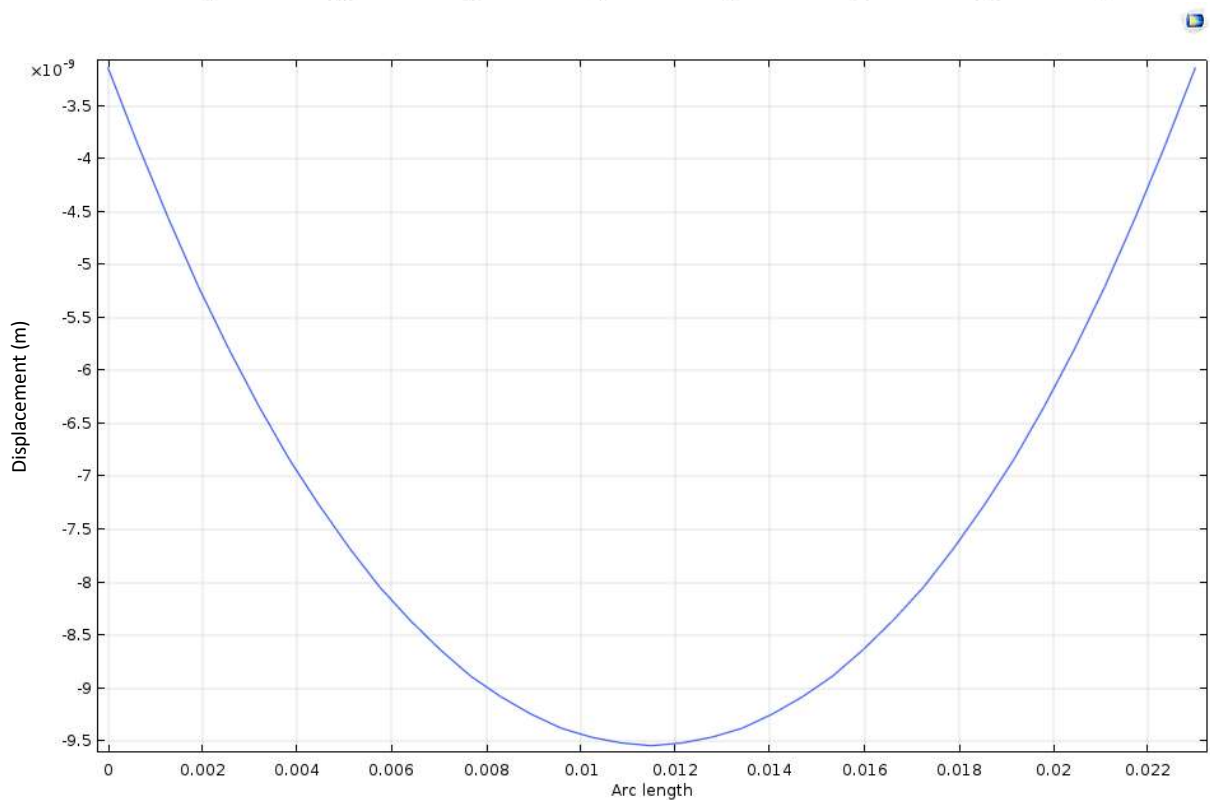
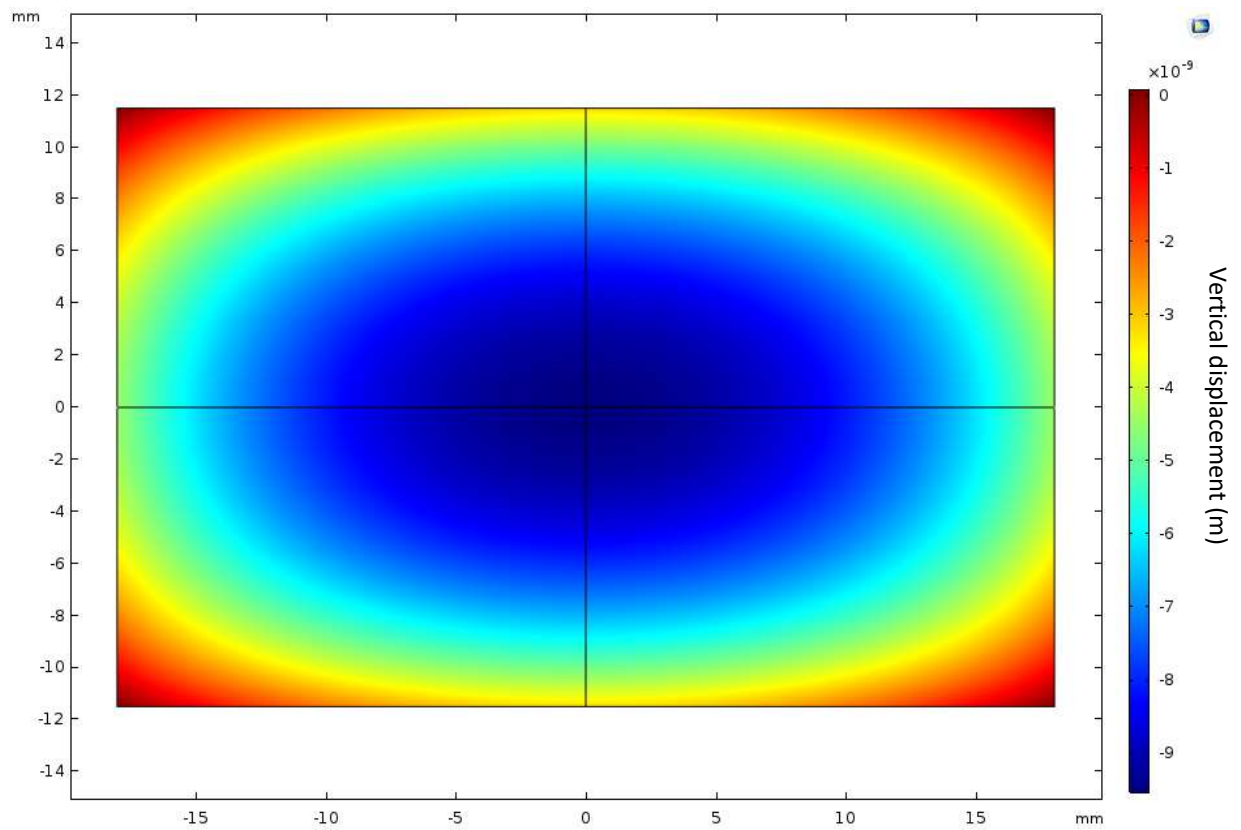


Figure 66 – (Top) Surface displacement of side cooled 'thin' crystal diffracting surface as a result of heating. (Bottom) Cross-section of sagittal plane (m), showing deformation variance of  $6.41 \times 10^{-9}$  m.

### 3.3.3.2 Bottom cooling

Considering the bottom cooled crystal, similar boundary conditions have been used as in the previous bottom cooled sections and as shown in Figure 67 below.

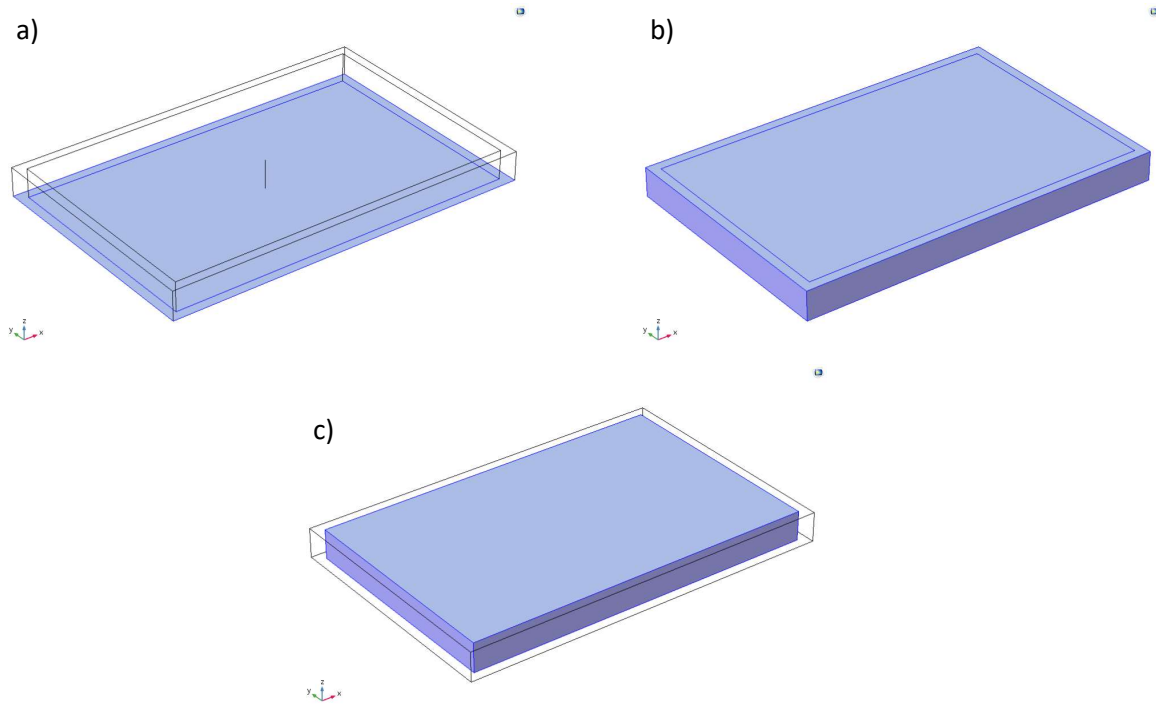


Figure 67 - Thermal boundary conditions for 'thin' crystal (bottom cooled): a) bottom surface of crystal held at constant 80 K; b) all exposed surfaces radiating to 80 K ambient temperature; c) central volume exposed to beam for heat deposition.

The peak temperature is much lower than that of the side cooled 'thin' crystal and much more in line with that seen in the other crystal designs, visible in Figure 68. The isothermals are somewhat more difficult to read, as all the isothermal layers lie parallel to the diffracting and cooled surfaces within the 3 mm bulk of the crystal, as shown in Figure 69. Unfortunately the reduced mechanical stability present in a thinner crystal offsets this improved linearity, with Figure 70 showing a diffracting surface deformation variance of  $6.11 \times 10^{-9}$  m, a half order of magnitude higher than that observed in the side cooled I20 crystal and comparable performance to the side cooled 'thin' crystal.

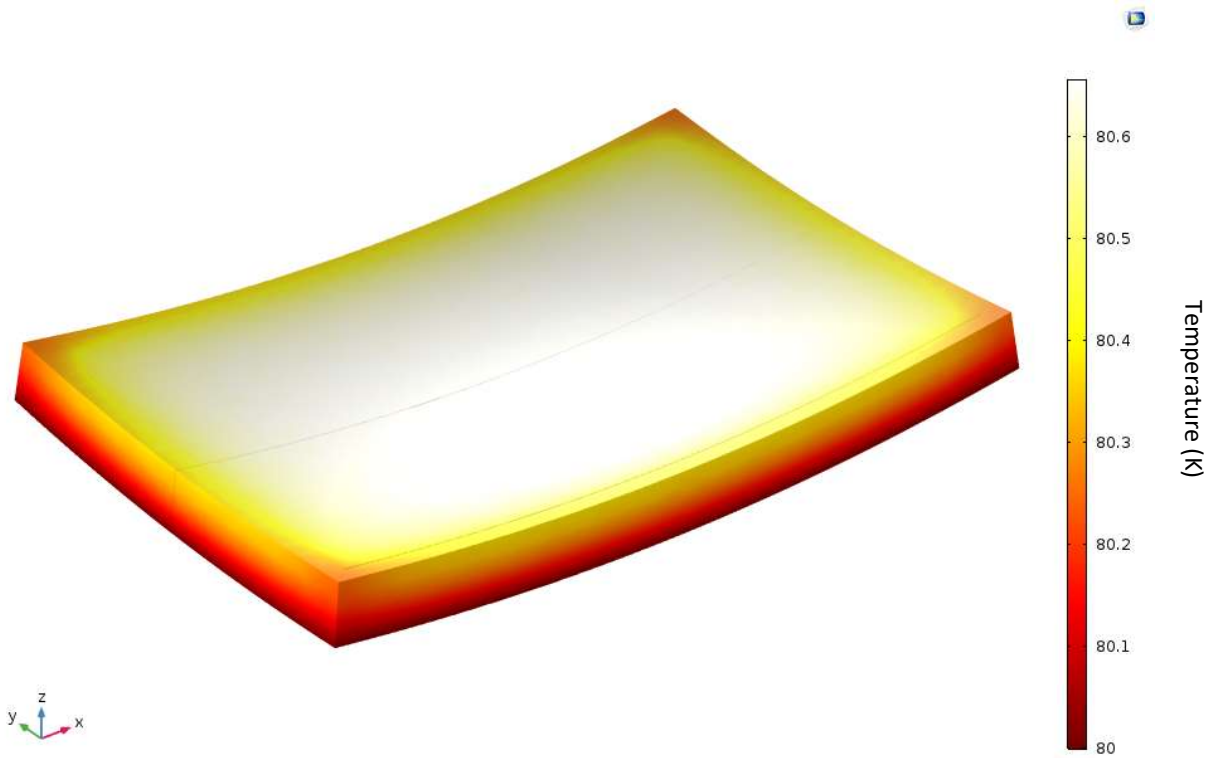


Figure 68 - Temperature surface plot of bottom cooled 'thin' crystal exposed to incident beam (K).

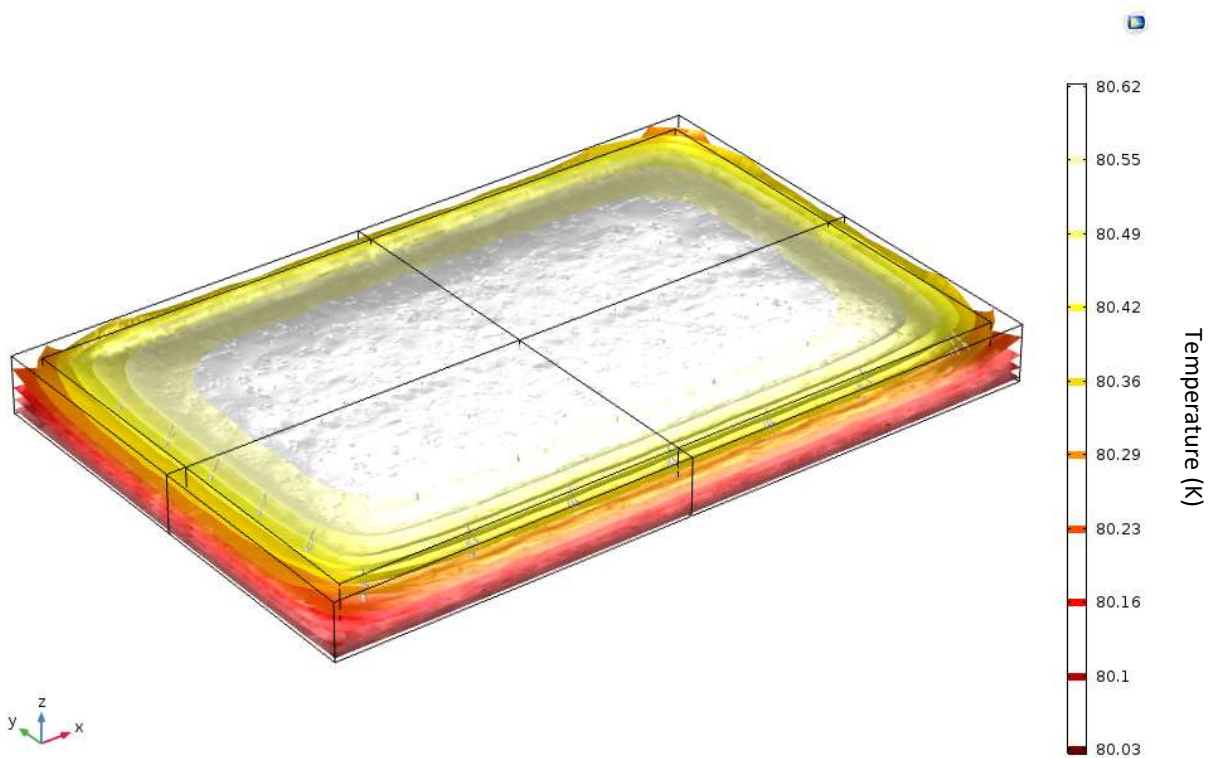


Figure 69 - Bottom cooled 'thin' crystal exposed to incident beam; isothermal layers mapped (K), with arrows showing movement of heat.

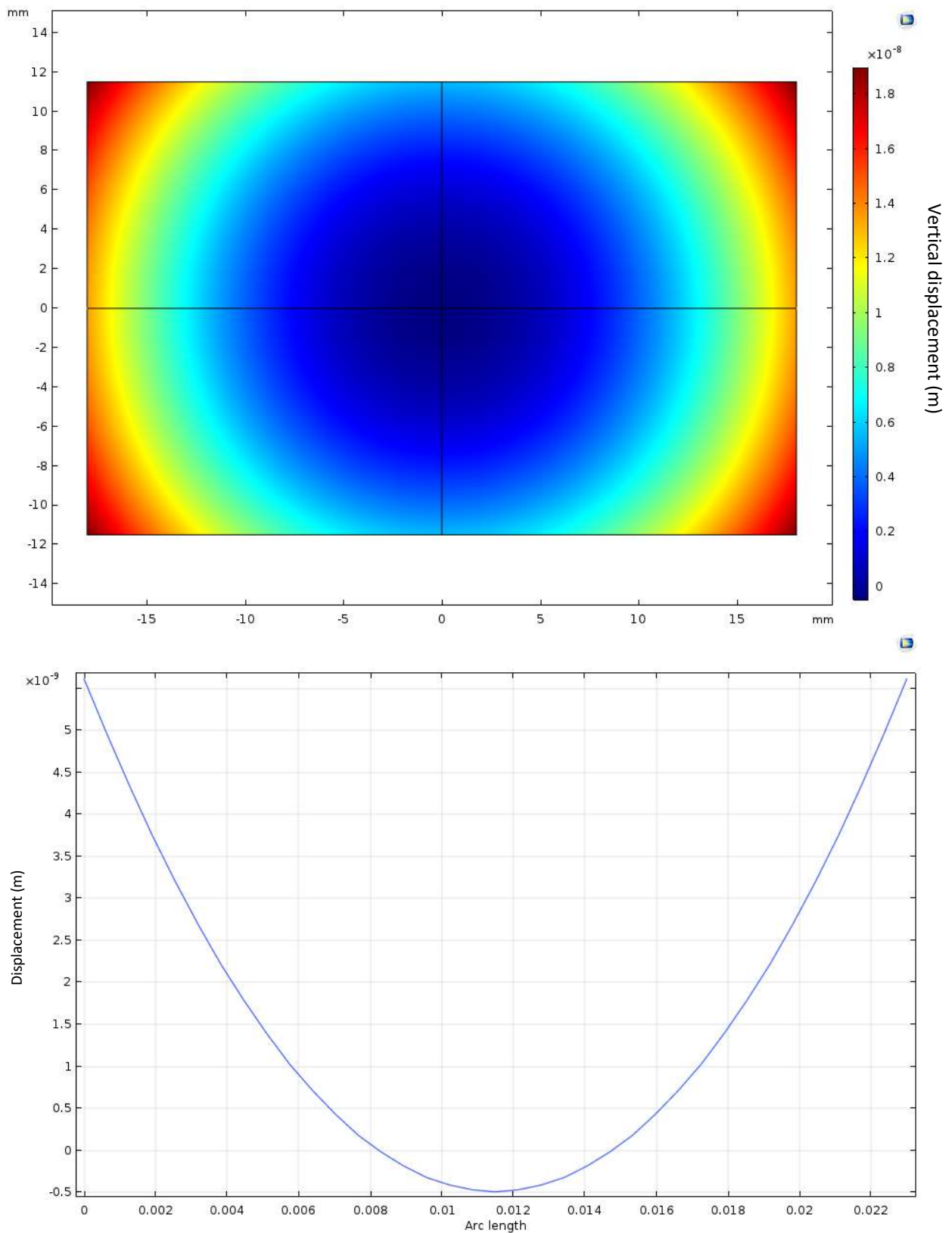


Figure 70 – (Top) Surface displacement of bottom cooled ‘thin’ crystal diffracting surface as a result of heating.

(Bottom) Cross-section of sagittal plane (m), showing deformation variance of  $6.11 \times 10^{-9}$  m.

### 3.3.4 'Wafer' Crystal

The final crystal design modelled took the concept behind the 'thin' crystal a step further. As the vast majority of the Bragg diffraction takes place in the first few lattice layers of the crystal (Golovchenko, 1981) a crystal was modelled with a depth of only 500  $\mu\text{m}$ . This crystal was modelled as a silicon wafer, hereafter referred to as the 'wafer' crystal, with a radius of 24 mm. This design would allow the bulk of the x-ray beam to pass through the crystal, with only a small amount of beam power being deposited without deteriorating the diffracted x-ray beam. The mechanical boundaries needed little modification for this design (Figure 71).

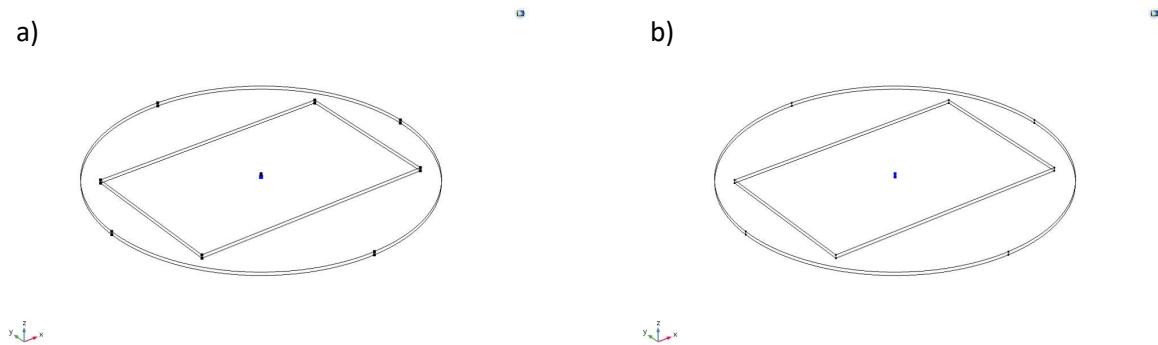
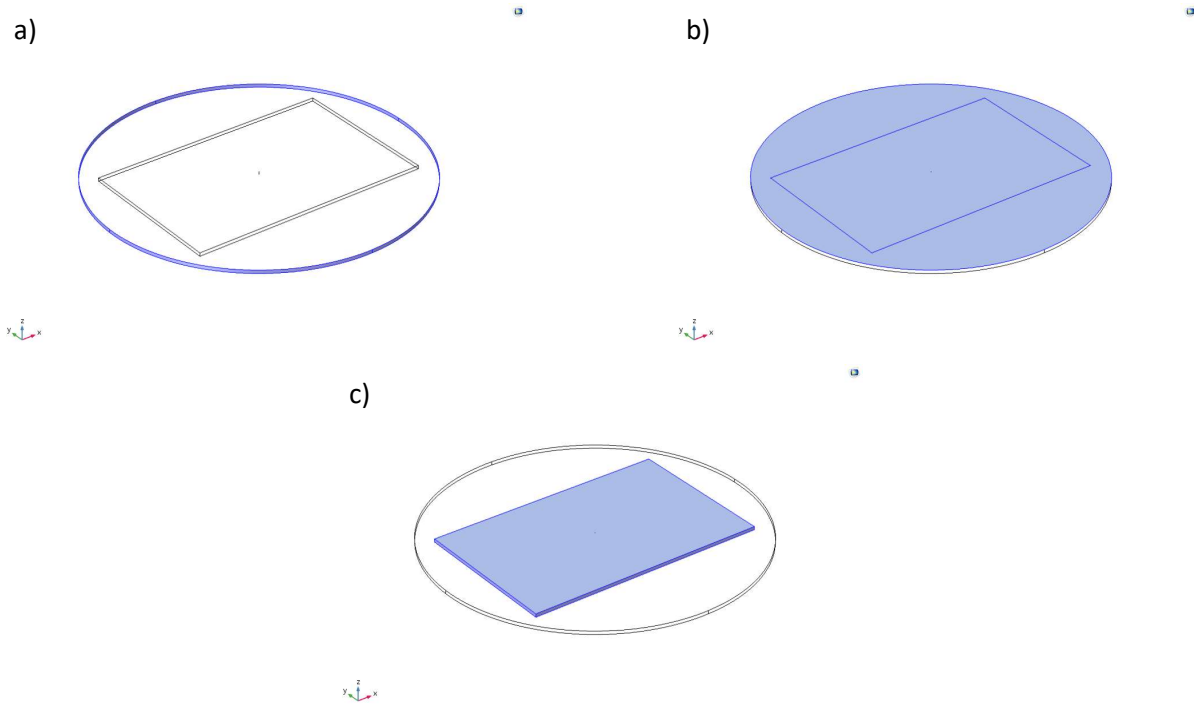


Figure 71 - Mechanical boundary conditions for 'wafer' crystal: a) central point on bottom surface held fully constrained; b) line running through centre of crystal in z-direction held in x- and y-directions to prevent rotation.

### 3.3.4.1 Side cooling

For the side cooled 'wafer' crystal, it was decided to cool all four perimeter sides as shown in Figure 72.



*Figure 72 - Thermal boundary conditions for 'wafer' crystal (side cooled): a) perimeter surfaces of crystal held at constant 80 K; b) all exposed surfaces radiating to 80 K ambient temperature; c) central volume exposed to beam for heat deposition.*

Considering the side cooled crystal, it quickly becomes apparent that the tiny size of the cooling surfaces is not sufficient to cool the crystal; a peak temperature is observed in Figure 73 on the order of  $10^3$  K, above the melting point of silicon. The isothermals show the heat radiating out from the beam footprint in Figure 74, with significant heat lost to the environment. The significant amount of heat in the crystal causes the centre to bulge significantly, with Figure 75 showing a deformation variance of  $2.90 \times 10^{-6}$  m, although in reality the heat would melt the crystal and eliminate any chance of a beam diffraction.

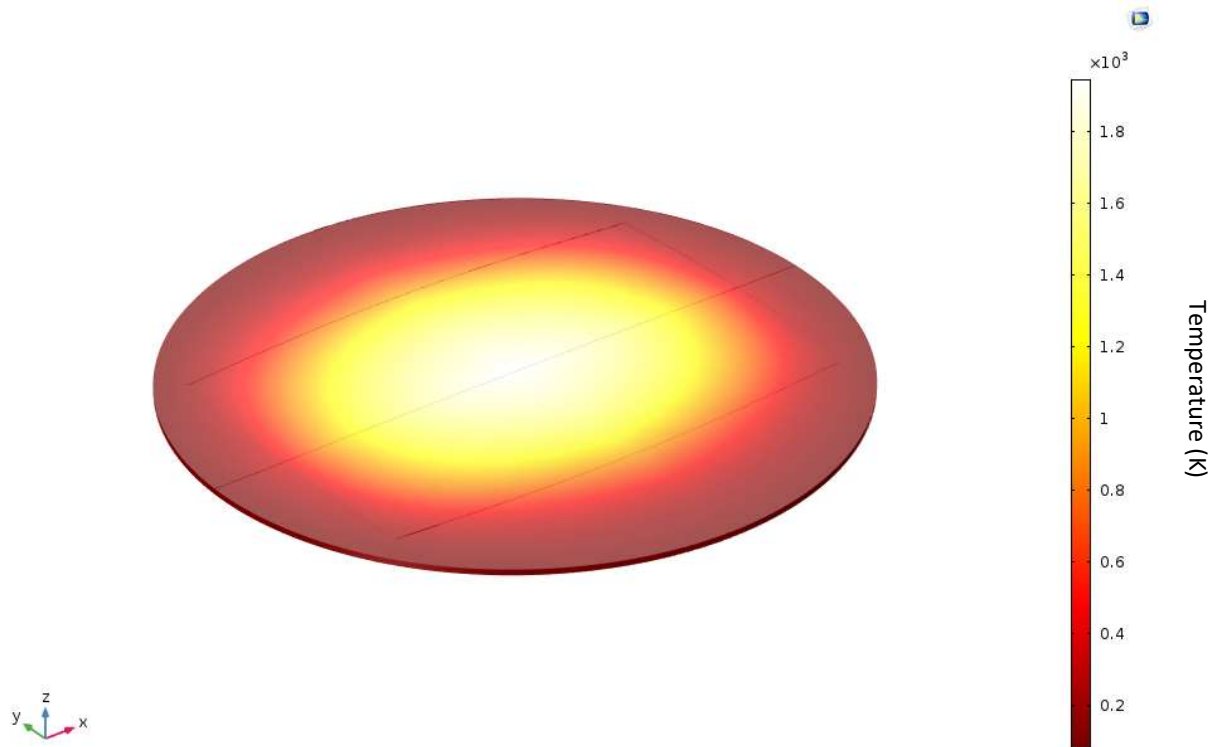


Figure 73 - Temperature surface plot of side cooled 'wafer' crystal exposed to incident beam (K).

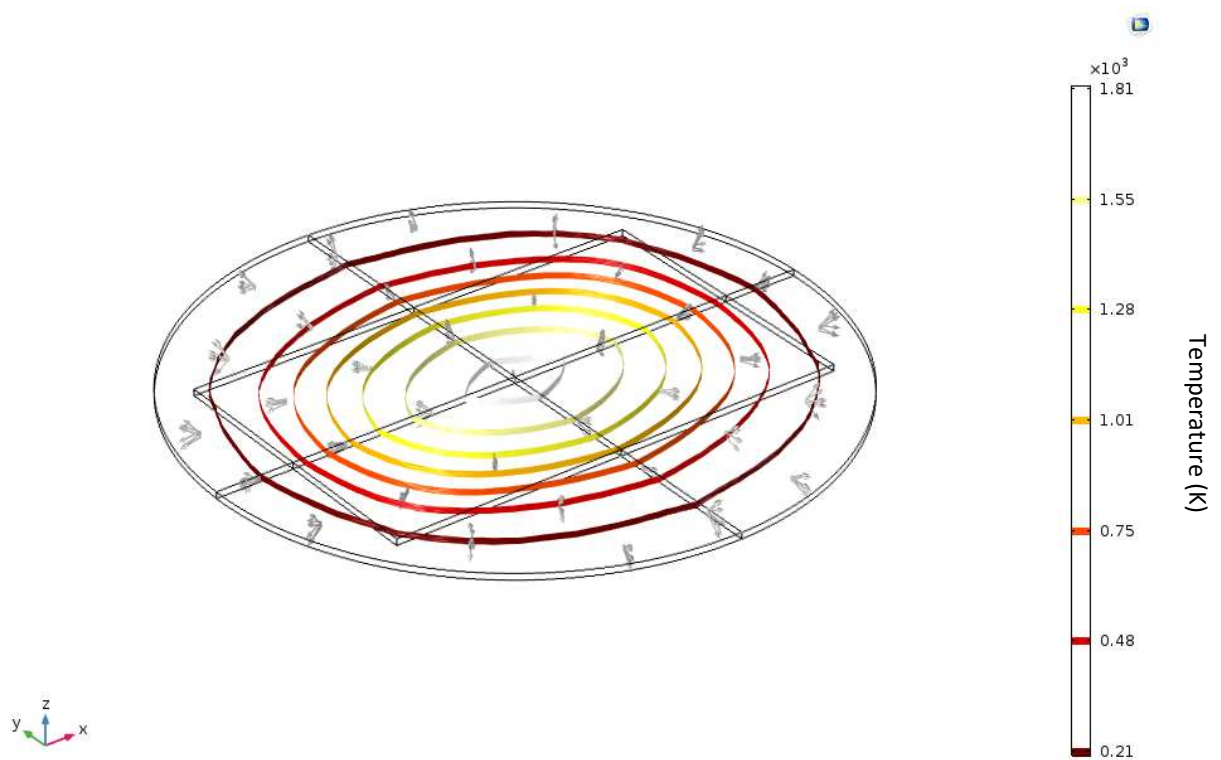


Figure 74 - Side cooled 'wafer' crystal exposed to incident beam; isothermal layers mapped (K), with arrows showing movement of heat.

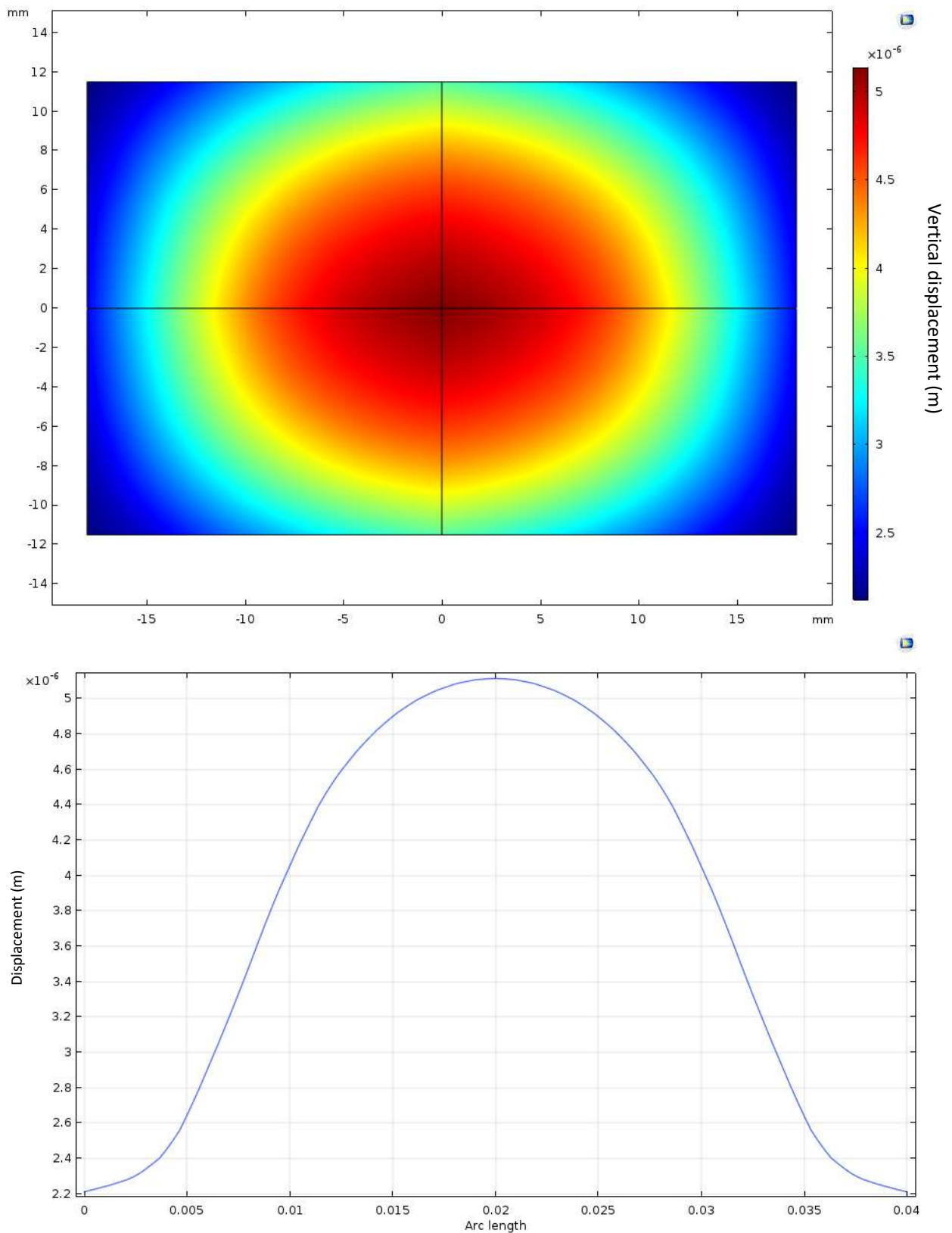


Figure 75 – (Top) Surface displacement of side cooled ‘wafer’ crystal diffracting surface as a result of heating. (Bottom) Cross-section of sagittal plane (m), showing deformation variance of  $2.90 \times 10^{-6}$  m.

### 3.3.4.2 Bottom cooling

For the bottom cooled crystal standard thermal boundary conditions were used as shown in Figure 76.

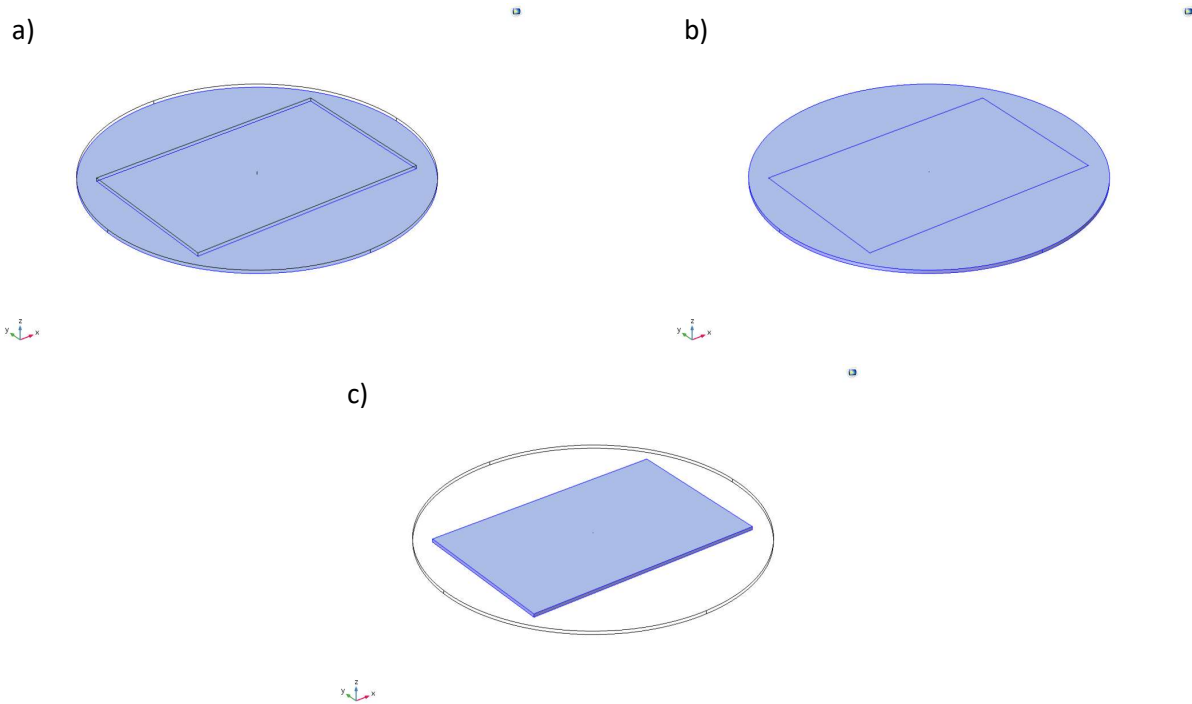


Figure 76 - Thermal boundary conditions for 'wafer' crystal (bottom cooled): a) bottom surface of crystal held at constant 80 K; b) all exposed surfaces radiating to 80 K ambient temperature; c) central volume exposed to beam for heat deposition.

Considering the bottom cooled crystal, we see a much lower peak temperature; it appears that with the larger cooled surface area the crystal works as intended, with much of the beam power passing through the crystal as seen in Figure 77. The isothermal view shows that the heat does not travel through much of the wafer, instead moving directly from the heated region to the cooled surface in a vertical path, shown in Figure 78. However, while these improvements show significant improvement and usability compared to the side-cooled 'wafer' crystal, this design shows a deformation variance of  $3.11 \times 10^{-8}$  m as shown in Figure 79, the most significant deformation variance observed in any bottom cooled crystal.

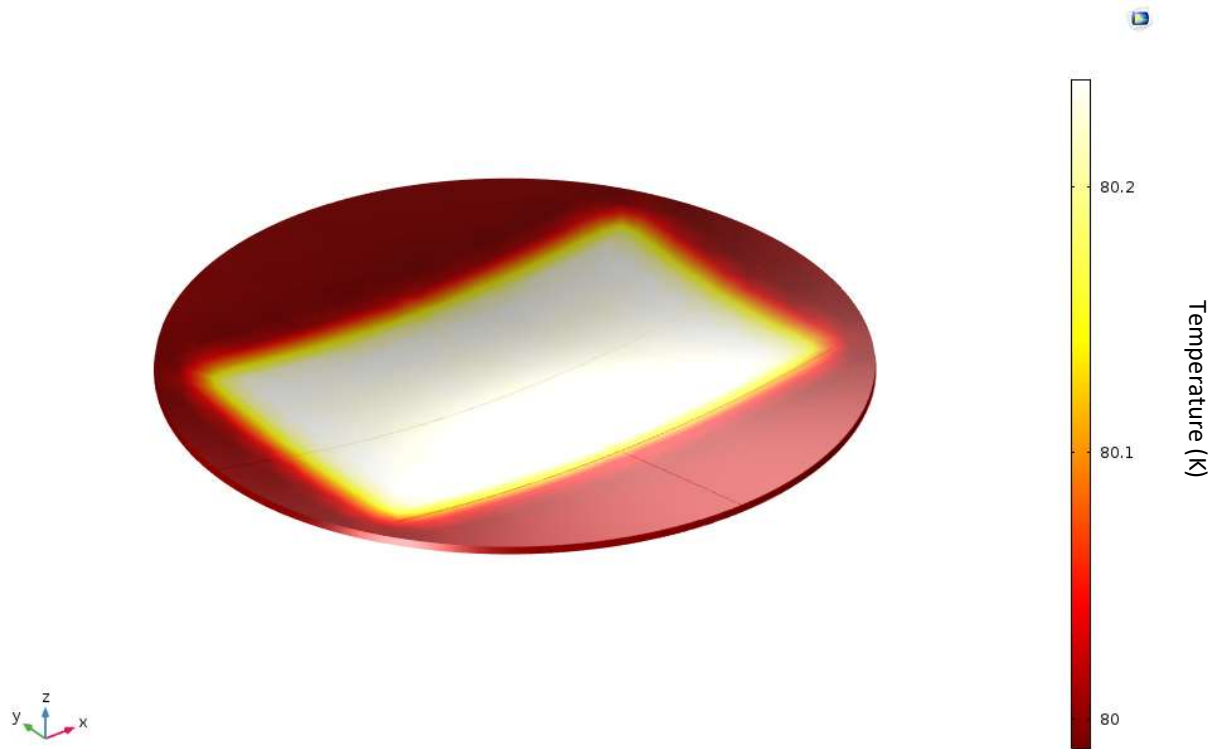


Figure 77 - Temperature surface plot of bottom cooled 'wafer' crystal exposed to incident beam (K).

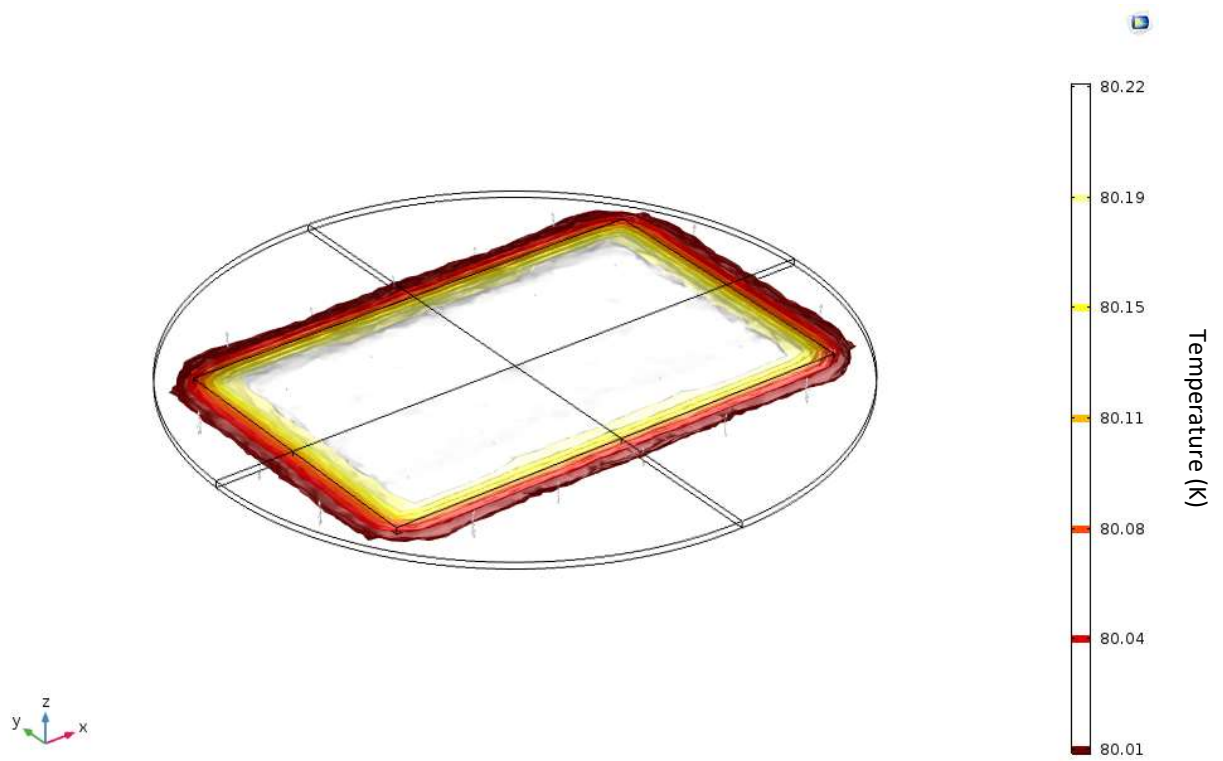


Figure 78 - Bottom cooled 'wafer' crystal exposed to incident beam; isothermal layers mapped (K), with arrows showing movement of heat.

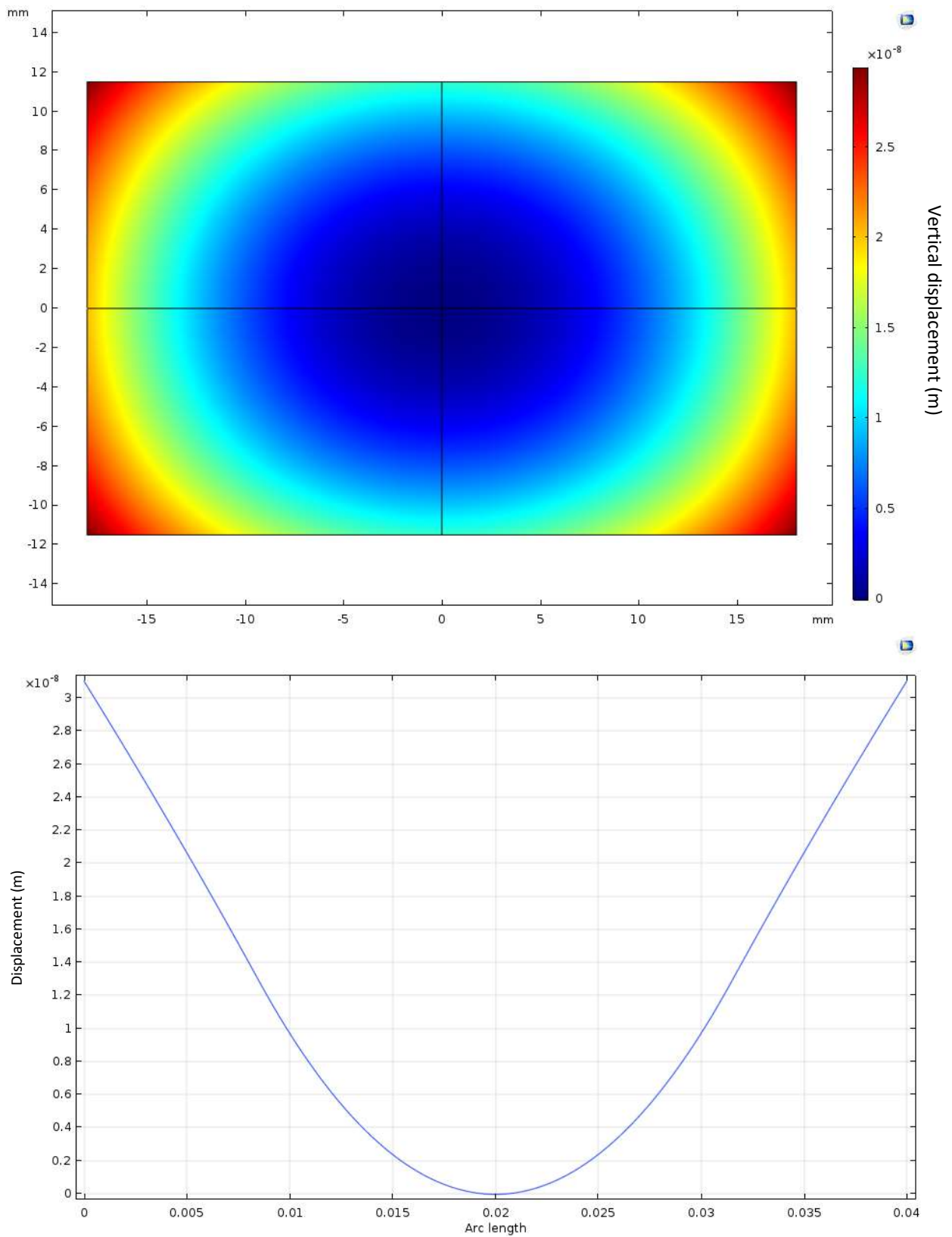


Figure 79 – (Top) Surface displacement of bottom cooled ‘wafer’ crystal diffracting surface as a result of heating.

(Bottom) Cross-section of sagittal plane (m), showing deformation variance of  $3.11 \times 10^{-8}$  m.

### 3.3.5 'Cut-back' Crystal

The models show bottom cooling the crystals causes a lower deformation, but in practice this would be difficult to achieve. However, experimental evidence showed that cutting back the indium foil by just 5 mm improved performance, it was decided to model just the I20 crystal with the cooling region separated by 5 mm from the diffracting surface as shown in Figure 32 on page 63, hereafter referred to as the 'cut-back' crystal to see if this effect could be replicated. Thus the mechanical boundary conditions are identical to those shown in Figure 33, while the thermal boundary conditions are modified to those shown in Figure 80 below.

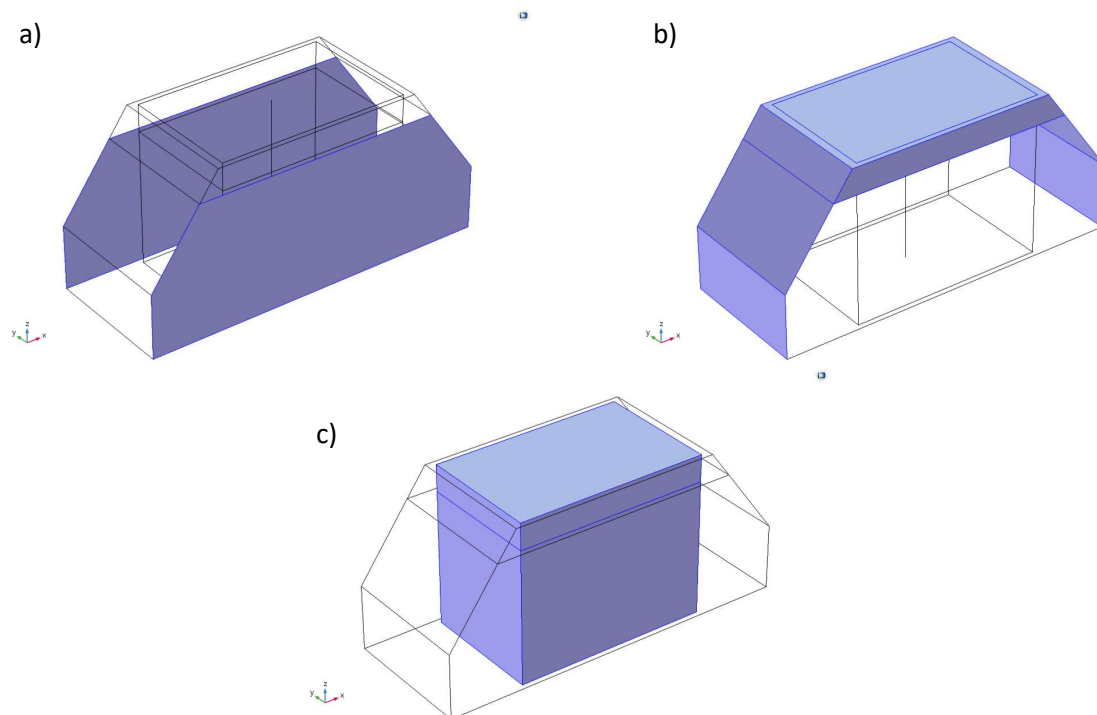


Figure 80 - Thermal boundary conditions for 'cut-back' crystal: a) long side surfaces of crystal held at constant 80 K from  $z = -5$  mm down; b) all exposed surfaces radiating to 80 K ambient temperature; c) central volume exposed to beam for heat deposition.

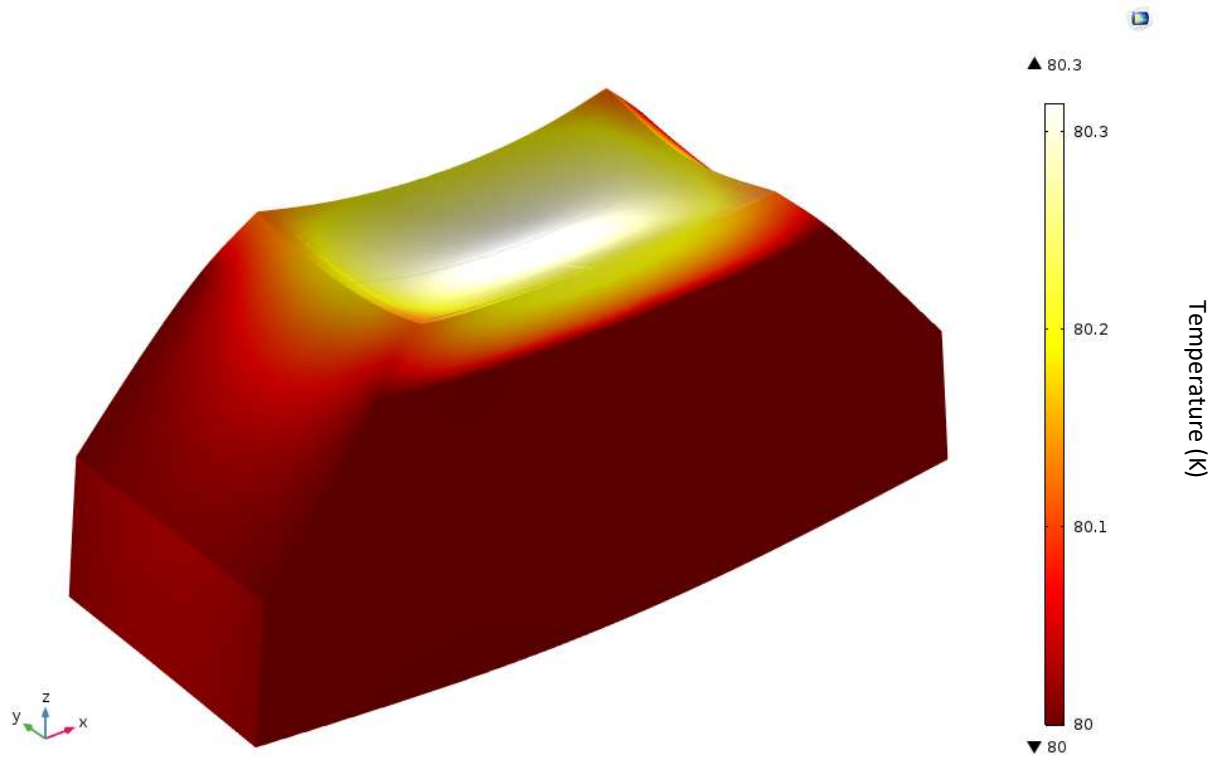


Figure 81 – Temperature surface plot of side cooled ‘cut-back’ crystal exposed to incident beam (K).

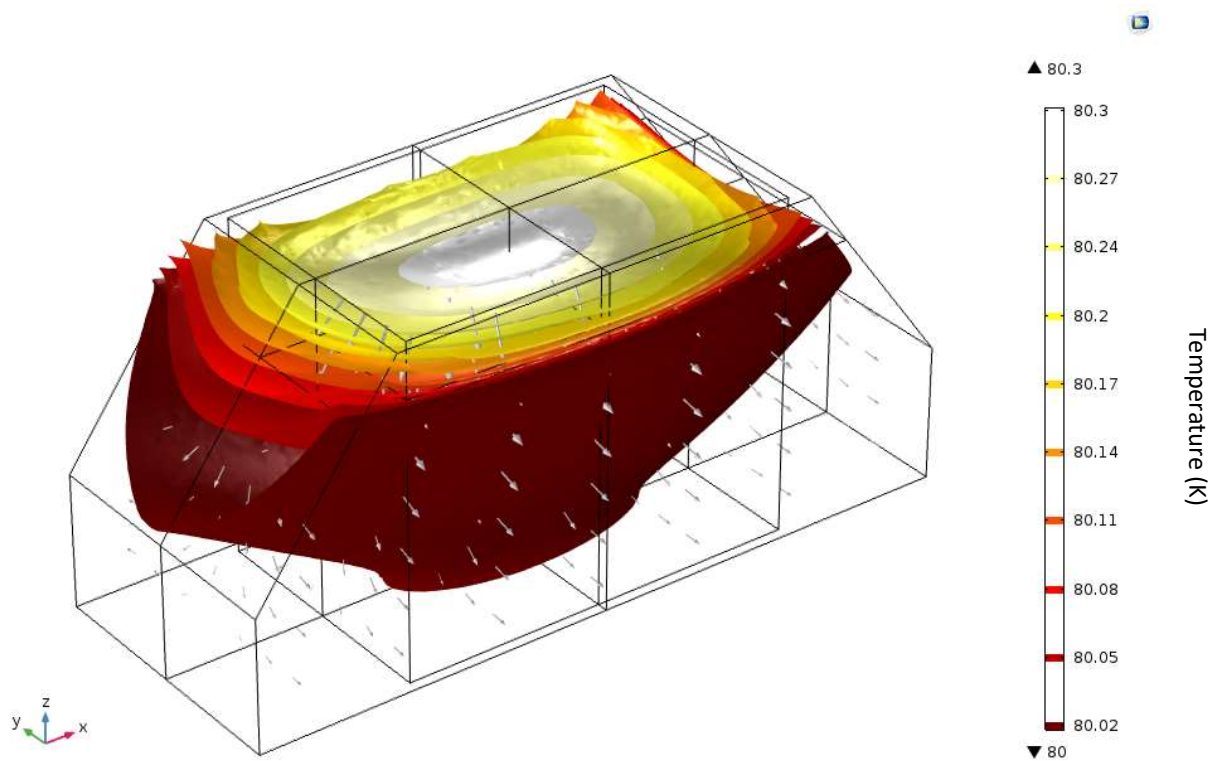


Figure 82 - Side cooled ‘cut-back’ crystal exposed to incident beam; isothermal layers mapped (K), with arrows showing movement of heat.

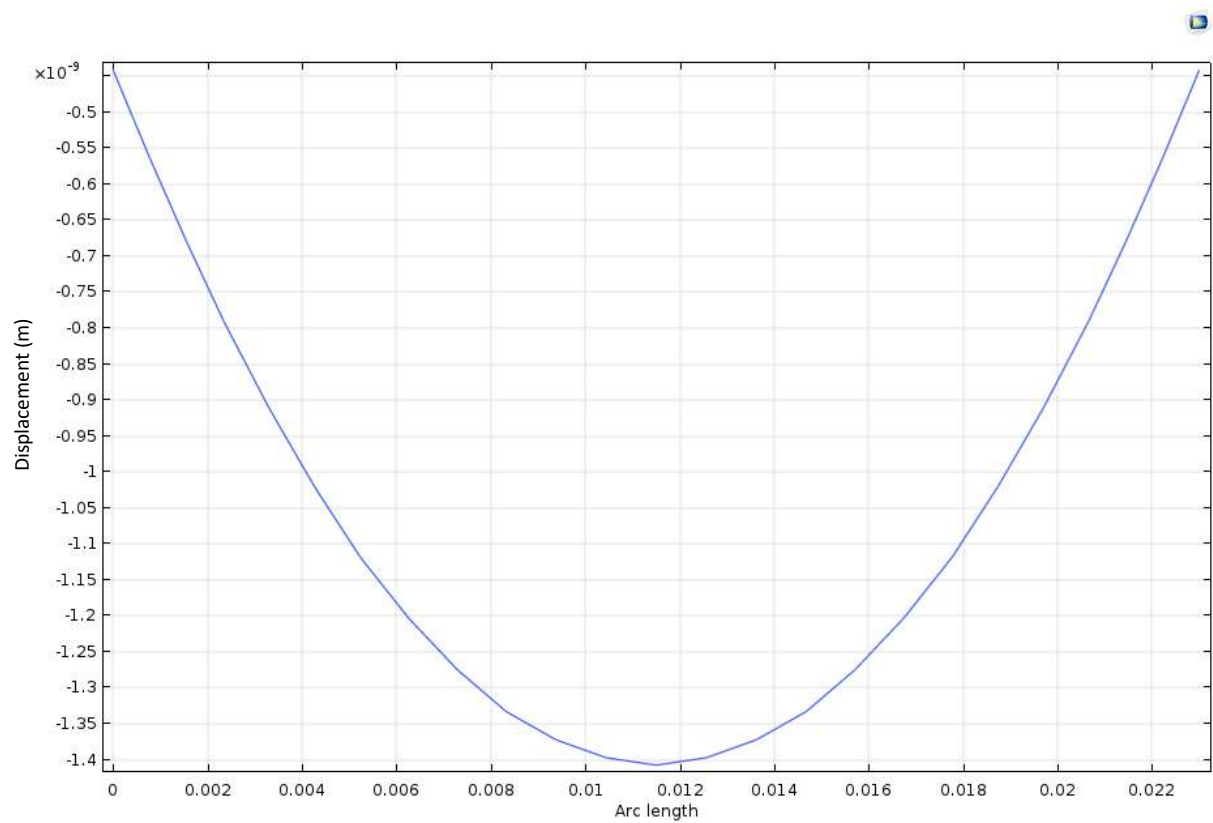
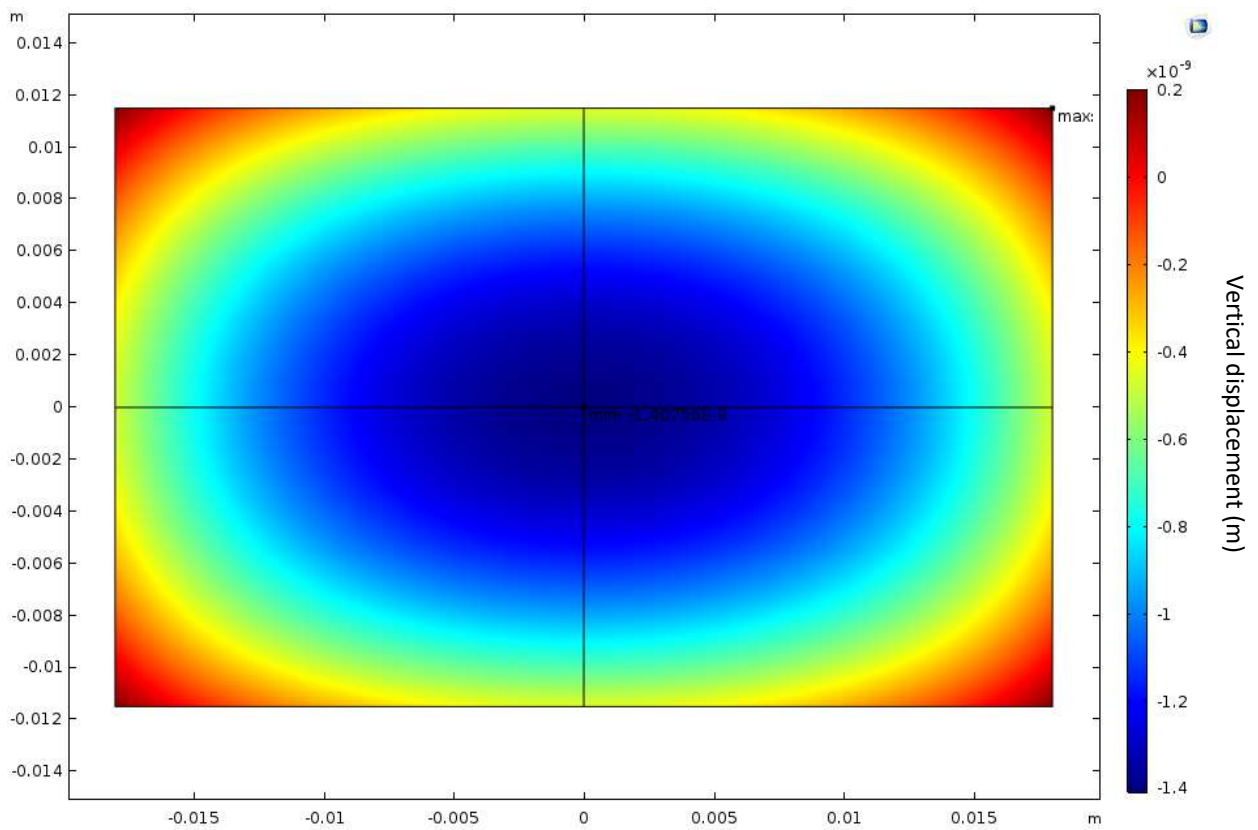


Figure 83 – (Top) Surface displacement of side cooled ‘cut-back’ crystal diffracting surface as a result of heating.

(Bottom) Cross-section of sagittal plane (m), showing deformation variance of  $9.66 \times 10^{-10}$  m.

As expected, separating the cooling areas from the heated surface has caused the peak temperature to increase by a small amount, as is visible by comparing Figure 81 below to Figure 37 on page 69. The isothermal layer plot (Figure 82) shows us how the heat initially moves in the z-direction to travel away from the absorption zone before beginning to move sideways towards the cooled areas. The diffracting surface deformation is shown in Figure 83 and shows us a deformation variance of  $9.66 \times 10^{-10}$  m, a marked improvement over the conventional design.

### 3.4 Comparing the Results of Different Crystal Designs

By comparing the difference in deformation variance between each of the form factors above, the first trend observed is that the bottom-cooled crystals, despite a higher temperature at the diffracting surfaces, deform less than their side-cooled counterparts. Figure 84 below shows the deformation variance for each design on a logarithmic scale; smaller bars indicate a lower deformation variance and therefore a flatter diffracting surface and a higher quality diffracted beam, with increased monochromaticity and collimation.

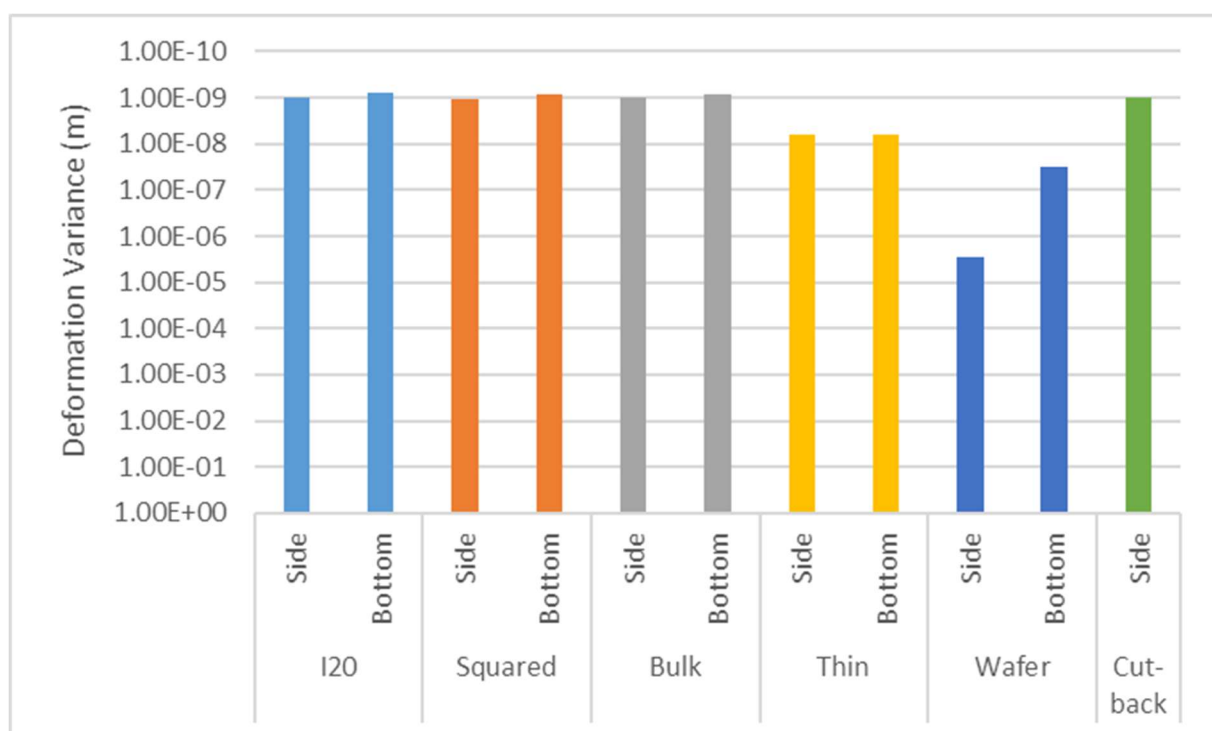


Figure 84 – Deformation variance of diffracting surface for all tested monochromator crystal designs and cooling locations; little of value can be observed due to the scale difference between the ‘thin’ and ‘wafer’ designs and the rest (note: y-axis on logarithmic scale).

At a glance it is apparent that the ‘thin’ and ‘wafer’ designs perform significantly worse than the rest of the designs, to the extent that a logarithmic scale is needed and detail is lost. This is due to the thinness of these crystals increasing their flexibility, resisting the thermal deformation less as a whole and allowing the crystal to bow to a more significant degree. As such, Figure 84 has been replicated in Figure 85 below with these values removed. With the smaller, non-logarithmic scale it

can be more easily seen that the side-cooled crystals do not perform as well as the bottom cooled variants, as increasing the thermal pathway in the crystal allows the diffracting surface to reach a more uniform deformation.

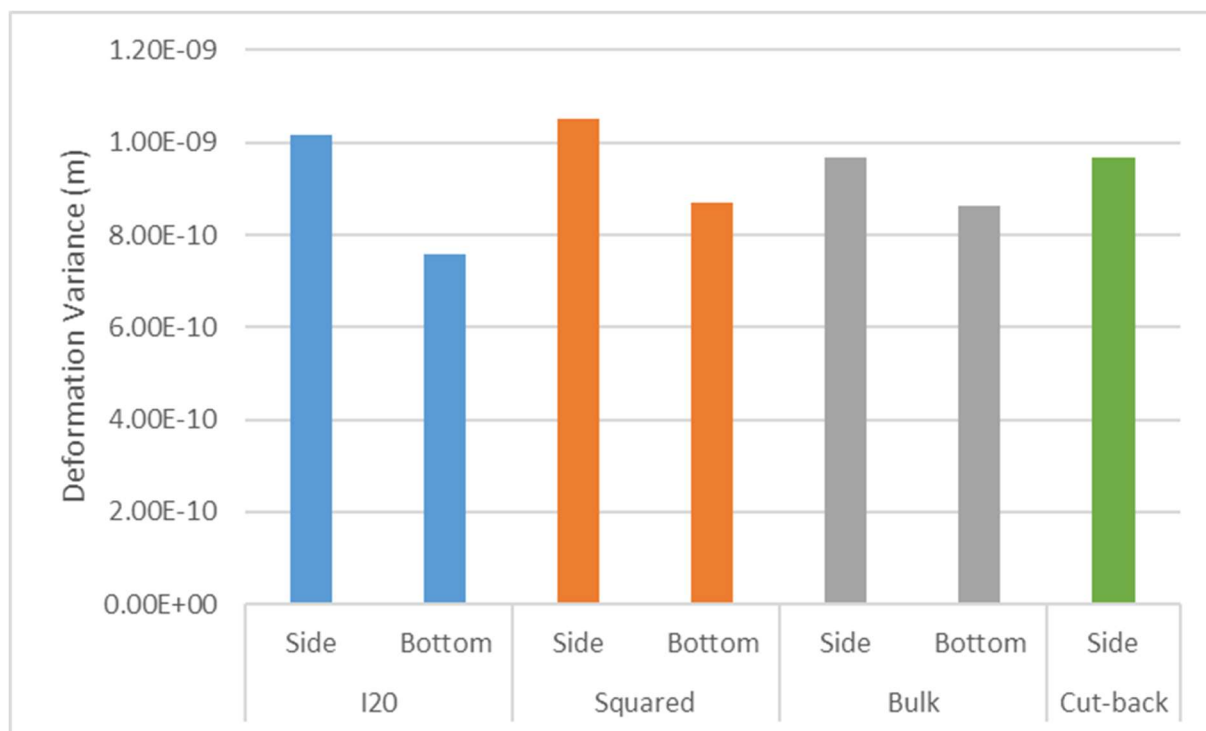


Figure 85 – Deformation variance of diffracting surface for all viable monochromator crystal designs and cooling locations (note: y-axis no longer on logarithmic scale).

Interestingly Figure 85 shows that the shoulders in the conventional I20 crystal design improve the performance of the monochromator by providing a lower deformation variance than the ‘squared’ crystal, though not by as much as the ‘bulk’ or ‘cut-back’ crystals. This is due to the shoulders replicating the effect of the ‘bulk’ and ‘cut-back’ crystals in one dimension; by increasing the size of the crystal away from the diffracting surface we allow the heat to spread out, normalising the thermal pathways. This effect is seen in the ‘bulk’ crystal, where the cooling areas are held at a further location from the edges of the diffracting region. This suggests an alternate design, wherein the shoulders are also present in the other dimension to create a truncated pyramid design with a large cuboid base. This would likely function similarly to the ‘bulk’ crystal design in practice and

would result in an increased crystal footprint, and so has not been modelled to date, although this design could be considered in further work.

A larger, 'bulk' crystal distances the cooling surfaces from the absorbing region in much the same way as bottom cooling does. By increasing the distance from where the power is absorbed to where the power leaves the crystal, i.e. between the diffracting surface and the cooled surfaces, the heat is allowed to spread out; as such the heated region comes to a more uniform temperature, which in turn normalises the thermal deformation experienced across the diffracting surface. However, the drawback of the 'bulk' design is that it increases the width of the monochromator crystal by almost 40%, increasing the size of optics hutch needed and reducing the possible number of beamlines around each storage ring.

Bottom cooled crystals showed the greatest performance, with the lowest deformation variance and most uniform temperatures, due to the normalisation of thermal pathway lengths. However, when considering physicality of the new designs it becomes very difficult to hold a crystal such that it is bottom cooled. However, the 'cut-back' crystal shows a greater performance than that of the side-cooled crystals and one on par with the 'bulk' crystal design. This suggests that a viable solution would be to side cool a smaller crystal some distance from the diffracting surface, allowing the thermal pathway lengths to normalise will still maintaining a smaller crystal footprint.

It is worth noting that despite the small scale of deformations observed, the monochromaticity and collimation of the beam can be damaged by values as low as  $10 \text{ \AA}$  as mentioned on page 10, Section 1.4; as such these deformations are a significant source of damage to the diffracted beam.

### 3.5 Conclusion

Overall, the current crystal design was surpassed only by the 'bulk' and 'cut-back' design when side-cooled. However, as the goal of the I20 beamline is to minimise the crystal footprint such that secondary beamlines can be installed around the same storage ring, a design that increases the crystal footprint does not fit the design brief. As such, the 'bulk' design has been disqualified for this application.

The most significant result that arises from these models is that the location of the cooled areas have a far greater effect on the quality of any diffracted beam than the shape of the crystal. This encourages a shift in design philosophy; rather than focusing on crystal shapes and designs, the focus should be on heat exchangers such that sufficient cooling is provided in the right locations to minimise the thermal deformation.

In addition, the small scale of the thermal deformations is dwarfed by the stress-induced warping shown in Figure 30 on page 58, Section 2.6; this shows another shift in design philosophy, that cooling is not as important as correctly clamping the crystals such that they are not deformed before the beam is incident.

One design that can be discounted at this point is the use of thinner crystals to allow some beam power to pass through. While this approach does reduce the peak temperature observed in the monochromator crystal, the loss of rigidity on a macroscale resultant from reducing the crystal thickness sufficiently to allow any of the incident beam to pass through unabsorbed is too great, allowing the crystal to bow much more easily under its non-uniform temperature. Thus, thin crystal designs have been discarded.

Throughout the work above, cooling the crystals on their bottom side (i.e. the surface most removed from the diffracting surface) reduced the deformation variance observed in the diffracting

surface. However, clamping a crystal such that this surface is the only one in contact with a heat exchanger would prove problematic in reality as it would be difficult to ensure good mechanical contact, and therefore good thermal contact, without applying forces directly to the diffracting surface; as such a compromise must be made. In this case, dislocating the side cooling some distance from the diffracting surface, as modelled in the 'cut-back' crystal design, allows the crystal footprint to be minimised and the crystal to be clamped while still observing a lower deformation variance and a flatter diffracting surface.

### [Executive Summary of Chapter 3](#)

The location of the cooling surface has been shown to be of far greater influence on the diffracting surface uniformity than the actual shape of any given crystal; this opens the priority of designing crystals such that they can be cooled in the correct locations.

By comparing the surface deformation variances to the isothermal plots, it becomes apparent that the more uniform the thermal pathways are, the more uniform the temperature of the diffracting surface is and the more uniform the surface is. This is a major contributor to the quality of the diffracted beam, and was carefully considered when designing the novel, interference fit crystal assembly.

Bottom cooling is the ideal method of making the thermal pathways uniform, but has significant challenges when trying to securely hold the crystal. However, displacing the cooling region from the diffracting region by a small distance improves the uniformity of the thermal pathways as in the bottom-cooled regime; if sufficiently separated, the crystal will perform similarly to a bottom-cooled crystal.

Thin crystals cannot be used, as their lower resistance to thermal deformation drastically increases the diffracting surface deformation.

## 4. Investigating the Differing Benefits to Direct and Indirect Cooling

### Review of the Thesis up to Chapter 4

The Literature Review identified a lack of research into the causes of deformation in monochromator first crystals; instead, most literature focuses on mitigating this deformation. Two factors – a requirement for increased synchrotron beam powers and more beamlines per storage ring facility – both require a redesign of monochromator first crystals to have a smaller footprint and be able to dissipate more heat.

Chapter 2, Examining Thermal Transport through the use of Theoretical Models, has shown that FEA modelling is suitable to examine crystal designs. The presence of three contrasting sets of material properties gives rise to deformation of the diffracting surface before the synchrotron beam is even incident, degrading the quality of the diffracted beam. This is a major factor and will need to be addressed in the novel design presented in this work.

Chapter 3, Exploring Various Crystal Geometries and Heat Exchange Locations, has shown that the conventional approach of cooling the sides of the crystal is inefficient, causing disparate thermal pathways and therefore a more deformed diffracting surface. Instead, the cooled area should be moved away from the diffracting surface such that the thermal pathways have sufficient distance to become more uniform. It has also been shown that crystal geometry is less important than cooling location, opening up more crystal structures as possibilities.

### 4.1 Introduction

Having identified that cooling location is key in designing a new monochromator assembly, there is a second factor to consider: monochromator crystals are cooled by one of two methods, either directly or indirectly. In an indirect cooling system, the crystal is held strongly against a heat exchanger, through which is channelled a coolant fluid that removes heat from the system. In a direct

cooling system, the coolant is channelled directly through the monochromator itself. While most synchrotron facilities use indirect cooling systems, direct cooling is perceived as more efficient and desirable. As such, the benefits and drawbacks of each will be compared to determine which should be used in the novel, interference fit assembly design.

Indirectly cooled crystals are designed to be held between two or more heat exchangers, through which coolant is channelled to extract heat. This design lends itself to smaller monochromator crystals with large cooling surfaces, clamped through the bulk of the crystal to ensure good thermal contact with the heat exchangers.

Indirect cooling is currently used at the I20 beamline at the Diamond Light Source. It is cheaper to set up, as the heat exchangers can be made of more easily machined materials, and seals and hoses can be welded onto these materials with less time and expense than for silicon. The heat exchanger is also used as the support and brace for the crystal, holding it in place and allowing the assembly to be adjusted and oriented. Indirect cooling can also reduce the vibrational load on the crystal, as cryogenic cooling devices pump the liquid nitrogen which produces vibrations. Indirect cooling also requires lower clamping forces on the monochromator crystal, and in general have a longer lifespan than a direct cooling system as the heat exchangers can be swapped out for a much lower price than the monochromator crystal itself.

Directly cooled crystals are designed to be coupled to two or more coolant exchangers, through which coolant is channelled through the crystal to rapidly extract heat. This design lends itself to larger crystals with more non-diffracting surface area, and due to the excessive forces required to form a gas-tight seal has seen coolant exchangers clamped only to the sides of the crystal through the use of strain relief cuts.

Direct cooling is used at a limited number of synchrotron facilities, although there is a wide interest in moving to direct cooling systems as these are seen to be more efficient and provide a more uniform monochromator crystal, both of which allow higher resolution outputs. Although it is more expensive to setup due to the high precision connections needing to be machined into the silicon itself, a material that is notoriously hard to machine, it can achieve lower temperatures directly in the middle of the monochromator crystal. Direct coupling to the coolant draws the heat from the crystal faster, reducing both times required to reach thermal equilibrium (i.e. the amount of time between assembling the monochromator and it being cold enough to be used) and the peak temperatures reached during operation. However, direct cooling tends to require more frequent maintenance, as the indium seals used to ensure the system is gas-tight are subject to greater thermal fatigues through multiple cycles between cryogenic and room temperature, which can stress and damage these components. If the gas-tight system fails, liquid nitrogen will vent into the optics at high rate, requiring the beamline to shut down. The only viable alternative to reduce the thermal fatigue is to maintain the crystal at cryogenic temperature at all times, which can be both expensive and difficult to ensure if there is an issue with the coolant on site.

Overall, the benefits of indirect cooling are repeatability, lower clamping force, and longer lifetime, while direct cooling has a higher efficiency and lower temperatures. While the benefits of direct cooling appear attractive at first glance, we must balance these factors to determine which method of cooling would be most advantageous for the novel monochromator assembly design. Another variable to consider is the differing design philosophy for indirectly and directly cooled crystals, which may have a direct influence on the diffracting surface deformation variation.

## 4.2 Investigating the Controlling Properties of Thermal Contact

With an indirect cooling system, one of the limiting factors is thermal contact between the monochromator crystal and the heat exchanger. As all of the heat deposited into the crystal needs to be extracted through the heat exchanger, the flow between the crystal and the heat exchanger sets a limit on the rate at which the heat can be extracted from the crystal. When two bodies come into contact, the flow of heat between them is governed by the thermal gap conductance, a value which is dependent on the bodies in contact and the force with which they are held together. Any two bodies brought together will make contact at only three points, as elaborated in Chapter 5. Once all three contact points are defined, any further contact is only created by exerting enough of a clamping force on the two bodies to deform them, allowing other points to come into contact.

This limitation leads to two non-intuitive considerations. First, increasing the size of the two bodies does not (directly) increase the thermal gap conductance. As increasing the size of the bodies does not increase the actual contact area, it does not directly increase the gap conductance; however, by increasing the size of the bodies it is possible to spread the contact points further from one another. This reduces the lengths of thermal pathways in the bodies, and can therefore reduce the overall temperature. Second, clamping force is the dominant factor, not clamping pressure. Again, as the size of the bodies does not directly increase the thermal gap conductance, increasing pressure (potentially by reducing the contact area) does not necessarily improve the thermal gap conductance. As such, the thermal gap conductance limits what we can achieve using indirect cooling methods.

There are a number of ways we can improve the thermal gap conductance in order to maximise the performance of our indirect cooling systems. First, the clamping force across the monochromator assembly can be increased. This will increase the effective contact area through elastic deformation

of the contacting surfaces, and possibly create secondary contact areas through which some of the heat can travel from the crystal to the heat exchanger.

Second, we can introduce an interstitial material between the crystal and the heat exchanger. The interstitial material is commonly a more malleable material which deforms to fit the crystal on one side and the heat exchanger on the other, creating a significantly larger surface area for the heat to pass through.

Finally, we can change how the surfaces are prepared. Most monochromator crystals and heat exchangers are polished to a very high smoothness on the sides in order to reduce the amount of force needed to form more contact areas between the two bodies.

Experimental work has been done to improve the thermal gap conductance through these methods, and is elaborated in Chapter 5.

As the quality of the diffracting surface is dependent on the uniformity of the surface, and therefore the uniformity of the temperature, a small change in the temperature at the boundary will not have a significant effect on the quality of the beam; the more important condition is the uniformity of the length of the thermal pathways. As such, it is more important that the thermal contact is uniform than that it is of a high value – in essence a uniformly low thermal gap conductance is more desirable than a non-uniform high one.

## 4.3 Comparing the Drawbacks and Benefits of Direct and Indirect Cooling

### 4.3.1 Direct Cooling

In order to assess the benefits of direct cooling, an isolated I20 crystal was modelled with two directly cooled channels taking the places of the steel bolts present in the conventional design. The mechanical boundary conditions are shown in Figure 86 and the thermal boundary conditions are shown in Figure 87, and are similar to those used in Chapter 3 except as detailed here: both long sides are subjected to a 1,140 N clamping force acting toward the centre of the crystal, and the two coolant channels are held at 80 K to simulate a flow of liquid nitrogen. The temperature profile is shown in Figure 88, the isothermal layer plot in Figure 89 and the diffracting surface deformation variance in Figure 90.

Direct cooling offers three benefits. First, it is not necessary to produce heat exchangers to attach to the monochromator crystal, as the crystal itself functions as the heat exchanger. This allows the crystal to cool at a faster rate during initial setup, reducing the time needed between assembly and usage. Second, the presence of the coolant within the crystal itself shortens the thermal pathways, allowing the crystal to maintain a lower temperature once the beam is incident and heat is being absorbed. By maintaining a lower temperature, the theory is that the crystal's diffracting surface can be kept flatter, improving the quality of the diffracted beam – however, as covered in Chapter 3, it is not the peak temperature of the crystal that is dominant but rather the uniformity of the temperature. Finally, the presence of the cooling channels within the crystal itself helps to normalise the thermal pathway length, causing the thermal transport to function more like a bottom cooled crystal than a side cooled one, which causes a drastic improvement as explained in Chapter 3 above.

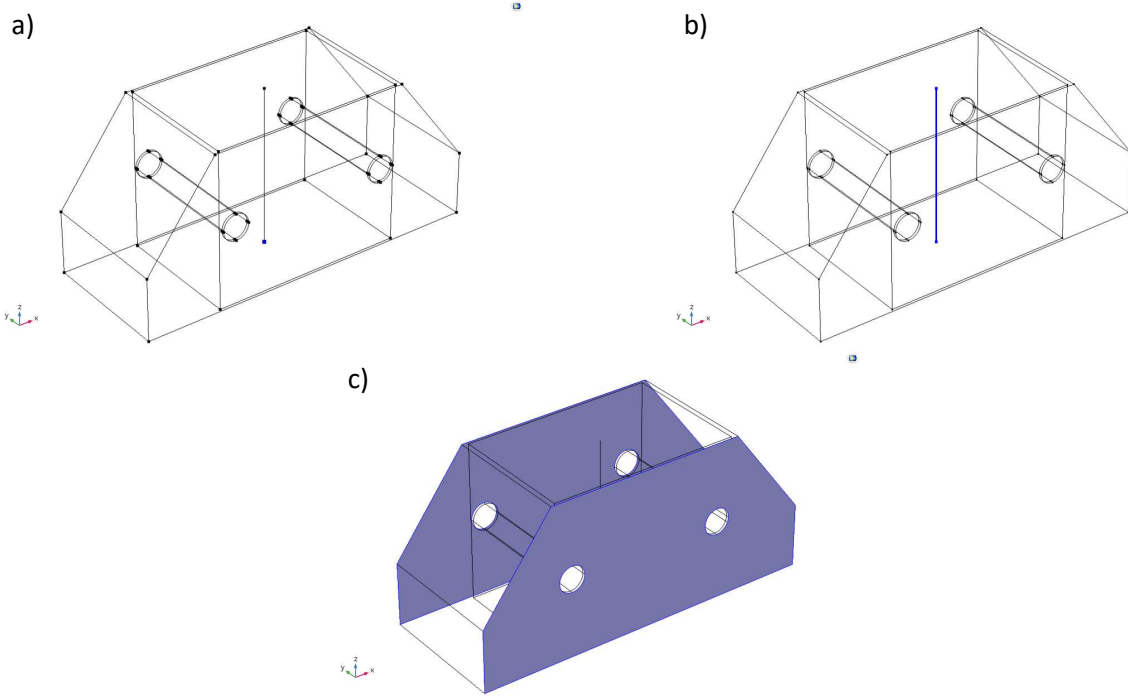


Figure 86 - Mechanical boundary conditions for directly cooled crystal: a) central point on bottom surface held fully constrained; b) line running through centre of crystal in z-direction held in x- and y-directions to prevent rotation; c) clamping force of 1,140 N applied on both outer faces.

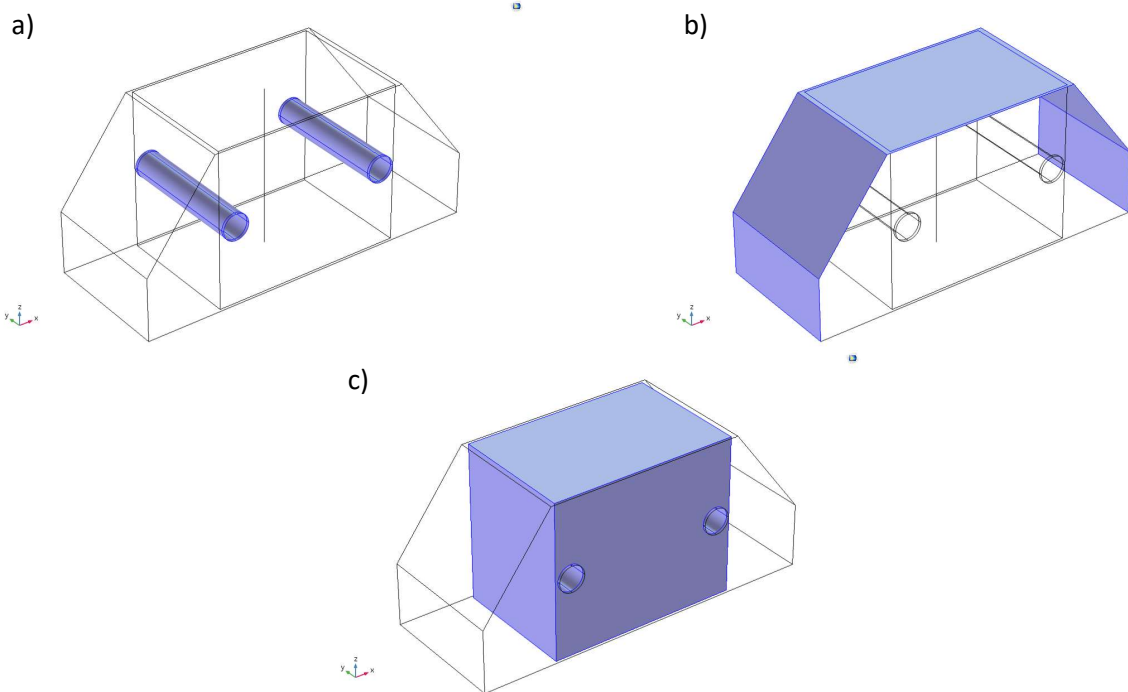


Figure 87 - Thermal boundary conditions for directly cooled crystal: a) coolant channels held at constant 80 K; b) all exposed surfaces radiating to 80 K ambient temperature; c) central volume exposed to beam for heat deposition.

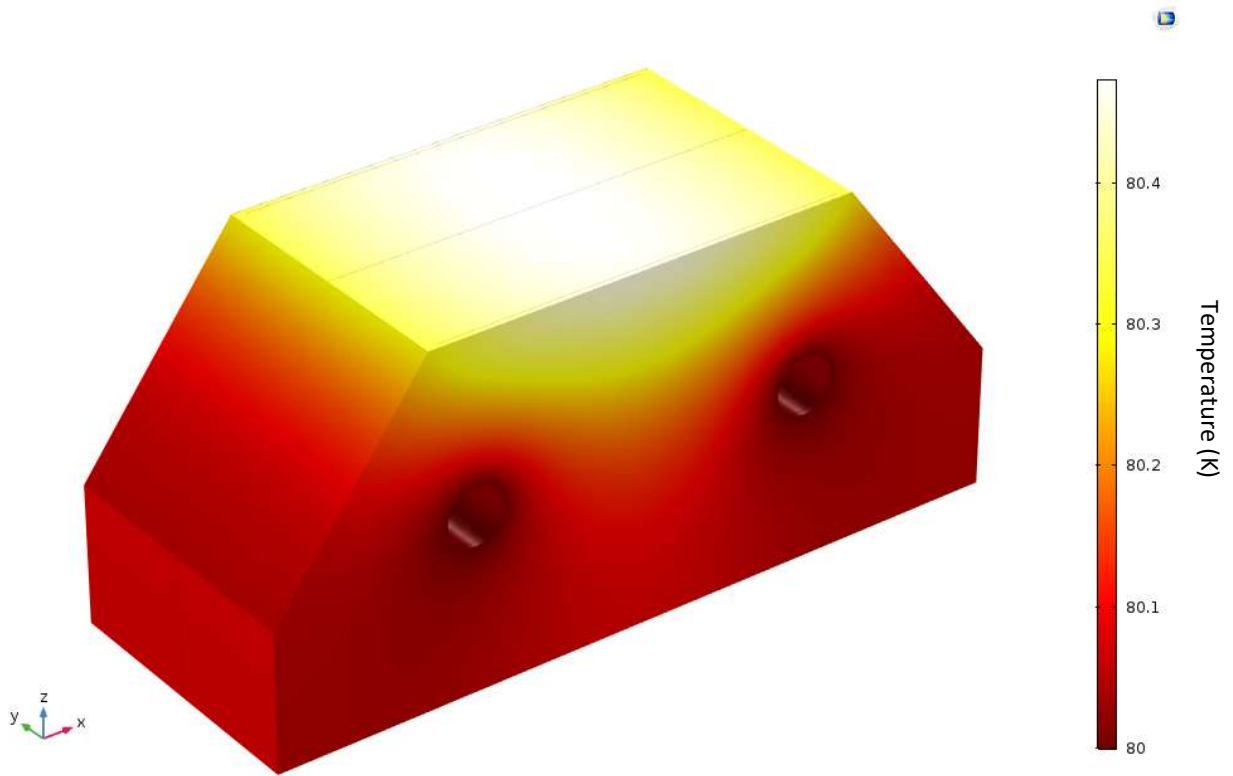


Figure 88 - Temperature surface plot of directly cooled crystal exposed to incident beam (K).

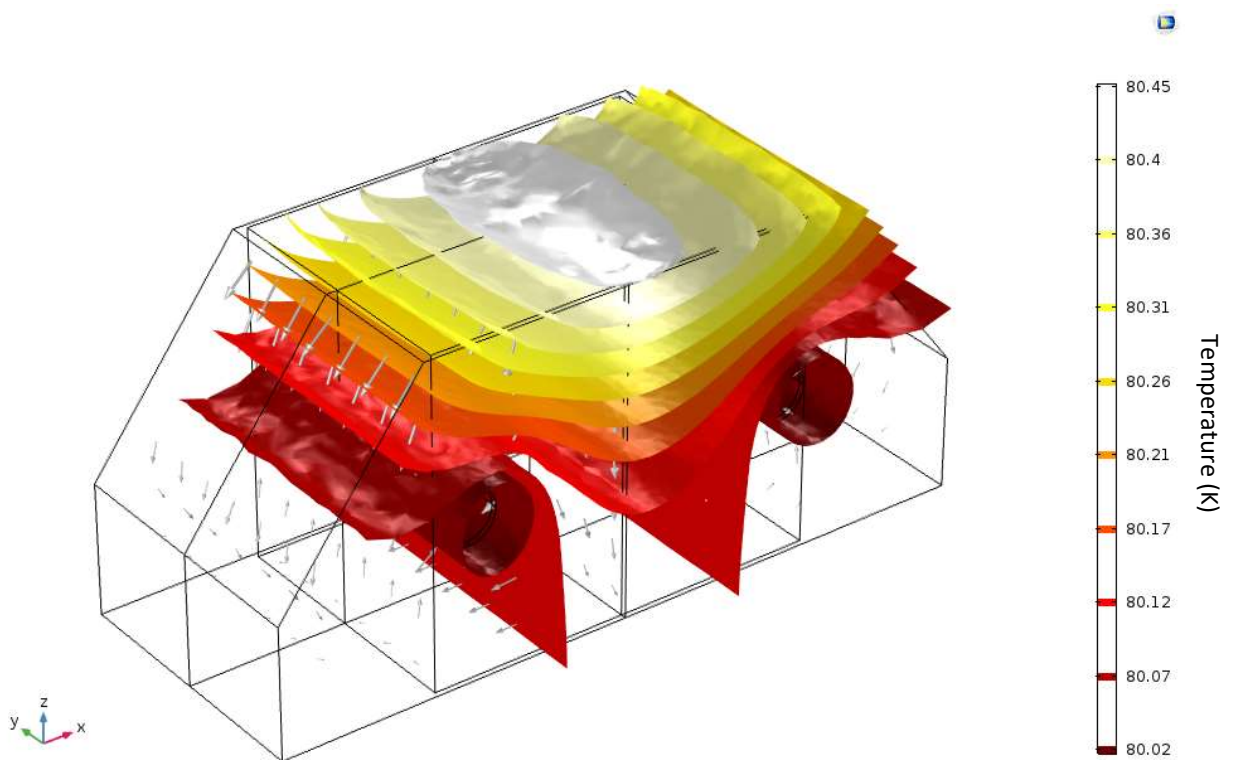


Figure 89 - Directly cooled crystal exposed to incident beam; isothermal layers mapped (K), with arrows showing movement of heat.

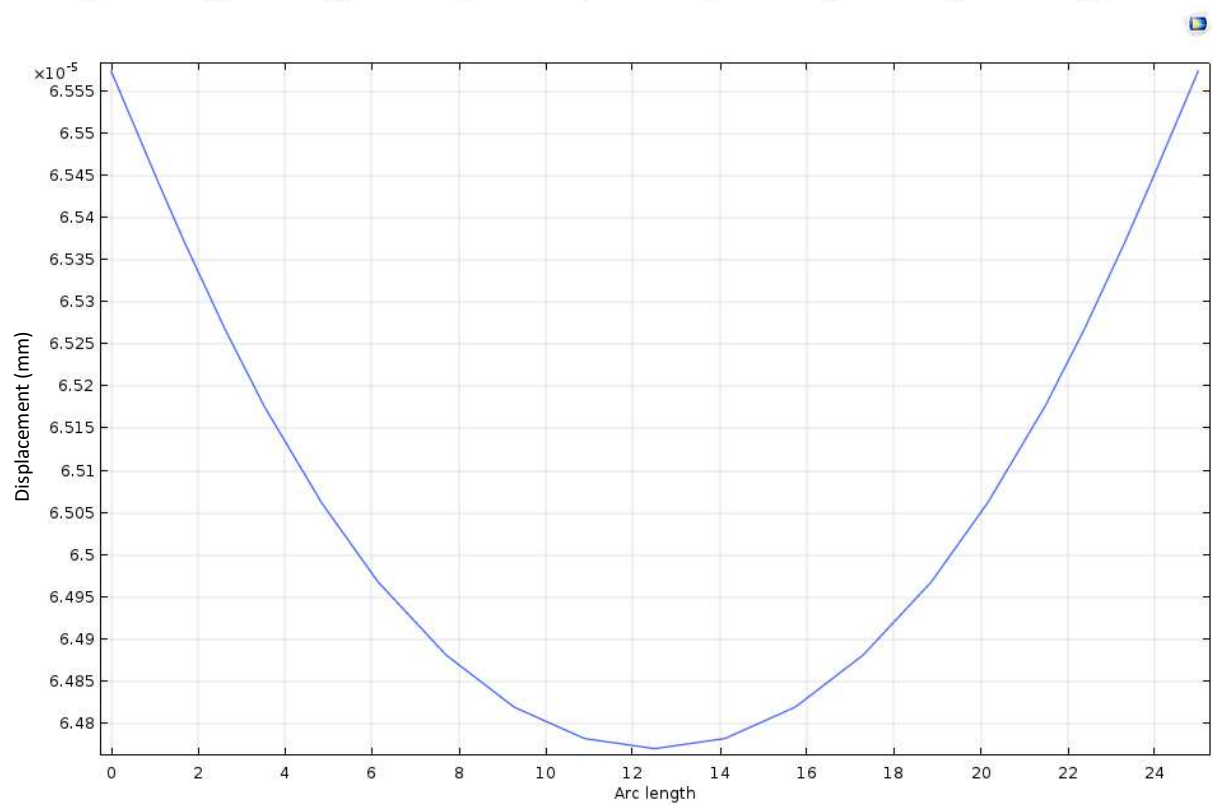
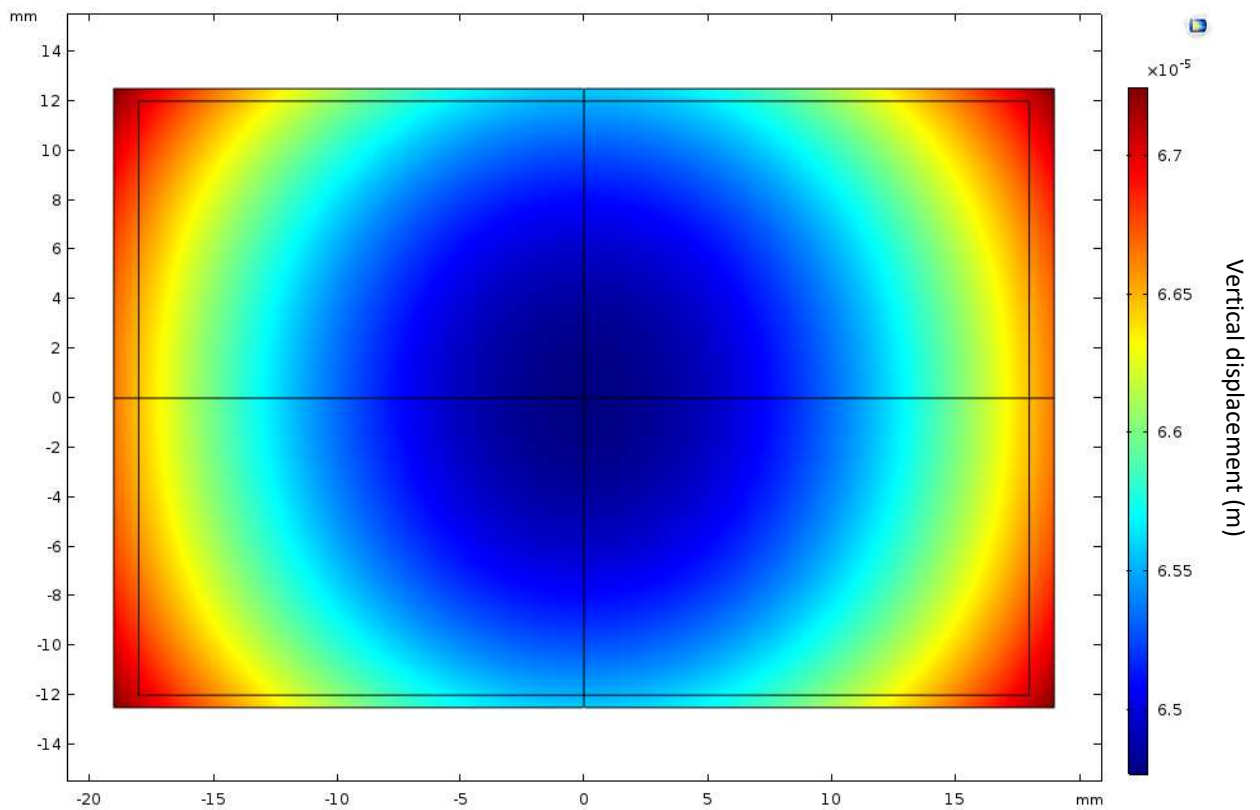


Figure 90 – (Top) Surface displacement of directly cooled crystal diffracting surface as a result of heating (m).  
 (Bottom) Cross-section of sagittal plane (m), showing deformation variance of  $8.045 \times 10^{-10}$  m.

Direct cooling does have drawbacks, however; in order to ensure a gas-tight seal is formed between the first crystal and the coolant exchanger, specialised gaskets must be used. While gaskets are also used in indirect cooling systems, these tend to be like-to-like seals, e.g. copper to copper, and as such the gaskets can be made and maintained more easily than when the two materials are different, such as the silicon to copper seal necessary for direct cooling. This adds to manufacture and machining costs, and reduces the lifespan of the system. The second drawback is that in order to maintain this gas-tight seal a direct cooling system requires a very high clamping force to be applied across the crystal. This high force can cause a mechanical strain in the monochromator crystal, in turn deforming the crystal in its entirety and the diffracting surface in particular and reducing the quality of the diffracted beam. The final drawback is that the cooling channels need to be machined into the silicon crystal directly; these channels are difficult to form, as silicon is a very hard, very brittle material, which increases the cost of the monochromator. Also, the repeated temperature cycles between room temperature and cryogenic temperatures cause thermal strain on these machined components, wearing them over time and damaging the seal.

### 4.3.2 Indirect Cooling

In order to assess the benefits of indirect cooling, an isolated I20 crystal was modelled with the steel bolts present in the conventional design. The mechanical boundary conditions are shown in Figure 91 and the thermal boundary conditions are shown in Figure 92, and are similar to those used in Chapter 3 except as detailed here: both long sides are subjected to a 570 N clamping force acting toward the centre of the crystal, and the two long sides are held at 100 K to simulate contact with a heat exchanger cooled by liquid nitrogen; in addition, the two steel bolts are modelled to correct size and with the correct material properties for stainless steel AISI 4340. The temperature profile is shown in Figure 93, the isothermal layer plot in Figure 94 and the diffracting surface deformation variance in Figure 95.

By contrast, indirect cooling increases the diffracting surface deformation variance both due to the side-cooled nature of the crystal and the requirement for the two steel bolts holding the assembly together. However, indirect cooling is easier to implement and maintain than direct cooling. As the monochromator crystal does not need coolant channels machined throughout, it can be made smaller and is easier to manufacture. The heat exchangers can be manufactured of copper and can be replaced easily when seals fail, using cheaper and sturdier gaskets due to the copper to copper seal with the coolant hoses and allowing threads to be tapped into the copper itself, something unachievable with silicon. In addition, the heat exchangers do not need to be clamped to the monochromator crystal with as high a clamping force as the direct cooling systems require. Overall this allows the monochromator crystal to go through more thermal cycles than in a directly cooled system; this either directly increases the lifespan of the crystal or removes the requirement of keeping the crystal at cryogenic temperatures for extended periods of time.

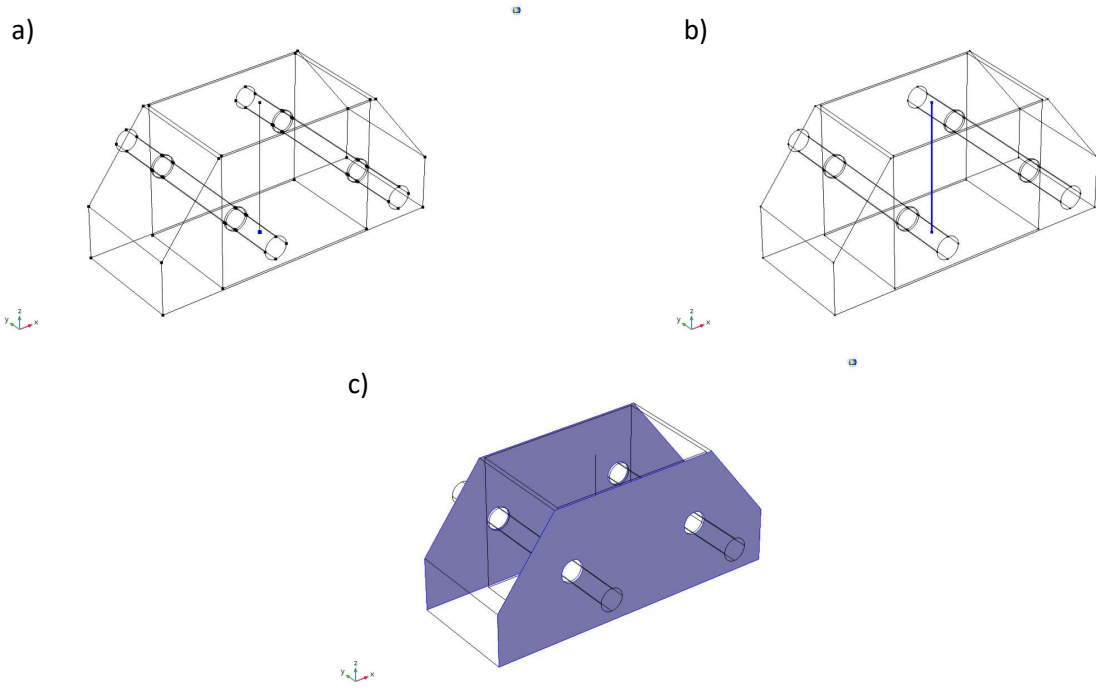


Figure 91 - Mechanical boundary conditions for indirectly cooled crystal: a) central point on bottom surface held fully constrained; b) line running through centre of crystal in z-direction held in x- and y-directions to prevent rotation; c) clamping force of 570 N applied on both outer faces.

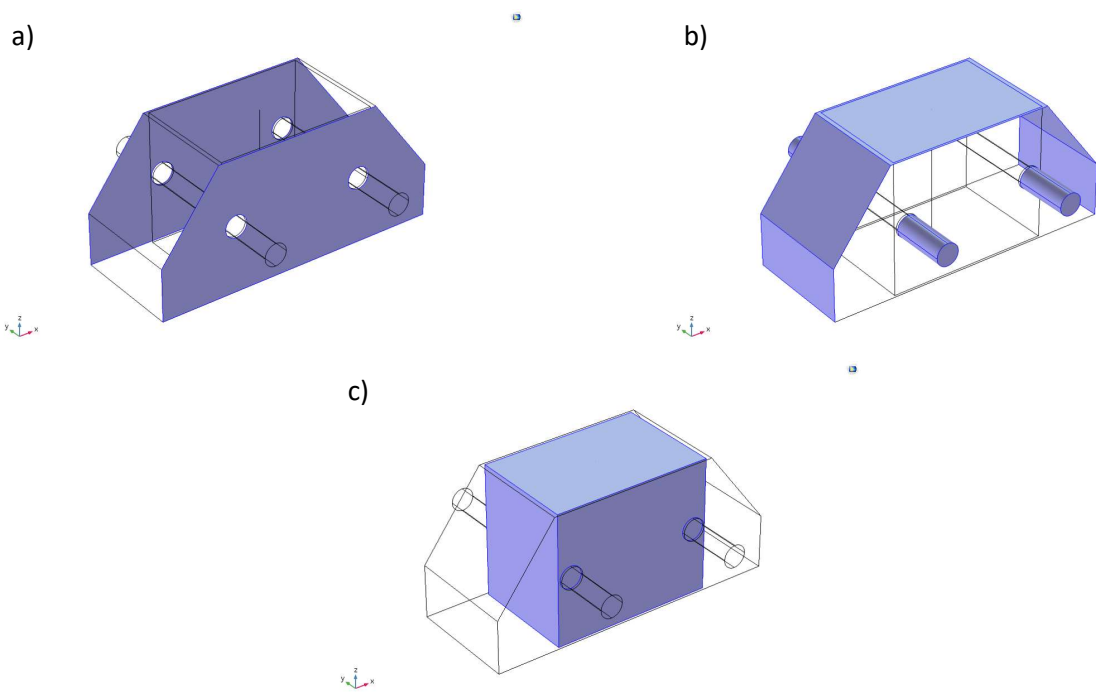


Figure 92 - Thermal boundary conditions for indirectly cooled crystal: a) long sides held at constant 100 K; b) all exposed surfaces radiating to 80 K ambient temperature; c) central volume exposed to beam for heat deposition.

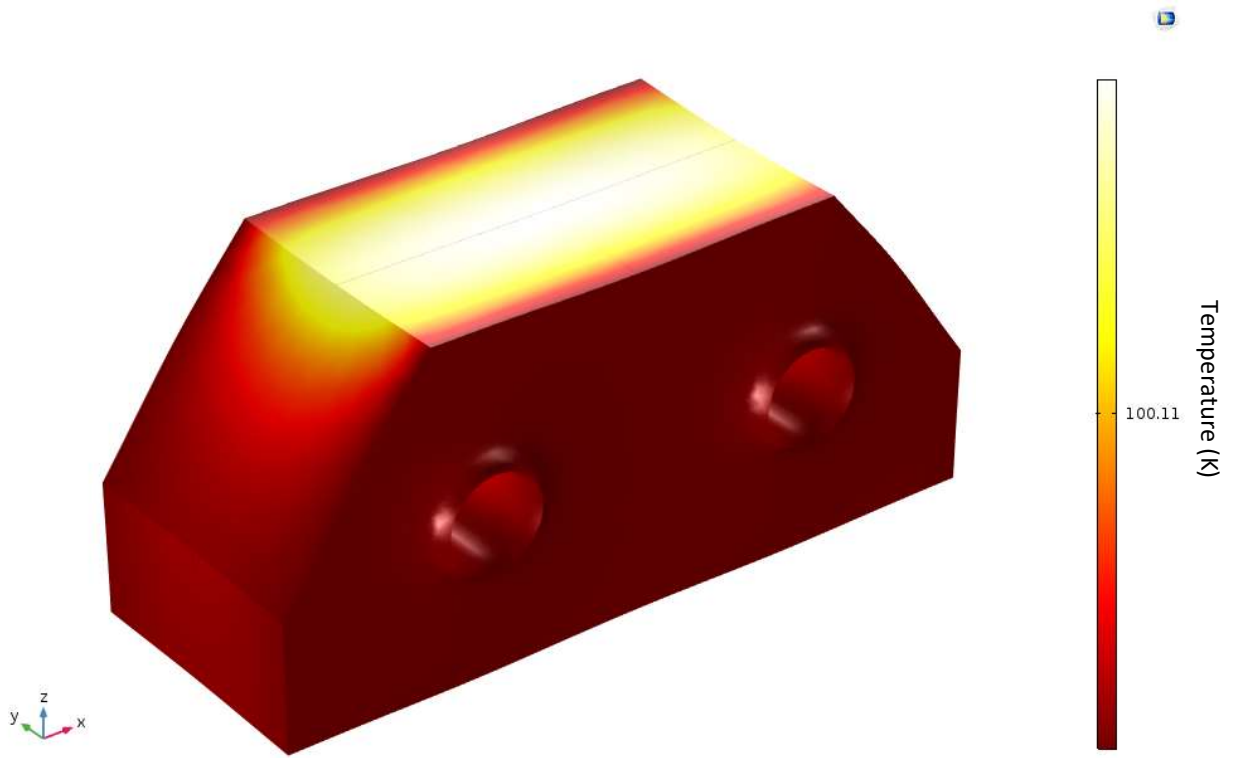


Figure 93 - Temperature surface plot of directly cooled crystal exposed to incident beam (K).

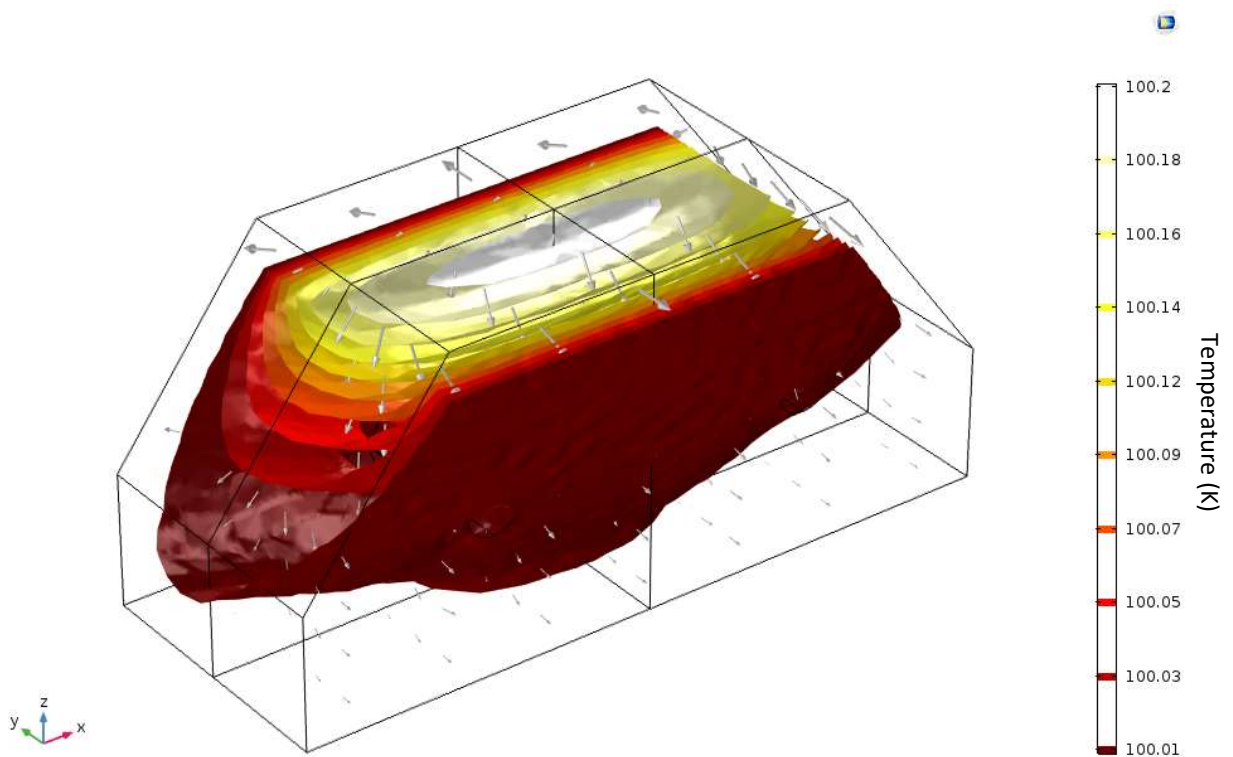


Figure 94 - Directly cooled crystal exposed to incident beam; isothermal layers mapped (K), with arrows showing movement of heat.

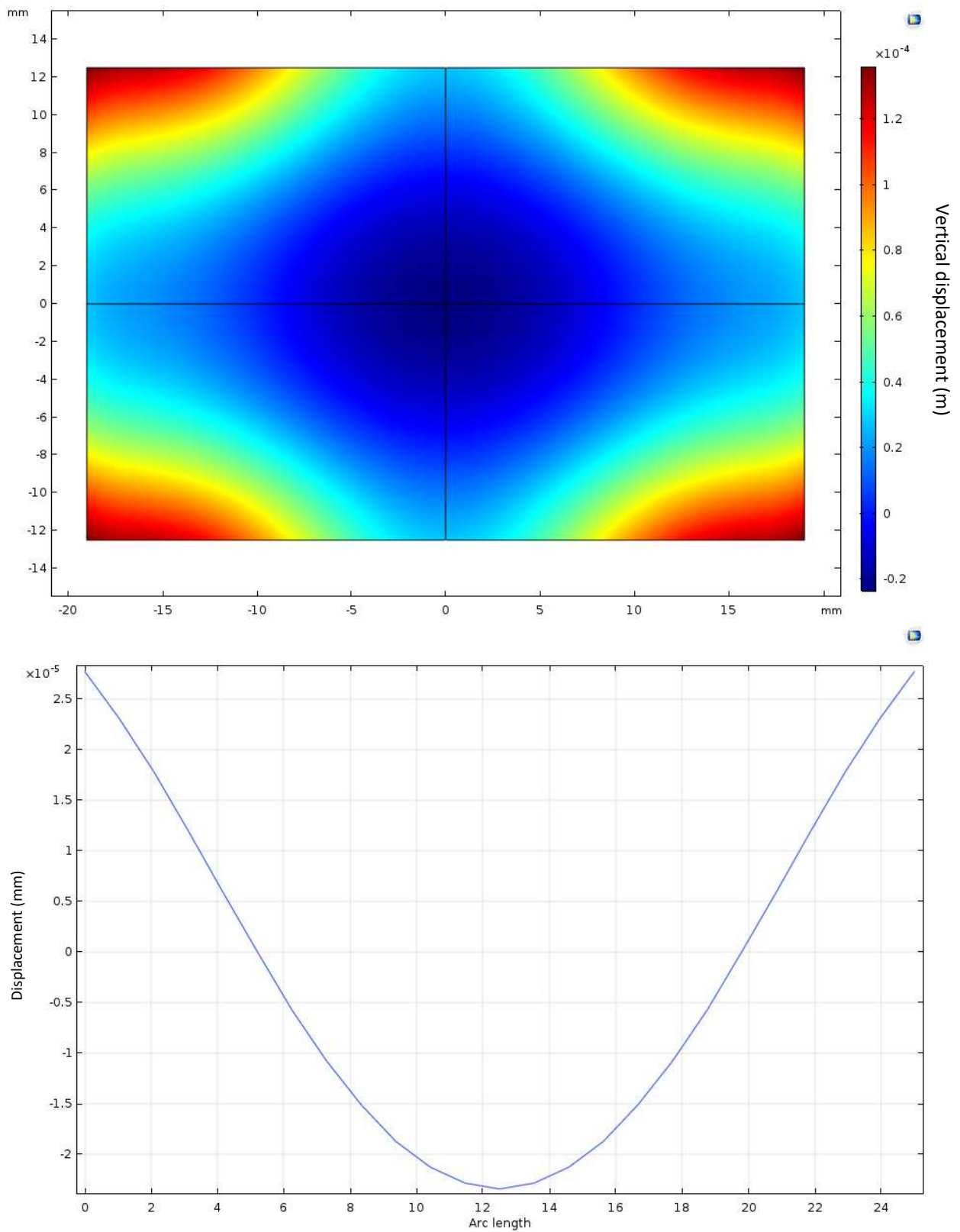


Figure 95 – (Top) Surface displacement of directly cooled crystal diffracting surface as a result of heating. (Bottom) Cross-section of sagittal plane (m), showing deformation variance of  $5.121 \times 10^{-8}$  m.

The major drawback of indirect cooling is the higher temperatures found in the crystal, along with the potential for a less uniform thermal pathway caused by the off-centre location of the cooling surfaces. Higher uniform temperatures have been shown not to be a direct problem, but should the cooling become non-uniform then the difference in thermal pathways could lead to increased surface deformation variance, damaging the uniformity of the diffracted beam. This can happen more easily in an indirectly cooled crystal than in a directly cooled crystal, as any damage or foreign object present in the interface between the crystal and the heat exchanger can cause a non-uniformity to develop.

#### 4.3.2 Comparison of Direct and Indirect Cooling

Overall, the difference between direct and indirect cooling has more direct effect on the peak temperature in the crystal than it does on the uniformity of the crystal temperature; as has already been remarked, the peak temperature is almost irrelevant provided it is within the same order of magnitude, whereas the uniformity of the temperature affects the diffracting surface deformation variance and therefore the uniformity of the diffracting surface itself. As such, the benefits of direct cooling do not outweigh its more significant drawbacks when compared to indirect cooling; observed improvements in performance in directly cooled systems are most likely attributable to the differing design philosophy for the two crystal styles. Instead, focus should lie on optimising the cheaper and more reliable indirect cooling method.

#### 4.4 Locating the Deformation Minimum with Increasing Clamping Force

Both direct and indirect cooling rely on clamping something, be it a coolant exchanger or a heat exchanger, to the silicon crystal. This requires a clamping force to be exerted through the crystal, which can in its own right deform the silicon crystal through compression and Young extension. In direct cooling this compression is unavoidable, as it is required to form the gas-tight seal which is imperative before the system is placed under vacuum; however, in an indirect cooling system this clamping force is proportional to the thermal gap conductance. As the clamping force is increased, the temperature of the crystal is reduced as the rate at which heat can flow from the crystal to the heat exchanger is increased, reducing thermal deformation. However, the higher clamping forces directly deform the crystal, introducing a structural deformation. At some value of clamping force there will be a local minimum where thermal deformation is replaced by structural deformation, resulting in a minimal deformation.

With a constant amount of heat being deposited into the crystal and a low clamping force, the thermal gap conductance is low and therefore the crystal reaches a much higher temperature. As the thermal gap conductance creates a bottleneck the thermal pathways are forced to deviate all the way to the bottom of the crystal, creating a longer pathway for the centre of the diffracting region than its edges; this causes the centre of the diffracting region to reach a higher temperature and therefore undergo a larger thermal deformation than the edges, resulting in a significant thermal deformation.

With a constant amount of heat being deposited into the crystal and a high clamping force, the thermal gap conductance becomes high and the thermal pathways become more uniform. However, the presence of a higher clamping force will cause the crystal to compress along the axis of the clamping force, resulting in an extension perpendicular to this axis. This expansion will be restrained

by the normal frictional force caused by the heat exchangers, resulting in the centre of the crystal expanding more than the edges and causing a significant structural deformation.

To find a local minimum point where the dominant regime changes and the sum of the two deformations is at its least, a parametric sweep was performed. The conventional I20 crystal assembly was modelled with a clamping force applied through the two axial steel bolts, as shown in Figure 96. This clamping force was modelled at a range of values, and the deformation variance across the crystal surface was plotted against the clamping force as shown in Figure 97. This approach revealed the clamping force where the deformation was at its lowest; at this point two deformation regimes, thermal and structural, crossed, creating a local minimum. This was measured to be located at 1,140 N. It is however important to note that this local minimum will vary from one crystal assembly to the next, and therefore this procedure should be repeated for each assembly design to find the optimal clamping force for indirect cooling.

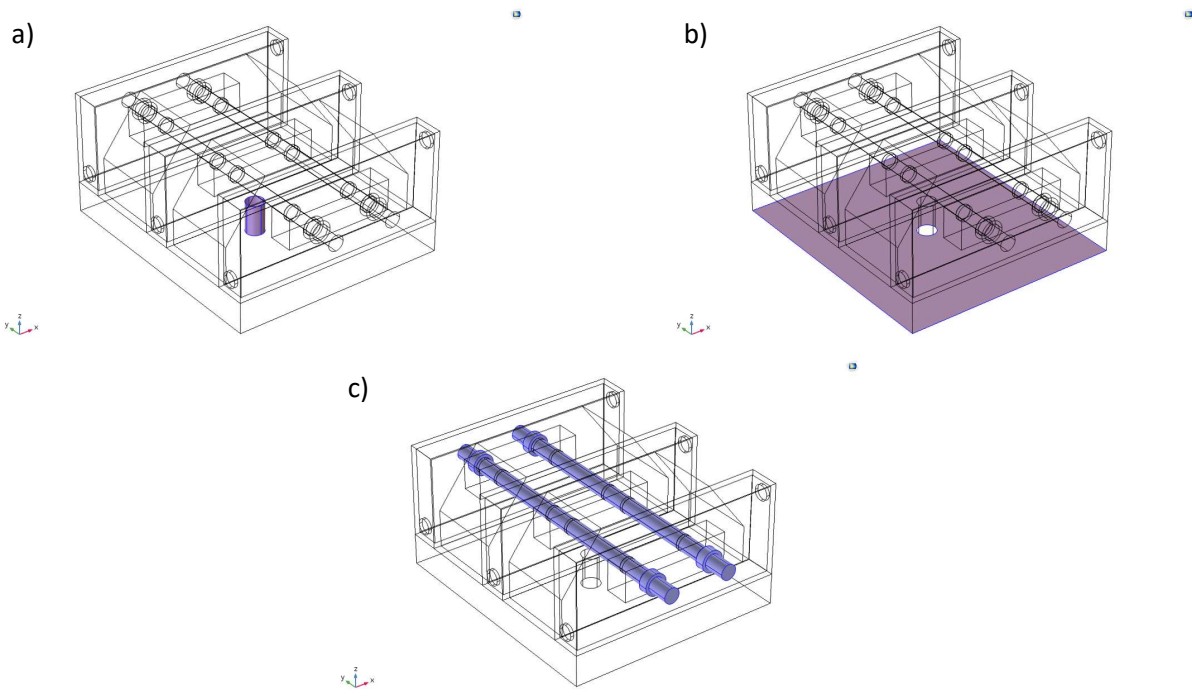


Figure 96 - Mechanical boundary conditions for indirectly cooled full crystal assembly: a) bolt on bottom surface held fully constrained; b) bottom surface of crystal assembly held in z-directions to prevent dropping; c) bolts pretensioned at varying clamping forces.

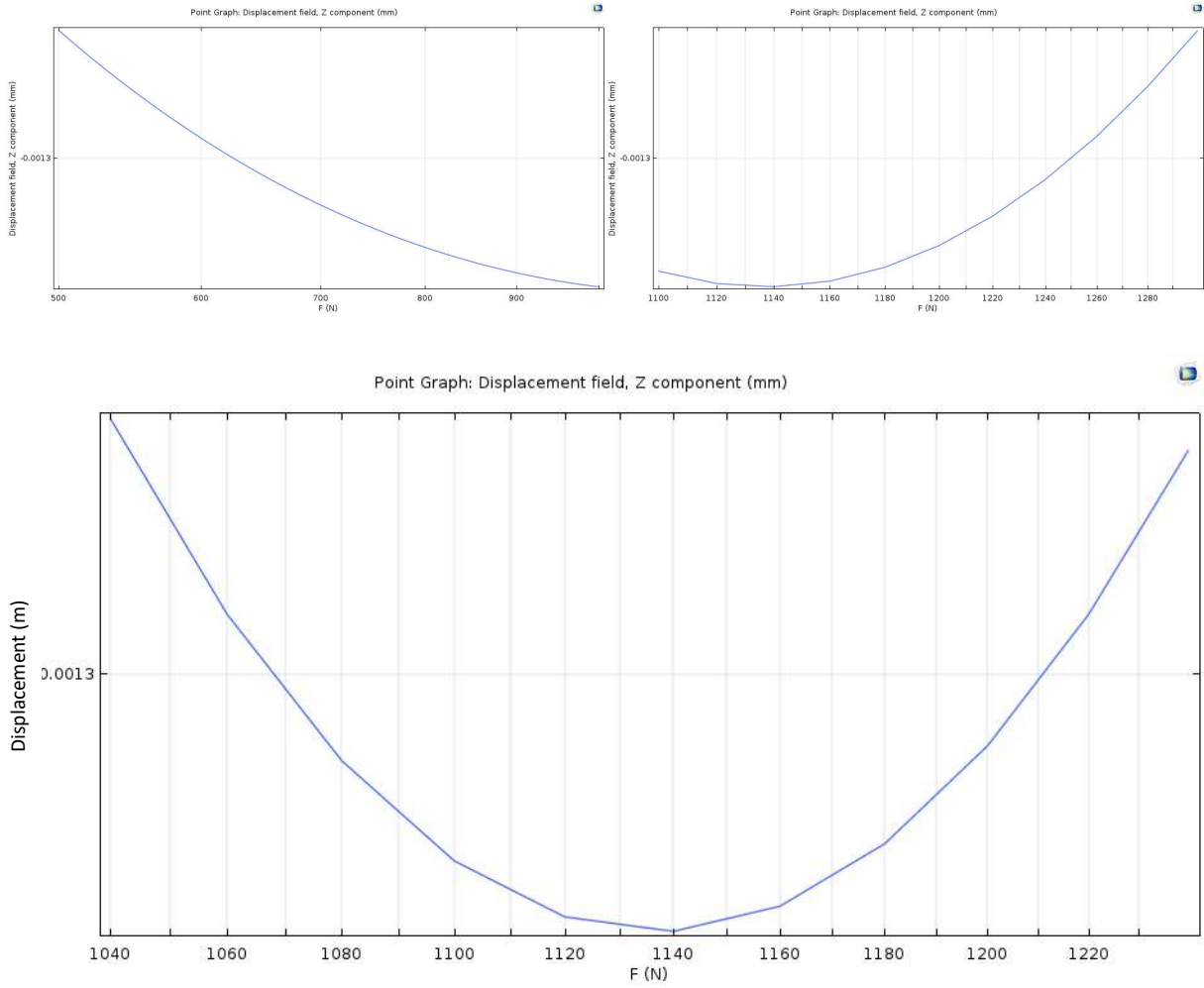


Figure 97 – Graphs showing peak diffracting surface deformation variance of the I20 crystal assembly as a function of clamping force.

## 4.5 Conclusion

Overall, directly cooling a monochromator crystal does improve the thermal transport when compared to indirect cooling and will result in a lower peak temperature in the monochromator crystal. This difference can be on the order of tens of degrees, due to the removal of gap conductance as a limiting factor in the cooling of the crystal; however, neither method in and of itself results in more uniform thermal pathways, which has been identified as the more important factor in maintaining a monochromatic, collimated beam in Chapter 3 above.

This leads to the conclusion that direct cooling does not represent a significant improvement in the performance of a monochromator crystal assembly when compared to indirect cooling; to the contrary, direct cooling is more difficult to achieve and maintain than indirect cooling, and if it is not posing a significant improvement in the performance of the crystal it should not be considered a priority.

Experimentally speaking, some synchrotrons have found improved performance when using a directly cooled monochromator crystal; however, these crystals tend to be larger than those used in an indirectly cooled system, and are more carefully isolated from any vibration induced by the cooling system. In addition the presence of the coolant channels within the body of the crystal itself causes the cooling to behave more as a bottom cooled crystal than a conventional side-cooled crystal. This difference in design philosophy between directly and indirectly cooled crystals produces a more stable and better constrained crystal, resulting in a higher quality diffracted beam; in effect, the directly cooled crystal is designed to function better than the indirectly cooled variants, and so they do. It is this difference in design philosophy that causes directly cooled systems to function better, rather than any benefit from the cooling method itself.

One major aspect in which directly cooled crystals benefit is the application of a decentralised clamping force to produce a gas tight seal. This decentralised, high intensity force differs from the indirectly cooled system, which tends to use a lower force that is applied through the bulk of the crystal. In an indirectly cooled system this force is often arbitrarily high in order to achieve a more efficient thermal contact conductance; however, a sufficiently high clamping force will induce a structural deformation in the crystal. There is a 'sweet spot' in each crystal assembly at which increasing the clamping force increases the structural deformation more than it reduces the thermal deformation; this value should be found for each crystal assembly to give the optimal beam quality.

Taking these findings into consideration, the optimal practice henceforth is to improve indirect cooling rather than try to apply direct cooling. This approach will give us a lower cost, more robust and more repeatable system that, while potentially reaching a higher peak temperature, produces the minimum diffracting surface deformation achievable in order to achieve the highest quality diffracted beam.

#### [Executive Summary of Chapter 4](#)

Direct cooling has been shown to be able to produce a reduction of the peak temperature on the order of tens of degrees. This value is low, and the improvement itself has negligible effects on the diffracted beam.

Direct cooling also requires far more crystal machining and higher clamping forces, both of which increase the difficulty of achieving and maintaining the cooling system compared to indirect cooling methods. In fact, the observed improved performance of directly cooled crystals is due to the normalisation of thermal pathways as explained in Chapter 3 and the precautions taken to accommodate the higher requirements of directly cooled systems.

In indirectly cooled systems a deformation minimum exists; in loosely clamped systems the crystal is more prone to thermal deformation, while in strongly clamped systems the crystal is more prone to structural deformations. By modelling various clamping forces, this crossover can be pinpointed giving the ideal clamping conditions for any given crystal assembly.

As such, the novel, interference fit crystal assembly design will use an indirect cooling system with consideration given to optimising the clamping force to minimise both thermal and mechanical deformations.

## 5. Examining the Effect of Varying Factors on Thermal Gap Conductance

### Review of the Thesis up to Chapter 5

The Literature Review found a lack of research into causes of deformation in monochromator crystals; most literature focuses on mitigating deformation. A growing need for increased beam powers and more beamlines per facility requires a redesign of monochromator first crystals to have a smaller footprint and dissipate more heat.

Chapter 2, Examining Thermal Transport through the use of Theoretical Models, showed that FEA modelling is suitable to examine crystal designs. The presence of contrasting sets of material properties causes stresses in the assembly before the beam is incident, degrading the quality of the diffracted beam.

Chapter 3, Exploring Various Crystal Geometries and Heat Exchange Locations, showed side cooling the crystal is inefficient, causing uneven thermal pathways and a more deformed diffracting surface. More distant cooled areas ensure thermal pathways have sufficient distance to become more uniform. Crystal geometry is less important than cooling location.

Chapter 4, Investigating the Differing Benefits to Direct and Indirect Cooling, has found that direct cooling does not offer significant benefits to outweigh the difficulties inherent in adopting this practice; therefore it has been decided to utilise indirect cooling in the novel, interference fit crystal design presented in this work with a priority to minimise both mechanical and structural deformation.

### 5.1 Introduction

As mentioned in Chapter 4 above, indirect cooling is largely controlled through the flow of heat from the silicon crystal into the copper heat exchangers, and from there into the liquid nitrogen coolant. Throughout this process, the major limitation is the conduction across the gap between the silicon and the copper. This thermal gap conductance needs to be as uniform as possible in order to

maintain uniform thermal pathways; otherwise the temperature of the crystal at the diffracting surface will be variable, resulting in varying thermal deformation and a non-uniform diffracting surface, degrading the monochromaticity and collimation of the diffracted beam.

In order to improve the thermal gap conductance, we first need to understand the theory behind thermal contact. This will be expanded upon later in this Chapter, but in brief the thermal contact occurs at three major sites, followed by a variable number of near-negligible minor sites. These major sites are responsible for the vast majority of the heat flow across the interface. All contact points begin first as single points, but with increased force can be made to truncate and therefore expand into small but finite areas; this drastically improves the heat flow. Although increasing the size of the two bodies in contact does not directly increase the flow of heat between them, it can result in the major contact sites become more dispersed across the contacting surfaces; this reduces the thermal conduction constriction and allows more heat to flow between the bodies. Areas not in contact are radiatively coupled, with heat radiating from the hotter body to the colder body, but this has a negligible effect.

The initial approach was to use COMSOL to model contact conductance between two bodies, such that boundary conditions and materials could be easily varied. This would allow easy comparison of a wide variety of parameters in quick succession and therefore find an optimal setup. However, how different factors affect thermal contact conductance is not fully known, and so a computer model could not adequately reflect the many various parameters. Instead, the gap conductance in various situations has been calculated from experimental measurements, and the calculated values have been fed back into a COMSOL model to ensure they are correct by comparing calculated values to those measured during the experiments.

The experimental method and results are explained thoroughly later in this Chapter. Two bodies were put in contact, one heated and the other cooled. The temperature was measured at various points through both bodies, and the temperature was extrapolated at either side of the interface. This temperature difference, combined with a thermal equilibrium state that indicated all power deposited into the system was being extracted, allowed us to calculate a value for the gap conductance. This procedure was repeated with variables altered in order to determine how the different factors affected the gap conductance and to determine the best way to improve thermal contact with a heat exchanger for an indirectly cooled system.

## 5.2 Investigating Thermal Contact Theory

Consider two bodies brought into contact with each other along a common axis,  $z$ . As the two bodies approach, they collide first with the highest common point along this  $z$ -axis. Once this point has made contact, the two bodies pivot around it until a second point comes into contact. The line between the first and second points will indicate the  $y$ -axis. Once these two points are in contact, the two bodies then hinge around this newly formed  $y$ -axis until a third point of contact is established; we define an  $x$ -axis such that it lies along this newly common plane. Now that three points of contact have been made, no more can occur; the bodies cannot hinge around any of the three axes without breaking contact with a prior established point.

There is one mechanism through which additional points of contact can be formed; by increasing the force between the two objects along the  $z$ -axis, the contacted points are made to deform either elastically or plastically. This deformation will allow further points to come into contact; however, this deformation also increases the contact area at each of the prior established points of contacts to such an extent that further contact points have a negligible effect on the conductance of heat across the boundary. Further increasing the force will further increase the flattening of the asperities, the raised points at which the two bodies have made contact, and will increase the contact area and thus the heat that can flow between the two bodies.

It is important to note that this relationship is dependent on clamping force, and not pressure, as pressure can be increased by reducing the surface area of the two bodies in contact; this would not increase the size of any asperities. As such it is important to define two area terms: the surface area of the bodies relates to the overall area of the surface to be brought into contact, and is relatively large, while the contact area is the region of the two bodies that actually comes into contact, and is orders of magnitude smaller. As the surface area has no effect on the contact area, and as this

contact area is very difficult to measure and very easily varied by applied force, the clamping force between the two bodies has been considered rather than any form of pressure.

Thermal contact theory suggests the application of an interstitial material (IM) between the two bodies heat is to flow between. An IM tends to be a more malleable material, and is intended to improve the thermal conductivity between the two bodies by deforming to fit the interface as shown in Figure 98 below, increasing the area in contact. When two bodies come into contact without an interstitial material, small pockets form where the materials do not meet. These pockets, if complete, can trap air within the system, or worse can leave a space present when exposed to vacuum. The trapped air allows heat to travel across the interface through convection, while the vacuum gaps require any heat transfer to occur via radiation; both of these mechanisms are by far less efficient than the conduction that occurs between two areas in contact. When the IM is introduced, however, it is deformed by the clamping force and fills the gaps between the two materials. This improved fit allows conduction to happen in more locations throughout the interface.

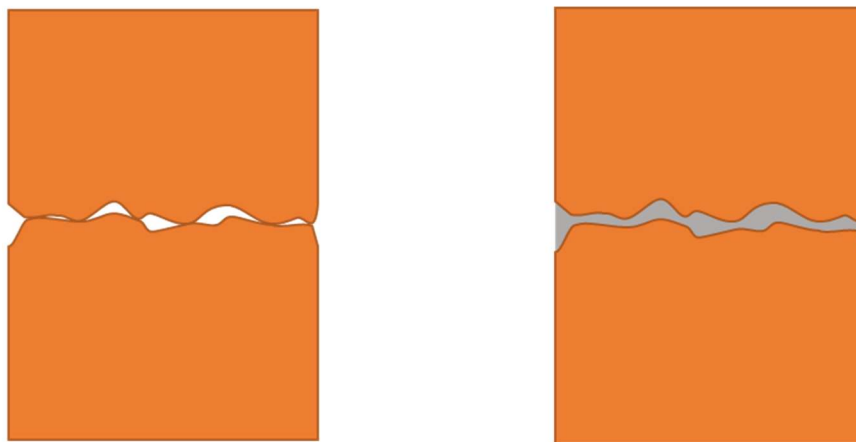


*Figure 98 – (Left) Two bodies in contact without an interstitial material, showing air gaps.*

*(Right) Two bodies in contact with an interstitial material, showing good fit.*

While thermal gap conductance has been the subject of many papers, they are mainly concerned with specialised conditions. Thermal gap conductance is a highly variable parameter, affected by the

absolute and relative temperatures of the hot and cold bodies, the materials used (including any IM or the lack thereof), environmental pressure and microstructures on the surface of the two bodies. As such, multiple factors have been addressed simultaneously in this work to determine which is dominant and what combination is ideal; both the clamping force and the IM used have been considered.

Calculating the thermal gap conductance is done using equation 11 below. However, as the temperature has been extrapolated to the boundaries, both the  $\Delta x_A$  and the  $\Delta x_B$  terms are reduced to zero, and equation 11 can be rewritten as equation 12 for simplicity.

$$q = \frac{T_A - T_B}{\frac{\Delta x_A}{k_A A} + \frac{1}{h_c A} + \frac{\Delta x_B}{k_B A}} \quad [11]$$

Where  $q$  is the power input into the system.

$T_A$  is the temperature of the hot body.

$T_B$  is the temperature of the cold body.

$\Delta x_A$  and  $\Delta x_B$  are the thermal expansion of the region between the measured temperature and the interface in the hot and cold body respectively.

$k_A$  and  $k_B$  are the thermal conductivity of the hot and cold body respectively.

$A$  is the cross-sectional area of the interface.

$h_c$  is the thermal conductivity of the gap.

$$h_c = \frac{q}{A(T_A - T_B)} \quad [12]$$

### 5.3 Modelling Thermal Contact with Various Factors

As the first approach to finding the effect of various factors on thermal contact, it was decided to produce a COMSOL model of two cylinders of copper with a cylinder of silicon between, aligned along their common z-axis. One of the copper cylinders, henceforth referred to as the 'hot body', would have heat deposited to simulate a heater, while the other, henceforth the 'cold body', would have an area fixed at a constant temperature to simulate a coolant system. All three cylinders would be considered insulated along their lengths to simulate perfect insulation, such that all heat deposited into the hot body would have to travel through the system to be removed from the cold body. All three cylinders would begin with an initial temperature of 289 K. The bottom surface of the cold body would be held fixed in space, while a variable load would be applied to the opposite surface of the hot body. To prevent rotation or ejection, all three cylinders would have an axis through their length held constant in the x- and y-directions. Three equidistant points along the z-axis within each cylinder would have their temperature monitored to extrapolate values to the interface boundaries. An overview of the model is shown in Figure 99. The mechanical boundary conditions are shown in Figure 100 below, and the thermal boundary conditions are shown in Figure 101. Any interstitial materials would be added in the form of two identical disks, separating the silicon cylinder from the copper cylinders.

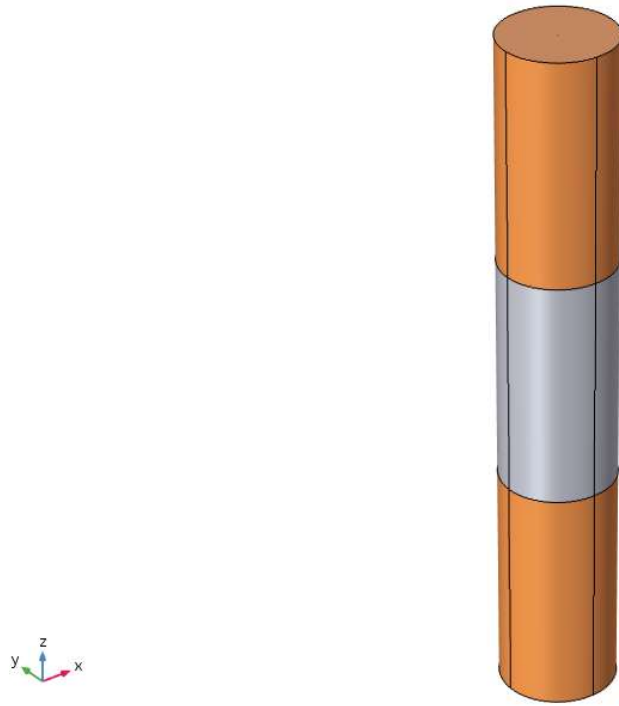


Figure 99 – Thermal gap conductance simulation structure; two copper cylinders sandwiching a silicon cylinder.

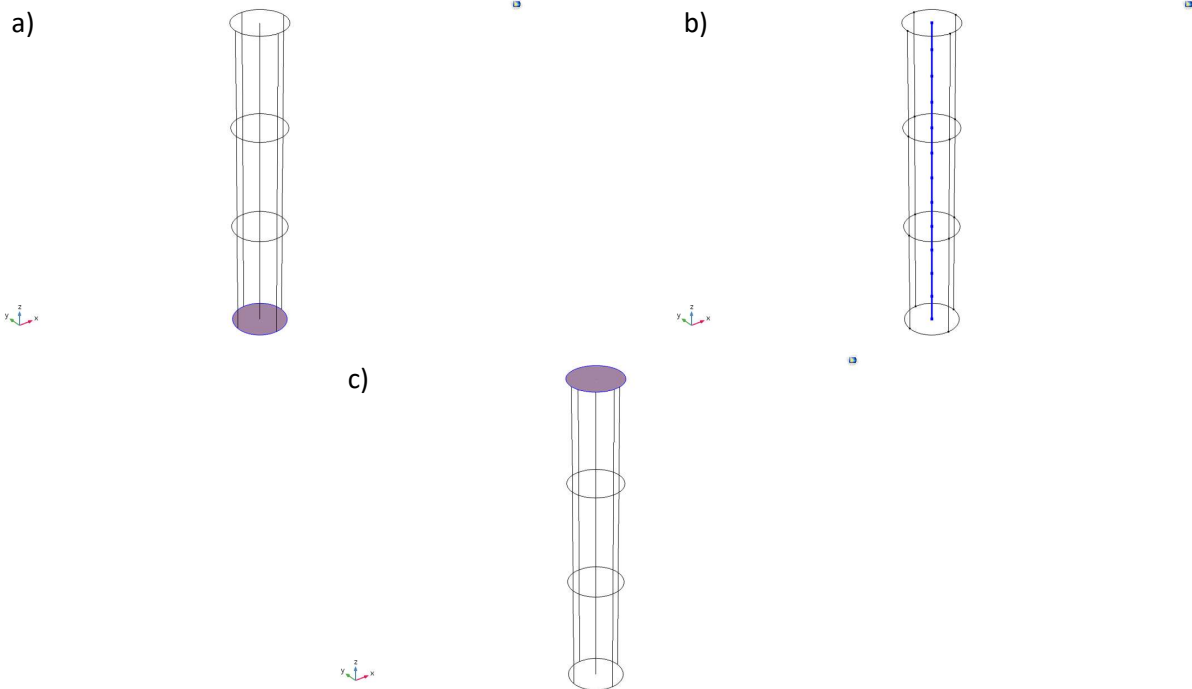
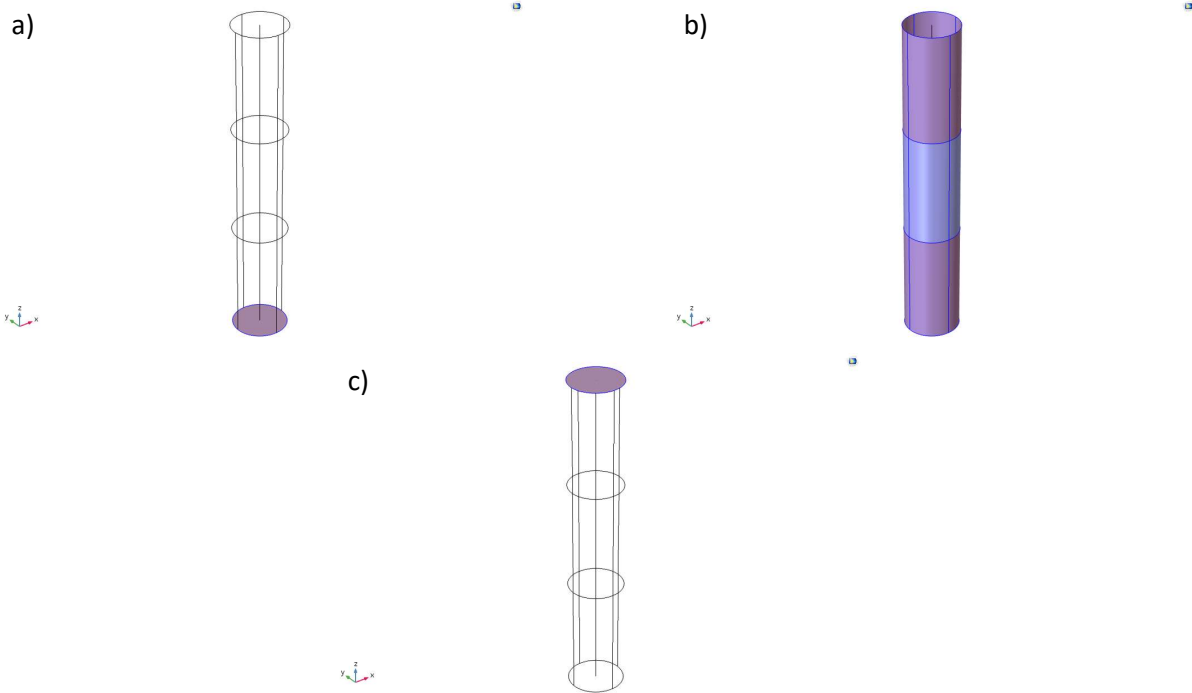


Figure 100 - Mechanical boundary conditions for thermal gap conductance simulation: a) bottom surface held fully constrained; b) common z-axis held in x- and y-directions to prevent ejection or rotation; c) boundary load applied through top surface.



*Figure 101 - Thermal boundary conditions for thermal gap conductance simulation: a) bottom surface held at constant 280 K; b) all exposed surfaces insulated thermally; c) top surface subjected to variable heat source.*

To maximise the accuracy of the simulation, it was decided to model the cooled surface as an actual cooling pipe in the cylinder. Two designs were tested for this coolant pipe: either one pipe of a 15 mm radius, or two pipes with a radius of 7.5 mm each. To determine which would provide more uniform temperatures, a quick model was run in two dimensions featuring just the two copper cylinders with an arbitrary gap conductance value, 60 W deposited in the hot body and either one or two cooled rings emulating the coolant pipes held at a fixed 283 K. For simplicity, only the two copper cylinders have been modelled. The results are shown in Figure 102 below; it became obvious that it did not matter whether one pipe or two was used, as the copper would thermalize over a region much smaller than the radius of the pipe and by the first temperature probe the temperature was the same in both scenarios. As it is easier to machine one hole than two, the single pipe structure was used.

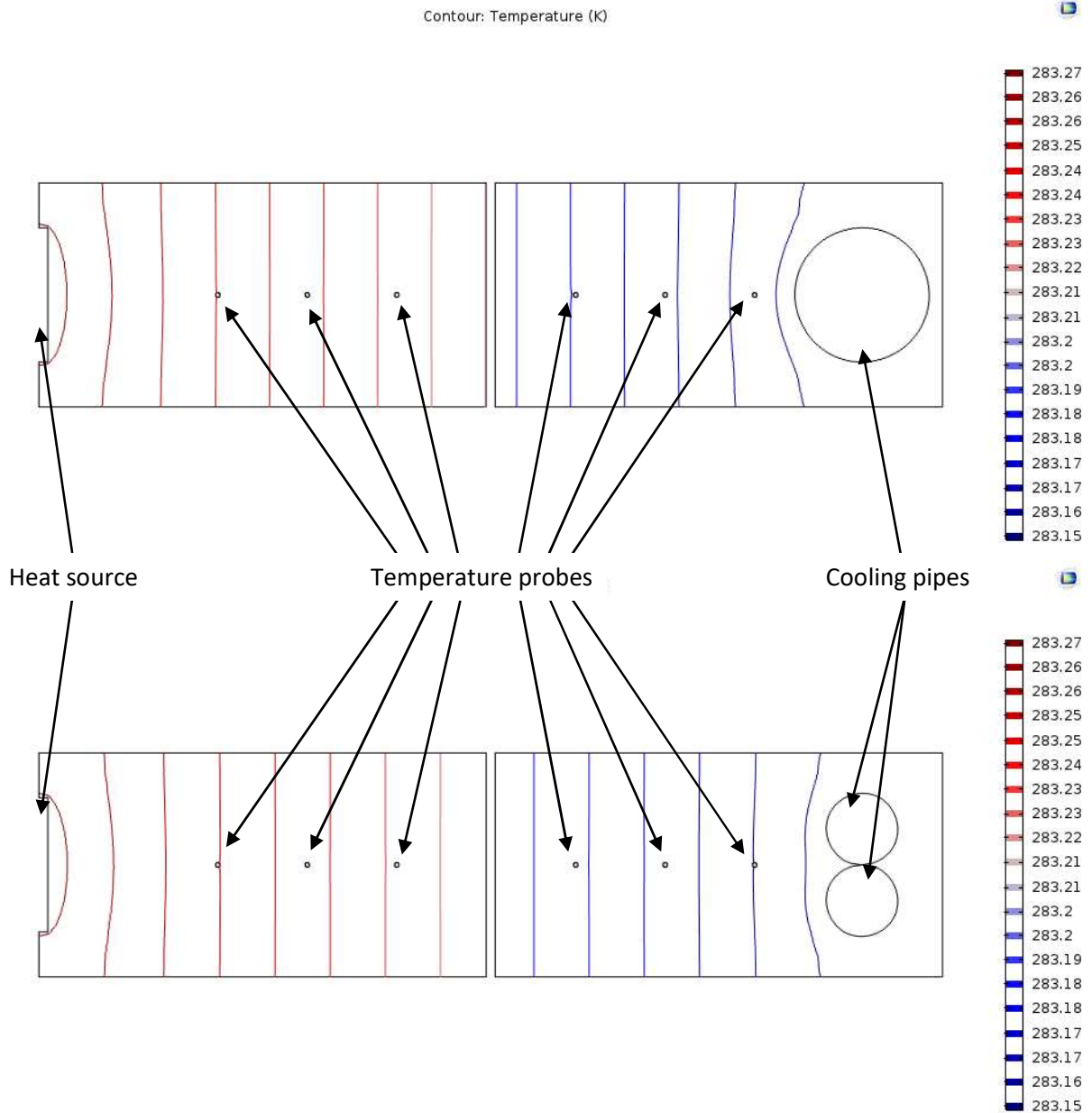


Figure 102 – Difference in temperature profile between one 15 mm cooling pipe (left) and two 7.5 mm cooling pipes (right).

However, once the model was fully assembled and ready to run, an issue became apparent; in order to model thermal transport across a contact interface, COMSOL requires a thermal gap conductance value to be input. This is due to the complexity in calculating the thermal gap conductance between two bodies. As such, the model could not be used to rapidly test a variety of gap conductance scenarios as intended; instead, it was decided to find the values experimentally and

use the model as a check – by inputting the same boundary conditions as used in the experiment and entering the calculated thermal gap conductance value, reverse engineered temperatures from the simulation could be compared to those measured from the experiment. If these agreed, it would signify that the thermal gap conductance had been calculated accurately.

## 5.4 Experimental Calculation of Thermal Gap Conductance Values

To find the gap conductance experimentally, a similar setup to that modelled above was used. However, experimentally it was not possible to mitigate the risk that when significant boundary load was applied the silicon cylinder might be ejected from the experimental apparatus; as such, the system was modified to use just the two copper cylinders as shown in Figure 103 below. One copper cylinder had a groove machined from its surface to allow an Ultramic© ceramic heater to sit below the surface of the cylinder; this would allow significant load to be applied without damaging the heater. The other copper cylinder had a 15 mm diameter hole drilled perpendicular to its length approximately 5 mm from the bottom surface; a 15 mm diameter copper pipe was inserted snugly into this hole such that it extended beyond the cylinder on both sides and was in good thermal contact throughout.

The ceramic heater was connected to a power supply, and the copper pipe was connected to a Hailea HC series chiller unit through the use of a header tank containing 5 L of water and two AllPondSolutions submersible pumps, circulating the water at a fixed temperature of 10 °C and a rate of 600 L/h. A Testometric stress test machine was used to apply the variable boundary loads. The copper cylinders were insulated from the environment by a double layer of aluminium foil, and insulated from the stress test machine by a double layer of PTFE plastic sandwiching a layer of standard fibreglass wool insulation. The temperature was measured at the six equidistant points, three in each cylinder, through the use of type J thermocouples inserted into holes drilled to the centre of the cylinders; each hole was drilled at 120° around the z-axis compared to the hole before it, such that no thermocouple hole infringed on the thermal pathways of any of the others. A schematic representation of the experimental apparatus is shown in Figure 103.

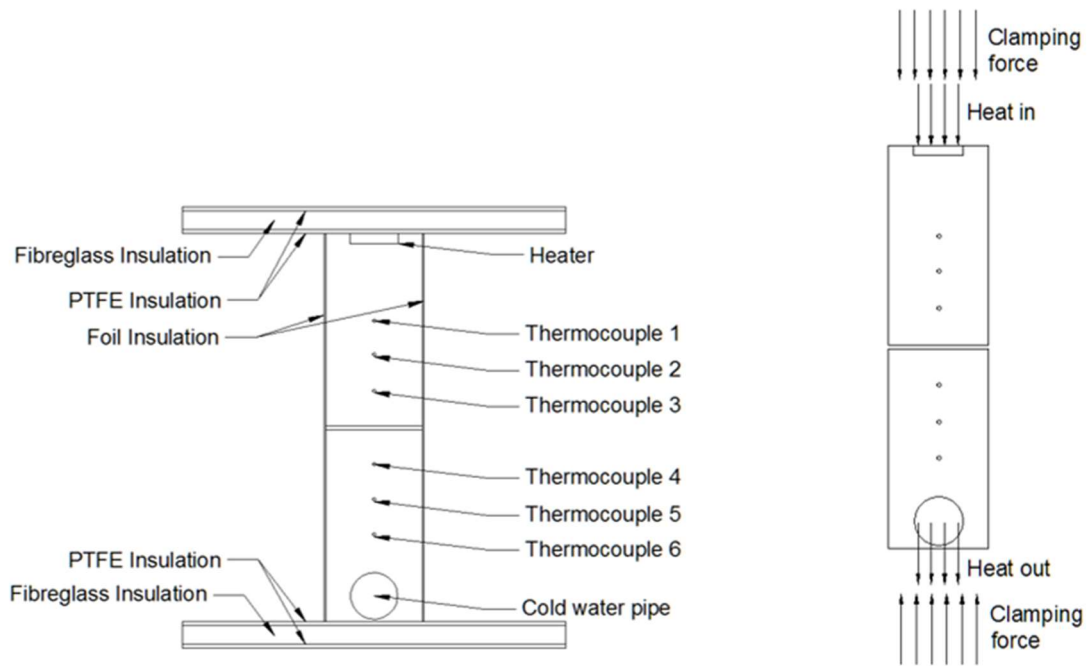


Figure 103 – (Left) Schematic representation of thermal gap conductance experimental apparatus. Coolant loop and power supply not pictured.

(Right) Force diagram of thermal gap conductance experimental apparatus.

The six thermocouples were connected to a data logger, which measured the temperature at a rate of 10 Hz. The system was brought to thermal equilibrium at 283 K, or 10 °C, before the heater was turned on with a power of 30 W. The temperature was logged for 15 minutes, after which the heater was deactivated and the system was allowed to return to a cooled state. Due to the high noise to signal ratio found in thermocouples, the data was plotted as a moving average of 100 values. An example of this data set can be seen in Figure 104 below, corresponding to a 10 N clamping force with no interstitial material. The temperature at each thermocouple was averaged over the last 1,000 readings, or 100 seconds, to find the temperature at this point. These temperatures could be plotted against the position of each thermocouple as shown in Figure 105, and extrapolated to show the temperature throughout the cylinder; this allowed us to ensure no heat was lost to the environment, as a properly insulated system would show linear temperatures within each body. Due to the large number of readings averaged, error values are too small to be visible on the graph.

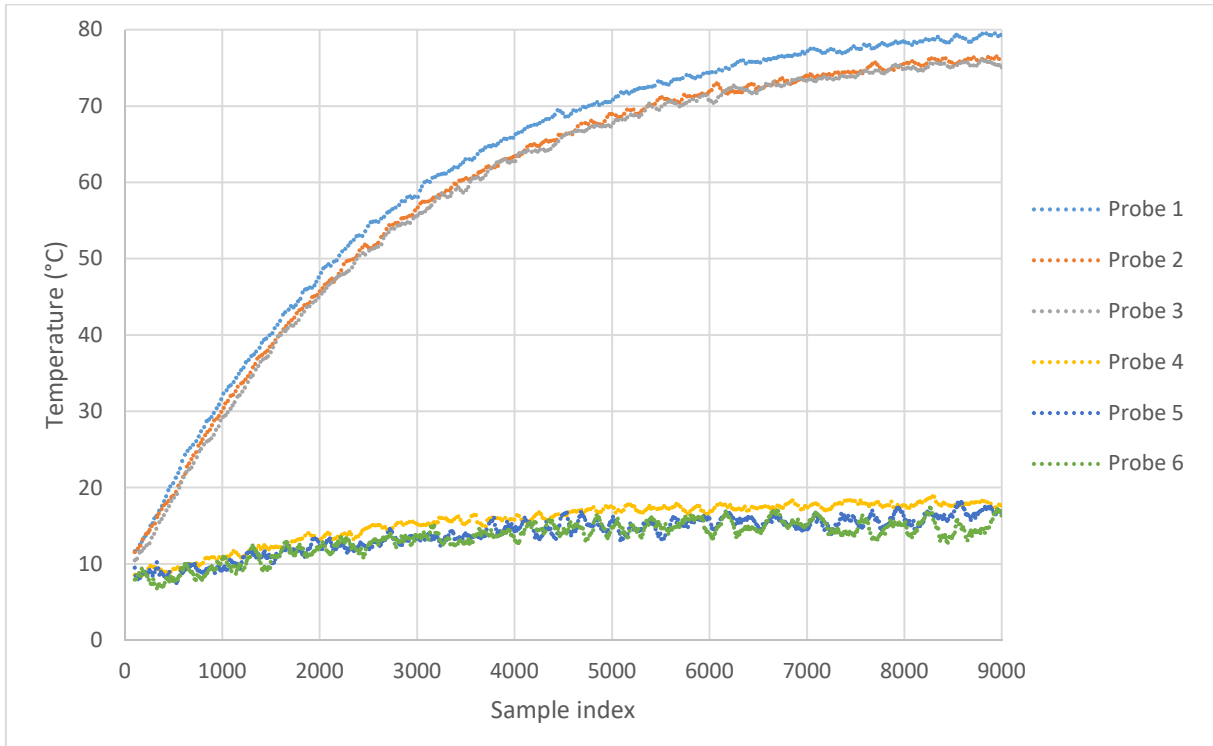


Figure 104 – Experimental data; temperature at each probe point was sampled at a rate of 10 per second. Probes are numbered 1 – 6 moving along the z-axis from the heater to the coolant.

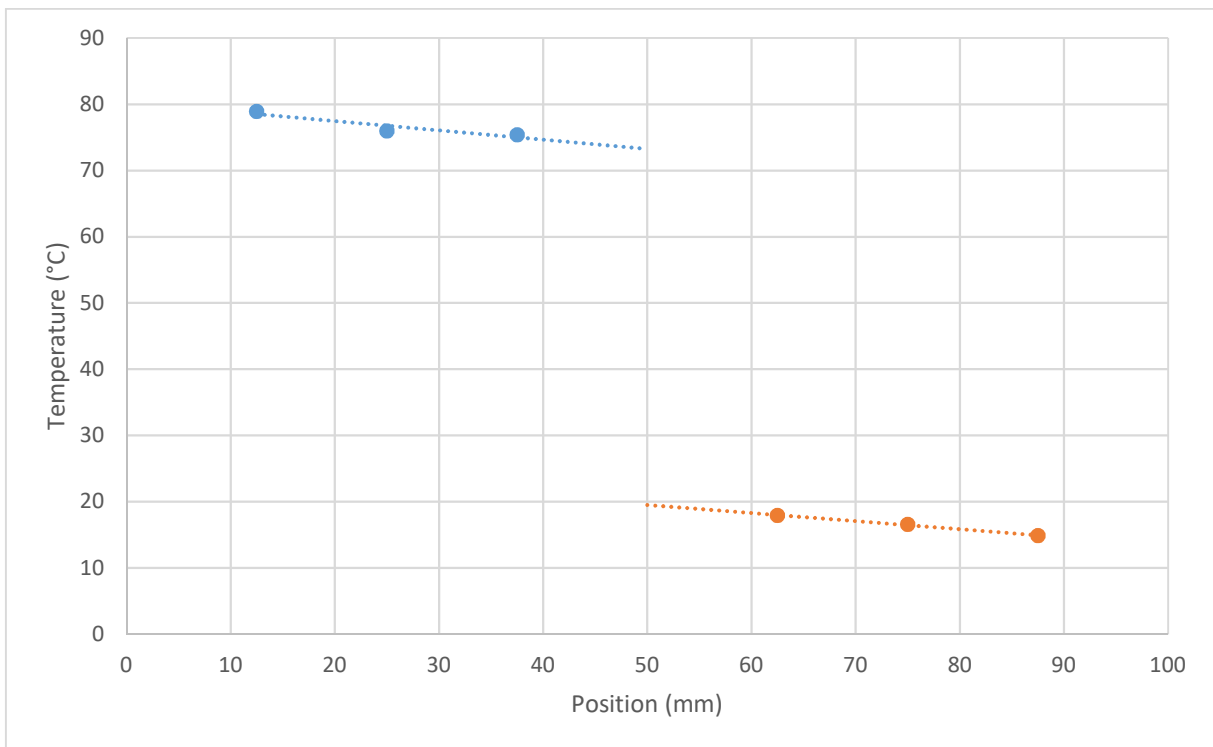


Figure 105 – Experimental data; temperature at each probe point at thermal equilibrium. Interface between two bodies was at 50 mm, visible as the end of each extrapolation.

In both figures the thermal gap is visible; the hot body is significantly hotter than the cold body at the interface. Once this temperature difference was measured, the thermal gap conductance across the interface was calculated using equation 12 as outlined on page 140 in Section 5.2 above. Throughout all of the tests, the cross-sectional area  $A$  of the interface remained the same at  $4.91 \times 10^{-4} \text{ m}^2$ , and the power input into the heater  $q$  remained at 30 W. By putting these values, along with those derived from Figure 105, into equation 12, we find a thermal gap conductivity of  $1.136 \text{ W / K m}^2$ .

The first factor considered was the application of various loads across the interface. To test this, the experimental apparatus was assembled as in Figure 103 and inserted into the stress test machine as shown in Figure 106 below.



*Figure 106 – Thermal gap conductance experimental apparatus. Stress test machine is visible on the right-hand side of the picture, with copper cylinders, heater and coolant pipe in place. Note that the foil insulation has been removed for this image. Header tank with pumps and chiller unit are visible on the left-hand side of the picture.*

The stress test machine was then set to a range of clamping forces: 10 N, 100 N, 1,000 N, and 10,000 N. For each of these clamping forces the experiment was performed as detailed above, and the thermal gap conductance was calculated. The thermal gap conductance as a function of clamping force is shown in Figure 107 below. Again, the high number of readings averaged renders the error too small to be visible on the graph.

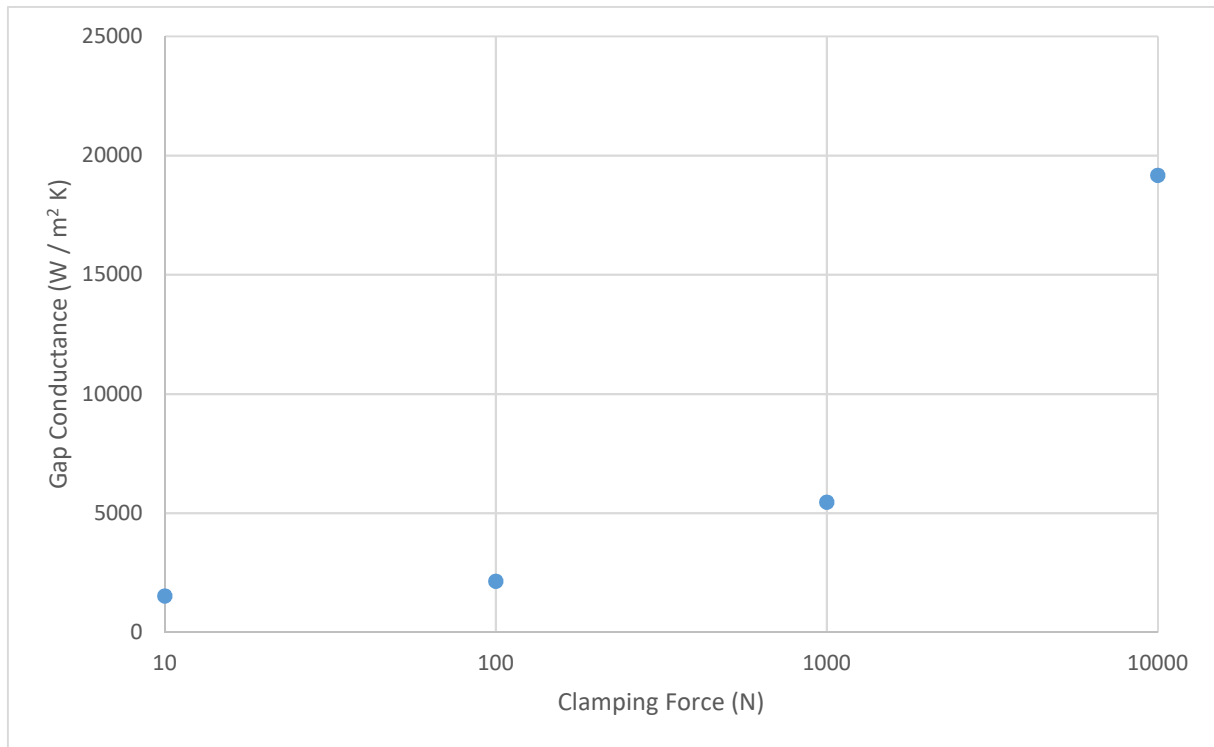


*Figure 107 – Experimental results: thermal gap conductance as a function of logarithmic clamping force with no interstitial material.*

From Figure 107 it is apparent that clamping force increases thermal gap conductance proportionally, as suggested by the literature. Having confirmed this, the next aspect to explore was the usage of an IM to improve the thermal gap conductance. The IMs selected, and the rationale behind the selections, are given in Table 2 below. Each interstitial material was tested at each of the clamping pressures described above, the results of which are shown in Figure 108 below; once again, the high number of experimental readings averaged results in an error value too low to be visible on the graph.

Table 2 – Details of interstitial materials tested for effect on gap conductance and reason material was chosen for testing.

Interstitial Material	Reason for testing
<b>Indium Foil (50 <math>\mu\text{m}</math>, 250 <math>\mu\text{m}</math>, 500 <math>\mu\text{m}</math>)</b>	Indium foil is widely used in cryogenic applications due to its high malleability at low temperatures. Many synchrotrons make efforts to use thin indium foils, as indium is a poor thermal conductor; therefore multiple thicknesses were tested to look for a trend.
<b>Indium Corporation Heat-Spring<sup>®</sup> (100 <math>\mu\text{m}</math>)</b>	A new product recently developed by the Indium Corporation, the Heat-Spring is a piece of indium foil with a regular pattern embossed in both surfaces in order to better distribute thermal contact points. This material was tested to verify its performance against conventional indium foils.
<b>Copper Foam (4 mm, 63% porosity)</b>	Copper foam is a sponge-like piece of copper created by bubbling inert gases, in this case argon, through molten copper. The porous structure should increase malleability without compromising the conductivity of the copper by an excessive amount. This material was tested to see if a high conductivity, reasonably malleable material would be better than a high malleability insulator.

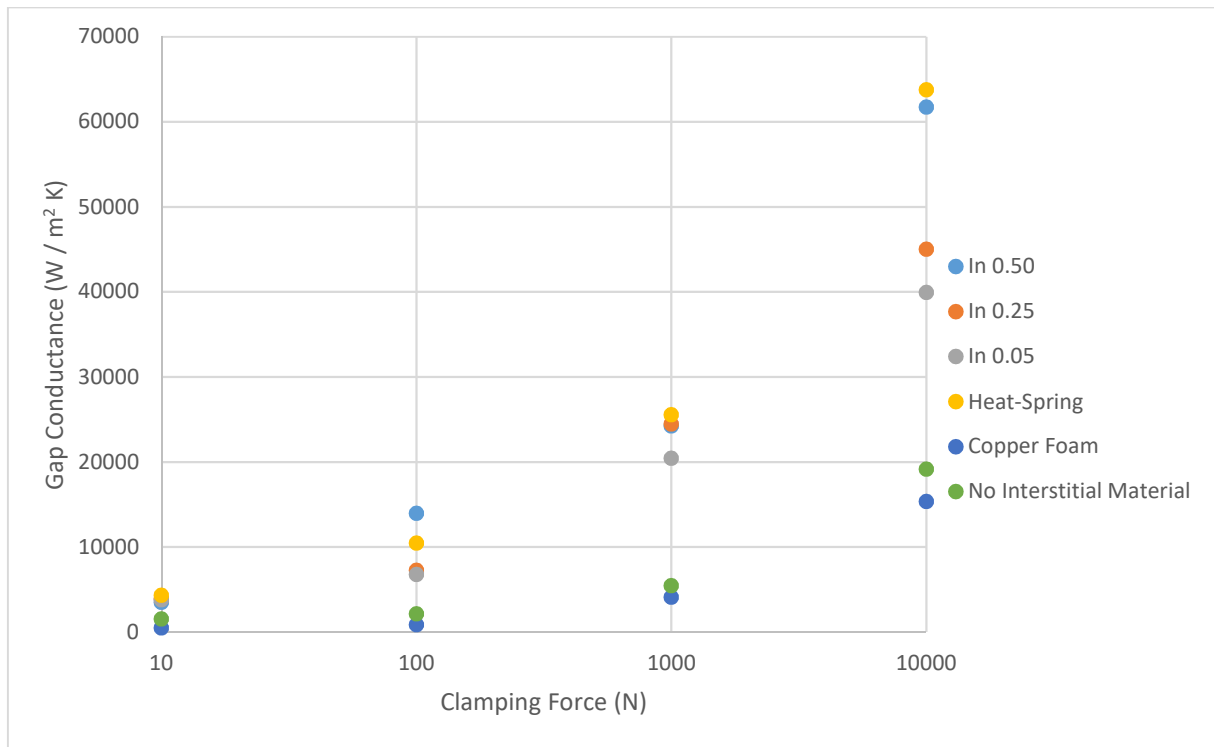


Figure 108 – Experimental results: thermal gap conductance as a function of logarithmic clamping force for various interstitial materials.

It is immediately apparent that indium foil improves the thermal gap conductance by a significant degree; the least effective indium foil, the 500 μm thickness, shows a marked improvement over the tests with no interstitial material – this trend is noted in the other three indium materials as well, with the 250 μm thickness improving the thermal gap conductance when compared to both the 50 μm and 500 μm thickness foils. The behaviour of the Heat-Spring material is of particular interest; despite its middling thickness when compared to the other indium foils, it significantly outperforms them in every test. The copper foam, however, performs worse than tests performed with no IM whatsoever.

The last factor tested was the re-use of IMs. At the I20 beamline, and indeed most beamlines at DLS, each piece of indium foil is used in only one assembly; once the assembly has been disassembled, the indium foil is discarded and a new piece is used. To identify whether this precaution was necessary, a series of tests were performed re-using indium foils; first, a piece of 500 μm indium foil

was tested at each of the clamping forces described above, then removed from the apparatus. The indium foil was removed, then realigned using striations imprinted from the copper cylinders before being tested again. The results of this test are given on Figure 109 below; again, error was too small to be visible on the graph. The pre-stressed indium foil has an increased thermal gap conductance when compared to a new piece of indium foil; this is due to the foil deforming to fit the faces of the two copper cylinders, improving the thermal contact.

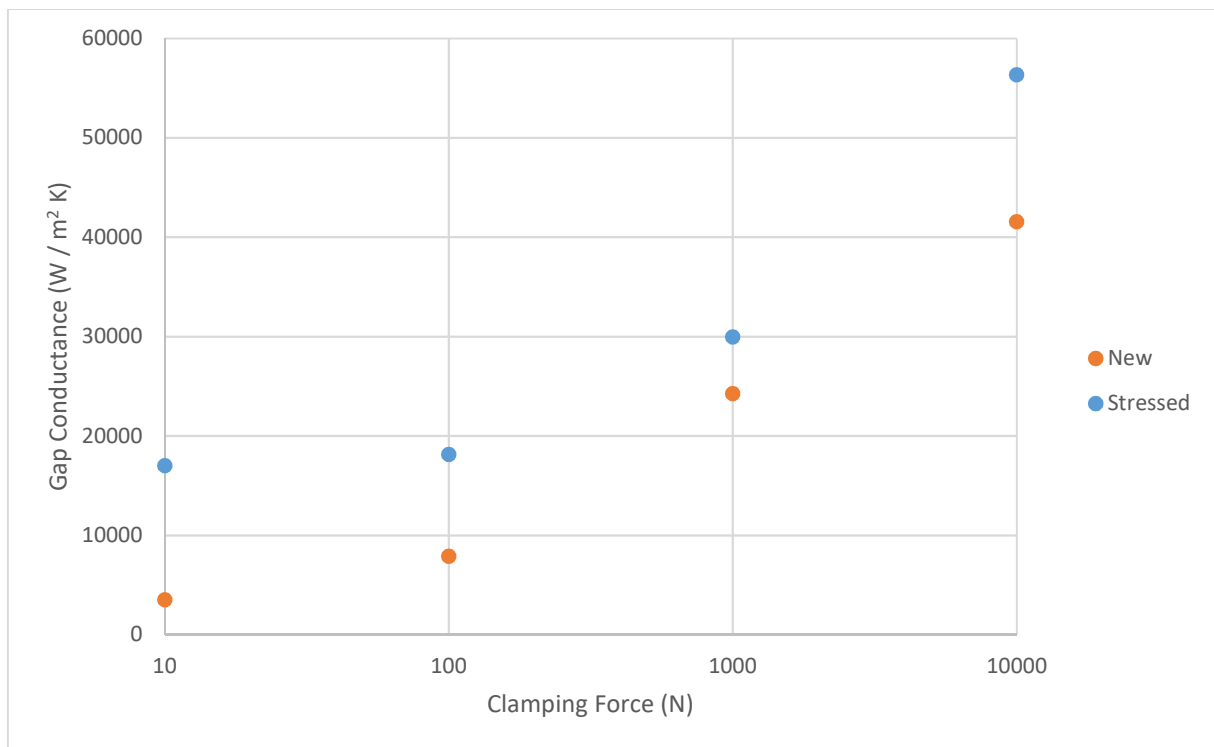


Figure 109 – Experimental results: thermal gap conductance as a function of clamping force for a new and pre-stressed piece of 500  $\mu\text{m}$  indium foil.

The previous pre-stressed IM tests represent a best-case scenario, one in which the IM remained well aligned with its previous position, preventing elastic deformation from having significant impact on the gap conductance. To test the worst-case scenario, a new piece of 500  $\mu\text{m}$  indium foil was tested at each pressure before the assembly was removed from the stress-test machine. The assembly was disassembled, and the indium foil was removed. In this test, the foil was then rotated 90 ° before the apparatus was reassembled and the tests were repeated. The results are shown in

Figure 110 below; due to the large number of data points averaged, the error is too small to be visible. In this test, both the new and the rotated foil are shown to behave in similar ways at 10 N and at 100 N. At 1,000 N, the rotated foil shows an improvement over the new foil, while at 10 000 N, the new foil shows a higher thermal gap conductance than the rotated foil. It seems the rotated foil may have been somewhat 'loosened' by its prior testing, allowing it to deform to match the copper to a greater degree at lower clamping forces; however, once the plastic deformation region was reached, the new foil was able to match the copper surfaces better, resulting in a higher thermal gap conductance.

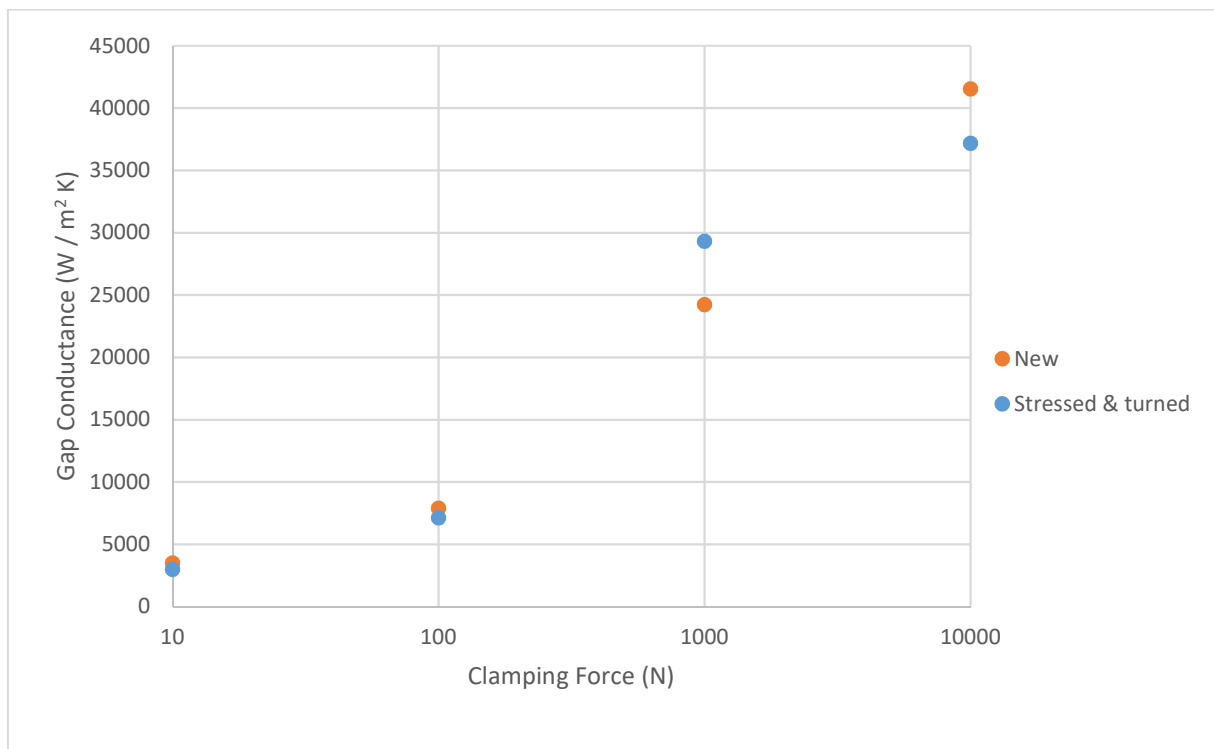
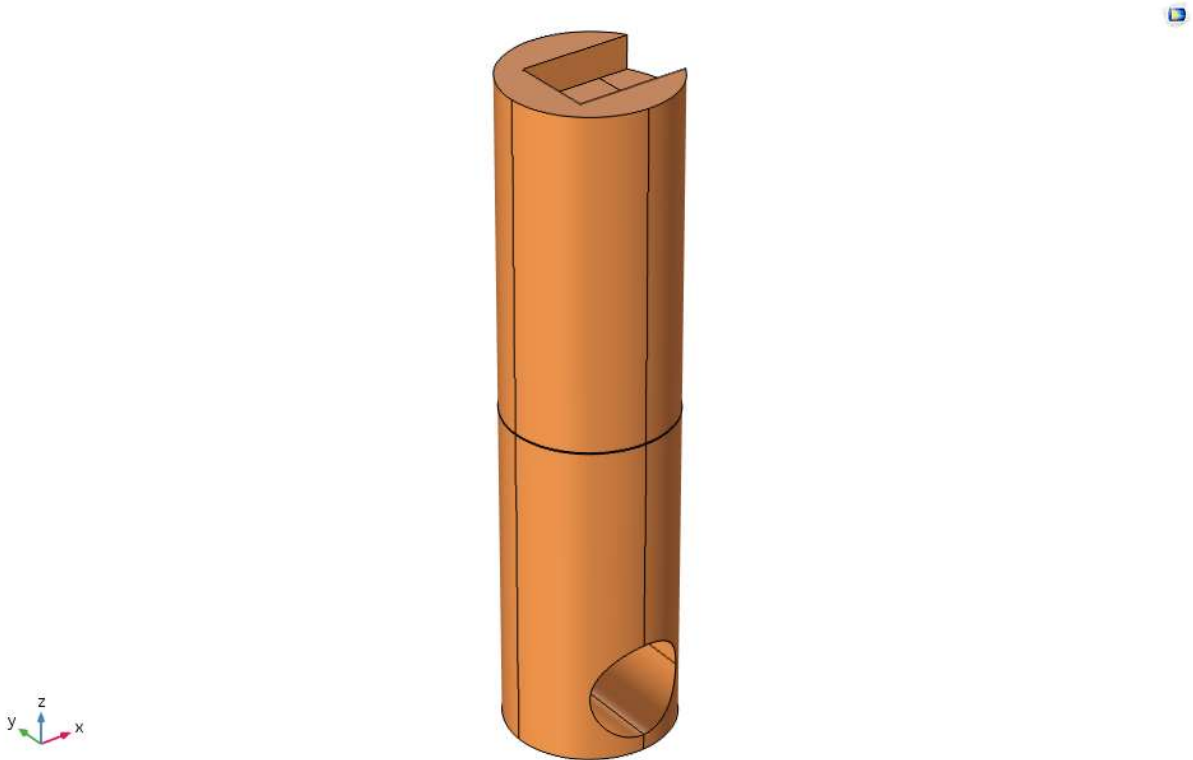


Figure 110 – Experimental results: thermal gap conductance as a function of clamping force for a new and pre-stressed piece of 500  $\mu\text{m}$  indium foil rotated 90  $^\circ$ .

## 5.5 Comparing the Results of the Theoretical Models with Experimental Results

To validate the above results, the experiment was replicated in COMSOL as shown in Figure 111 below. For brevity, the same example experiment has been modelled as shown in Section 5.4 above. Using known material properties, and duplicating boundary conditions from the experiment as shown in Figure 112 (mechanical) and Figure 113 (thermal), the calculated thermal gap conductance of  $1\,136\text{ W / m}^2\text{ K}$  was modelled and the temperature calculated throughout the system. A surface plot of the temperature across the two cylinders is shown in Figure 114 and a plot of temperature against z-position is shown in Figure 115.



*Figure 111 – Model of paired copper cylinders used in thermal gap conductance experiment; recess for heater at top of hot body and machined hole for coolant pipe at bottom of cold body.*

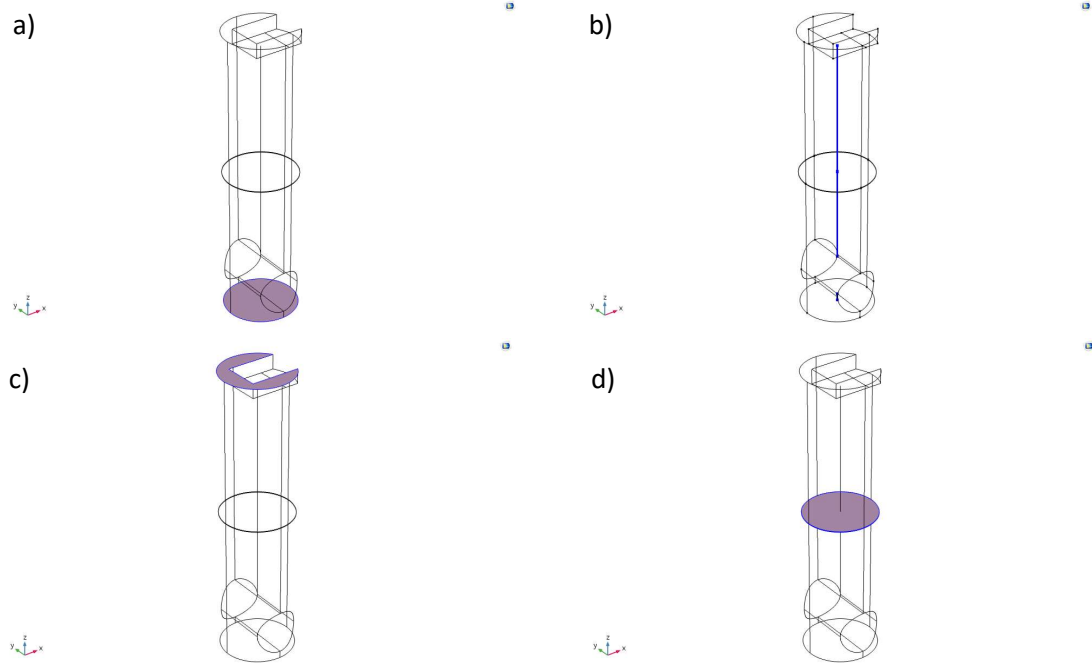


Figure 112 – Mechanical boundary conditions for paired copper cylinders: a) bottom surface of cold body is held fully constrained; b) common z-axis held restrained in x- and y-directions; c) boundary load of 10 N in  $-z$  direction applied to top surface of hot body; d) paired faces in mechanical contact.

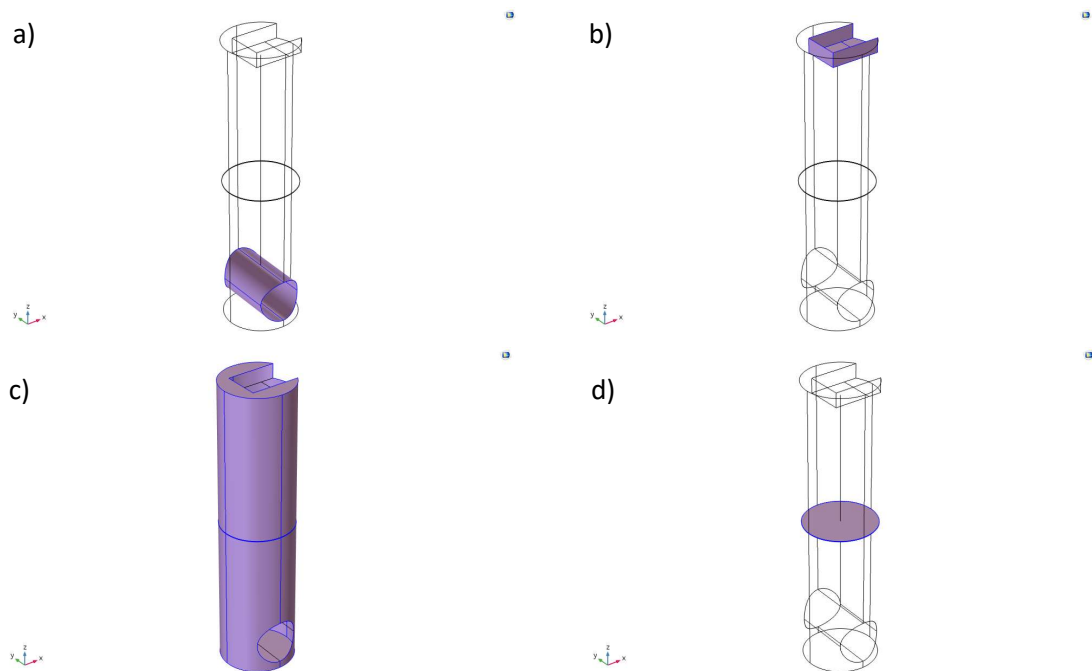


Figure 113 – Thermal boundary conditions for paired copper cylinders: a) internal surfaces of coolant pipe in cold body held at 13 °C; b) internal surfaces of heater recess in hot body subject to boundary heat source of 30 W; c) all external faces maintained as perfect insulators; d) paired faces in thermal contact with gap conductance of 1 136 W / m<sup>2</sup> K.

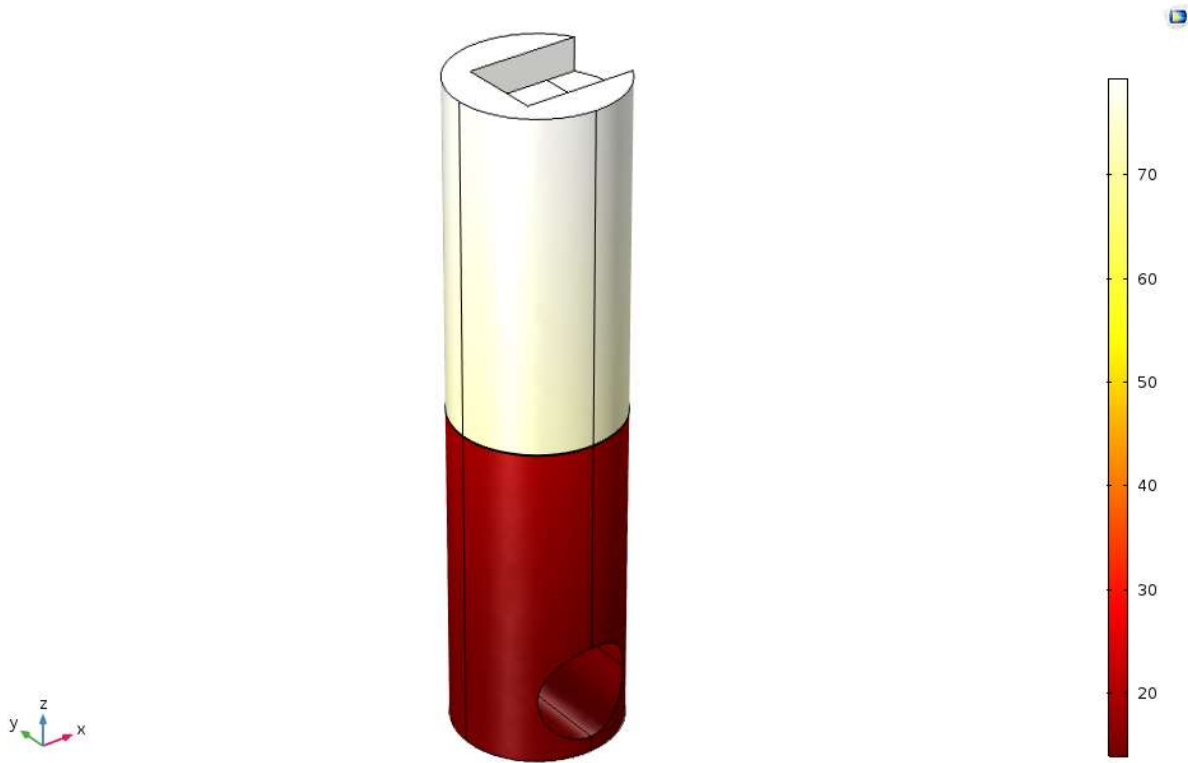


Figure 114 – Temperature surface plot of paired copper cylinders at thermal equilibrium.

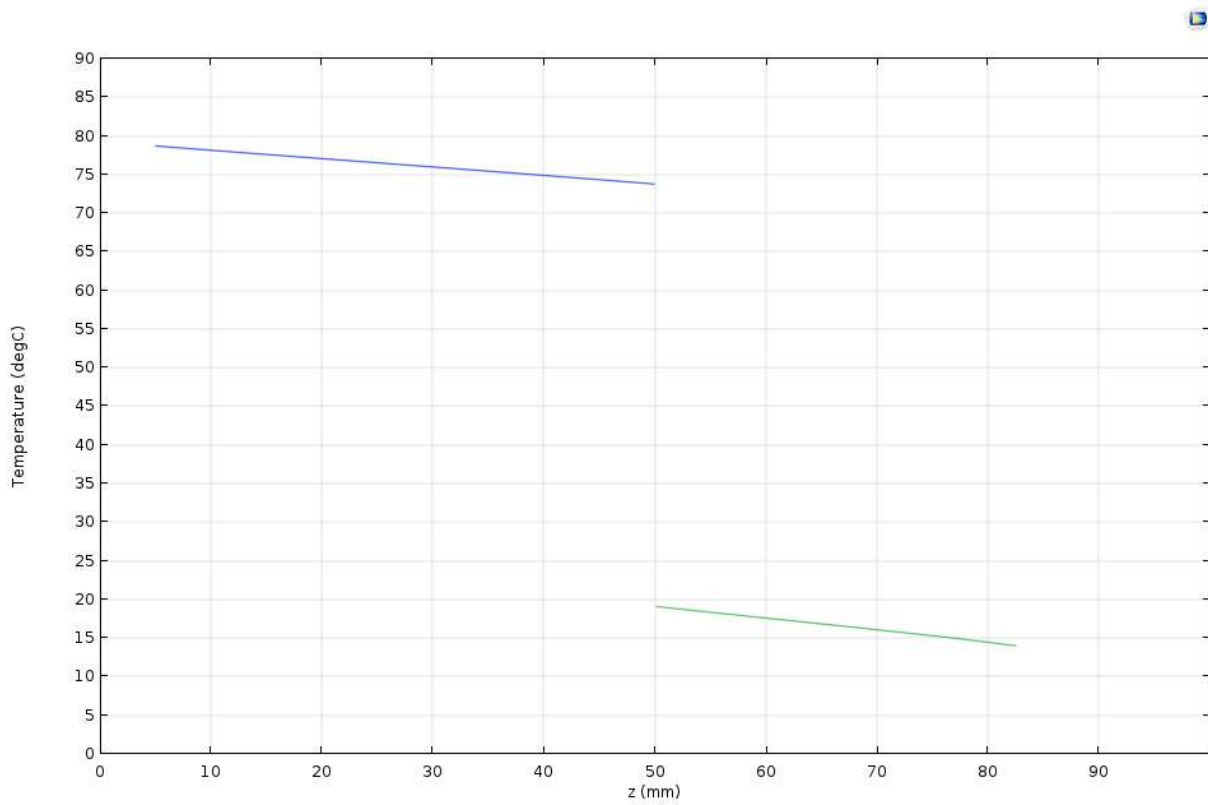


Figure 115 – Calculated temperature throughout paired copper cylinders at thermal equilibrium.

The temperatures found in the model are a very good match for those observed in the experiments, as shown in Figure 116; this provides confidence that our experimental method was accurate and our calculations correct. The trends also match, with the temperature gradients seen in Figure 115 matching those in Figure 105, and the temperature gap observed from the simulation lying well within experimental error bounds. Taken altogether, this validates the experimental method used in this work and gives confidence in the calculated thermal gap conductance values.

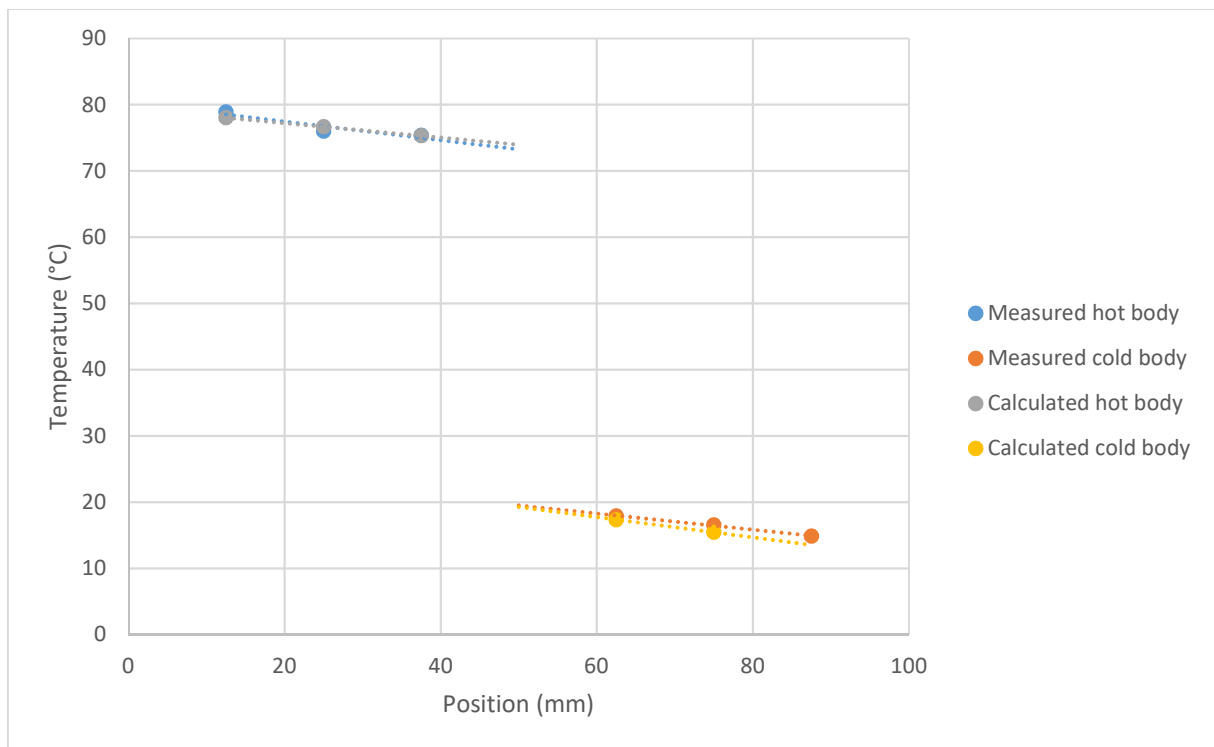


Figure 116 – Measured and calculated temperatures throughout paired copper cylinders at thermal equilibrium.

## 5.6 Conclusion

The highly dependent nature of thermal gap conductance means that if a study has not been performed on the exact circumstances required, the body of research is of very limited use. The main focus of this work was to identify how mixed factors could impact the thermal gap conductance, where previous studies have picked one factor to compare. As such, the function of interstitial materials as a function of force is the primary output; with further work, more factors would be included such as surface preparation to modify the microscale surface roughness of the contacting surfaces, as well as a variation of the hot- and cold-body materials.

Due to the difficulty in calculating thermal gap conductance, it was decided to find the value of the thermal gap conductance for various scenarios experimentally and confirm them using a COMSOL model. The thermal gap conductance is difficult to determine due to the sheer quantity of variables that factor into it, including microscale roughness, microhardness, asperity size and slope profile, but is easily measured using input power, temperature and cross-sectional area.

Due to the highly dependent nature of the thermal gap conductance to the specific situation, the exact values measured in this work are not of eminent use unless working with two copper contacts of similar preparation, size and temperature. However, what is translatable to other systems is the trends visible in the data gathered, and the relative performance of the interstitial materials relative to one another. In this regard, the tests have proved that the Heat-Spring indium material is a superior material, and that higher clamping forces correlate directly to a higher thermal gap conductance. In addition, a trend emerges in the plain indium foils; the 100  $\mu\text{m}$  foil outperformed both the 50  $\mu\text{m}$  and the 500  $\mu\text{m}$  foil. This indicates that while a thicker foil works to some extent, at some point the thickness of the foil becomes a drawback and negatively impacts the thermal gap conductance. This is likely due to macroscopic physical constraints: with a very thin foil, tension in

the material can in effect reduce the surface malleability by limiting the degree to which the foil can bend; at the other extreme, once the foil becomes thick enough its poor conductivity begins to reduce the performance beyond the benefit imparted by a high malleability. Another result was that the copper foam did not perform well at all, despite its conductivity exceeding that of any other material tested. This indicates that the malleability of the material is more important than its conductivity. Furthermore, it has been observed that within the regime used in synchrotron facilities indium foil gives a higher thermal gap conductance after it has been subjected to high load clamping forces, and can be used repeatedly without losing performance.

The measured thermal gap conductance was verified through the use of a COMSOL model; by duplicating the boundary conditions used in the experiment and introducing the measured gap conductance between the two bodies, the simulated temperatures could be compared against the temperatures measured in the experiments. As the two temperature profiles showed a good match it supported the experimentally measured thermal gap conductance values to a great degree of confidence.

### [Executive Summary of Chapter 5](#)

The major trend noted was that a higher clamping force results in a much higher thermal gap conductance. However, this is not necessarily beneficial in the field of synchrotron monochromator assemblies, as excessive clamping force results in mechanical deformation of the diffracting surface.

The use of an IM can improve the thermal gap conductance to an order of magnitude higher than that achieved by increasing the clamping pressure by an order of magnitude. This indicates that the use of a suitable IM can by far improve the thermal performance of a system.

Of the IMs tested, the best results were those from the use of the indium Heat-Spring material; this design outperformed all of the plain indium foils, including those thicker and thinner than itself.

Re-use of IM has been shown to be viable and, within the regime used in crystal assembly systems, beneficial when compared to the use of new IMs.

For the novel design presented as the culmination of this work, two approaches will be considered: a more uniform clamping force to reduce the deformation, either instead of or in addition to the use of the Heat-Spring material.

## 6. Utilising an Interference Fit as a Clamping and Cooling System

### Review of the Thesis up to Chapter 6

The Literature Review showed a lack of research into the underlying causes of deformation in first crystals; most literature focuses on mitigating deformation. Growing need for increased beam powers and more beamlines requires a redesign of monochromator first crystals to have a smaller footprint and be able to dissipate more heat.

Chapter 2, Examining Thermal Transport through the use of Theoretical Models, showed that FEA modelling is suitable to simulate monochromator crystals. Three contrasting sets of material properties cause excessive stresses in the crystal assembly before the beam is incident, degrading the diffracted beam. This is a major factor and will need to be addressed in the novel design presented in this work.

Chapter 3, Exploring Various Crystal Geometries and Heat Exchange Locations, showed that side-cooling the crystal is inefficient, causing a more deformed diffracting surface. Instead, introducing space between the cooled area and the diffracting surface allows thermal pathways to become more uniform. Crystal geometry is less important than cooling location.

Chapter 4, Investigating the Differing Benefits to Direct and Indirect Cooling, found that benefits of direct cooling do not outweigh the drawbacks; it has been decided to use indirect cooling in the novel crystal design presented in this work to minimise both thermal and structural deformation.

Chapter 5, Examining the Effect of Varying Factors on Thermal Gap Conductance, has found that the use of an IM increases the thermal gap conductance by improving thermal contact between the crystal and the heat exchanger. In addition, the re-use of such IMs improves their performance. It has been decided that the novel, interference fit design presented in this work will make use of a repeatable thermal contact system with high enough clamping force to treat the inner layer of the heat exchanger as an IM.

## 6.1 Introduction

Chapter 5 above has shown that the use of sufficient clamping loads can cause IMs to deform to give a very high thermal gap conductance, and that while the controlling factor in the performance of an IM is its malleability the conductivity also plays a factor. As an alternate approach to the use of IMs, by providing a high intensity, uniform clamping force uniformly around the crystal a very good thermal contact could be formed directly between the crystal and the heat exchanger, using the inner layer of the copper itself as an IM. In order to create this high intensity, highly uniform clamping force, it has been decided to test an interference fit.

An interference fit is the name given to a clamping force caused by two materials attempting to occupy the same space. This is often used in automobile manufacture, in which an interference fit can be caused either through heat or by the use of high amounts of force. The two components to be fitted are referred to as the hub and the shaft. The hub will have a hollow region normally slightly too small to accommodate the shaft. In a thermal interference fit, the hub is heated so that its internal radius expands; while expanded the hub is placed over the end of the shaft. As the hub cools, it shrinks, and comes into contact with the shaft. When the hub cools to such an extent that it would otherwise be too small for the shaft, it begins to exert a considerable stress on the shaft. This stress can be used as a high intensity, very high uniformity clamping force, holding the hub securely to the shaft as shown in Figure 117.

By making the clamping force more uniform the mechanical deformation caused in the clamped object also becomes more uniform; if the clamped body is subjected to a non-uniform clamping force, the regions under greater stress will deform more than those under less stress. A uniform radial clamping force normalises the deformation, making it more uniform and improving the deformation variance on non-clamped surfaces. If the stress field is sufficiently uniform, and the clamped body

sufficiently unconstrained, the clamped body can deform in a uniform fashion; as the entirety of the clamped body is compressed radially it can expand linearly in the perpendicular direction by extruding uniformly from a non-clamped face. This uniform deformation, while likely higher than that observed in a more gently clamped system, minimises the deformation variance and can be used to create a more collimated, more monochromatic diffracted beam.

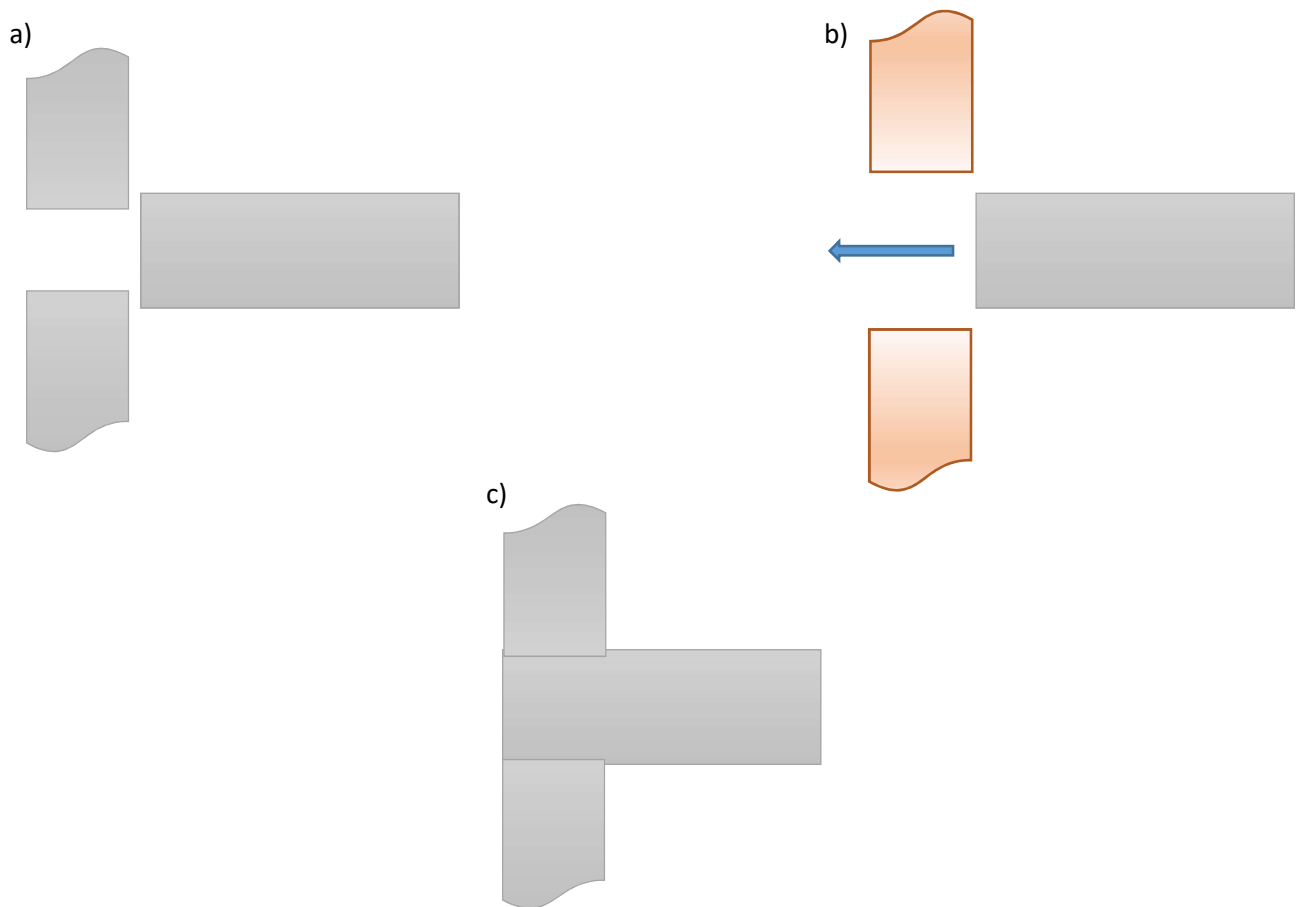


*Figure 117 – Thermal interference fit; a) both components cold, shaft cannot fit in hub; b) hub heated up, shaft pushed into place; c) after hub has cooled, strong grip on shaft.*

The description of a standard interference fit given above is the most common method, usually using two like materials such as the axle and wheel of a car, both made of steel. In monochromator assemblies disparate materials are used; one crystalline, in order to make use of Bragg diffraction, and one metallic, in order to make use of the superior machinability and thermal properties. In this

case the monochromator crystal will be made of single-crystal silicon and the heat exchanger of oxygen-free copper, as is the norm at DLS. Silicon and copper have very disparate material properties, as established in Section 2.5 above. In this case, manufacturing the two components such that the internal radius of the copper heat exchanger is smaller than the external radius of the silicon crystal would result in such high clamping pressures at cryogenic temperatures that one or both components would be destroyed, due to copper exhibiting a CTE an order of magnitude higher than that of silicon. However, by manufacturing a cylindrical silicon crystal to take the place of a shaft, and a tubular copper heat exchanger to take the place of the hub, such that the two are a slide fit at room temperature the disparate CTEs will result in an interference fit at cryogenic temperatures.

An interference fit design has another benefit over conventional designs: as the copper shrinks it will grip onto the silicon, removing the need for a separate clamping component such as the steel rods present in the conventional I20 crystal assembly. These clamping components are a significant cause of deformation variance, as they introduce a non-uniform element into the design. As such, removing them will reduce the deformation variance, improving the monochromaticity and collimation of a diffracted x-ray beam.

In addition, the clamping force imparted by the interference fit is set by the gap between the components at room temperature. This allows the magnitude of this clamping force to be set by modifying the internal radius of the tubular heat exchanger.

## 6.2 Modelling of an Interference Fit

The silicon crystal was first defined as a cylinder of radius 12.5 mm and length 50 mm, and the copper heat exchanger as a tube of length 40 mm and wall thickness 5 mm. The reduced length of the heat exchanger compared to the crystal was designed to take into account the displaced cooling surface suggested in Chapter 3, allowing 5 mm of the silicon crystal to protrude from either end of the heat exchanger. In order to identify the magnitude of the gap to be left between the silicon crystal and the copper heat exchanger at room temperature equation 13, the equation for pressure caused by an interference fit, was used to model the pressure induced by a gap of 0  $\mu\text{m}$  to a gap of 100  $\mu\text{m}$  as each model was cooled from 300 K to 80 K. This produced Figure 118, a three-dimensional graph of pressure as a function of room temperature gap and temperature.

$$P = \frac{d_{so} - d_{ho} + \Delta T(k_s - k_h)d_{hi}}{\frac{d_{hi}}{E_h} * \left( \frac{d_{ho}^2 + d_{hi}^2}{d_{ho}^2 - d_{hi}^2} + \nu_h \right) + \frac{d_{so}}{E_s} * \left( \frac{d_{so}^2 + d_{si}^2}{d_{so}^2 - d_{si}^2} - \nu_s \right)} \quad [13]$$

Where  $P$  is the pressure caused by the interference fit.

$d_{hi}$ ,  $d_{ho}$ ,  $d_{si}$  and  $d_{so}$  are the inner and outer diameters of the hub and shaft respectively.

$\Delta T$  is the change in temperature.

$k_h$  and  $k_s$  are the coefficients of thermal expansion of the hub and shaft respectively.

$E_h$  and  $E_s$  are the Young's modulus of the hub and shaft respectively.

$\nu_h$  and  $\nu_s$  are the Poisson's ratio of the hub and shaft respectively.

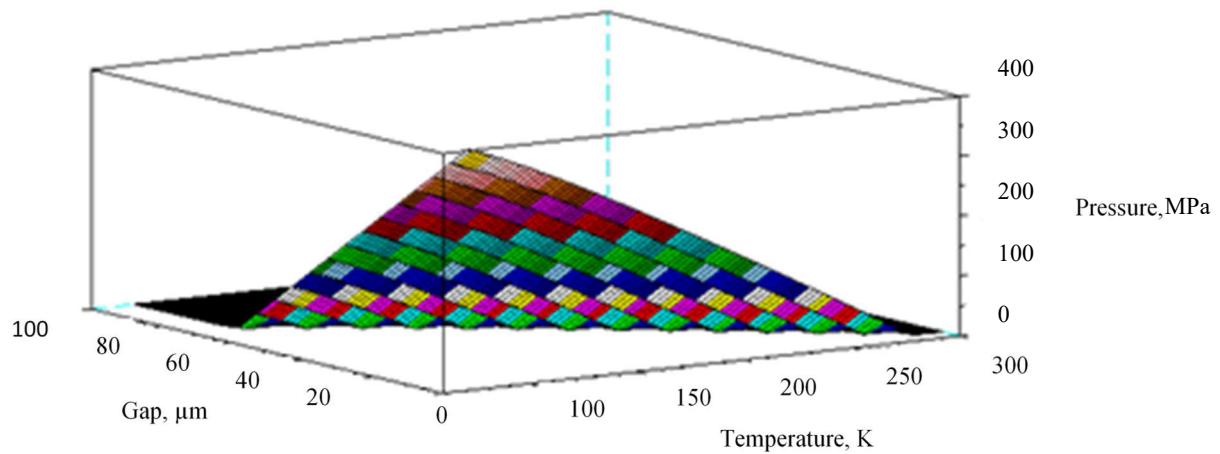


*Figure 118 – Pressure caused by interference fit as a function of room-temperature gap and current temperature.*

By considering the ultimate compressive stresses of silicon and copper, respectively 700 MPa (Petersen, 1982) and 358 MPa (National Institute of Standards and Technology (NIST), 1992), it was observed that in cases of significant pressure the copper would fail before the silicon, protecting the crystal. Due to the desire for a flat diffracting surface, it was decided the limiting factor for interference fit pressure would be such that the force of linear expansion, calculable using equation 14 below, became equal to the clamping pressure. Provided the linear expansion force exceeds that of the clamping force normal, the crystal would be able to extrude linearly from the heat exchanger; should the clamping force exceed the expansion force, the sides of the crystal would be held constrained while the centre was relatively free, causing a significant deformation variance. Solving equation 13 and equation 14 together give a desired room temperature gap of 30 μm.

$$F = kYA\Delta T \quad [14]$$

Where  $F$  is the force produced by the linear extension.

$k$  is the coefficient of thermal expansion.

$Y$  is the Young's modulus.

$A$  is the cross-sectional area.

$\Delta T$  is the change in temperature.

To verify the values calculated above, the novel design, hereafter referred to as the 'interference' assembly, was modelled in COMSOL as shown in Figure 119. The crystal is modelled as a silicon cylinder, with a radius of 12.5 mm and a length of 50 mm. The heat exchanger is modelled as a copper tube, with an internal radius of 12.53 mm, an external radius of 17.53 mm, and a length of 40 mm such that 5 mm of the crystal extrudes from each end. The heat exchanger is modelled as hollow with 1 mm walls and 1.5 mm radius holes to represent coolant inflow and outflow.

A point at the centre of the rear face of the crystal is held constrained, and the rear surface of the heat exchanger is prevented from moving in the z-direction. A line running through the z-axis is held in the x- and y-directions to prevent rotation. The crystal and sleeve are in mechanical contact. These mechanical boundary conditions are shown in Figure 120.

The inner faces of the heat exchanger are held at 80 K to simulate contact with liquid nitrogen. All external faces are modelled as radiating to an environment at 80 K. The crystal and sleeve are in thermal contact. These thermal boundary conditions are shown in Figure 121.

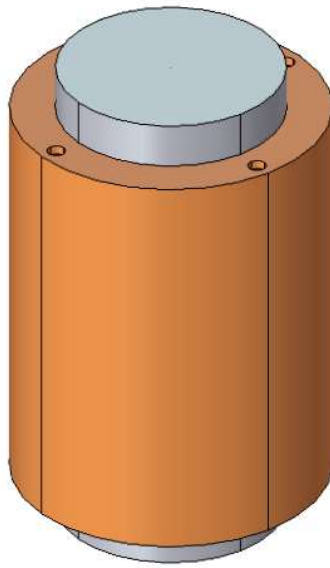


Figure 119 – Model of ‘interference’ assembly; 30 µm gap between sleeve and crystal, sleeve hollow to function as heat exchanger..

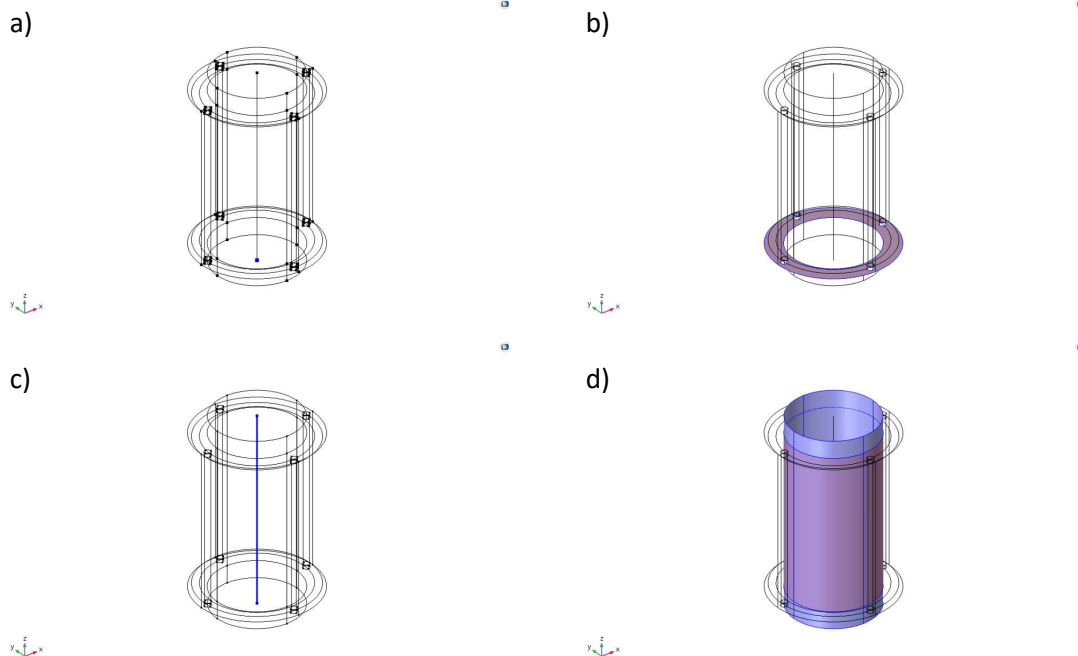
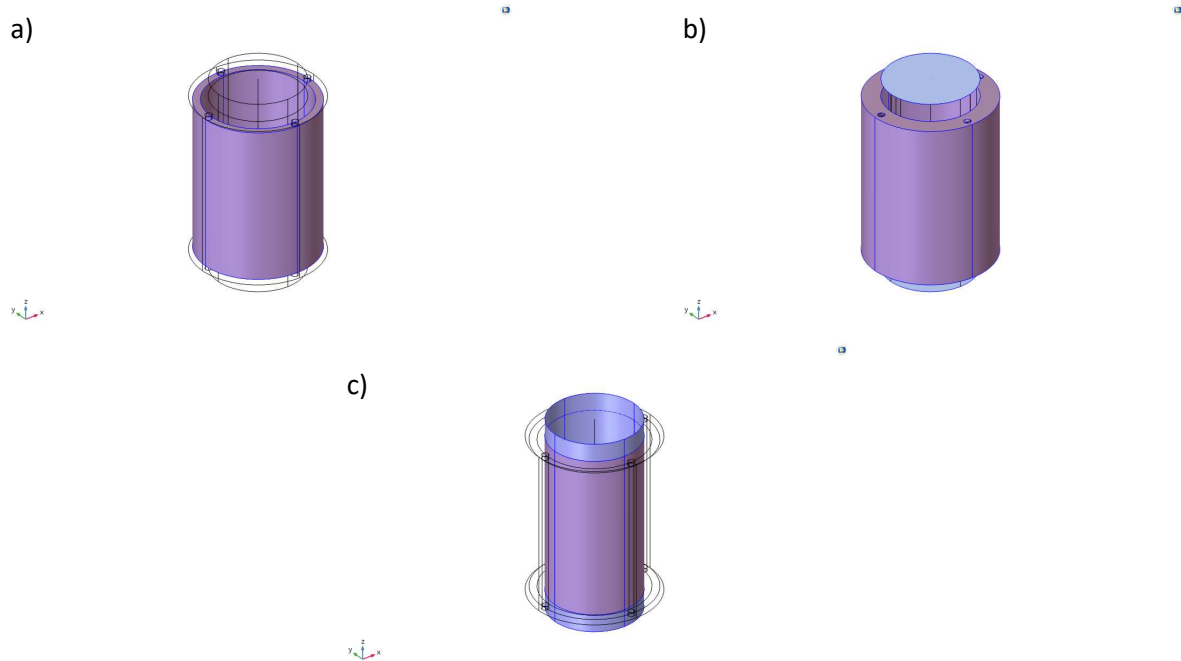


Figure 120 – Mechanical boundary conditions for ‘interference’ assembly: a) point at bottom of crystal is held fully constrained; b) bottom surface of heat exchanger is held restrained in z-direction; c) common z-axis held restrained in x- and y-directions; d) paired faces in mechanical contact.



*Figure 121 – Thermal boundary conditions for ‘interference’ assembly: a) internal surfaces of heat exchanger held at 80 K; b) all external faces radiating to 80 K environment; c) paired faces in thermal contact.*

A surface temperature plot is shown in Figure 122, and the deformation of the diffracting surface is shown in Figure 124. Due to the only temperature difference being a slight difference between the crystal and the heat exchanger all of the isothermal layers lie in this region. As such, the isothermal layer plot has been omitted here. From Figure 122 it is apparent that the two bodies have come into contact, as otherwise the crystal would not reach the same temperature as the heat exchanger. This indicates that as hypothesised the copper has shrunk more than the silicon, moving into its space. Figure 124 shows a very small deformation variance in the diffracting surface of only 1  $\mu\text{m}$ , with the entirety of the surface displaced approximately 5.2  $\mu\text{m}$  compared to its room temperature location. In solely thermal systems the silicon would have shrunk a greater distance than this, indicating the Young expansion has taken place in a majority linear fashion. For comparison purposes, the temperature plot of the conventional I20 first crystal assembly, as modelled in Section 2.6, has been included as Figure 123 and the diffracting surface as Figure 125, showing a diffracting surface deformation variance of 17  $\mu\text{m}$ , an order of magnitude greater than that shown in Figure 124.

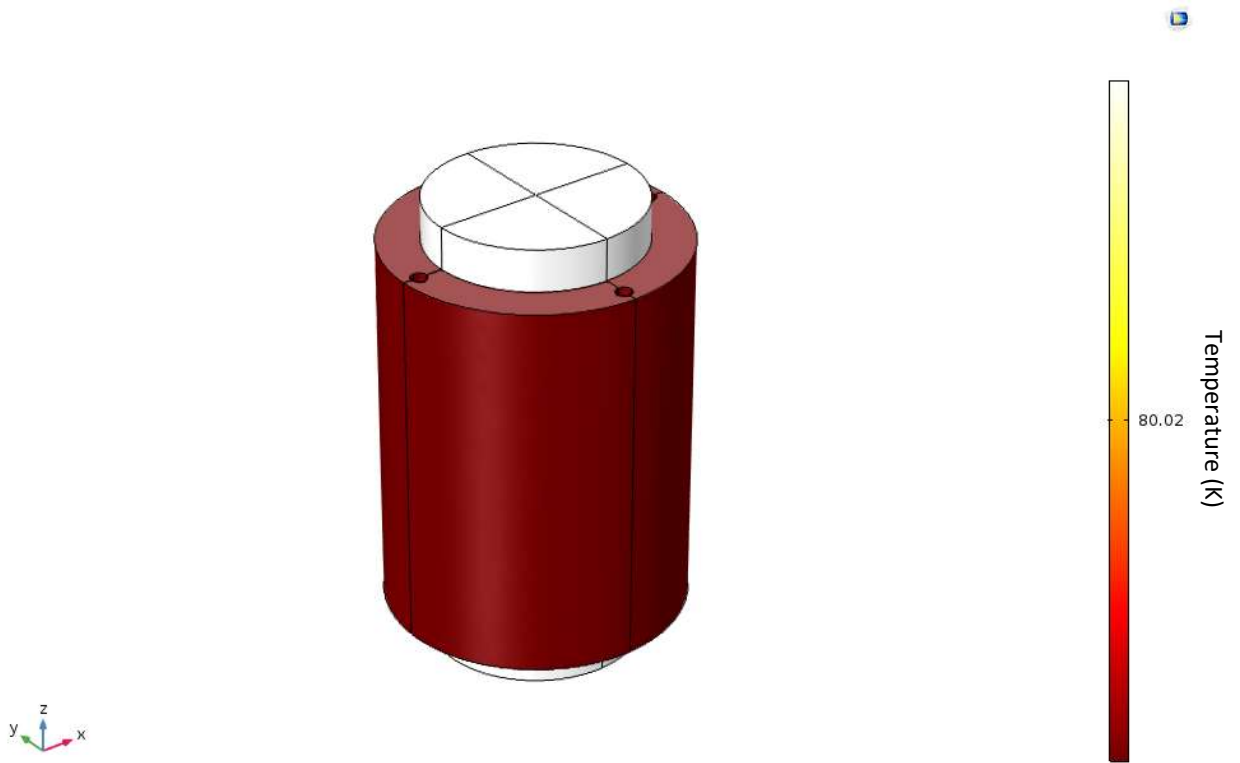


Figure 122 – Temperature surface plot of 'interference' assembly at thermal equilibrium (K).

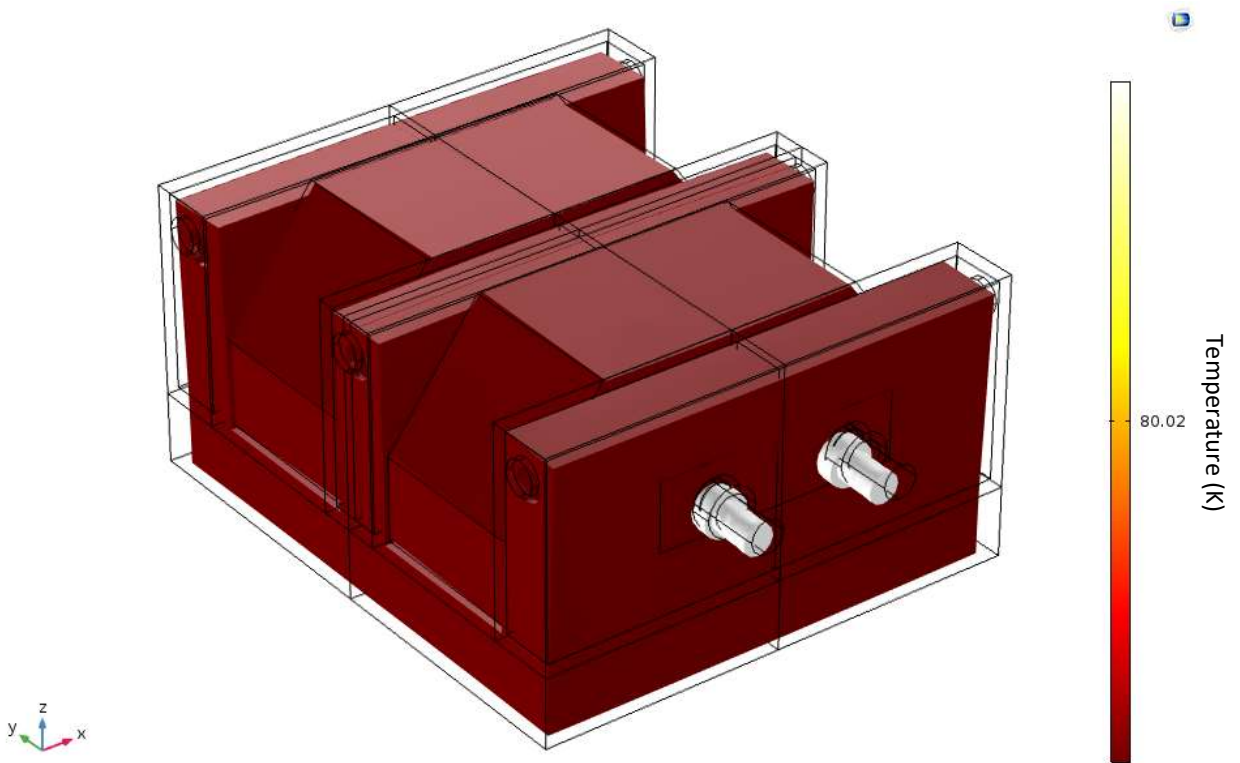


Figure 123 – Temperature surface plot of '120' assembly at thermal equilibrium (K).

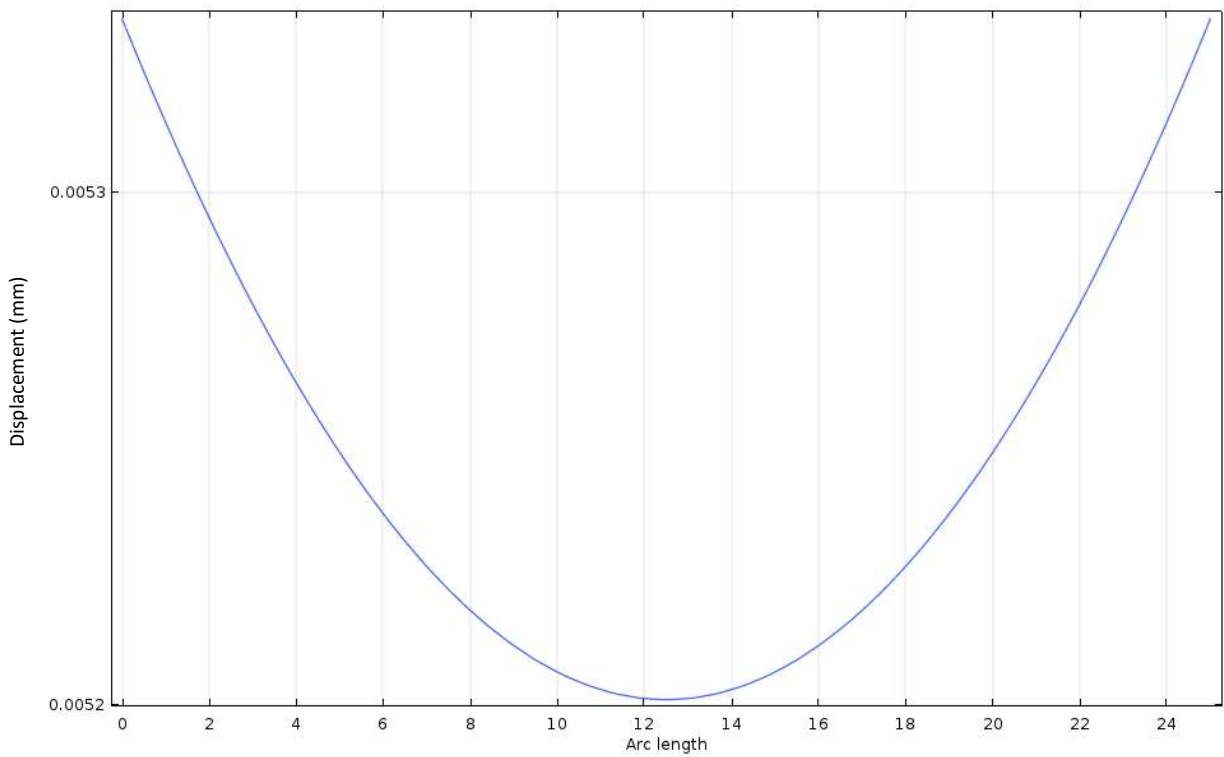
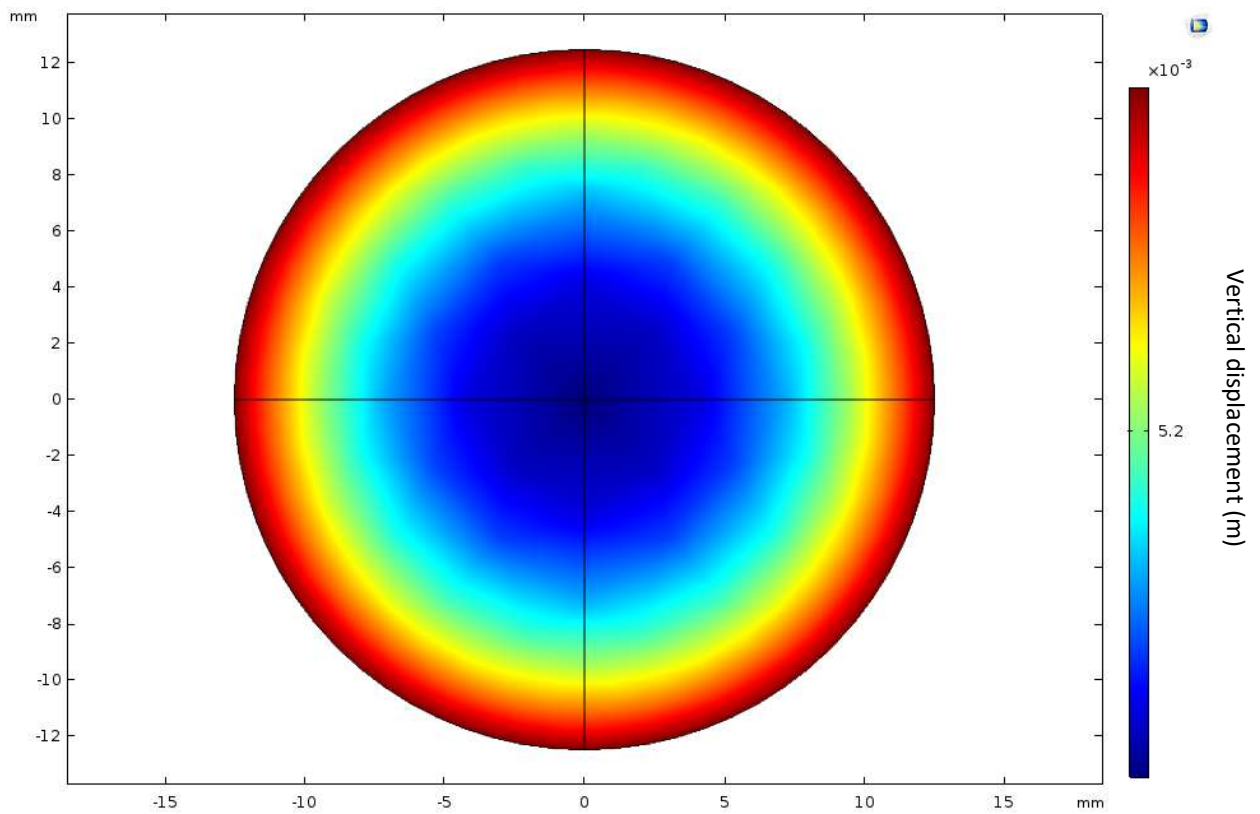


Figure 124 – (Top) Surface displacement of ‘interference’ assembly diffracting surface as a result of clamping. (Bottom) Cross-section of sagittal plane, showing deformation variance of  $1 \times 10^{-6}$  m.

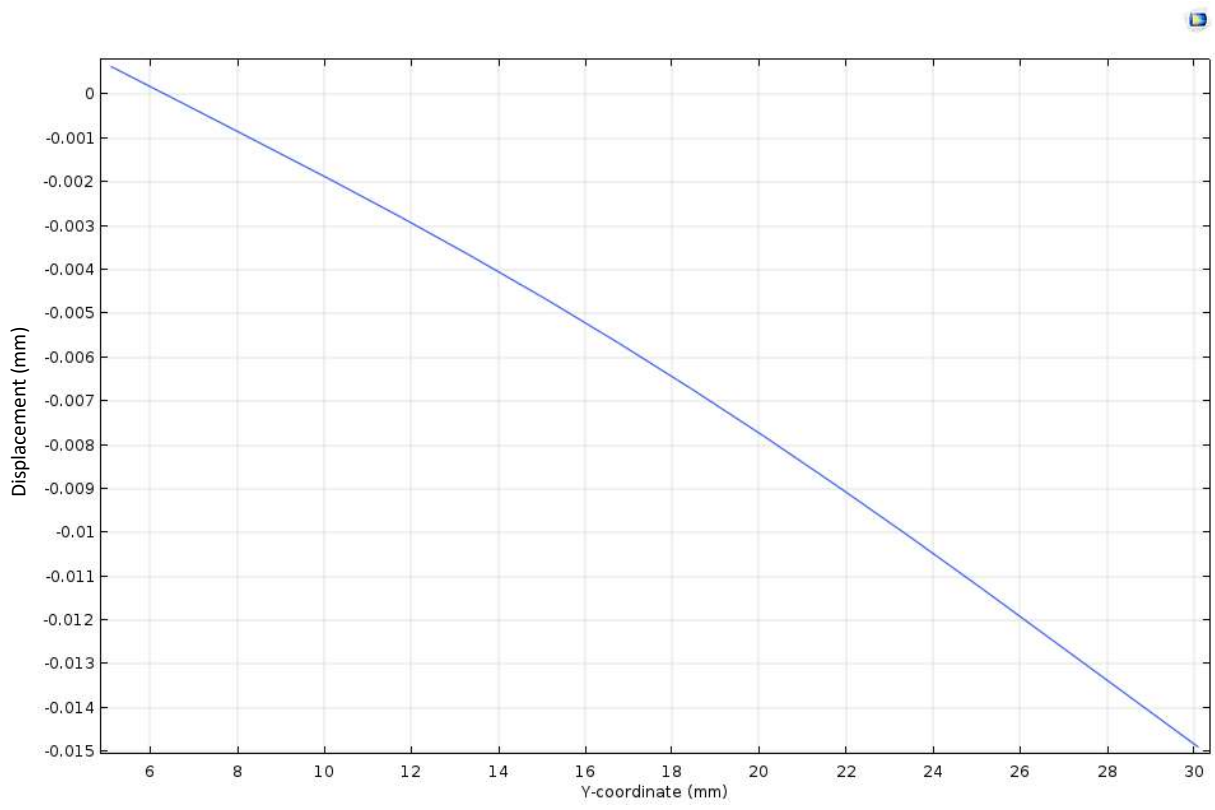
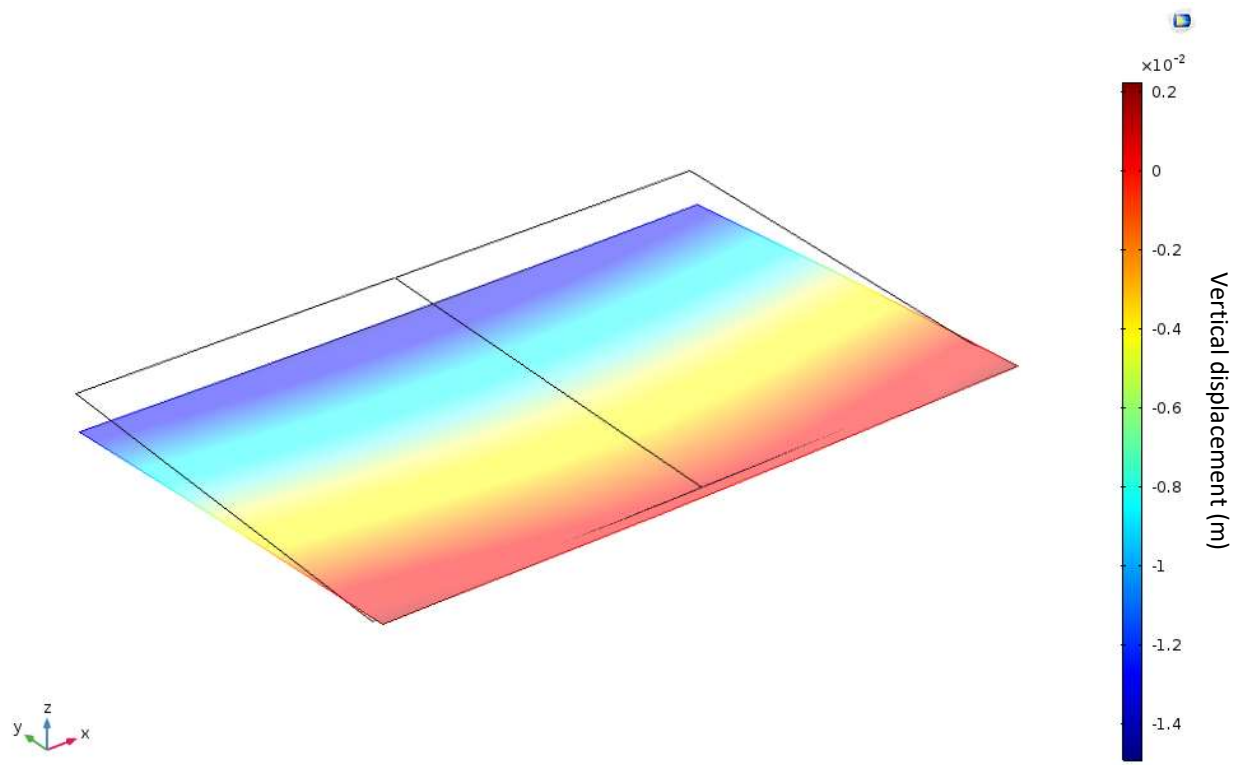


Figure 125 – (Top) Surface displacement of conventional I20 crystal assembly diffracting surface as a result of clamping.

(Bottom) Cross-section of sagittal plane, showing deformation variance of  $17 \times 10^{-6}$  m.

These results give great promise to the concept of using an interference fit as both a clamping and cooling method. By applying the clamping force in a more uniform manner around the entirety of the crystal the deformation is channelled into a linear extrusion, rather than a twisted or bowed deformation.

### 6.3 Designing a New Monochromator Assembly Utilising an Interference Fit

The first step of manufacturing the novel design for testing was to have the silicon crystals manufactured. Due to the experimental nature of the new design, it was decided to have the silicon crystals manufactured by Pi-KEM Ltd., a company that specialises in the manufacture of silicon wafers, rather than a company that specialises in the production of monochromator crystals; as Pi-KEM produces wafers for a wide range of applications they were able to produce the silicon cylinders at a much lower cost and with a similar degree of accuracy to that accomplished by more specialist companies, with the only drawback being a lower grade polish on the diffracting surfaces. These crystals were perfectly functional for proof of concept and basic testing, although it is unlikely they have sufficient radius of curvature of the diffracting surface to be used in X-ray testing. Once concern raised by the Diamond Light Source was that a with perfectly cylindrical crystal in a perfectly tubular heat exchanger, there was no way to influence which direction the crystal would travel in should a catastrophic failure occur. As such, the crystals were manufactured with a light taper, such that the diffracting surface was narrower than the rear end; this ensured that should the system fail catastrophically, the crystal would be ejected through the rear of the sleeve into the empty vacuum vessel, and not the front, into the vessel window and other testing apparatus.

Once the silicon crystals had been manufactured, they were taken to DCE Holne, a precision engineering firm, to have matched sleeves made. The crystal had a matched sleeve made such that there was a constant 30  $\mu\text{m}$  gap between the crystal and the sleeve along their entire length. As this production run was mainly for proof of concept tests it was decided to manufacture the sleeves as solid copper, rather than hollow, and cool the sleeve indirectly as this would save time and budget. As the equation governing interference fit pressure is only concerned with inner and outer hub radius, making the cylinders solid instead of hollow would continue to satisfy the conditions thus far. In order to prevent the crystal being slowly ejected from the rear of the sleeve instead of being

clamped during the interference fit, a series of small brass retention pegs were also manufactured. These screwed into the bottom of the sleeve after the crystal had been inserted such that the crystal could not be removed, and would be restrained during the clamping process. An assembled 'interference' assembly and schematic is shown in Figure 126, and a disassembly of all component parts is shown in Figure 126.

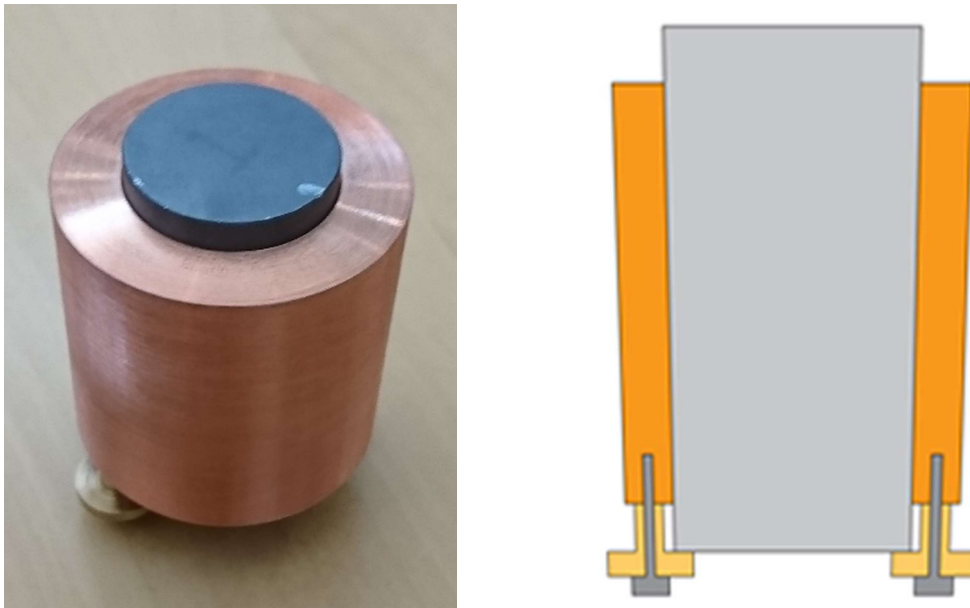


*Figure 126 – Complete 'interference' assembly;*

*(Left) Silicon crystal inside copper heat exchanger. Brass retention peg visible at bottom left. Note that top of crystal has not been polished at this stage.*

*(Right) Schematic view of 'interference' assembly, showing silicon crystal in copper heat exchanger. Brass retention pegs held on with steel bolts. Taper has been exaggerated to be easily visible.*

As the heat exchangers manufactured were solid copper, it was not possible to directly cool them. Indeed, as will be detailed later in this Chapter, it would not have been possible to use direct cooling even if the heat exchangers were capable of it. Instead, it was decided to use a device referred to as a 'cold finger' to indirectly cool the heat exchanger through the use of a copper clamp, as detailed below and shown in Figure 128.

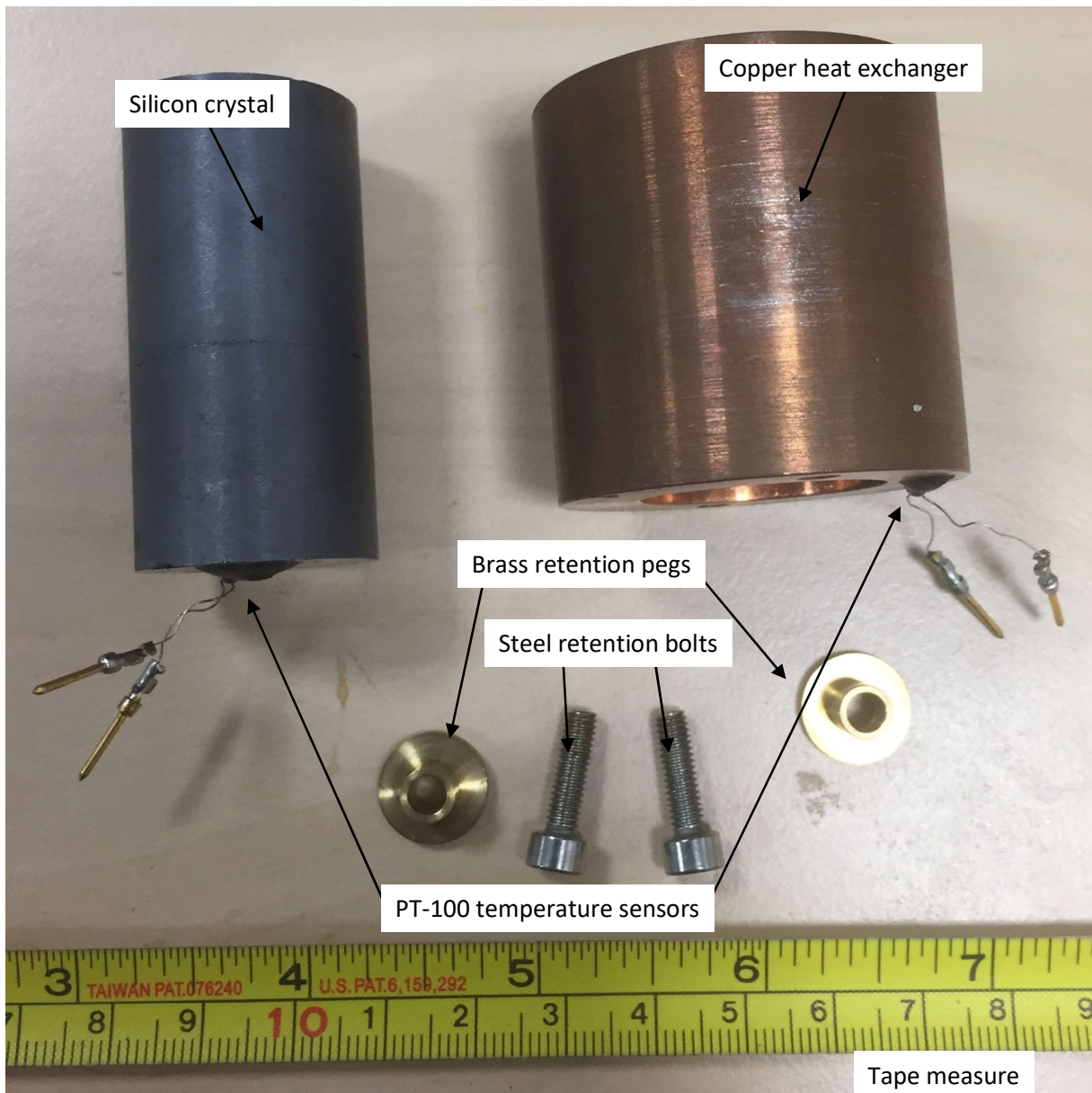


Figure 127 – 'Interference' assembly components disassembled; tape measure at bottom for scale.

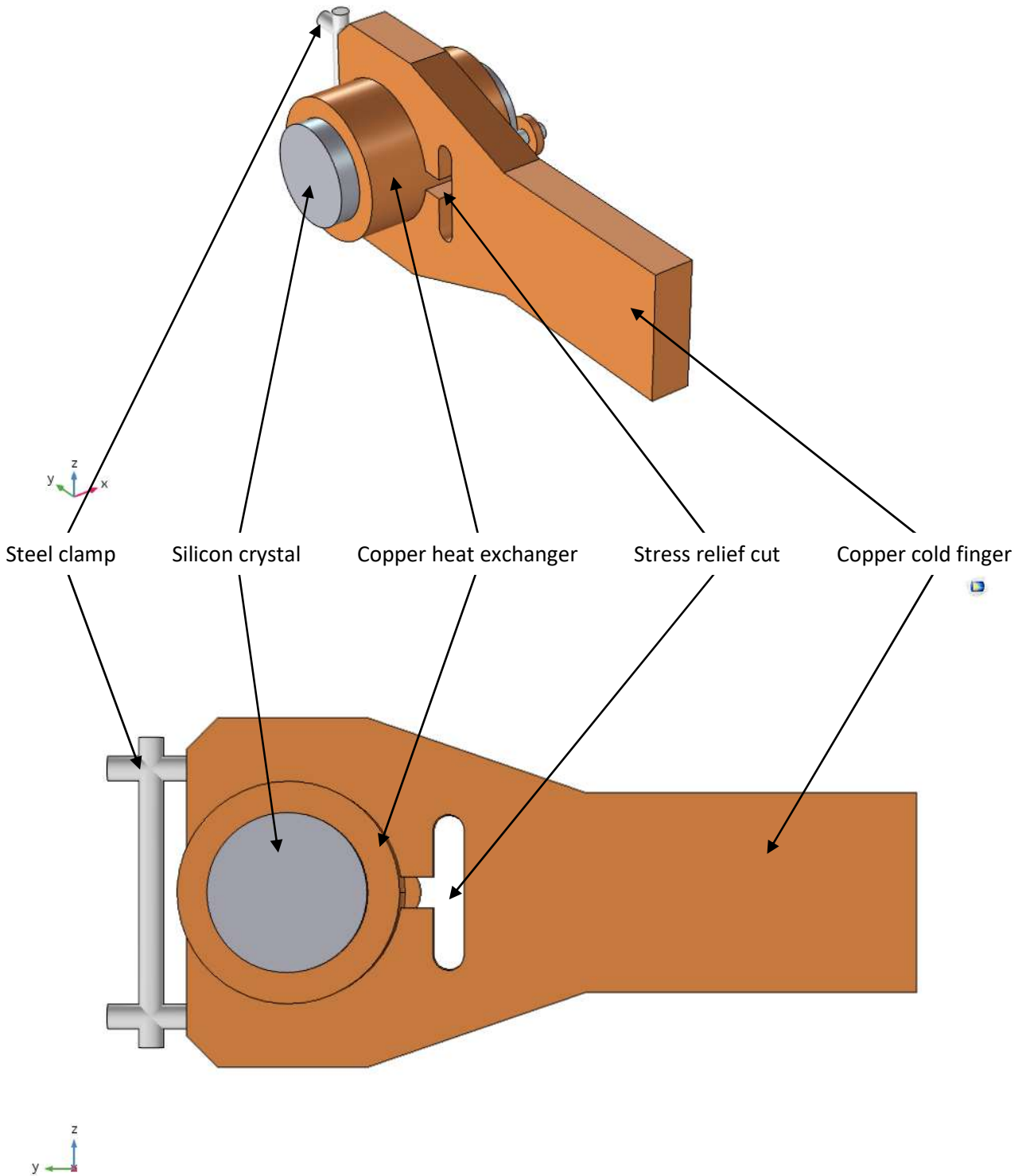


Figure 128 – ‘Interference’ assembly held in cold finger; cold finger continues to liquid nitrogen coolant receptacle to right.

## 6.4 Investigating the Performance of an Interference Fit Monochromator Assembly

To test the performance of the 'interference' assembly, it was decided to measure the flatness of the diffracting surface using a mini Fizeau interferometer, a device that measures distances by using timed laser pulses. In order to test the flatness of conventional crystal assemblies clamped and unclamped, the crystals are first placed freely in front of the interferometer and measurements are taken of the surface flatness, resulting in a three dimensional image of the crystal surface. Following this, the crystals are placed into their assemblies and clamped and another measurement is taken; by subtracting one measurement from the other, the deformation caused by the clamping process is found. However, as the 'interference' assembly can only be clamped by cooling to liquid nitrogen temperatures, a new procedure was required. The crystal was inserted into the sleeve and fastened in place through the use of the retention pegs. A PT-100 temperature sensor was attached to the rear face of the crystal, and a second was attached to the adjacent region of the heat exchanger. The assembly was then inserted into a specialised copper clamp mounted inside a vacuum vessel with an optical grade window between the diffracting surface and the interferometer. The vacuum vessel was sealed, and a measurement of the crystal face was taken as a baseline. The vessel was then pumped down to vacuum, a pressure of  $10^{-8}$  mPa, and another image was taken. These two images were compared, and it was found that pumping down to vacuum had a negligible effect on the crystal, and deformation of the window was not visible in the same region.

The next step was to cool the 'interference' assembly to cryogenic temperatures in order to find how clamping and cooling deformed the diffracting surface of the crystal. However, as the vacuum vessel available for this testing was not rated for rapid evacuation should the liquid nitrogen coolant leak, it was not safe to directly cool the heat exchanger. Instead, the heat exchanger was fastened into a specially designed clamp mounted to a long, hollow copper rod which passed through one end-plate of the vacuum vessel. Mounted to the end plate was a large cylindrical receptacle, such that

the copper rod extruded into it revealing holes into the interior of the rod. This coolant system was referred to as a 'cold finger'. To cool the assembly, liquid nitrogen was poured into this receptacle and maintained at a constant level as it evaporated, rapidly cooling the assembly to approximately 80 K. Photographs of the vacuum vessel, clamp and cold finger are presented in Figure 129.

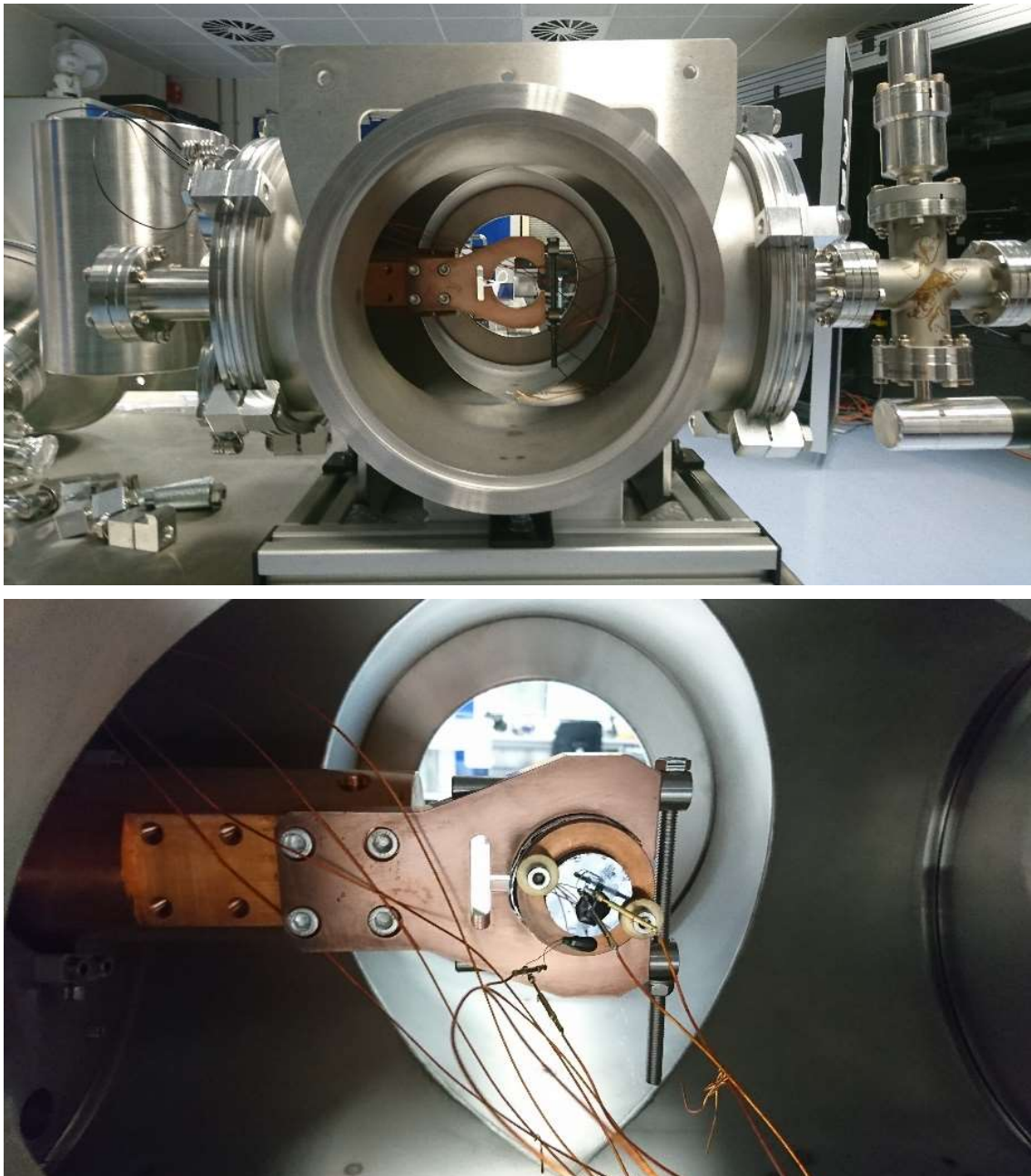


*Figure 129 – 'Interference' assembly experimental apparatus.*

*(Top) Vacuum vessel with clamp centred and cold finger running to liquid nitrogen receptacle on left.  
(Bottom) 'Interference' assembly located in clamp. Stress relief cut visible to left of assembly. PT-100s on rear of crystal and heat exchanger.*

A sample interferometer scan is shown in Figure 130 below, taken at room temperature and vacuum.

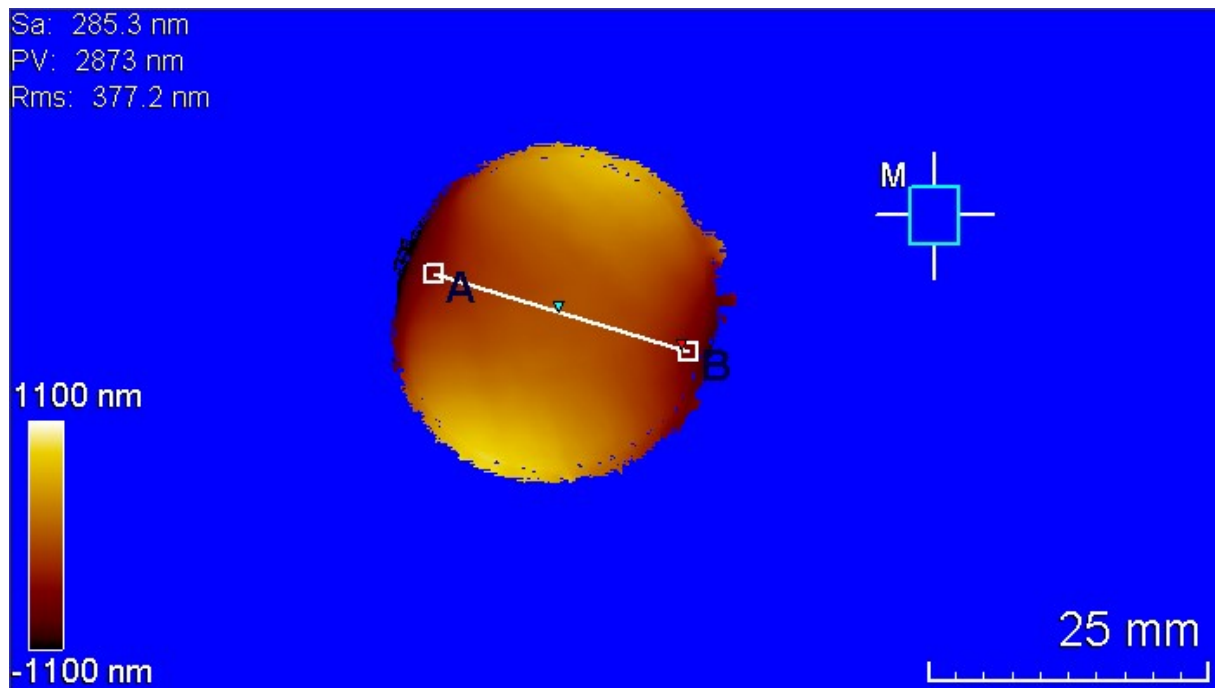


Figure 130 – ‘Interference’ assembly experiment: scan of diffracting surface at room temperature and vacuum.

This scan was subtracted from one taken at cryogenic temperatures to produce Figure 131, the surface deformation caused in the crystal by cooling and clamping it. The total deformation variance across the crystal diffracting surface was 30 nm. This procedure was repeated four times, and on the final thermal cycle the deformation of the diffracting surface was measured as the crystal warmed from 90 K up to 140 K. The profile measurements are shown in Figure 132 below. Comparing these to the calculated surface deformation from the COMSOL model in Figure 124 we see a much smaller surface deformation than expected. This is due to COMSOL modelling the two surfaces as a perfect match, with all of the surface coming into contact at once and exerting pressure on the crystal, where in practice microstructures and imperfect polishing allow less of the surfaces to contact, reducing the stress and therefore deformation of the crystal.

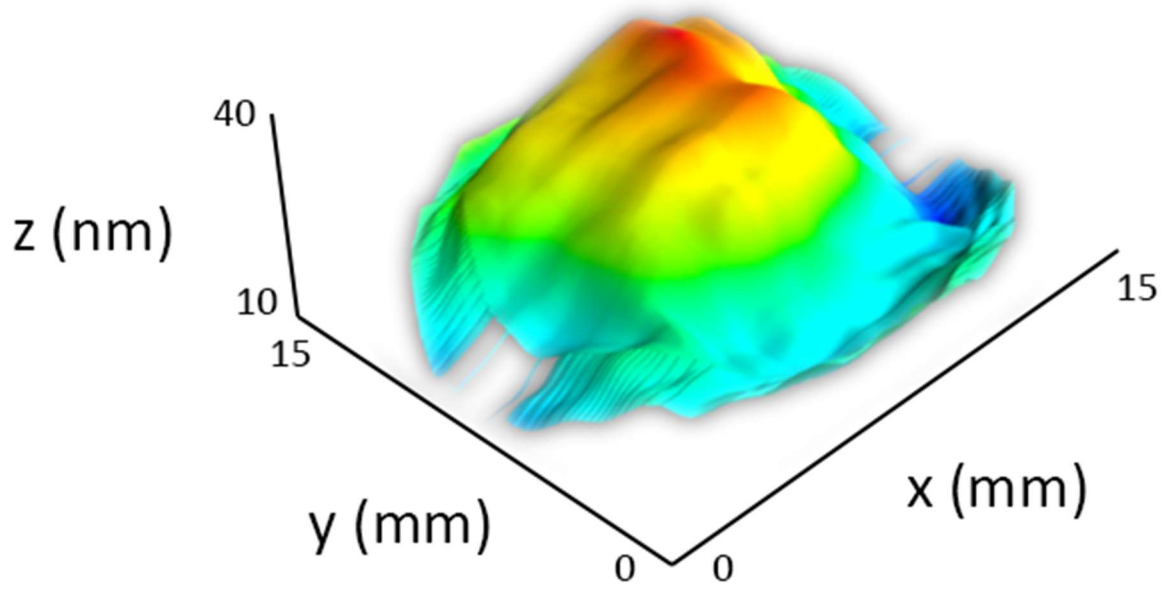


Figure 131 – Experimental data: surface displacement of diffracting surface as a result of clamping and cooling showing diffracting surface deformation variance of 30 nm.

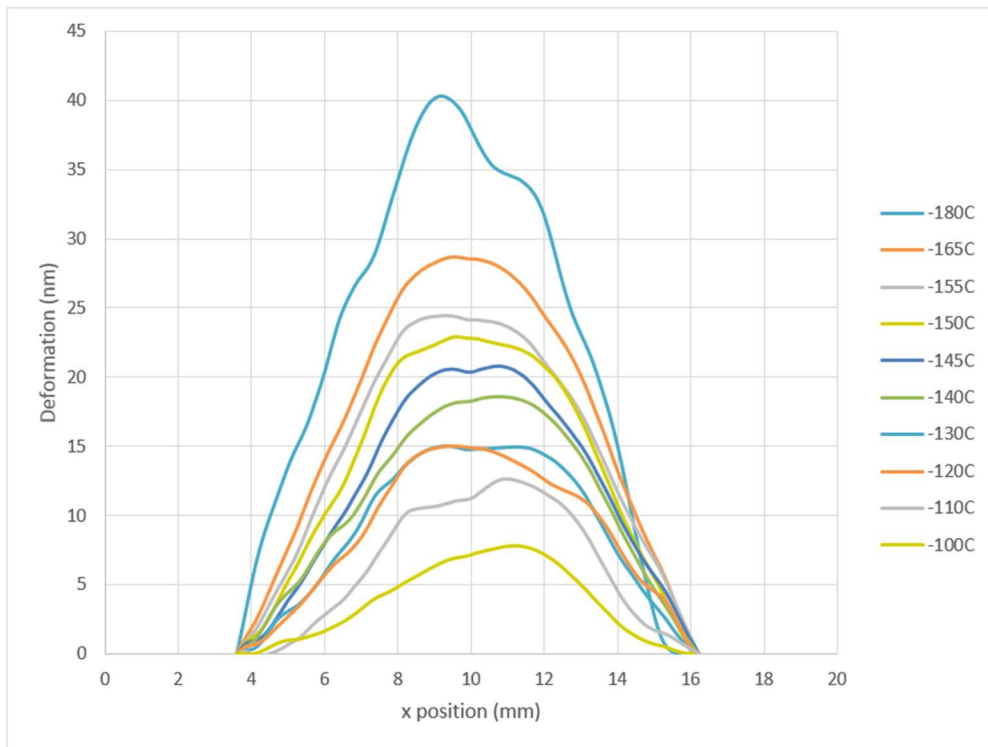


Figure 132 – Experimental data: surface profile of diffracting surface as a result of clamping and cooling showing deformation at various temperatures. Note that lines on graph are in same order as series on legend.

Both components had attached PT-100 temperature sensors to monitor the cooling rates. This allows us to evaluate the effectiveness of the heat exchanger as an indirect cooling device; the better the performance of the cooling, the closer the temperatures of the two bodies would remain. As shown in Figure 133, the heat exchanger does not initially cool the crystal; however, after approximately nine minutes, the copper heat exchanger shrinks sufficiently to make a good thermal contact with the silicon crystal, and the two bodies reach thermal equilibrium rapidly. Once the two bodies are in equilibrium they remain so for the rest of the experiment, through to approximately 80 K. The second y-axis in Figure 133 shows the calculated gap between the two bodies; this is calculated using the temperatures marked on the graph and the known initial sizes. Once the gap value drops to zero the two bodies are in contact, and once it drops below zero they are interfering with one another.

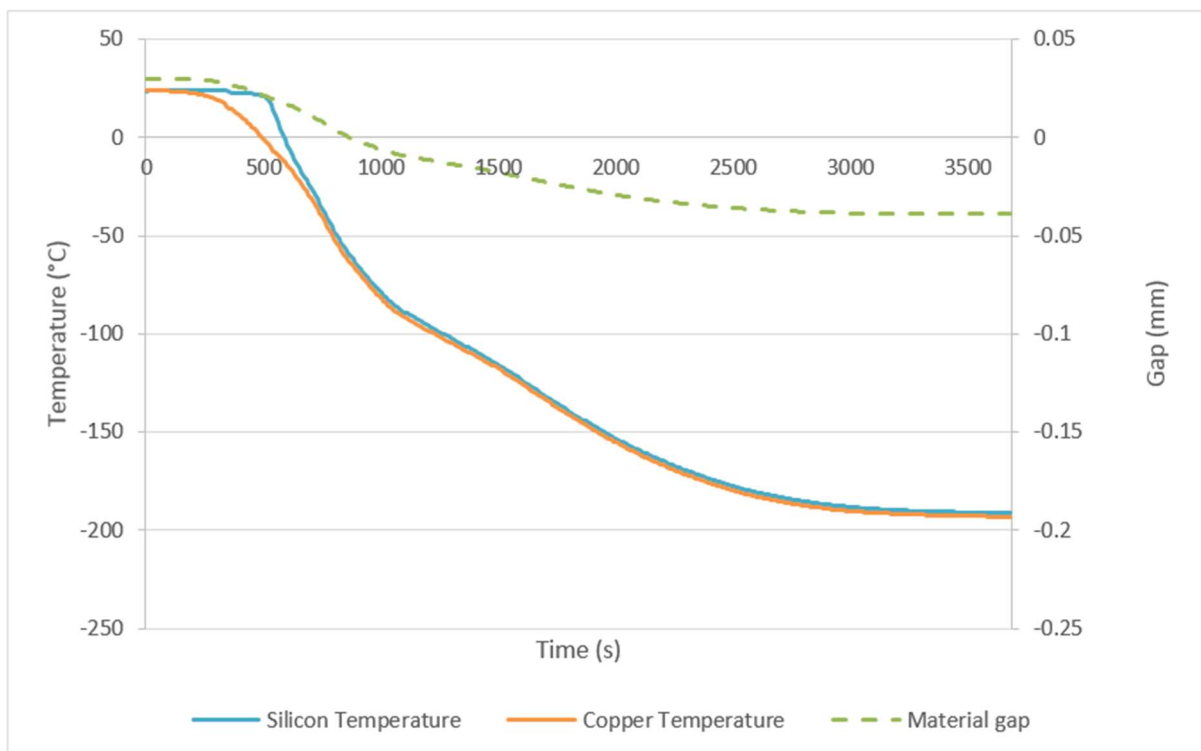
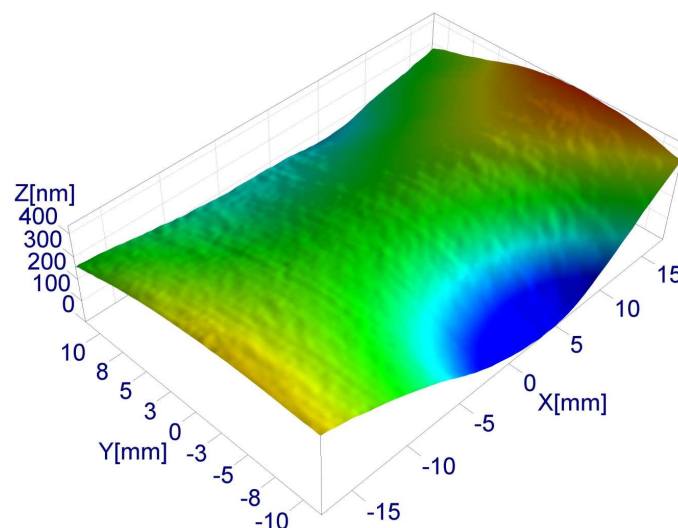


Figure 133 – Experimental data; graph of temperature of both silicon and copper components and calculated gap as a function of time. Note that once calculated gap becomes zero, the two components are in contact.

## 6.5 Comparing the Performance of an Interference Fit to that of a Conventional Design

A similar body of work was performed with the conventional I20 crystal, with one major consideration: as the I20 crystal does not require to be cooled to cryogenic temperatures for clamping to take place, all tests were done clamped. As such, the I20 crystal tests reflect cooling exclusively, and do not include structural deformations caused by clamping, whereas the ‘interference’ tests reflect both mechanical and thermal deformations. Despite this difference, the I20 tests, as shown in Figure 134 below, show deformation variances of up to 400 nm across the diffracting surface, a full order of magnitude higher than those observed in the ‘interference’ design’s clamping and cooling tests.



*Figure 134 – Conventional I20 assembly experiment: surface deformation of diffracting surface as a result of cooling showing diffracting surface deformation variance of 400 nm.*

A second benefit of the ‘interference’ design is its high level of repeatability. In the aforementioned previous work done with the I20 crystal, it was found that the assembly needed to be adjusted after each thermal cycle to realign the crystal and retighten bolts; in this work the ‘interference’ design was put through multiple consecutive thermal cycles with no loss of performance.

The new design does have some drawbacks of its own; each heat exchanger sleeve fits only one crystal, due to the high accuracy required for the interference fit. This means that should a crystal be damaged or broken, the sleeve will need to be replaced along with the crystal. The new design has not been tested yet with liquid nitrogen flowing through the heat exchanger; as such, it is unknown what vibrations if any this modification will induce.

## 6.6 Conclusion

The initial model demonstrated the benefits of the interference fit as a solution to the stresses that arise through both clamping and cooling conventional assemblies. By harnessing the material properties, rather than trying to mitigate them, it was possible to create a new and more robust design.

This hypothesis was supported through experimental results. Not only was the deformation variance observed an order of magnitude less than that seen in the conventional I20 crystal assembly, the system also proved to be more repeatable, performing four consecutive runs with no deterioration, and achieved a very high level of thermal contact between the heat exchanger and the crystal through the application of very high, very uniform forces. The use of the retention pegs and slightly conical crystals removes any safety concerns, and the rapid thermalisation even through the cold finger cooling method all show promise for the novel 'interference' design to outperform conventional monochromator devices by a significant margin.

The 'interference' assembly deals with a number of known flaws with conventional designs: where conventional designs struggle in terms of repeatability, requiring adjustment and correction after every thermal cycle, the 'interference' design is capable of completing repeated thermal cycles without being adjusted. Where conventional designs require nanoscale accuracy, often through the use of macroscopic adjustments, the 'interference' design is self-orienting within its heat exchanger and has no adjustable parts. Where conventional designs struggle to mitigate strains and deformations caused by conflicting material properties, the 'interference' assembly harnesses these properties in order to create a high intensity, highly uniform clamping force.

The most important improvement the 'interference' design has over the conventional design is its reduced thermal-induced deformation. As the differing mechanical properties and the crystal

geometry are harnessed to create a high intensity clamping force during the cooling process, the crystal exhibits a lower thermal deformation. This prevents the system from becoming non-uniform before the beam is even incident, helping maintain a high-quality, flat diffracting surface once the beam is incident.

One more factor to consider is what modifications will be required to replace the first crystal within the I20 QBCM. The crystals at present are independent; each is mounted to a steel rotation plate, and each pair of plates, i.e. the first and second, the third and fourth, are mounted to a secondary rotation plate, allowing the crystals to rotate independently while maintaining the beamline. To install the new monochromator assembly, the first rotational plate would need to be removed and replaced with a new rotational plate bearing a clamp to hold the new assembly. This would be easily done, allowing the new design to be installed with minimal downtime.

#### [Executive Summary of Chapter 6](#)

The interference fit first crystal assembly was suggested and modelled with an ideal gap calculated to lie at a 30  $\mu\text{m}$  room temperature gap between the cylindrical silicon crystal and the tubular heat exchanger.

The novel 'interference' assembly was manufactured as a proof of concept to the specifications identified through the initial modelling.

The 'interference' assembly was tested, and showed an order of magnitude lower deformation variance when cooled and clamped (30 nm) compared to that shown by a conventional crystal taking into account cooling alone (400 nm).

## 7. Discussion

### 7.1 Introduction

In this work, five key concepts have been considered to find their effect on the performance of a monochromator first crystal assembly. The first of these areas is the effect of disparate mechanical properties in the assembly; as each component of the assembly is constructed of a different material, and different materials have different temperature dependent properties, the act of cooling an assembly designed to function at room temperature causes each component to behave differently as they cool. This has a significant effect, as some components can expand or contract at a rate differing by orders of magnitude.

The second area considered was how the shape of the diffracting crystal affects the performance once the synchrotron beam is incident upon them; each differing design could give rise to different thermal pathways, as well as the macroscopic design affecting the microscopic behaviour of the diffracting surface. The other aspect explored in this Chapter was how moving the heat exchangers could affect the thermal pathways, comparing cooling the sides of the crystals to cooling the base. This was shown to have significant impact on the thermal pathways.

The third area considered was whether direct cooling systems, those that expose the crystal directly to the coolant, have significant benefits when compared to indirect cooling systems, those that use a heat exchanger of some form. The drawbacks of direct cooling are widely known, including higher pressures required to attain a gas-tight seal and the use of indium gaskets that are only able of withstanding a small number of thermal cycles, but the benefits had not been studied.

The fourth area explored was the direct effects of clamping forces on the diffracting surface; the conventional wisdom in the synchrotron community is to use high clamping forces to maximise the performance of indirect cooling systems or to form gas-tight seals in direct cooling systems, but this

is balanced by an increase in Young compression induced deformation. While this is acknowledged, very little work had been done to find at what point increasing the clamping force moves from reducing the thermal deformation to increasing the mechanical deformation.

The fifth and final area explored was the role of thermal gap conductance in indirect cooling. Thermal gap conductance controls the movement of heat between two bodies in contact, such as a monochromator crystal and its heat exchanger. Much work has been done in the field of gap conductance, but the majority of this work is in regards to specific systems; minimal work has been done to establish a universal equation or database of the effect of varying contributing factors on the thermal gap conductance.

## 7.2 Material Properties: Benefit or Bane

A standard crystal assembly, such as that used at the I20 beamline at DLS, is composed of four basic components of varying materials; the diffracting crystal itself is made of single-crystal silicon, the heat exchanger of oxygen-free copper, an IM in the form of an indium foil between the two and bolts of steel or invar running through the middle of all the previous components. This assembly is then clamped to a known clamping force at room temperature before being mounted in the optics hutch and cooled to liquid nitrogen temperatures.

During this cooling process, the materials react very differently. The silicon contracts at a slow rate until it reaches 120 K, at which point it expands for the remaining 40 K cooling. The copper contracts at ten times the speed of the silicon, never reaching a zero expansion point; the same is true for the steel. The indium foil shrinks at an intermediate rate. However, due to the varying tensile and compressive strengths of the materials, the copper and steel distort around the silicon, exerting very high forces upon it. The indium, due to its thinness and low strength, has the least effect of the four materials. However, at cryogenic temperatures it has been shown that the silicon is pushing the steel up while the copper pulls it down, the steel pulling in and opposed by the silicon. This interplay of forces results in misalignment of the diffracting crystal, along with deformations of the diffracting crystal caused by the forces exerted by the copper and steel.

It has been shown that rather than opposing these contrasting forces it is possible to harness them. By removing the steel and indium components and dealing with only copper and silicon, we can construct a novel assembly that makes use of these forces to create the clamping force between the crystal and the heat exchanger. This has been done by means of an interference fit, constructing the heat exchanger such that it attempts to shrink to smaller than the size of the silicon at cryogenic temperatures, causing a very high, very uniform stress field to link the two. By contrast, in the

conventional I20 design, the force shifts during the cooling process becoming higher and lower at times than the desired 190 N.

The novel 'interference' design does so, utilising a room temperature gap of 30  $\mu\text{m}$  such that the clamping force at cryogenic temperatures reaches a clamping pressure of  $10^8$  Pa uniformly across the entire cooling surface of the crystal. This is achieved through the contrasting material properties, with the crystal held in place in the heat exchanger at room temperature through the use of brass retention pegs.

### 7.3 Assembly Geometry: Importance of Heat Exchange Location

The I20 conventional crystal assembly makes use of a rectangular crystal with both short edges of the diffracting surface sheared off to form 'shoulders'. This design deviates from an industry standard cuboid crystal due to the space restrictions of the I20 beamline; the removed sections would otherwise interpose either in the diffracted beam or by grinding against the second crystal in the monochromator. However, it has been shown that these shoulders actually improve the uniformity of thermal pathways through the crystal such that the diffracting surface remains more uniform. Many varying crystal geometries were tested to find how the crystal shape affects the movement of heat through the bulk of the crystal, but the trend that emerged was that the location of the heat exchanger had far more effect on the performance of the crystal than its shape.

When the heat exchanger is modelled as mounted on the two long sides of the crystal, as it is in the I20 conventional assembly, it has been shown that the thermal pathways are of varying lengths. This is due to the cooling surface being too close to the diffracting surface; energy absorbed at the edges of the diffracting surface has a very small distance to travel to the cooled surface, whereas energy absorbed at the centre of the diffracting surface is forced to travel through the bulk of the crystal until it can reach an unclaimed section of the cooled surface. This results in the centre of the diffracting surface reaching a greater temperature than that attained by the edges, and causes significant deformation variance in the diffracting surface.

The second drawback caused by side cooling the crystal is mechanical deformation; as the crystal is clamped along the entirety of the cooling surface, the diffracting surface is directly subject to the clamping force. This causes a mechanical deformation due to Young expansion: where the crystal is compressed by the clamping force, it is forced to expand axially resulting in further surface deformation.

By moving the heat exchangers to the bottom of the crystal, the thermal pathways become much more linear – the heat absorbed at the diffracting surface all travels uniformly along the z-axis until it reaches the cooling surface, where it is removed. This uniform thermal pathway length results in a very uniform, if slightly higher, diffracting surface temperature; this causes a more uniform deformation across the diffracting surface.

However, it is physically difficult to constrain a crystal such that it is only held by its bottom surface with any significant force, especially considering crystals in monochromator devices are rotated to select different x-ray wavelengths. As such, and due to supporting anecdotal evidence, it was decided to move the diffracting surface such that it still cooled the sides of the crystal, but was dislocated from the cooling surface by 5 mm. This was modelled and found to improve the performance of the conventional I20 crystal significantly, on par with increasing the size of the crystal by 40 %.

As this compromise reduces the thermal and mechanical deformation significantly while still being achievable physically, it was decided to design the novel 'interference' assembly such that the crystal would extrude 5 mm from the heat exchanger, allowing the thermal pathways to normalise and the clamping force to be applied some distance away from the diffracting surface.

## 7.4 Cooling Methods: Direct vs Indirect

Many synchrotron facilities have been considering making the change from indirect to direct cooling, due to the improved performance of directly cooled crystals seen in the few facilities where they are used. However, this would be a major undertaking as it would require the crystals and assemblies to be redesigned and replaced; as such, the benefits of direct cooling have been compared to the drawbacks in this work to determine if such a switch would be widely beneficial.

The simplest comparison to make to see the benefits of direct cooling is to look at the difference in temperatures observed in the two systems. In a direct cooling system, the sections of the crystal that are directly exposed to liquid nitrogen are maintained at a temperature of 80 K. In an indirect cooling system, the sections of the heat exchanger that are directly exposed are maintained at 80 K; the thin design of the heat exchanger will limit and temperature rise between this region and the region in contact with the crystal to 85 K, and even assuming a poor thermal gap conductance this should maintain the cooled region of the crystal at approximately 100 K. This shows that direct cooling can provide a temperature reduction of 20 K at the cooled region.

The major benefits observed in direct cooling are instead a result of the design philosophy – direct cooling exerts a far greater clamping force to create a gas-tight seal, and as such the clamping is often performed between the coolant exchanger and a small section of the crystal through the use of fastenings inserted in stress relief cuts, rather than through the body of the crystal as a whole. In addition, the presence of cooling channels through the crystal itself cool the crystal some distance from the diffracting surface, a benefit which is described above.

As direct cooling does not inherently provide sufficient improvements to countermand its significant drawbacks, the priority should instead fall on applying and better improving the performance of indirect cooling than retrofitting existing beamline optics with direct cooling systems.

As such the novel 'interference' assembly has been designed to be indirectly cooled through the use of a tubular copper heat exchanger, contacting fully around the crystal with the exception of a 5 mm extrusion from either end.

## 7.5 Deformation: Optimising Thermal Induced and Stress Induced Deformation

When either direct or indirect cooling systems are attached to the crystals they are done so through the use of clamping forces. In an indirectly cooled system, these clamping forces have a direct effect upon the cooling efficiency of the system; as such, crystals are often clamped with very high forces to keep them cooled. However, the higher the clamping force the more mechanical deformation is created within the crystal.

It has been shown that for each assembly design there exists a local minimum where both mechanical and thermal deformations are at minimum; increasing the clamping force will increase the mechanical deformation more than it reduces the thermal deformation, and reducing the clamping force will increase the thermal deformation more than it decreases the mechanical deformation.

To locate this value for various designs, the easiest method is to use a parametric sweep; the assembly can be modelled in COMSOL or a similar program such that the clamping force is applied accurately across the heat exchangers and the crystal, and the beam is depositing power into the crystal. A parametric sweep is performed by modelling this setup with varying clamping forces and plotting the deformation variance as a function of the clamping force.

As the novel design is making use of an interference fit rather than conventional heat exchangers clamped to the exterior, and as it is being designed from scratch, an alternative approach was available. Instead of a parametric sweep, two equations were solved simultaneously: the equation for pressure caused by an interference fit, and the equation for force incurred by an expanding body. By ensuring the expansive force was greater than the clamping force, the 'interference' assembly was designed to ensure it could freely extend as it was clamped without being prohibitively clamped.

## 7.6 Thermal Gap Conductance: Highly Dependent Limiting Factor

The reason the clamping force increases the performance of an indirect cooling system as explained above is that the thermal gap conductance is directly proportional to the clamping force. The thermal gap conductance is the method by which two bodies in contact conduct heat from one to the other. This parameter is highly sensitive to clamping force, surface profile of the bodies, and the use of an interstitial material and so despite being well understood is very difficult to calculate without experimental data.

The experiments performed on gap conductance showed that in addition to clamping force being directly proportional to thermal gap conductance, the selection of IM was also important. It was found that indium foils were a far better IM than a more conductive material such as copper; this is because the role of the IM is to deform to match the two contacting surfaces, thereby increasing the surface area in physical contact. However, if the indium foil is too thin, it cannot suitably deform to match; and if it is too thick, the insulating properties of indium reduce the gap conductance. As such, malleability is the most important factor but consideration must be made as to the insulating properties of the material.

An industry standard approach is to use each piece of indium foil only once before discarding it. However, it was shown that re-use of indium foils as IMs is not only acceptable but often leads to higher thermal gap conductances than those observed when using new pieces of foil. This is due to the IMs deforming in a mixture of elastic and plastic deformation such that they can be more easily worked in future applications, in much the same way as a balloon that has been stretched already is easier to inflate than one that has not.

The novel 'interference' design has an alternate solution; rather than inserting an IM into the interface between the silicon and the copper and introducing a third set of material properties to

consider, the novel 'interference' design used clamping forces high enough to deform the copper into the surface structure of the silicon. This gave a much greater thermal contact than the conventional use an IM, instead allowing the heat exchanger to fulfil the role of IM itself.

## 7.7 Conclusion

This work has given rise to a number of key points. The first key point to consider is the significant deformations observed as a result of contrasting material properties. These material conflicts have been shown to cause significant deformations in the diffracting surface before the beam is even incident upon the crystal. This has shifted the focus for this project from how to improve cooling to instead improve the clamping and crystal assembly structure entirely while keeping cooling uniform. Rather than combating these conflicting material properties, it has been decided to instead harness them, utilising the disparate temperature dependent material properties to provide the clamping for the novel 'interference' design.

The second key point arose from modelling a range of crystal geometries, cooled in different locations. While crystal geometry does have some effect on the cooling of the system, it has been shown that the dominant factor affecting the thermal deformation of the crystal diffracting surface is the uniformity of the temperature, with an uneven temperature across the diffracting surface resulting in a non-uniform thermal expansion and a deformed diffracting surface. The dominant factor in this uniformity was the length of thermal pathways in the crystal – the distance heat had to travel from the absorption point to reach a cooled region. The more uniform these pathways are, the more uniform the diffracting surface remains. This is primarily achieved through dislocating the cooling surfaces from the diffracting surface, such as by bottom cooling the crystal. However, due to the real-world difficulties involved in securing a crystal exclusively by its rear surface, it was instead decided to use a functional compromise; the novel 'interference' crystal would be held such that a small region extended beyond the heat exchanger, allowing the thermal pathways to normalise before the heat was extracted from the crystal. This effort to normalise the thermal pathways also gave rise to the circular profile of the novel crystal.

The third key point is in regard to the difference between directly and indirectly cooling the crystal. There has been an interest in the synchrotron community in moving towards directly cooled crystals, as they are perceived to have a higher cooling efficiency and to result in a more uniform diffracting surface. However, it has been shown that the improvements observed in directly cooled crystals are a direct result of mitigations employed to minimise drawbacks of direct cooling, such as by using a larger crystal or bolting through stress relief cuts to dislocate the very high clamping forces used. As such, the benefits of direct cooling lie mainly in the design philosophy used, rather than in the method of cooling itself. As such, the novel 'interference' design has considered lessons learned from direct cooling mitigations but has been designed to use an optimised indirect cooling system.

The fourth key point is concerned with how the crystal assembly is clamped and held. It was shown that there were two processes causing deformation of the clamping surface: thermal deformation, where the power from the beam causes a variable temperature across the crystal diffracting surface resulting in variable thermal expansion; and mechanical deformation, where the process of clamping the crystal caused it to deform due to Young compression. It was shown that for each crystal assembly there would be a local minimum where the two regimes were at a common minimum. As such the novel 'interference' assembly has been designed such that the clamping force is as high as possible without resulting in constrained expansion, minimising the mechanical deformation induced in the crystal.

The fifth and final key point lies in the examination of thermal gap conductance. The gap conductance is functionally the limiting factor of an indirect cooling system; as the gap conductance is reduced, the system becomes less efficient at removing heat and the thermal pathways are forced to spread through the crystal, resulting in non-uniform lengths. Thermal gap conductance was shown to be majorly reliant on both clamping force and the use of an interstitial material, applied so that

the two surfaces in contact had fewer gaps between them. It was shown that the thermal gap conductance relies less on the conductivity of the IM, and more upon the malleability such that the two bodies remained in good contact as the system cooled and deformed. As such, the novel 'interference' assembly was designed such that a very good thermal contact could be achieved and maintained between the two bodies without the need for an IM.

## 8. Conclusions

### 8.1 Overview

This work began with a base principle study of the mechanisms through which heat moves through a crystal and then through an assembly. Having grasped the base principles, a one dimensional model was assembled to ensure the base principles were fully understood, then used to check the performance of a three dimensional model using FEA software. At this stage a hypothesis was constructed, a novel design composed and modelled, and then the novel design was manufactured and tested and found to perform to a greater standard than the conventional system.

The conventional design of the I20 assembly fulfils the requirements of a monochromator first crystal. It consists of a silicon crystal capable of diffracting an x-ray beam polished to a high flatness and coupled to heat exchangers on both sides such that the assembly can be cooled with liquid nitrogen. The assembly is held together with steel bolts, as is standard in these assemblies. However, while the I20 design would work on a beamline with a smaller beam footprint or if scaled up, its small form factor does not enable it to function as desired on the I20 beamline. As such, a radical redesign was required.

One oversight of the conventional crystal design was that it is clamped in such a way that the edges of the diffracting surface are in direct contact with the heat exchanger. This allows the sides of the diffracting surface to cool at a much more rapid rate than the centre, resulting in a variant temperature across the surface of the crystal and therefore variable thermal deformations. The location of the heat exchanger also exerts the clamping force directly onto the diffracting surface, resulting in mechanical deformation of this surface. Both of these deformations act individually to impact the monochromaticity and collimation of the diffracted beam.

A novel 'interference' assembly design has been presented here that removes these drawbacks and incorporates lessons learned from this work to produce a new, novel design that experiences an order of magnitude less mechanical deformation during clamping and cooling and provides a superior thermal gap conductance when compared to conventional crystals, resulting in a better performance.

## 8.2 Limitations of the Conventional Assembly Design

The conventional I20 design is constructed of two silicon crystals leaved between three copper heat exchangers, each of which is fastened to the copper baseplate. A piece of indium foil is inserted between each of the interfaces between crystal and heat exchanger such that it covers the entire contact area.

The assembly is clamped together with steel nuts and bolts, and the crystal is aligned by adjusting its angle before being clamped to 190 N through the application of a set number of rotations of the nut beyond 'finger tight'.

This assembly is then located in the beamline in the optics hutch, where the liquid nitrogen manifolds are attached to each of the copper heat exchangers, introducing torque forces into the assembly, before the beamline is pumped down to high vacuum. The assembly is then cooled to liquid nitrogen temperatures, around 80 K, by flowing liquid nitrogen through the heat exchangers at high pressure. At this point the copper and steel contract at ten times the rate of the silicon, until the assembly reaches 120 K; from this point onwards the copper and steel continue to contract while the silicon expands, causing great strain within the components of the assembly.

The vertical interaction copper of the shrinking while the silicon expands results in the steel bolts being pulled into an 'm' shape, resulting in sections of the silicon being pushed up or down depending on their location and the copper pulling away from the silicon along much of its length. This results in a poor thermal contact between the copper and the silicon as well as significant deformation in the diffracting surface before the beam is incident upon it.

### 8.3 Application of a Cut Back Heat Exchanger

One mitigation that has shown promise at the I20 beamline is to cut back the indium foil such that 5 mm of the silicon is not in contact with the copper. This was attempted to reduce the strain on the diffracting surface as a result of clamping; however, it has also allowed the heat to travel through the silicon in more uniform thermal pathways as well, reducing the thermal deformation present in the silicon.

This is one step toward the bottom cooling approach suggested in Chapter 3; however, while cutting back the indium does prevent a high efficiency thermal contact as suggested in Chapter 5, the very high clamping forces present in the conventional assembly will result in some contact occurring and result in a less than ideal temperature profile across the diffracting surface. Instead, as suggested above, the heat exchanger itself should be pulled back such that the top 5 mm of the crystal is not at risk of contact, rather than just the indium foil.

By pulling back the heat exchanger, the crystal will reach a higher temperature. However, as identified above, it is not the absolute temperature of the crystal that needs to be maintained but rather the uniformity of the temperature of the diffracting surface. By making the thermal pathways more uniform the temperature of the diffracting surface will follow suit, reducing the variable thermal deformation and therefore the overall deformation of the diffracting surface.

## 8.4 Interference Fit Crystal Assemblies: A Novel Solution

The novel 'interference' fit design proposed in Chapter 6 works by harnessing the differing material properties that cause stresses and deformation in the conventional design. By simplifying the system such that it consists of two materials rather than four, the properties of these two materials can be used together to create a clamping force rather than having to be mitigated.

By redesigning the crystal and heat exchanger into a cylinder and sleeve design, the stress applied by clamping the crystal becomes far more uniform. As it is applied uniformly around the entirety of the crystal, the diffracting surface is extruded linearly rather than being deformed, reducing the deformation variance across the diffracting surface.

The second benefit of applying the heat exchanger and clamping force as a cylinder is that it significantly increases the cooled surface area of the crystal; compared to the conventional I20 crystal assembly, the cooled area has been increased by over 200 %. This will allow the novel 'interference' design to extract more heat from the crystal than the conventional design, allowing higher beam powers to be used.

The third benefit is that all of the components in the novel design have a common longitudinal axis, as the crystal, heat exchanger, retaining pegs and coolant channels are all designed to lie in the same direction. This is in contrast to the conventional design, in which the steel bars, diffracting surface and coolant channels were all perpendicular to one another, introducing additional torques and cross-forces.

The final benefit of the novel 'interference' assembly is that the unit is 'set and forget'. Once the assembly has been put together it will remain as such, and does not need to be disassembled or aligned; the clamping force incurred by the interference fit will cause the crystal to self-align into the best fit available. Even when removed from the beamline, the novel design can be transported and

stored intact thanks to the brass retaining pegs holding the crystal in place at room temperature. The assembly was tested with four repetitions and no drift was observed.

## 8.5 Summary

While the conventional design has been assembled in accordance with the standard design philosophy for an indirectly cooled system, its small scale – notably that the diffracting surface is no larger than the beam footprint - has unfortunately brought many of the errors in this design philosophy to light simultaneously, resulting in a poor overall performance.

The simplest improvement that can be made to the existing I20 assembly is to have the heat exchangers remade such that they leave 5 mm of the diffracting crystal exposed; this will allow the thermal pathways to normalise within the crystal, as well as reducing the stress applied to the diffracting surface of the crystal. This work has found that all crystal designs could benefit from this new design element.

This work has found that direct cooling does not present a significant improvement when compared to indirect cooling; indeed, the drawbacks of direct cooling are far outweigh any benefit observed from a minimal reduction of peak temperature in the crystal. However, the indirect cooling method can be better applied to the considered systems, making use of trends in the performance of IMs and finding a balance point between thermal and mechanical deformation.

The most significant outcome of this work is the novel ‘interference’ design. This design addresses the five key problems identified in assembly design philosophy:

By harnessing and focusing the material properties such that they create the desired clamping force at cryogenic temperatures, they do not need to be mitigated as an uncontrollable source of deformation.

By redesigning the crystal to be a cylinder, and redesigning the heat exchanger to be a sleeve originating 5 mm below the diffracting surface, the clamping forces can be far more uniform and the

thermal pathways can be caused to normalise within the crystal, reducing the thermal and mechanical deformations.

By indirectly cooling the crystal but using design philosophies from direct cooling, the crystal can be cooled with peak efficiency without significant barriers to attaining or maintaining the cooling.

By carefully selecting the room temperature gap between the two components, the clamping force can be tuned such that the crystal is allowed to contract and expand unconstrained and still retain a strong clamping force at cryogenic temperatures.

By exerting such force through the copper that it deforms to match the surface profile of the silicon, the crystal and heat exchanger can be brought into very good thermal contact without the need for IMs; in fact, the copper can function as an IM.

Having designed these solutions to the five major issues in monochromator first crystals, a test assembly was manufactured, assembled and tested. Results were found to be significantly better than those observed in similar tests with the conventional crystal with a deformation across the diffracting surface of 30 nm, compared to the current assembly deformation of 400 nm, showing an order of magnitude improvement. In addition, very good thermal contact was observed with the crystal remaining within a degree of the heat exchanger once contact was established. As such, the novel 'interference' assembly has been deemed worthy of more testing in further work, utilising the synchrotron beam to test performance in situ.

## Bibliography

- Aragão, D. *et al.* (2018) 'MX2: a high-flux undulator microfocus beamline serving both the chemical and macromolecular crystallography communities at the Australian Synchrotron', *Journal of Synchrotron Radiation*, 25(3), pp. 885–891. doi: 10.1107/S1600577518003120.
- Beaumont, J. H. and Hart, M. (2001) 'Multiple Bragg reflection monochromators for synchrotron X radiation', *Journal of Physics E: Scientific Instruments*. IOP Publishing, 7(10), pp. 823–829. doi: 10.1088/0022-3735/7/10/014.
- Beer, A. (1852) 'Bestimmung der Absorption des rothens Lichts in farbigen Flüssigkeiten', *Annalen der Physik und Chemie*, 86(5), pp. 77–88.
- Bilderback, D. H. (1986) 'The potential of cryogenic silicon and germanium X-ray monochromators for use with large synchrotron heat loads', *Nuclear Instruments and Methods in Physics Research Section A: Accelerators, Spectrometers, Detectors and Associated Equipment*, 246(1–3), pp. 434–436. doi: 10.1016/0168-9002(86)90126-9.
- Bilderback, D. H. *et al.* (2000) 'The historical development of cryogenically cooled monochromators for third-generation synchrotron radiation sources.', *Journal of synchrotron radiation*, 7(Pt 2), pp. 53–60. doi: 10.1107/S0909049500000650.
- Boldeman, J. W. (2002) 'The Australian Synchrotron Light Source', in *Proc. of EPAC 2002, (Paris)*, pp. 650–652.
- Bonse, U. *et al.* (1976) 'Perfect-Crystal Monochromators for Synchrotron X-radiation', *Journal of Applied Crystallography*. International Union of Crystallography, 9(3), pp. 223–230. doi: 10.1107/S0021889876011011.
- Bragg, W. H. and Bragg, W. L. (1913) 'The Reflexion of X-rays by Crystals', in *Proceedings of the Royal Society of London*. The Royal Society, pp. 428–438. doi: 10.1098/rspa.1913.0040.
- Cannon, J. R. (1984) *The One-Dimensional Heat Equation*. Cambridge University Press.
- Carpentier, P. *et al.* (2001) 'Synchrotron monochromator heating problem, cryogenic cooling solution', *Nuclear Instruments and Methods in Physics Research, Section A: Accelerators, Spectrometers, Detectors and Associated Equipment*, 456(3), pp. 163–176. doi: 10.1016/S0168-9002(00)00578-7.
- Collins, K., Wagner, U. and Rau, C. (2010) *Design of a Horizontally Deflecting Quadruple Crystal Monochromator (QCM) For I13 at Diamond* Presenting author: Andrew Peach Organisation: Diamond Light Source.
- 'COMSOL Multiphysics' (2013). COMSOL.
- Crystal Scientific* (2011). Available at: [http://www.crystal-scientific.com/crystal\\_channel\\_cut.html](http://www.crystal-scientific.com/crystal_channel_cut.html) (Accessed: 21 November 2018).
- Desai, P. D. and Ho, C. Y. (1978) *Thermal Linear Expansion of Nine Selected Aisi Stainless Steels, Cindas Report 51*.

- Docker, P., Alcock, S. and Nistea, I. (2013) 'I20 Crystal Clamping Project'.
- Dooryhée, E. *et al.* (2004) 'Synchrotron X-ray analyses in art and archaeology', *Radiation Physics and Chemistry*, 71(3–4), pp. 863–868.
- Fitzpatrick, M. E. and Lodini, A. (2003) *Analysis of residual stress by diffraction using neutron and synchrotron radiation*. Taylor & Francis.
- Fourier, J. (1822) *Theorie analytique de la chaleur, par M. Fourier*.
- Glassbrener, C. J. and Slack, G. A. (1964) 'Thermal conductivity of silicon and germanium from 3°K to the melting point', *Physical Review*. New York: Physical Review, 134(4A), pp. A1058–A1069.
- Goldstone, D. C. *et al.* (2011) 'HIV-1 restriction factor SAMHD1 is a deoxynucleoside triphosphate triphosphohydrolase', *Nature*. Nature Publishing Group, a division of Macmillan Publishers Limited. All Rights Reserved., 480(7377), pp. 379–382. doi: 10.1038/nature10623.
- Golovchenko, J. A. (1981) 'X-ray monochromator system for use with synchrotron radiation sources', *Review of Scientific Instruments*. AIP Publishing, 52(4), p. 509. doi: 10.1063/1.1136631.
- Gooden, J. S., Jensen, H. H. and Symonds, J. L. (1947) 'Theory of the proton synchrotron', *Proceedings of the Physical Society*. IOP Publishing, 59(4), pp. 677–693. doi: 10.1088/0959-5309/59/4/315.
- Hill, C. *et al.* (2011) 'Fermilab - a plan for discovery', *Frontiers: A Journal of Women Studies*, p. 39.
- Hills, D. A. (2009) 'Residual Strain Analysis', *The Journal of Strain Analysis for Engineering Design*, 44(1), pp. i–iv. doi: 10.1177/030932470904400101.
- Holman, J. P. (1997) *Heat Transfer, 8th Edition*. McGraw-Hill.
- Huang, X. R. *et al.* (2012) 'Dispersive spread of virtual sources by asymmetric X-ray monochromators', *Journal of Applied Crystallography*. International Union of Crystallography, 45(2), pp. 255–262. doi: 10.1107/S0021889812003366.
- IUPAC (2006) 'Compendium of Chemical Terminology'. Blackwell Science, p. 450. doi: 10.1351/goldbook.
- Kaviany, M. (2002) *Principles of Heat Transfer*. John Wiley & Sons.
- Kreith, F., Manglik, R. M. and Bohn, M. S. (2010) *Principles of Heat Transfer Solutions*. Wiley.
- Lambert, J. H. (1760) *Photometria sive de mensura et gradibus luminis colorum et umbra*. Leipzig, W. Engelmann.
- Madhusudana, C. V. (2014) *Thermal Contact Conductance*. Cham: Springer International Publishing (Mechanical Engineering Series). doi: 10.1007/978-3-319-01276-6.
- Marion, P., Zhang, L. and Goirand, L. (2006) 'Cryogenic cooling of monochromator crystals: Indirect or direct cooling?', in *Proceeding MEDSI 2006*. Grenoble.
- Marquardt, E. D., Le, J. P. and Radebaugh, R. (2000) 'Cryogenic Material Properties Database', *11th International Cryocooler Conference*, 12(6), pp. 1–7. doi: 10.1016/0142-1123(90)90249-E.

- Matsushita, T. and Hashizume, H. (2009) *X-Ray Monochromators*.
- McMillan, E. M. (1945) 'The Synchrotron – A Proposed High Energy Particle Accelerator', *Physical Review*, 68(143), pp. 1–4.
- Milanez, F. H., Yovanovich, M. M. and Culham, J. R. (2002) 'Effect of surface asperity truncation on thermal contact conductance', in *InterSociety Conference on Thermal and Thermomechanical Phenomena in Electronic Systems, IITHERM*, pp. 186–192. doi: 10.1109/IITHERM.2002.1012456.
- Mishina, H. and Buckley, D. H. (1984) 'Friction behavior of silicon in contact with titanium, nickel, silver and copper'. doi: 10.1038/nature03880.
- Moorefield, D. (1993) 'Precision machine design', *Precision Engineering*. Prentice Hall, pp. 51–52. doi: 10.1016/0141-6359(93)90288-L.
- Mosselmans, F. (2018) *I20 Beamline Schematic*. Available at: [https://www.diamond.ac.uk/Instruments/Spectroscopy/I20/XAS\\_XES\\_Beamline/Specification.html](https://www.diamond.ac.uk/Instruments/Spectroscopy/I20/XAS_XES_Beamline/Specification.html) (Accessed: 21 November 2018).
- Murphy, B. M. *et al.* (2010) 'Degradation Of Parchment And Ink Of The Dead Sea Scrolls Investigated Using Synchrotron-Based X-Ray And Infrared Microscopy', in *Holistic Qumran: Trans-disciplinary Research of Qumran and Dead Sea Scrolls*. Brill, pp. 77–98. doi: 10.1163/ej.9789004181526.i-210.53.
- National Institute of Standards and Technology (NIST) (1992) 'Properties of Copper and Copper Alloys at Cryogenic Temperatures', Monograph, p. 270. Available at: <http://nvlpubs.nist.gov/nistpubs/Legacy/MONO/nistmonograph177.pdf>.
- NSLS-II Source Properties and Floor Layout* (2010). New York.
- Okada, Y. and Tokumaru, J. (1984) 'Precise determination of lattice parameter and thermal expansion coefficient of silicon between 300 and 1500 K', *Journal of Applied Physics*, 56(2), pp. 314–320.
- Petersen, K. E. (1982) 'Silicon As a Mechanical Material.', *Proceedings of the IEEE*, 70(5), pp. 420–457. doi: 10.1109/PROC.1982.12331.
- Roessle, M. (2012) 'Basics of X-ray Scattering'. Luebeck University of Applied Science, p. 49.
- Rogers, G. F. C. and Mayhew, Y. R. (1967) *Engineering, Thermodynamics, Work & Heat Transfer*. Second. Longman.
- Salerno, L. J. and Kittel, P. (2003) 'Thermal contact conductance', *Journal of Materials Processing Technology*, 135(2–3), pp. 204–210. doi: 10.2514/2.6203.
- Seltzer, S. and Hubbell, J. (1995) 'Table and graphs of photon mass attenuation coefficients and mass energy-absorption coefficients for photon energies 1 keV to 20 MeV for elements Z= 1 to 92 and some dosimetric materials', *National Institute of Standards and Technology*.
- Shah, J. S. and Straumanis, M. E. (1972) 'Thermal expansion behavior of silicon at low temperatures', *Solid State Communications*, 10(1), pp. 159–162. doi: 10.1016/0038-1098(72)90371-7.
- Sham, T. K. and Rivers, M. L. (2002) 'A Brief Overview of Synchrotron Radiation', *Reviews in Mineralogy and*

*Geochemistry*, 49(1), pp. 117–147. doi: 10.2138/gsrmg.49.1.117.

Snaith, B., O’Callaghan, P. W. and Probert, S. D. (1984) ‘Interstitial materials for controlling thermal conductances across pressed metallic contacts’, *Applied Energy*. Elsevier, 16(3), pp. 175–191. doi: 10.1016/0306-2619(84)90019-9.

Stimson, J. *et al.* (2016) ‘Analytical model for heat absorption: Lessons learned from a one dimensional model’, in *AIP Conference Proceedings*, p. 040028. doi: 10.1063/1.4952900.

Stimson, J. *et al.* (2017) ‘A Thermal Exploration of Different Monochromator Crystal Designs’, in *Proceedings of MEDSI2016, Barcelona, Spain*. JACOW, Geneva, Switzerland, pp. 176–178. doi: 10.18429/JACOW-MEDSI2016-TUPE10.

Stimson, J. *et al.* (2017) ‘The application of interference fits for overcoming limitations in clamping methodologies for cryo-cooling first crystal configurations in x-ray monochromators’, in *IOP Conference Series: Materials Science and Engineering*, p. 012055. doi: 10.1088/1757-899X/278/1/012055.

Stronger, F. and To, L. (1991) *Materials Science and Engineering*. ASM International. doi: 10.1177/00220345850640051201.

Tipler, P. A. (1999) *Physics for scientists and engineers*. W.H. Freeman/Worth Publishers.

Torikoshi, M. *et al.* (2001) ‘Design of synchrotron light source and its beamline dedicated to dual-energy x-ray computed tomography.’, *Journal of biomedical optics*. International Society for Optics and Photonics, 6(3), pp. 371–7. doi: 10.1117/1.1383062.

Veksler, V. I. (1944) ‘A new method of accelerating relativistic particles’, *Comptes Rendus (Doklady) de l’Academie Sciences de l’URSS.*, 43(8), pp. 329–331. Available at: <http://lhe.jinr.ru/rus/veksler/wv0/publikacii/1944Veksler.pdf> (Accessed: 13 August 2018).

Venkenna, B. K. (2010) *Fundamentals of heat and mass transfer*. PHI.

Wagner, U. H. *et al.* (2013) ‘Beamline design and instrumentation for the imaging and coherence beamline I13L at the Diamond Light Source’, in *Journal of Physics: Conference Series*, p. 182006. doi: 10.1088/1742-6596/425/18/182006.

Wilson, E. J. N. (1996) ‘Fifty years of synchrotrons’, in *5th European Particle Accelerator Conference*. Spain, pp. 135–139.

Zhang, L. *et al.* (2013) ‘Thermal deformation of cryogenically cooled silicon crystals under intense X-ray beams: Measurement and finite-element predictions of the surface shape’, *Journal of Synchrotron Radiation*, 20(4), pp. 567–580. doi: 10.1107/S0909049513009436.

Zheng, S. *et al.* (2001) ‘Structural studies of the HIV-1 accessory protein Vpu in Langmuir monolayers: Synchrotron X-ray reflectivity’, *Biophysical Journal*. Cell Press, 80(4), pp. 1837–1850. doi: 10.1016/S0006-3495(01)76154-1.



## Appendix A: “Analytical Model for Heat Absorption: Lessons Learned from a One Dimensional Model” – Presented at SRI 2015, published in AIP Conference Proceedings 2016 (Stimson et al., 2016).

**Abstract.** An analytical model was constructed of a single silicon crystal monochromator. This model was used to examine the heat transfer processes within the monochromator. It was discovered that extracting heat from the top surface of the monochromator could cause the peak temperature to be below the surface of the crystal; this dislocation was shown to be approximately 10% of the thickness of the crystal when 20% of the input power was extracted from the top surface.

### UNDERSTANDING THE PROBLEM – THE CURRENT SYSTEM

Most X-ray synchrotron facilities use monochromators composed of single crystals of silicon to extract X-rays of a selected wavelength from the broad spectrum emitted by the radiation source. The unwanted radiation heats the crystal non-uniformly as it is absorbed, inducing strains that broaden the diffracted beam, increase its divergence and degrade its bandwidth<sup>1</sup>. To deal with this heat load, many facilities use liquid nitrogen to cool their crystals<sup>2-4</sup>, while facilities with lower heat loads use water cooling systems<sup>4</sup>. Such cooling systems are classified as direct if the coolant is in contact with the crystal and indirect if a path of thermally conducting materials separates the coolant from the crystal.

Current cooling designs have been sufficient until now, but planned increases in the X-ray flux generated by synchrotrons and X-ray free electron lasers are intensifying the demands on their performance. This work details the preliminary findings of a collaborative PhD program associating the Diamond Light Source and Birmingham City University. The first crystal of the indirectly cooled 4-bounce silicon-crystal monochromator (Fig. 1.a) in use on the Diamond beamline I20 will be reviewed here as a practical case for future improvements in cooling.

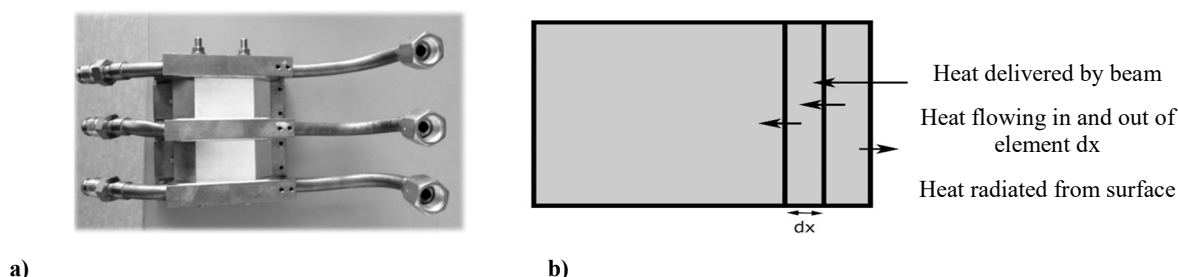


**FIGURE 1.** a) The monochromator crystal assembly as used at Diamond Light Source, consisting of two single silicon crystals held in a copper heat exchanger. An indium foil is visible between these, as well as the copper pipes that carry the liquid nitrogen to the heat exchanger.

b) Simple one dimensional model showing the heat transfer processes present in the crystal.

The thermal distortion of the monochromator crystals is now limiting the performance of many synchrotron sources and the development of an effective monochromator cooling system is therefore a priority for all synchrotron sources. The analysis of such a complex structure is necessarily complicated as it involves many different types of material, thermal and mechanical junctions, all of which can lead to results that are particularly difficult to interpret. In order to better understand heating and the resultant distortion of the monochromator we have developed a simple one dimensional analytical model, shown above in Fig. 1.b). This will help us to investigate the basic physics of power absorption, heat flow and deformation, particularly in a simple, bulk crystal. A one-dimensional model is justified if the incident beam illuminates the crystal surface uniformly (as could be done with a wiggler beam), if the cooling occurs only at the crystal surface opposite the incident beam, all the crystal’s side surfaces are perfectly insulated and the cooling is applied to the end surface of the crystal.

### UNDERSTANDING THE PHYSICS - THE ANALYTICAL MODEL

To begin to understand the underlying physics of the system we designed and built a one dimensional analytical model. We first considered the general heat diffusion equation as shown in Eq. a,

$$\frac{\partial}{\partial x} \left[ k(T(x,t)) \frac{\partial T(x,t)}{\partial x} \right] = k(T(x,t)) \frac{\partial^2 T(x,t)}{\partial x^2} + \frac{\partial k(T(x,t))}{\partial T} \left( \frac{\partial T(x,t)}{\partial x} \right)^2 = \rho c \frac{\partial T(x,t)}{\partial t} - P(x) \quad \text{a)}$$

where  $x$  is the length coordinate,  $t$  is elapsed time,  $\rho$  is the density of the material,  $c$  is the specific heat capacity,  $T(x,t)$  is the temperature,  $k(T(x,t))$  is the linear thermal conduction as a function of temperature and  $P(x)$  is the input power at the given point  $x$ .

This equation governs the heat flow within any solid body. In this case, the input power of the system,  $P(x)$ , is the power deposited by the light beam, as given in Eq. b. Here we have assumed a monochromatic beam; in reality both the initial intensity and attenuation coefficient would change with each wavelength. Also, we have not accounted for the amount of energy carried away by the Bragg diffracted beam as this would be very low compared to the intensity of the sum of the other wavelengths.

$$P(x) = \mu I_0 e^{-\mu x} \quad \text{b)}$$

where  $\mu$  is the attenuation coefficient (dependent on the wavelength of light and material) and  $I_0$  is the intensity of the beam at the surface.

We have simplified the heat diffusion equation by considering the crystal to be in the steady state:

$$\frac{d}{dx} \left[ k(T(x)) \frac{dT(x)}{dx} \right] = -\mu I_0 e^{-\mu x} \quad \text{c)}$$

As a first approximation we have simplified our calculations by assuming  $k$  to be independent of temperature. This is expected to be valid for a thin crystal that exchanges little power with its surroundings, as then the temperature should be nearly uniform along the crystal's length. This gives us the following equation:

$$\frac{d^2 T(x,t)}{dx^2} = -\frac{\mu I_0 e^{-\mu x}}{k} \quad \text{d)}$$

The other process present in the crystal is heat loss due to radiation, as shown in Eq. e below. Rather than being included in the heat diffusion equation this process is applied separately as an iterative process; the radiation is reliant on the surface temperature, but also changes it. As such we must recalculate the power loss iteratively until we reach equilibrium. It is important to note that in situ a heat shield cooled by liquid nitrogen has been installed opposing the monochromator crystal; this allows radiation from the crystal to the shield for a net loss of energy, rather than from the environment to the crystal for a net gain.

$$dP = \varepsilon \sigma (T_{crystal}^4 - T_{shield}^4) A \quad \text{e)}$$

where  $dP$  is the number of joules lost to the environment per unit time,  $\varepsilon$  is the emissivity of the material,  $\sigma$  is the Stefan-Boltzmann constant,  $T_{crystal}$  is the temperature of the hot surface of the crystal,  $T_{shield}$  is the temperature of the heat shield, maintained at 80K to optimize radiation, and  $A$  is the surface area.

As our simple analytical model was based on a second order differential we required two boundary conditions. Equation (e) is already one boundary condition, but because this is complex, the temperature and the temperature gradient at the rear surface of the crystal have been chosen here. The former was set to 80K to emulate a flow of liquid nitrogen, while the latter was defined in terms of the percentage of incident power such that we could model the radiation from the opposite surface, which here is treated as a small perturbation that balances the total power flow into and out of the crystal.

## RESULTS - THE PEAK TEMPERATURE

We ran our analytical model using the values given in Table 1 below. The absorption coefficient was chosen assuming a 12keV beam, as this is the peak power at the aforementioned I20 beamline. The intensity at the surface assumes the beam delivers 500W uniformly across the crystal surface, 1mm on each side. The thermal conductivity used is that of silicon at 80K, as is the emissivity. The cross-sectional area and crystal thickness are not those used at the I20 but are simplifications.

**TABLE 1.** Description of variables used throughout simulations.

Variable Name	Represents	Value	Units
$\mu$	Absorption coefficient	48.42 [5]	1/m
$I_0$	Intensity at surface	5e8	W/m <sup>2</sup>
$k$	Thermal conductivity	1900 [6]	W/m/K
$\varepsilon$	Emissivity	0.7 [7]	
$A$	Cross-sectional area	1e-6	m <sup>2</sup>
$x$	Crystal thickness	0.1	m

The first observation we made was that contrary to popular belief, thinner crystals are less susceptible to overheating, as shown in Figure 2.a). The most important factor here appears to be the distance between the absorbing region and the

cooling system. This means thicker crystals have a larger region at constant positive temperature gradient, giving rise to a peak temperature dependent on the thickness of the crystal.

The second interesting discovery was that the hottest part of the crystal is not at the surface. As the penetration depth of X-rays in silicon is significant<sup>7</sup> and energy is lost from the surface in the form of grey body radiation, the point with the highest temperature is actually some distance inside the crystal. This phenomenon was first observed assuming significant heat loss due to grey body radiation; approximately 20% loss gave the results shown in Fig. 2.a). Note that the range of temperature shown in Fig. 2.a) is indeed small enough (about 6 K) to validate the initial assumption of temperature-independent thermal conductivity.

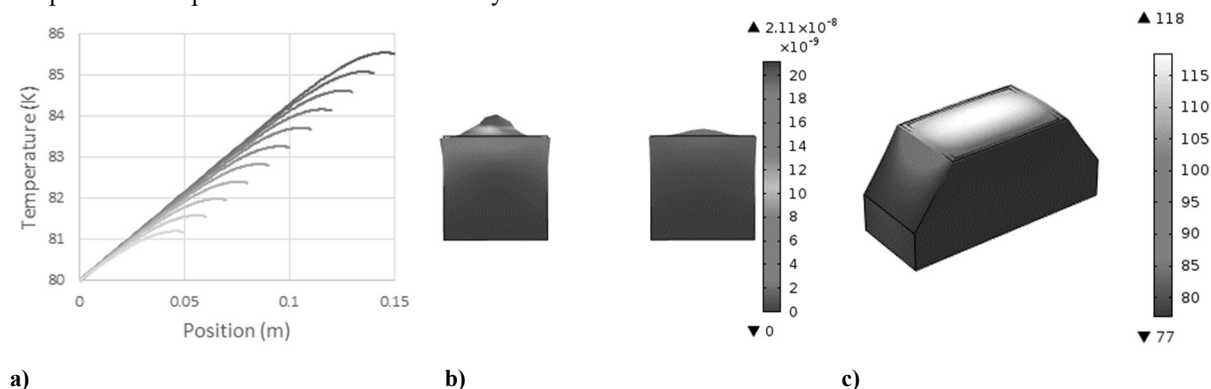


**FIGURE 2.** a) Graph showing the temperature at varying depths; each line shows a different length of crystal from 0.05m to 0.15m. b) Finite element simulation showing the difference between a plateau lift (left) with heat source within the block and a heat bulge (right) with surface heat source; both heat sources are 10W point sources. The colour bar shows deformation in metres. c) Finite element simulation of a monochromator crystal with incident beam power of 500 W. Deformation is scaled x100. The colour bar shows absolute temperature in deg K.

We then ran the analytical model with more physical terms, based on the I20 beamline at the Diamond Light Source; the beam was modelled as 25mm x 38mm delivering a total power of 500W. We also modelled a heat shield, setting the cold temperature for the grey body radiation at 80K. However, due to the region reaching peak temperatures being within the beam footprint, which is only on the scale of millimeters, and with the hottest region barely reaching 200K, the energy loss is very small – approximately 60mW. This only pushes the peak heat below the surface an order of nanometers. However, we note that in this case more accurate treatments of Eq. (c) are required because the thermal conductivity varies from  $19.5 \text{ W cm}^{-1} \text{ K}^{-1}$  at 80 K to  $3.2 \text{ W cm}^{-1} \text{ K}^{-1}$  at 200 K, invalidating the initial assumption that thermal conductivity is independent of temperature for a model of more realistic dimensions. Methods for obtaining such solutions are now under development.

Although this shows us that the phenomenon is not significant in practice it gives rise to an interesting possibility; if we were to cool the surface of the crystal sufficiently to drive the temperature peak into the body of the crystal, it should be possible to cause the thermal distortion to produce a plateau lift rather than a bulge, as shown in Fig. 2.b). By reducing the variation of the deformation we would diffract fewer wavelengths of light, reducing both the wavelength spread and the divergence. This would require us to extract approximately 20% of the incident power from the surface, either through radiation, surface cooling or a mixture of both.

## THE THIRD DIMENSION - FINITE ELEMENT ANALYSIS

Although a one dimensional model is useful to help us understand the mechanisms at work within the crystal, it is far from physically complete. In order to truly understand the heat flow in the system, we needed to consider all three dimensions. While it is possible to build an analytical model from base principles in three dimensions it is very constrained as to what boundary conditions it can model. Instead we have used finite element analysis software, namely COMSOL Multiphysics. This has allowed us more freedom, as we can enter more varied physical constraints.

We first used the FEA software to confirm our earlier findings, running the same boundary conditions as those given in Table 1 above to ensure our results were accurate. The exception to this was the thermal conductivity; as COMSOL is a more powerful program than our analytical model we were able to read in a full range of thermal conductivities from 0K to 400K, apply an interpolation and interrogate it for the appropriate  $k(T)$ . Once again we observed a peak temperature within the material, showing that our earlier models were correct.

Once this was complete, we moved on to modelling complete silicon crystals as shown in Figure 2.c). These simulations used the dimension of the silicon monochromator crystals used at the I20 beamline at Diamond Light Source. The crystals are 0.038m thick, with a diffracting surface of 0.025m x 0.018m. We also used the interpolated thermal conductivity mentioned above and the physical constants from Table 1. So far, we have assumed a universal intensity across the surface of the crystal akin to that produced by a wiggler emission source. This has shown us that although the

system only reaches a peak temperature of 118K, there is quite a varied thermal deformation across the surface; this broadens the bandwidth of the diffracted beam.

Currently our focus is on the mechanisms through which the X-rays interact with the crystal. We are considering a number of mechanisms, including Bragg diffraction, Fresnel reflection, photon-phonon interactions, and free hole and electron production - the last of which could lead to a higher thermal conductivity than previously expected.

## REFERENCES

- <sup>1</sup> L. Zhang, M. Sánchez Del Río, G. Monaco, C. Detlefs, T. Roth, A.I. Chumakov, and P. Glatzel, *J. Synchrotron Radiat.* **20**, 567 (2013).
- <sup>2</sup> D.H. Bilderback, a K. Freund, G.S. Knapp, and D.M. Mills, *J. Synchrotron Radiat.* **7**, 53 (2000).
- <sup>3</sup> P. Marion, L. Zhang, and L. Goirand, in *Proceeding MEDSI 2006* (Grenoble, 2006).
- <sup>4</sup> P. Carpentier, M. Rossat, P. Charrault, J. Joly, M. Pirocchi, J.L. Ferrer, O. Kaïkati, and M. Roth, *Nucl. Instruments Methods Phys. Res. Sect. A Accel. Spectrometers, Detect. Assoc. Equip.* **456**, 163 (2001).
- <sup>5</sup> S. Seltzer and J. Hubbell, *Natl. Inst. Stand. Technol.* (1995).
- <sup>6</sup> C.J. Glassbrener and G.A. Slack, *Phys. Rev.* **134**, A1058 (1964).
- <sup>7</sup> ICRU, *Radiation Quantities and Units* (Bethesda, 1980).

## Appendix B: “A Thermal Exploration of Different Monochromator Crystal Designs” – Presented at MEDSI 2016, published in Proceedings of MEDSI2016, 2017 (Joshua Stimson et al., 2017).

### *Abstract*

Eight potential monochromator crystal designs were subjected to a combination of three different beam powers on two different footprints. The temperature and thermal deformation were determined for each. It was found that thermal deformation of the lattice is negligible compared to the surface curvature, and that while the thinnest crystal wafer showed the smallest temperature increase, crystals cooled from the bottom alone demonstrated a far more uniform thermal deformation and a larger radius of curvature.

### INTRODUCTION

In this work we have explored various monochromator crystal designs. Monochromator crystals are used to select a single wavelength of x-rays from the broad spectrum produced in a synchrotron device [1-2]. The high energies these crystals are subjected to causes them to heat up significantly, leading to thermal deformations that distort the uniform surface of the crystal, leading to multiple wavelengths being selected [3-4]. This is problematic as it is not always obvious whether the change in wavelength at the detector is due to thermal distortion of the monochromator or interaction with the sample being tested.

In order to attempt to reduce or even eliminate this thermal deformation it must be understood how different variables affect the system. To this end we have modelled several different designs of monochromator crystal to see what effect changing the geometry has on the thermal deformation.

As we are concerned primarily with thermal behaviours, we have made a number of approximations. The cooled surfaces remain at 80 K throughout to approximate the flow of liquid nitrogen with an ideal thermal contact [5]. This is a very non-physical boundary condition, which means the results are not directly comparable to real world systems. However, for the purpose of this work it has been used to create a directly comparable baseline between the different models.

It is also assumed that each crystal has thermalized prior to exposure to the beam, and therefore is initially at a uniform temperature of 80 K.

Three beam powers were considered; 110 Watts, 550 Watts and 1100 Watts. This was to simulate exposure to low power, high power and future high power beams as used at the Diamond Light Source. Each of these powers had to be applied using the Beer-Lambert law of beam transmission [6], as shown in Eq. (1) below.

$$I = I_0 e^{-\mu x} \quad (1)$$

In Eq. (1)  $I$  is the intensity of the beam,  $I_0$  is the intensity of the beam at the surface,  $\mu$  is the absorption coefficient and  $x$  is the distance into the material.

As the beam produced by the I20 beamline is broad spectrum, this calculation was done for each energy and then integrated across all energies as shown in Eq. (2).

$$I = \int I_0(E) e^{-\mu(E)x} dE \quad (2)$$

In Eq. (2)  $I_0(E)$  is the intensity of the beam at the surface for x-rays of a given energy and  $\mu(E)$  is the absorption coefficient for x-rays of the given energy in silicon.

This was done for the measured intensities of each wavelength at the I20 beamline for the given power values. The intensity penetrates the surface, decreasing as it propagates.

Two major factors were considered; the deformation of the diffracting surface could change both the spacing of the lattice layers and change the angle of incidence, both of which can damage the Bragg diffraction desired by modifying lattice layer structure [1].

These are only an issue if they are non-uniform across the diffracting surface, as a uniform change can be allowed for when angling the monochromator crystal. As such the radius of curvature of the diffracting surface has been calculated at the centre of the surface for each design.

The curvature,  $k$ , can be calculated by mapping some function  $y$  to the deformation of the surface, then applying Eq. 3 [7].

$$k = \frac{\left(\frac{d^2y}{dx^2}\right)^{\frac{3}{2}}}{1 + \left(\frac{dy}{dx}\right)^2} \quad (3)$$

The radius of curvature is simply the reciprocal of the modulus of curvature [7], as shown in Eq. 4.

$$R = \frac{1}{|k|} \quad (4)$$

A larger radius of curvature relates to a flatter crystal surface, i.e. the larger the radius of curvature the better.

The lattice spacing as a function of temperature was also calculated, to see if a non-uniform temperature gave rise to a non-uniform lattice that would have affected the Bragg diffraction. However, calculations showed that between 150 K and 80 K the lattice spacing varied only by  $5.5e-15$  m, a statistically negligible change given the lattice spacing is only of the order of Angstroms. This shows that the variance of the lattice spacing directly due to temperature is unlikely to impact the Bragg diffraction.

Despite varying designs between the different crystals, the mechanical boundary conditions used stay the same; each crystal is anchored by a single fixed point in the centre of its base, with a line extending from this point to the diffracting surface prescribed movement in the  $x$ - and  $y$ -directions. The entire crystal is also mounted to a spring foundation of ten Newtons per metre. This combination of boundary conditions enables us to model free thermal expansion, giving an accurate image of how each crystal would behave.

## METHOD

Eight monochromator crystal designs were considered, varying structure and/or cooling method: the current monochromator design for Diamond's I20 beamline, a number of modifications to that crystal and then a silicon wafer. These designs are subjected to each of the incident powers in both the minimum and maximum angles of the beam footprint, i.e. at a footprint of  $36$  mm x  $25$  mm representing an incident beam angle of  $30^\circ$  to the crystal and at a footprint of  $5$  mm x  $25$  mm representing an incident beam angle of  $6^\circ$  to the crystal.

The first design modelled was the crystal currently used in Diamond Light Source's I20 beamline as shown in Fig. 1. The crystal is based on a rectangle with the top edges removed; this is to allow the beam to pass, as the I20 beamline features very little space between the monochromator crystals. The entire crystal is thermalized at  $80$  K, to represent liquid nitrogen cooling reaching an equilibrium.

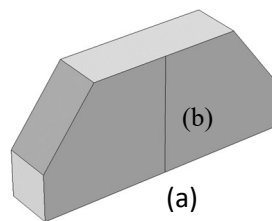


Figure 1: a cutaway view of the existing I20 monochromator crystal design. Point (a) is held fixed while line (b) is restrained in the  $x$ - and  $y$ -directions.

The next model simulated was using the same crystal design as shown in Fig. 1, but this time cooling only the bottom surface. This was to allow the heat to dissipate more evenly through the crystal, and was anticipated to produce less overall cooling and a higher peak temperature but a more uniform deformation across the diffracting region.

In order to explore alternate designs we next simulated a five-hundred-micron silicon wafer as shown in Fig. 2. Theoretically by reducing the thickness of the crystal we should allow more of the waste X-ray to pass through, reducing the thermal load on the crystal and therefore the peak temperature.

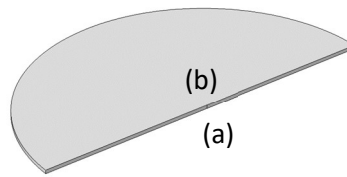


Figure 2: a cutaway view of the silicon wafer monochromator crystal design. Point (a) is held fixed while line (b) is restrained in the x- and y-directions.

## RESULTS

Although eight crystal structures were modelled, in the interest of brevity we have chosen the existing crystal and the two most interesting results to explore here in depth. Figures 3, 4 and 5 show the temperature distribution and resulting deformation caused by the 1100 W power in the 30° configuration.

In the current I20 crystal with both sides cooled as well as the base, the temperature profile is drastic as shown in Fig. 3; the centre of the diffracting surface is somewhat hotter than the edges, resulting in stresses in the diffracting surface. There is high stress particularly in the centre of the diffracting region; this could cause a stress dislocation, where the lattice misaligns as a result of the stress on it. The crystal surface distorts by fifty-five picometres over a width of twenty-five millimetres, giving rise to a radius of curvature of 688,000 m (3s. f) at the centre of the diffracting surface.

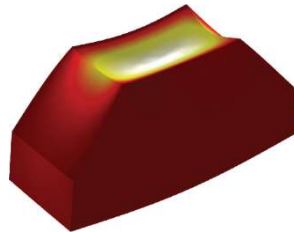


Figure 3: The current I20 monochromator after thirty second exposure to the 1100 W beam at a 30o angle of incidence.

With only the bottom cooled, we see a far more uniform temperature profile in the diffracting region as shown in Fig. 4. There is very little stress in the diffracting region; what stress is found is on the edges of the crystal and is formed by the surface contracting; in essence the crystal is attempting to curl up. Although the crystal as a whole deforms more, it is worth noting that the relative deformation of the diffracting region is largely constant due to the lack of cooling on the sides. The diffracting surface deforms by forty picometres over a width of 25 mm, giving a radius of curvature of 917,000 m (3s.f.) at the centre.

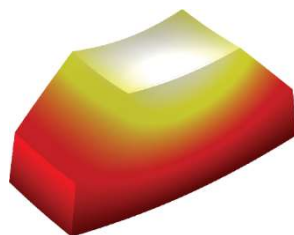


Figure 4: The current I20 monochromator cooled from the bottom only after thirty second exposure to the 1100 W beam at a 30° angle of incidence.

As theorised the thinner crystal does accomplish a slightly lower temperature than that of the current crystal design. However, due to the thinness of the crystal it bows very easily under the lower temperature as shown in Fig. 5; the diffracting surface deforms by six hundred picometres, resulting in a radius of curvature of 103,000 m (3s.f.) at the centre.

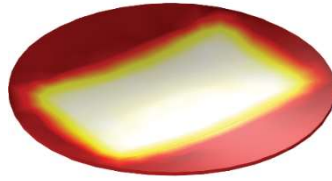


Figure 5: The silicon wafer monochromator after thirty second exposure to the 1100 W beam at a 30° angle of incidence.

## CONCLUSION

To help analyse the performance of the crystals the radius of curvature of each design at each power has been plotted on Figs. 6 & 7 for the 30° and 6° angle of incidence respectively.

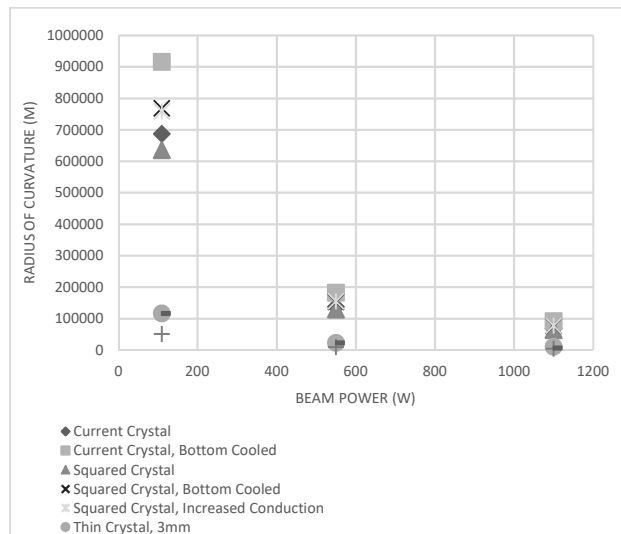


Figure 6: Radius of curvature as a function of beam power deposited in a 36 mm footprint.

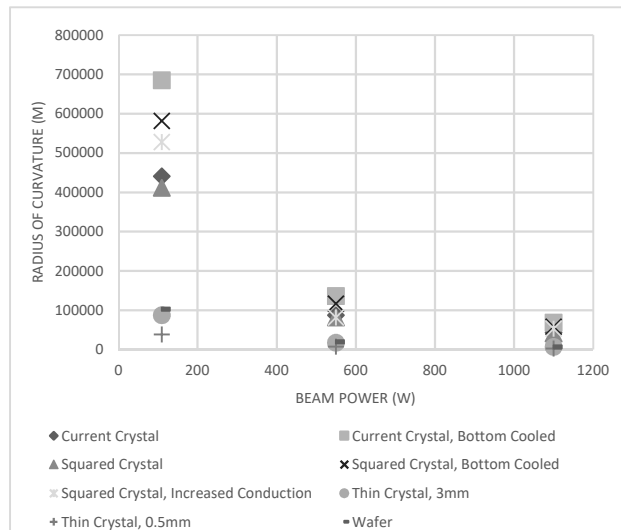


Figure 7: Radius of curvature as a function of beam power deposited in a 5mm footprint

A common feature of all the models tested is that the thinner the crystal, the lower the maximum temperature. This is due to the heat conducting to the cooled surface in less time when the crystal is thinner. However, due to their flexibility these designs also show significant bowing with a lower radius of curvature.

The models with consistently the highest radius of curvature, and therefore the least bowing, are thicker crystals cooled from the bottom alone. This design allows the heat to dissipate more evenly, though more slowly, throughout the crystal, resulting in less variation in the deformation and a higher radius of curvature.

The next step is to explore the mechanical side of these designs; how would they be held in good thermal contact with the heat exchangers and what steps can be taken to minimise mechanical stresses upon them. Many synchrotron facilities clamp their monochromator crystals between heat exchangers to hold them in the beam path; this design is not compatible with the concept of cooling the crystal from the base alone. However, bolting directly down to a heat exchanger or cooling the bolting plate itself could cause stresses to develop in the diffracting surface as the crystal contracts from the surface. Further work is needed to ascertain the feasibility of this approach.

## REFERENCES

- [1] W. H. Bragg and W. L. Bragg, "The Reflexion of X-rays by Crystals," in *Proceedings of the Royal Society of London*, 1913, pp. 428–438.
- [2] J. A. Golovchenko, "X-ray monochromator system for use with synchrotron radiation sources," *Rev. Sci. Instrum.*, vol. 52, no. 4, p. 509, Apr. 1981.
- [3] P. Carpentier, M. Rossat, P. Charrault, J. Joly, M. Pirocchi, J. L. Ferrer, O. Kaïkati, and M. Roth, "Synchrotron monochromator heating problem, cryogenic cooling solution," *Nucl. Instruments Methods Phys. Res. Sect. A Accel. Spectrometers, Detect. Assoc. Equip.*, vol. 456, no. 3, pp. 163–176, 2001.
- [4] L. Zhang, M. Sánchez Del Río, G. Monaco, C. Detlefs, T. Roth, A. I. Chumakov, and P. Glatzel, "Thermal deformation of cryogenically cooled silicon crystals under intense X-ray beams: Measurement and finite-element predictions of the surface shape," *J. Synchrotron Radiat.*, vol. 20, pp. 567–580, 2013.
- [5] D. H. Bilderback, a K. Freund, G. S. Knapp, and D. M. Mills, "The historical development of cryogenically cooled monochromators for third-generation synchrotron radiation sources.," *J. Synchrotron Radiat.*, vol. 7, no. Pt 2, pp. 53–60, 2000.
- [6] A. Beer, "Bestimmung der Absorption des rothen Lichts in farbigen Flüssigkeiten," *Ann. Phys.*, vol. 162, no. 5, pp. 78–88, 1852.
- [7] A. Borovik and M. G. Katz, "Who Gave you the Cauchy-Weierstrass Tale? The Dual History of Rigorous Calculus." 2011.

## Appendix C: “The Application of Interference Fits for Overcoming Limitations in Clamping Methodologies for Cryo-Cooling First Crystal Configurations in X-Ray Monochromators” – Presented at CEC-ICMC 2017, published in IOP Conference Series, 2017 (J. Stimson et al., 2017).

**Abstract.** The work detailed here describes how a novel approach has been applied to overcome the challenging task of cryo-cooling the first monochromator crystals of many of the world’s synchrotrons’ more challenging beam lines. The beam line configuration investigated in this work requires the crystal to diffract 15 Watts of 4-34 keV X-ray wavelength and dissipate the additional 485 watts of redundant X-ray power without significant deformation of the crystal surface. In this case the beam foot print is 25 mm by 25 mm on a crystal surface measuring 38 mm by 25 mm and maintain a radius of curvature of more than 50 km. Currently the crystal is clamped between two copper heat exchangers which have LN2 flowing through them. There are two conditions that must be met simultaneously in this scenario: the crystal needs to be clamped strongly enough to prevent the thermal deformation developing whilst being loose enough not to mechanically deform the diffracting surface. An additional source of error also occurs as the configuration is assembled by hand, leading to human error in the assembly procedure. This new approach explores making the first crystal cylindrical with a sleeve heat exchanger. By manufacturing the copper sleeve to be slightly larger than the silicon crystal at room temperature the sleeve can be slid over the silicon and when cooled will form an interference fit. This has the additional advantage that the crystal and its heat exchanger become a single entity and will always perform the same way each time it is used, eliminating error due to assembly. Various fits have been explored to investigate the associated crystal surface deformations under such a regime

### 1. Introduction

A synchrotron device is a cyclic particle accelerator. Electrons are raised to considerable speed by a linear accelerator before being injected into an initial “booster ring”, a circular beam path with pulsed magnetic fields in which the particle is further accelerated. Once the electron has reached near-relativistic speeds, it is ejected into a larger “storage ring”, in which the velocity of the electron is maintained. At intervals around the storage room there are insertion devices, each of which consists of a series of high strength opposed dipoles, which undulate the electron’s path. As the electron is moving at relativistic speeds, whenever it is accelerated it emits the excess energy in the form of a photon. The high velocity of the electron coupled with the minor permutations of the path induced by the insertion device causes the electron to remain close to the emitted photons, resulting in the emitted light falling into the X-ray range. (1–3)

This raw light is produced as a broad spectrum, from which one wavelength is selected via Bragg diffraction (4) using a series of single crystal silicon monochromator as shown in figure 1. These silicon crystals diffract the selected X-ray wavelength, dependent on the angle of incidence, and absorb the rest of the spectrum. As these synchrotron facilities are upgraded these first crystals are expected to absorb more power to the point that the current cooling methods have reached a plateau where any further increase to beam power results in significant thermal deformation of the diffracting surface (5).

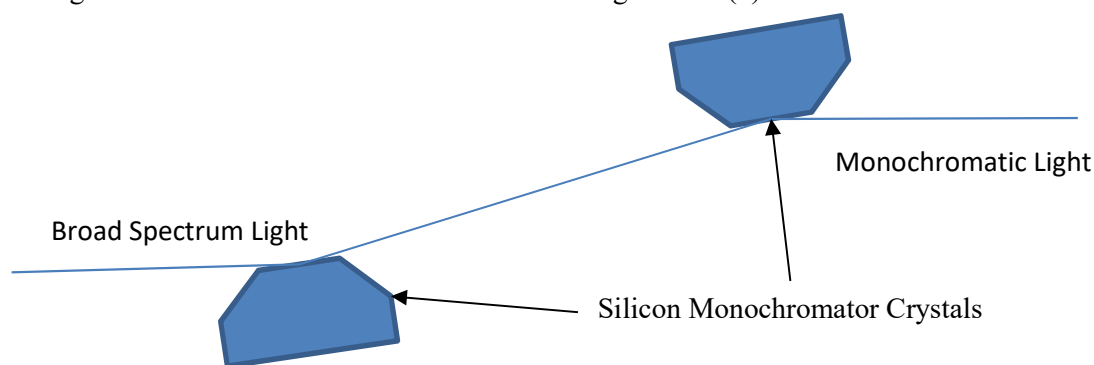


**Figure 1.** The path of a beam through the monochromator series.

There are two main approaches to cooling the silicon crystals: they are most often cooled indirectly, through contact with a heat exchange unit with a through flow of liquid nitrogen; in some cases they are cooled directly, by flowing liquid nitrogen through the body of the crystal itself. Indirect cooling has become the industry standard mainly because heat exchangers are easily constructed, whereas direct cooling requires delicate seals which are only functional for a finite number of cycles before they must be replaced, resulting in far greater costs (6). Until now indirectly cooling the monochromators has been sufficient, but with rising power levels many facilities are looking for new solutions to handle higher heat loads.

The efficiency of indirectly cooling the crystals is dominated by the force applied (7), so that the best way to improve indirect cooling efficiency is to increase the force applied. This is due to only a small number of asperities on the two surfaces actually coming into contact; increasing the force applied deforms these asperities, allowing more to contact. Thus, in order to cool the crystal in the most efficient fashion we need to apply greater and greater forces. However, these forces can in themselves mechanically deform the diffracting surface, potentially causing a greater issue than the heat itself. This means that increasing the clamping forces reduces thermal deformation, but increases mechanical deformation. This suggests that there would be a point where the mechanical deformation overcame the thermal as the dominant deformation, although a literature search found no documentation on such an occurrence.

The final factor to consider for such a cooling system is the distribution of the stress field. If the stress field is applied in a non-uniform pattern, it would cause a non-uniform deformation of the monochromator crystal before any thermal load was even applied (8). As such it is vital that the stress field is uniform.

A current limitation of the system is that the physical assembly of the monochromator imparts multiple stress vectors of varying magnitude and direction, through tightening bolts, attaching the liquid nitrogen manifold and differing thermal expansion coefficients of different materials. Any new system should be adapted to avoid these shortfalls, by not tightening the assembly with bolts, applying the liquid nitrogen manifold parallel to the diffracting surface and minimizing or utilizing the varying thermal expansion characteristics of the materials used.

## 2. Method

In order to produce a high intensity, uniform stress field an interference fit was modelled using the COMSOL MultiPhysics Finite Element Modelling software, with the copper heat exchanger designed as a sleeve around the silicon crystal as shown in figure 2.

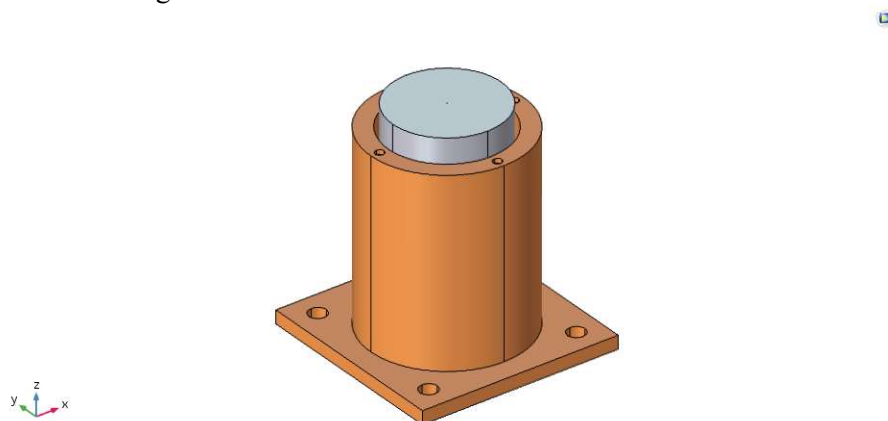


**Figure 2.** An interference fit monochromator design with copper sleeve as the hub component and single crystal silicon shaft as the shaft component.

An interference fit is created when two objects attempt to occupy the same space, interfering with each other. In most cases it is achieved by heating the hub component, expanding it thermally, and then slotting it over the shaft component. As the hub cools, it shrinks, bringing it into contact with the shaft component (9). However, with two dissimilar materials such as copper and silicon, it becomes more complex. First, copper has a thermal expansion coefficient an order of magnitude greater than that of silicon. Secondly, silicon

experiences a negative thermal expansion coefficient beneath 120 K, causing it to expand when the silicon is cooled. These thermal expansion coefficients are shown in figure 3 (10–12).

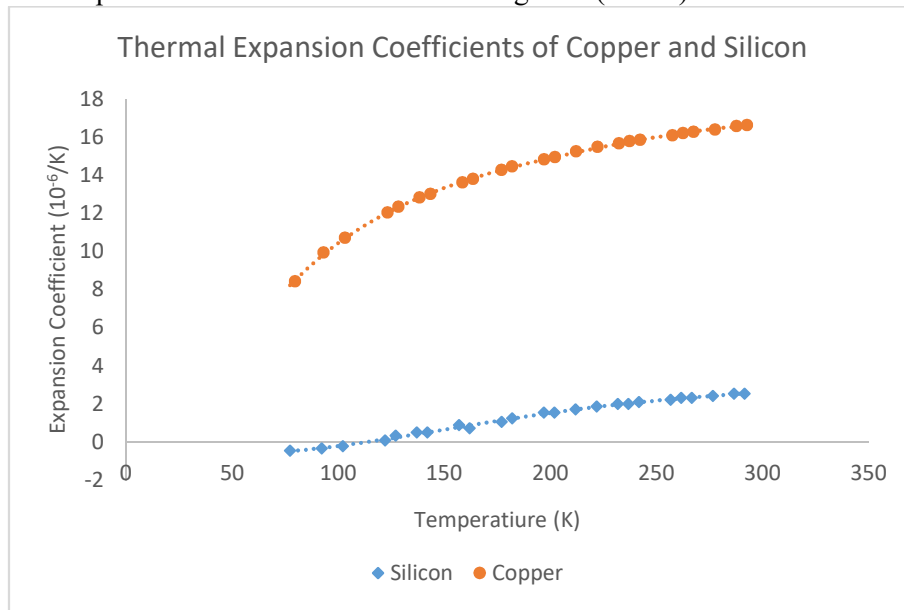


**Figure 3.** Thermal expansion coefficients of Silicon and Copper.

Due to the extreme variation between the two coefficients, it is possible to leave a gap at room temperature and still achieve a high pressure interference fit after cooling. In order to identify whether there should be a gap, and if so what size, the equation below (9) was used to model the pressure achieved during cooling at bare contact and at a range of room temperature gap values analytically in SciLab, the output of which is shown in figure 4.

$$P = \frac{d_{so} - d_{ho} + \Delta T(\alpha_s - \alpha_h)d_{hi}}{\frac{d_{hi}}{E_h} * \left( \frac{d_{ho}^2 + d_{hi}^2}{d_{ho}^2 - d_{hi}^2} + \nu_h \right) + \frac{d_{so}}{E_s} * \left( \frac{d_{so}^2 + d_{si}^2}{d_{so}^2 - d_{si}^2} - \nu_s \right)} \quad (1)$$

Where:

$d_{hi}$  is the inner diameter of the hub

$d_{ho}$  is the outer diameter of the hub

$d_{si}$  is the inner diameter of the shaft

$d_{so}$  is the outer diameter of the shaft

$E_h$  is the Young's modulus of the hub

$E_s$  is the Young's modulus of the shaft

$\nu_h$  is the Poisson's ratio of the hub

$\nu_s$  is the Poisson's ratio of the shaft

$\Delta T$  is the temperature difference between assembly and operation

$\alpha_s$  is the thermal expansion coefficient of the shaft

$\alpha_h$  is the thermal expansion coefficient of the hub

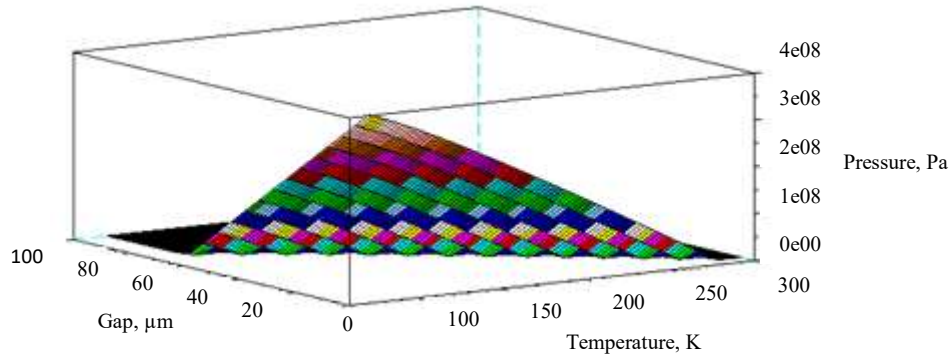


**Figure 4.** Pressure as a function of temperature and gap at room temperature.

To determine the pressure we wanted to induce in the system we considered three factors. First we compared the ultimate compressive stresses of silicon and copper in literature, coming to values of 700 MPa (11) and 358 MPa (12) respectively. As the value for silicon is nearly twice that of copper, we can be confident that the copper sleeve will plastically deform around the silicon, rather than crushing it.

Next, in order to maintain a flat diffracting surface we needed to ensure that the force of linear expansion produced by the silicon's expansion, as shown in equation 2, would be greater than the friction caused by the copper clamping on the silicon, as shown in equation 1 above. (13). Equation 2 allows us to calculate the force generated from the thermal deformation of either material should they be constrained and unable to move. By solving equation 2 simultaneously for the silicon and copper components we are able to find the axial clamping force. If the axial clamping force exceeds the linear expansion force, the interference face of the silicon would be restrained while the core is relatively free, resulting in a bulge in the center of the diffracting face; whereas if the expansion force were to be greater the silicon interference face would slip against the copper. We can tune this axial clamping force by leaving a gap between the two materials at room temperature, as shown in Figure 4 above.

$$F = \alpha Y A \Delta T \quad (2)$$

Where:

- $F$  is the force produced
- $\alpha$  is the coefficient of thermal expansion
- $Y$  is the Young's Modulus of Elasticity
- $\Delta T$  is the change in temperature

Finally we had to consider the performance of the current system; to produce a comparable thermal transport we would have to at least match the clamping pressure of the existing system, which is set at 190 N.

### 3. Results

Solving equations 1 and 2 together we came to an optimal room temperature gap value of 60 μm in order to give us the highest possible pressure without mechanically constraining the interference face of the silicon. We then built another FMA model in COMSOL using this gap, the boundary conditions of which are shown in Figure 5. By assigning the bottom-most surface as unable to move in the z-direction and a central axis as unable to move in the x- or y- directions, we produce a stable and well-constrained model that is subject to thermal expansion. We then held the inner surfaces of the hollow copper sleeve constant at 80 K to simulate the flow of liquid nitrogen, and all outer surfaces of the copper as radiating to a temperature of 80 K to simulate a heat shield.

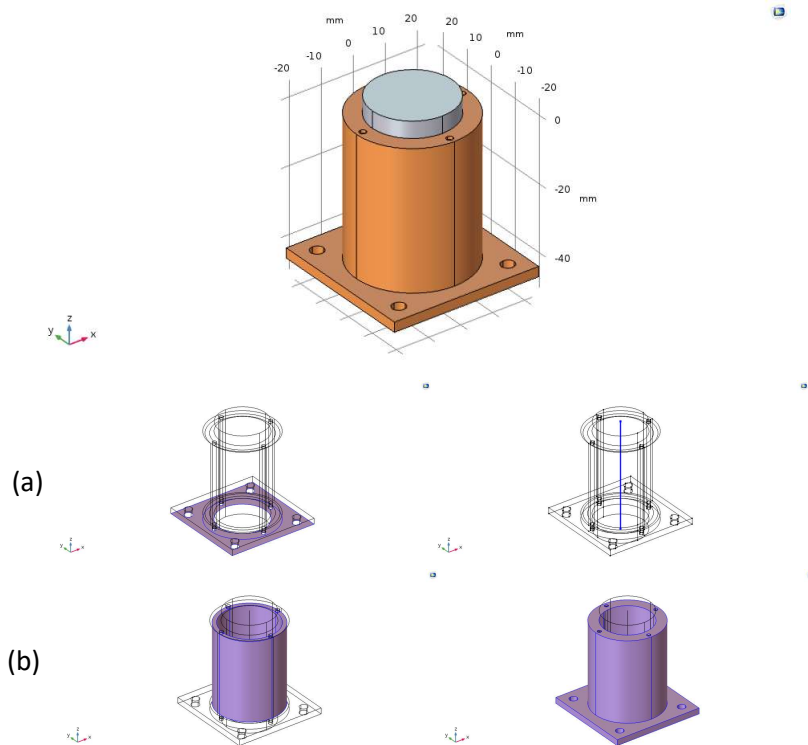


**Figure 5.** Copper and silicon interference fit model with a 60  $\mu\text{m}$  gap at room temperature.  
 a) Mechanical boundary conditions, left to right: Shaded surface subject to prescribed displacement ( $z = 0$ ); Bold line subject to prescribed displacement ( $x$  &  $y = 0$ ).  
 b) Thermal boundary conditions, left to right: Shaded surfaces subject to fixed temperature (80 K); Shaded surfaces subject to diffuse surface (to 88 K).

After the model reached a steady state, effectively cooling from 300 K to 80 K, the resulting surface profile is shown in Figure 6. The entire surface is pushed up 5.2  $\mu\text{m}$ , and the edge is raised a further 0.1  $\mu\text{m}$ . The surface is also very uniformly deformed, due to the circular stress field acting on a circular crystal.

Surface: Displacement field, Z component (mm) Max/Min Surface: Total displacement (mm)

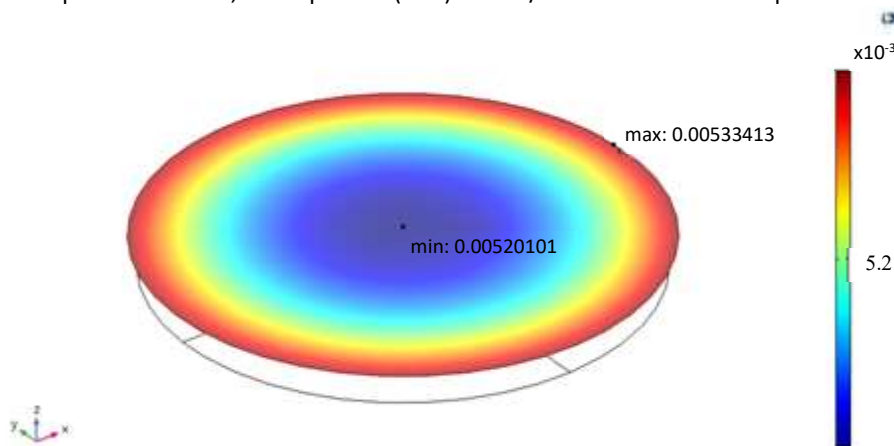


**Figure 6.** Deformation of diffracting surface after applied mechanical pressure.

We compared this surface deformation of our new design to one generated by a model of the existent system, as shown in Figure 7.

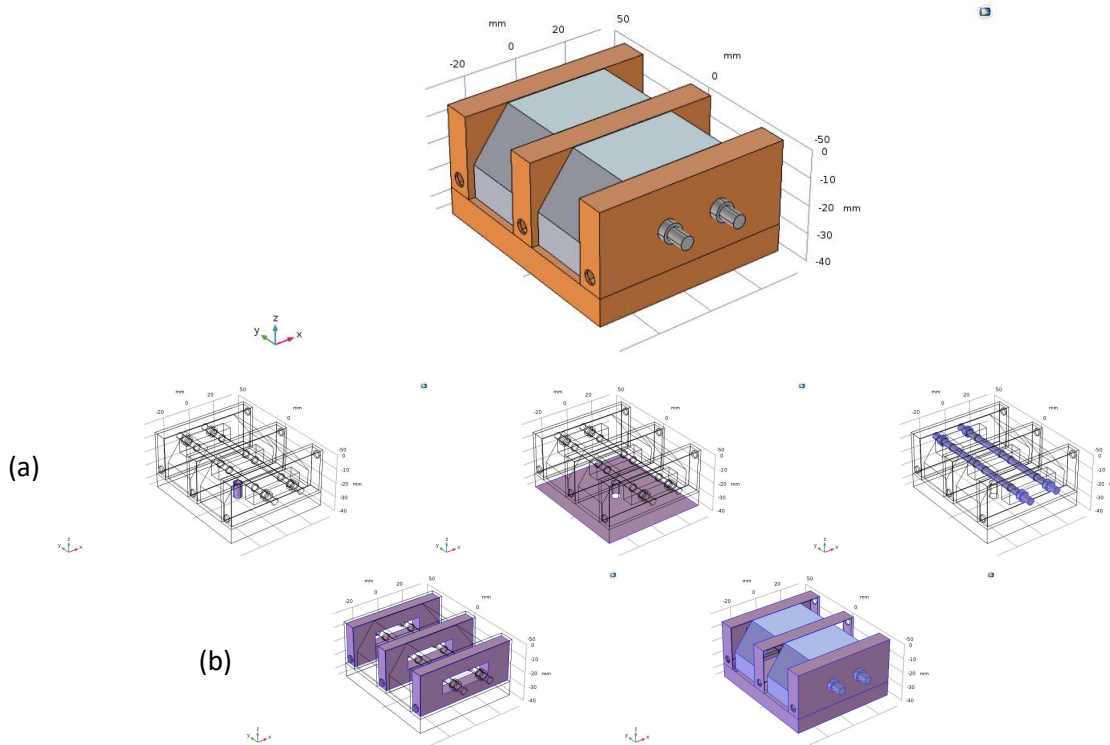


**Figure 7.** Copper and silicon standard assembly model.

- a) Mechanical boundary conditions, left to right: Shaded surface subject to fixed constraint; Shaded surface subject to prescribed displacement ( $z = 0$ ); Shaded volume pretensioned (190 N).
- b) Thermal boundary conditions, left to right: Shaded surface subject to fixed temperature (80 K); Shaded surface subject to diffuse surface (to 88 K).

Figure 7 shows the first crystal monochromator assembly currently used at the I20 beamline at Diamond Light Source in Oxford, with a copper base-plate and heat exchange attached to two silicon crystals by way of two stainless steel bolts. Matching boundary conditions were used where possible, with the bottom surface secured in the  $z$ -direction and the fastening bolt for the assembly treated as a true fixed domain. The bolts in this model were pre-tensioned with a 190 N force to match standard operating procedure. Again, the inside of the heat exchangers were fixed at 80 K to simulate the flow of liquid nitrogen, and all outer surfaces were treated as radiating to 80 K to simulate a heat shield.

The surface profile of one of the silicon crystals is shown in Figure 8. The surface is bent in a “V” shape by the differing expansion coefficients of the various materials, with the center being pulled down by  $17.8 \mu\text{m}$  and the outer corners being raised by  $2 \mu\text{m}$ . The deformation varies significantly along the  $x$ -axis, due to the differing materials exerting different stress profiles on the crystal.

Surface: Displacement field, Z component (mm) Max/Min Surface: Total displacement (mm)

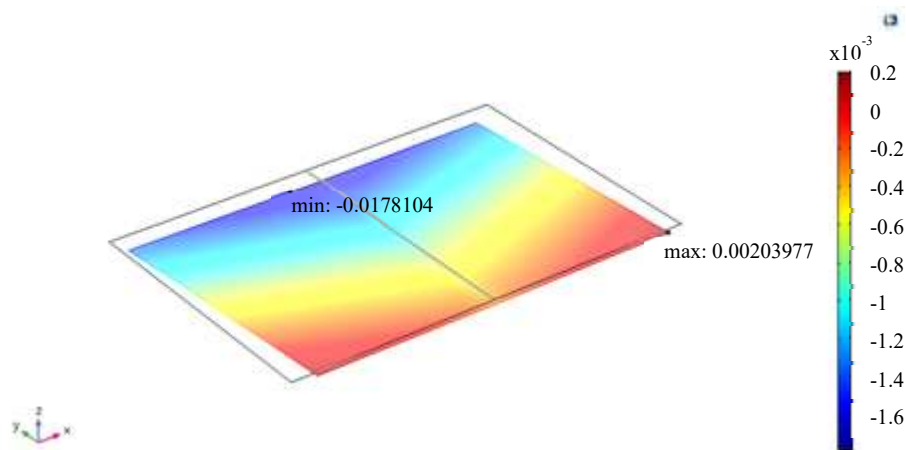


**Figure 8.** Deformation of diffracting surface after applied mechanical pressure.

#### 4. Discussion

The results show that an interference fit is capable of applying enough force to parallel that used in the existing system without applying such force that the diffracting surface would be significantly mechanically deformed. This means an interference cooled crystal will be capable of giving us a reduced surface deformation compared to a standard rectangular crystal and heat exchange assembly, due to the far more uniform stress field and higher force between the crystal and the heat exchange. This would allow us to use higher beam powers without deforming the diffracting surface such that the beam is lost.

In addition, by clamping the crystal using an interference fit we would not be introducing strains and rotations to the assembly as are conventionally incurred by manually assembling the system using bolts. It will also give us a far more precise control over the clamping pressure than achieving it by turning nuts. The use of fewer materials, and the application of the differing material properties to create the clamping, results in a more uniform temperature profile.

#### Further Work

In light of the models presented in this work, we are now in the process of manufacturing heat exchangers to fit cylindrical silicon crystals. A Fizeau interferometer will be used to measure the surface deformation imparted by interference fits of varying magnitudes.

In addition, we will be exploring the application of the interference fit to produce a gas-tight seal by decreasing the gap, possibly even to the extent of interference fitting above room temperature. The pressures involved should be able to produce a gas-tight seal without significantly deforming the diffracting surface of the crystal. To test this theory, the heat exchange sleeves will be tested to see if they are able to hold a gas-tight seal.

#### References

1. McMillan EM. The Synchrotron – A Proposed High Energy Particle Accelerator. *Phys Rev.* 1945;68(143):1–4.
2. Wilson EJN. Fifty years of synchrotrons. In: 5th European Particle Accelerator Conference. Spain; 1996. p. 135–9.
3. Sham TK, Rivers ML. A Brief Overview of Synchrotron Radiation. *Rev Mineral Geochemistry.* 2002;49(1):117–47.
4. Bragg WH, Bragg WL. The Reflexion of X-rays by Crystals. In: *Proceedings of the Royal Society of*

- London. The Royal Society; 1913. p. 428–38.
5. Zhang L, Sánchez Del Río M, Monaco G, Detlefs C, Roth T, Chumakov AI, et al. Thermal deformation of cryogenically cooled silicon crystals under intense X-ray beams: Measurement and finite-element predictions of the surface shape. *J Synchrotron Radiat.* 2013;20(4):567–80.
  6. Marion P, Zhang L, Goirand L. Cryogenic cooling of monochromator crystals: Indirect or direct cooling? In: *Proceeding MEDSI 2006. Grenoble; 2006.*
  7. Salerno LJ, Kittel P. Thermal contact conductance. *J Mater Process Technol.* 2003;135(2–3):204–10.
  8. Malvern LE. *Introduction to the mechanics of a continuous medium.* Prentice-Hall; 1969. 713 p.
  9. Bower AF. *Applied Mechanics of Solids.* 1st ed. 2011. 820 p.
  10. Shah JS, Straumanis ME. Thermal expansion behavior of silicon at low temperatures. *Solid State Commun.* 1972 Jan;10(1):159–62.
  11. Petersen KE. Silicon as a Mechanical Material. *Proc IEEE.* 1982;70(5):420–57.
  12. National Institute of Standards and Technology (NIST). *Properties of Copper and Copper Alloys at Cryogenic Temperatures.* 1992;Monograph:270. Available from: <http://nvlpubs.nist.gov/nistpubs/Legacy/MONO/nistmonograph177.pdf>
  13. Moorefield D. Precision machine design. Vol. 15, *Precision Engineering.* 1993. p. 51–2.

## Appendix D: “On the Effect of Clamping Force and Interstitial Materials on Room Temperature Thermal Contact Conductance” – Under Review for Publication

J. Stimson<sup>1</sup>, M. Ward<sup>1</sup>, P. Docker<sup>2</sup>

1. School of Engineering and the Built Environment, Birmingham City University, Curzon Street, Birmingham, B4 7XG
2. Diamond Light Source, Diamond House, Fermi Ave, Harwell Science Campus, Oxfordshire, OX11 0DE

### 1. Abstract

Thermal contact conductance was measured between two cylinders of copper (C101) at varying pressures and with various interstitial materials. It was found that higher pressures improve the thermal gap conductance, but with diminishing returns; thicker interstitial materials were more efficient than thinner pieces; and that the malleability of the interstitial material has a greater effect on gap conductance than its conductivity.

### 2. Introduction

Many processes used in manufacturing, processing and research produce waste heat<sup>1,2</sup> which needs to be removed in order for the mechanism to continue functioning. There are two main methods to extract this heat; direct cooling, where the hot body is exposed to some form of coolant, and indirect cooling, where the hot body is put in contact with a heat exchanger.<sup>1,3</sup> Both direct and indirect cooling methods have both benefits and drawbacks; indirect cooling tends to have a lower cost and greater lifespan, while direct cooling has greater higher efficiency.<sup>4</sup> This work looks to two of the major factors of indirect cooling: the contact force holding the hot body to the heat exchanger, and the use of interstitial materials to improve conductance.

In indirect cooling, a discrete heat exchanger is attached to the body in need of cooling. This discrete heat exchanger is cooled by means of an integrated coolant system, often some form of cycling liquid, such as water or colder substances such as liquid nitrogen depending on application.<sup>5</sup> There are many factors that affect the efficiency of such systems; in this work we are looking to address the effects of varying clamping force, i.e. the force used to mechanically hold the two bodies together.

When two bodies are brought into contact, very few parts of the two surfaces actually touch due to the micro-asperities on even well-polished surfaces. Any two surfaces will initially contact in three points; first, the location where both surfaces are most proud will meet, after which the two bodies pivot around this point until the next proudest points meet, and finally the bodies will rotate around the line created by the previous two points until a third contact is made. At this point the bodies can no longer freely move toward one another, as they are in contact; further application of force will cause the asperities in contact to deform and flatten, increasing the contact area at these points and allowing more, lower points to come into contact.<sup>6</sup>

A common method to improve the performance of thermal contact conductance is to introduce an interstitial material between the two bodies; this is often a more malleable material, used to help improve the number and distribution of contact points between the two bodies.<sup>7,8</sup>

Here we wish to investigate the performance of various interstitial materials, as well as the reliance of thermal contact conductance on clamping force. To this end an experimental apparatus has been designed and used to test a range of conventional interstitial materials, as well as a couple of novel designs.

### 3. Method

Two copper cylinders were machined from C101 grade copper (99.9% purity) which measured 25mm diameter and 50mm long. One of these cylinders, hereafter referred to as the “hot body”, had a relief cut into it to fit a Watlow® Ultramic® Ceramic Heater such that the top most point of the heater was below the surface of the cylinder. The other cylinder, hereafter referred to as the “cold body”, had a cylindrical hole drilled through it such that a length of 2 cm diameter copper pipe could be fed through and fastened in place. Into both cylinders three 12.5 mm deep by 1 mm diameter holes were drilled, separated by 12.5 mm along the long axis and rotated by 120 ° relative to each other, such that they were equidistantly spaced along the cylinder with their ends along the central axis, with no two boreholes aligned with each other. For clarity their positions in the experimental set up can be seen in Figure 1 below.

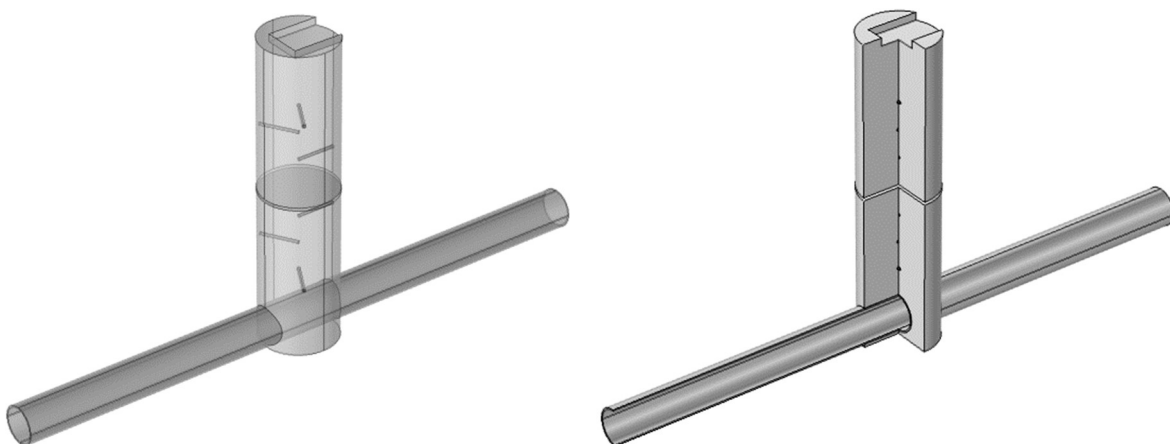


*Figure 1 – Thermal contact conductance testing apparatus. Left image shows translucent full assembly; right image shows solid assembly with cutaway to show alignment of thermocouple boreholes.*

Each of the six narrow boreholes (three in each cylinder) was fitted with a type-K thermocouple, such that the joint was positioned at the centre of the cylinder. Each of these thermocouples was secured in place with a conductive metal epoxy resin. For ease of reference the thermocouples were named 1 – 6 from top to bottom, such that 1 was closest to the heater, 1-3 were in the hot body, 4-6 were in the cold body and 6 was nearest the water cooling system.

The assembly was mounted in a Testronic® stress-test machine with a sheet of PTFE plastic above and below the assembly, as shown in Figure 2 below, as well as a double layer of aluminium foil sandwiching a layer of fibreglass wool insulation between the heater and the PTFE. In order to ensure linear heat flow and minimise heat loss to the environment, the assembly was wrapped in two layers of aluminium foil.

The heater at the top of the hot body was powered with a Delta Elektronika SM 52-30 1500 W power supply set to maintain a power output of 60 W. The copper pipe at the bottom of the cold body was connected to a HAILEA HC-100A chiller unit set to 18 °C with a header tank of 10 L. Two AllPondSolution AQ-600 submersible pumps were used, one to circulate water between the chiller and the tank and the other to circulate water through the cooling pipe at a rate of 600 litres per hour.

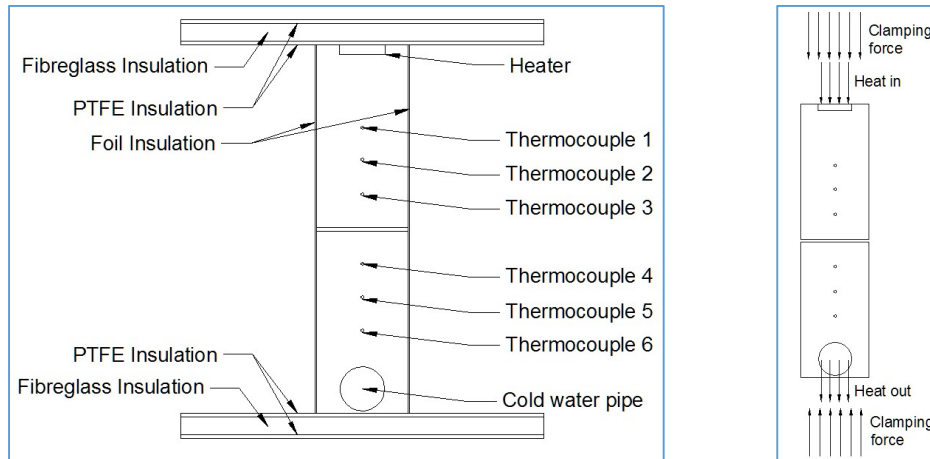


Figure 2 – Left: gap conductance assembly schematic, with thermocouple locations numbered.  
Right: gap conductance force diagram, with clamping forces and heat movement labelled.

Before each series of tests, the chiller unit and both pumps were powered on and run until the header tank had reached 18 °C. Each test started by supplying power to the heater, from which point the readings of the six thermocouples were logged at 10 samples per second for 20 minutes to ensure the system had reached a thermal equilibrium.

The last 1000 temperature readings for each thermocouple were averaged to remove noise and plotted against the position of the thermocouples. Due to the insulation in the apparatus, the heat transfer is linear and restrained to within the body of the cylinders. This causes the three temperature readings in each body to fall on a straight line, the gradient of which is dependent on the thermal conductivity of the copper and the temperature the heater reaches. This straight line was then extrapolated to the boundary for both cylinders, allowing us to estimate the temperature on both sides of the thermal contact with a degree of confidence.

Using this forecast, we can calculate the gap conductance using Equation 1 below.<sup>9</sup>

$$q = \frac{T_A - T_B}{\frac{\Delta x_A}{k_A A} + \frac{1}{h_C A} + \frac{\Delta x_B}{k_B A}}$$

Equation 1

Where  $q$  is the power input into the system,  $T_A$  and  $T_B$  are the respective temperatures of the hot and cold bodies,  $\Delta x_A$  and  $\Delta x_B$  are the respective thermal expansions of the hot and cold bodies between the location

the temperature readings were taken and the location of the boundary,  $k_A$  and  $k_B$  are the respective coefficients of thermal conduction for the hot and cold bodies,  $A$  is the cross-sectional area of the interface between the two bodies and  $h_c$  is the thermal conductance coefficient of the gap.

As we have extrapolated the temperature at the boundary,  $\Delta x_A$  and  $\Delta x_B$  both become zero, allowing us to simplify Equation 1 into Equation 2 as shown below.

$$q = \frac{T_A - T_B}{\frac{1}{h_c A}}$$

$$\frac{q}{h_c A} = T_A - T_B$$

$$h_c = \frac{q}{A(T_A - T_B)}$$

*Equation 2*

By inserting the appropriate values into Equation 2 we can find the thermal contact conductance for each setup.

We first tested the effect of clamping force on gap conductance, and then moved on to differing interstitial materials, which were inserted between the hot and cold bodies. Another avenue of investigation was the reuse of the indium foils; in many applications the indium foil is considered single use before it must be replaced, so the conductance of reused samples was tested to investigate the possibility of reusing foils. The variables tested are detailed in Table 1 below.

*Table 1 – variables tested for thermal gap conductance*

<b>Variable</b>	<b>Range</b>
Added Load (Clamping force)	10 N 100 N 1 000 N 10 000 N
Interstitial Materials	None Indium foil (50 $\mu\text{m}$ thickness) Indium foil (250 $\mu\text{m}$ thickness) Indium foil (500 $\mu\text{m}$ thickness) Indium Corporation Heat-Spring® Copper foam (63% porosity, 3.32 $\text{g}/\text{cm}^3$ density, 4 mm thickness)
Interstitial Material Reuse	Indium foil (250 $\mu\text{m}$ thickness) unmoved Indium foil (250 $\mu\text{m}$ thickness) rotated 90°

In addition to standard indium foils as interstitial materials, we are also testing a novel material produced by the Indium Corporation, their Heat-Spring® Thermal Interface Material (TIM). The Heat-Spring® is manufactured from an indium alloy, with a specially engineered surface profile as shown in Figure 3 below. The surface profile is designed to distribute contact points throughout the material, helping to spread the thermal load through the entirety of the interface. The sample obtained for this work is 100  $\mu\text{m}$  thick.

Another novel material we are testing is a copper foam produced by GoodFellow (CU003804/3)<sup>10</sup>. This is a sponge-like copper structure, produced by bubbling argon gas through liquid copper. The resulting solid foam has a porosity of 63%, reducing its density significantly compared to bulk copper. The intention was to trial a material more malleable than solid copper but less so than indium, although a far better conductor in its own right than indium. The sample obtained for this work was 4 mm thick.

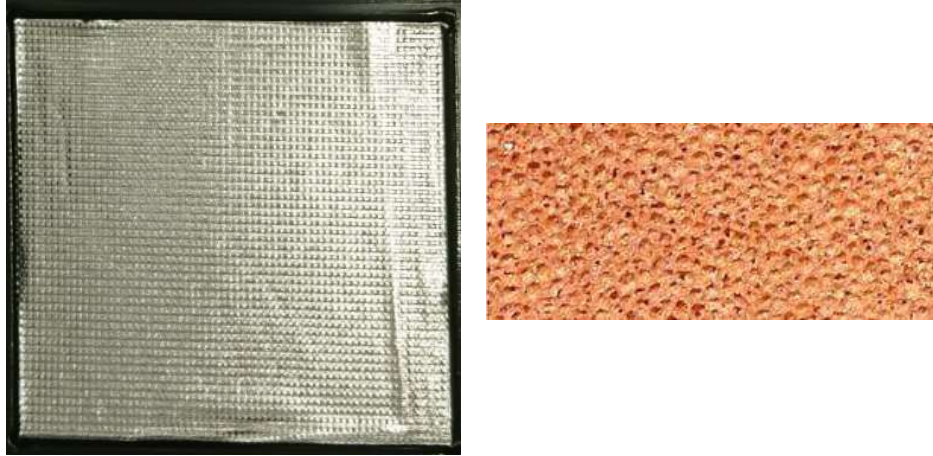


*Figure 3 – Top: Heat-Spring Thermal Interface Material (TIM) produced by the Indium Corporation. Surface profile is designed to distribute thermal contact points across a wider area compared to conventional interstitial materials.*

*Bottom: Copper foam surface profile produced by GoodFellow. Material is 63% porous.*

#### **4. Results**

The time-dependent temperature logs proved to be in keeping with theory – for each test, the temperature at each probe rose slowly before plateauing. Once all six probes were at plateau, the system was at thermal equilibrium. The spacing between each of the three hot body probes and each of the three cold body probes was evenly distributed, with a larger gap between probes 3 and 4. An example is shown in Figure 3 below, for a 100N load with a fresh piece of 50  $\mu\text{m}$  indium foil.

The final 1000 readings were averaged for each probe, and plotted against the position of the probe. A trendline was fitted to each of the bodies, which was then forecast to the boundary in each body as shown in Figure 4.

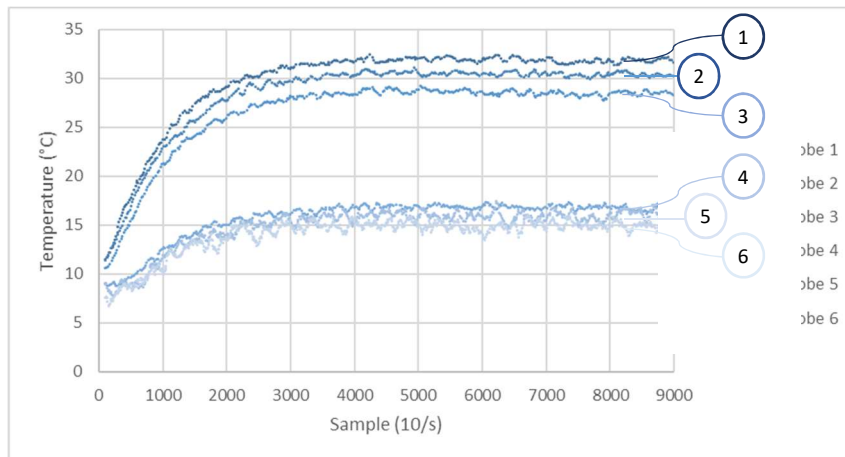


Figure 4 – graph showing temperature at all six probe locations over time. Note the large gap between probes 3 and 4, located either side of the boundary.

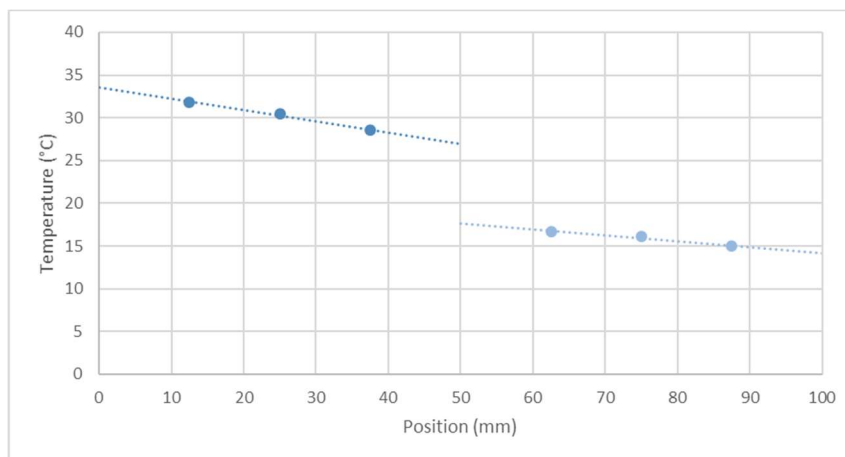


Figure 5 – graph showing the equilibrium gap temperature. The temperature was measured at the six points and the trend lines were linearly forecast to the ends of the hot and cold body.

Using this interfacial temperature difference and Equation 2 above, we were able to calculate the gap conductance for each combination of clamping forces and interstitial materials. Our findings are represented graphically in Figure 5 to Figure 7 below.

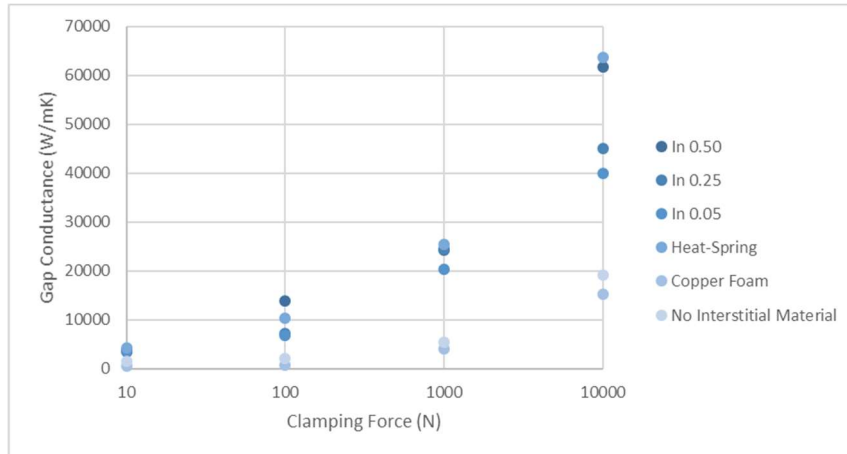


Figure 6 – graph showing gap conductance as a function of clamping force for various interstitial materials

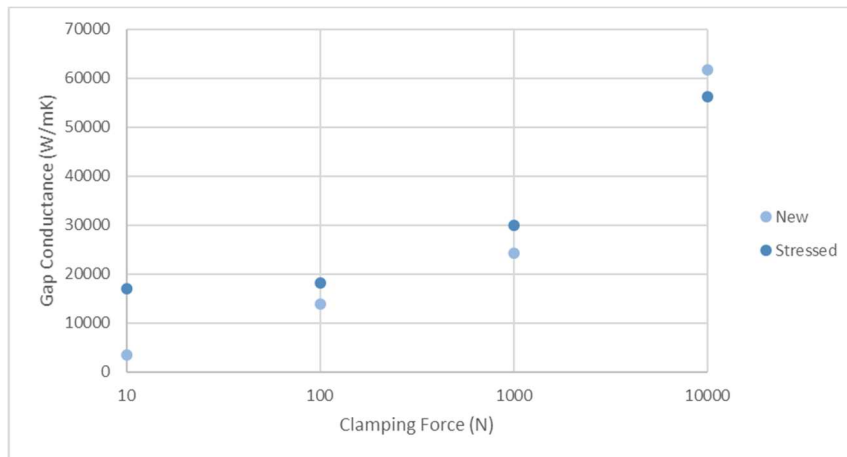


Figure 7 – graph showing gap conductance as a function of clamping force for a new piece of 50 μm indium foil compared to a piece that has been used (i.e. stressed to 10 000 N) and re-used.

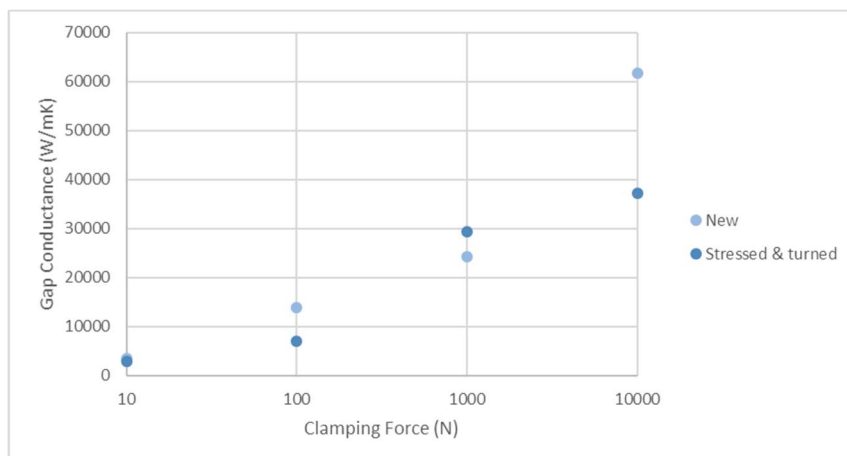


Figure 8 – graph showing gap conductance as a function of clamping force for a new piece of 50 μm indium foil compared to a piece that has been used (i.e. stressed to 10 000N), rotated 90° and re-used.

## 5. Discussion

Looking first at Figure 6, a trend is suggested; the thicker the piece of indium foil used, the greater the improvement in gap conductance calculated. This is potentially counter-intuitive, as the indium foil is an insulator with very poor thermal conductance. However, when we compare the performance of the indium foils to the performance of the copper foam, it becomes more clear – despite the vastly higher thermal conductivity of the copper foam, it does not perform nearly as well as the indium foil; in fact, the copper foam proved to be a worse interstitial material than placing nothing between the hot and cold bodies. This gives rise to the concept that it is the malleability of the material that affects its performance as an interstitial material, independent of its thermal conductivity.

The one notable exception to this is the Heat-Spring® material, which is only 100 µm thick and yet improves the thermal gap conductance more than the 250 µm and 500 µm foils. This shows that better distributing the thermal contact points improves the efficiency of the gap conduction. This is likely due to the thermal constriction that occurs around the contact points; the more scattered the conduction points are, the shorter the average length of the thermal pathways for heat to move from the hot body to the cold.

Notably the improvement of the Heat-Spring® material over the thicker indium foils seems to be less pronounced at 10 000 N. This is likely due to the high clamping forces causing plastic deformation of the Heat-Spring surface, destroying the surface structure and rendering the material little more than a standard sheet of indium.

## 6. Conclusion

The most useful results to come out of this work are that with the introduction of even just a 50 µm thick layer of indium foil, the gap conduction is improved as if the force had been increased by an order of magnitude, while the 500 µm foil improves gap conduction as though the force had been increased by two orders of magnitude. This shows that using a thicker layer of indium foil can allow us to significantly reduce clamping forces.

This will allow us to use much lower clamping forces for comparable contact conductance, which will reduce the mechanical deformations introduced into our cooled body. In many applications this can improve results or increase the lifetime of the cooled systems.

Further work is required to find the limit of this effect, i.e. the thickness beyond which increasing the thickness of indium foil reduces the gap conductance.

## 7. References

1. Rogers, G. F. C. & Mayhew, Y. R. *Engineering, Thermodynamics, Work & Heat Transfer*. (Longman, 1967).
2. Tipler, P. A. *Physics for scientists and engineers*. (W.H. Freeman/Worth Publishers, 1999).
3. Venkenna, B. K. *Fundamentals of heat and mass transfer*. (PHI, 2010).
4. Marion, P., Zhang, L. & Goirand, L. Cryogenic cooling of monochromator crystals: Indirect or direct cooling? in *Proceeding MEDSI 2006* (2006).
5. Bilderback, D. H., Freund, a K., Knapp, G. S. & Mills, D. M. The historical development of cryogenically

- cooled monochromators for third-generation synchrotron radiation sources. *J. Synchrotron Radiat.* **7**, 53–60 (2000).
6. Salerno, L. J. & Kittel, P. Thermal contact conductance. *J. Mater. Process. Technol.* **135**, 204–210 (2003).
  7. Snaith, B., O’Callaghan, P. W. & Probert, S. D. Interstitial materials for controlling thermal conductances across pressed metallic contacts. *Appl. Energy* **16**, 175–191 (1984).
  8. Madhusudana, C. V. *Thermal Contact Conductance*. (Springer International Publishing, 2014). doi:10.1007/978-3-319-01276-6
  9. Holman, J. P. *Heat Transfer, 8th Edition*. (McGraw-Hill, 1997).
  10. Copper Foam CU003804 - Goodfellow Catalogue. (2018). Available at: [http://www.goodfellow.com/catalogue/GFCat4I.php?ewd\\_token=xb2DkeH5AMoYPhDhydXz3PLruPgOwx&n=LEbGGPtE1aKUH9pHXKJyxjk5LTCMk&ewd\\_urlNo=GFCat411&Catite=CU003804&CatSearNum=1](http://www.goodfellow.com/catalogue/GFCat4I.php?ewd_token=xb2DkeH5AMoYPhDhydXz3PLruPgOwx&n=LEbGGPtE1aKUH9pHXKJyxjk5LTCMk&ewd_urlNo=GFCat411&Catite=CU003804&CatSearNum=1). (Accessed: 30th August 2018)

## Appendix E: “Application of Interference Fits on Cylindrical Monochromator Crystals to Overcome Clamping and Cooling Deformations” – Accepted, pending publication in Journal of Synchrotron Radiation

Joshua Stimson<sup>a\*</sup>, Michael Ward<sup>a</sup>, John Sutter<sup>b</sup>, Sofia Diaz-Moreno<sup>b</sup>, Simon Alcock<sup>b</sup> and Peter Docker<sup>b</sup>

<sup>a</sup>CEBE, Birmingham City University, Curzon Street, Birmingham, West Midlands, B4 7XG, UK

<sup>b</sup> Diamond Light Source, Fermi Ave, Didcot, OX11 0DE, UK

Correspondence email: joshua.stimson@bcu.ac.uk

**Synopsis** A novel monochromator assembly design utilising an interference fit is suggested, tested and analysed and comparison has been made to previous work performing similar tests on conventional side clamped crystal cooling designs. The new design was found to have an order of magnitude less deformation and a high level of repeatability without using indium foil.

**Abstract:** In order to provide adequate cryogenic cooling of both existing and next generation crystal monochromators a new approach to produce an optimum thermal interface between the first crystal and its copper heat exchanger is proposed. This will ensure that the increased heat load deposited by higher X-ray powers can be properly dissipated.

Utilising a cylindrical silicon crystal, a tubular copper heat exchanger and by exploiting the differing thermal and mechanical properties of the two, a very good thermal interface was achieved at liquid nitrogen temperatures. The surface flatness of the diffracting plane, one end of the cylindrical crystal, was measured at room temperature while unconstrained. The crystal was then placed into the copper heat exchanger, a slide fit at room temperature and then cooled to liquid nitrogen temperatures. At -200 °C the slide fit had become an interference fit. This room temperature ‘loose’ fit was modelled using FEA to obtain the desired fit at cryogenic temperatures by prescribing the fit at room temperature. Under these conditions the diffraction surface was measured for distortion due to thermal and mechanical clamping forces. The total deformation was measured to be 30 nm, an order of magnitude improvement over deformation caused by cooling alone with the original side clamped design this concept method is set to replace. This new methodology also has the advantage that it is repeatable and doesn’t require macro-scale tools to acquire a nanometre accuracy mounting.

**Keywords:** Monochromator design; interference fit; first crystal cooling.

## 1. Introduction

As synchrotrons see more varied use (Wilson, 1996), it is beneficial to optimise the usage of space by spurring additional beamlines off of existing ones. A major limit to this, however, is the size of the optics; in order to minimise the effect of deformations introduced through clamping and cooling monochromator assemblies it is industry practice to make monochromator crystals significantly larger than the footprint of the beam incidental on the surface, often by a factor of two or more (Bilderback *et al.*, 2000).

In addition, there is a demand for greater powers to be generated at the synchrotrons as the incident power has a directly proportional relation to the resolution of any generated image and the minimum sample size of any detected material (Odier *et al.*, 2009). The traditional response to the use of higher powers has been to increase the size of the crystal, such that the diffracting surface in the beam footprint fits within the relatively flat central section.

The vast majority of monochromator assemblies are composed of a silicon crystal held within copper heat exchangers by use of steel or invar bolts, often with a foil of indium between the copper and silicon to mitigate some of the deformation and improve thermal contact (Bilderback *et al.*, 2000; Carpentier *et al.*, 2001). By introducing three sets of independent material properties, such as thermal expansion coefficients and heat capacities, this introduces not only clamping pressures and torques when the components are assembled but also causes the elements of the assembly to deform thermally at different rates.

In this work we suggest a novel solution to the aforementioned issues: the use of a cylindrical silicon crystal, held in a cylindrical copper sleeve manufactured such that the two bodies are in loose mechanical contact at room temperature, however in good intimate contact at cryogenic temperatures. This will give a lower uniform stress distribution and avoid complex mechanical clamping procedures and stresses.

## 2. Theory

The theory behind the novel design has been examined in detail in a previous paper (Stimson *et al.*, 2017), and so only a brief review will be detailed here.

The core concept behind an interference fit is well known (Tipler, 1999); by causing two objects to attempt to occupy the same space, usually by either forcing the two bodies together mechanically or by enlarging one object thermally such that it contracts into the other's space when cooled, we can induce a very high, uniform stress field. However, due to the drastically different thermal expansion coefficients of silicon and copper (Petersen, 1982; Shah & Straumanis, 1972; National Institute of Standards and Technology (NIST), 1992; Middelman *et al.*, 2015) and the very low temperatures used in synchrotron monochromators (Carpentier *et al.*, 2001) we find that to cause an interference fit at room temperature causes destructively high pressures when cooled. Instead, by cooling the copper to liquid nitrogen temperatures (approximately 80 K) we can cause the copper sleeve to contract faster and to a greater degree than the silicon, forming a uniform, high pressure mechanical and thermal contact across the entirety of the inner surface of the copper sleeve. The

previous work (Stimson *et al.*, 2017) found that the appropriate room temperature gap was approximately 30  $\mu\text{m}$  between the silicon and copper at all points; this would cause a uniform stress field on the order of  $10^8$  Pa. This was required to provide optimal thermal contact with minimal mechanical deformation.

### 3. Method

In order to test the new design, a number of cylindrical crystals and heat exchanger sleeves were manufactured. The crystals had a radius of 12.5 mm and a length of 50 mm; they were marginally tapered, presenting a slightly conical profile; as such, the narrow ends were polished such that any latitudinal movement was directed away from the polished surface. The sleeves matched the slope of the crystal, with an internal radius of 12.53 mm, an external radius of 17.53 mm and a length of 40 mm, and brass stoppers with a length of 8 mm and a radius of 3 mm for the first 5 mm of length and a radius of 6 mm for the remaining 3 mm of length secured on stainless steel AISI 304 bolts were fitted to the bottom of the sleeves to ensure the appropriate fit was achieved. The crystal was inserted such that the optically polished, flat end of the cylinder extended approximately 5 mm beyond the level of the copper heat exchange, forming the crystal assembly as shown in Figure 1 below.

This assembly was inserted into a vacuum vessel, held in location by a copper clamp attached to a hollow copper tube referred to as a “cold finger”. The cold finger extended through the vacuum vessel and terminated within a stainless steel receptacle; by filling the receptacle with liquid nitrogen, we could rapidly cool the assembly to  $-190$  °C. An optical grade window on the front of the vacuum vessel allowed a direct view of the crystal’s diffracting surface as shown in Figure 2 below. The vessel was aligned in front of a mini-Fizeau interferometer, which was used to measure the flatness of the diffracting surface.

The crystal–sleeve assembly was imaged at room temperature with no vacuum, at room temperature at  $10^{-8}$  mbar and at liquid nitrogen temperatures ( $\sim -190$  °C) at vacuum. The surface profile imaged at room temperature under vacuum was subtracted from that imaged at liquid nitrogen temperatures under vacuum to find the deformation caused by the system cooling and the copper clamping the silicon.

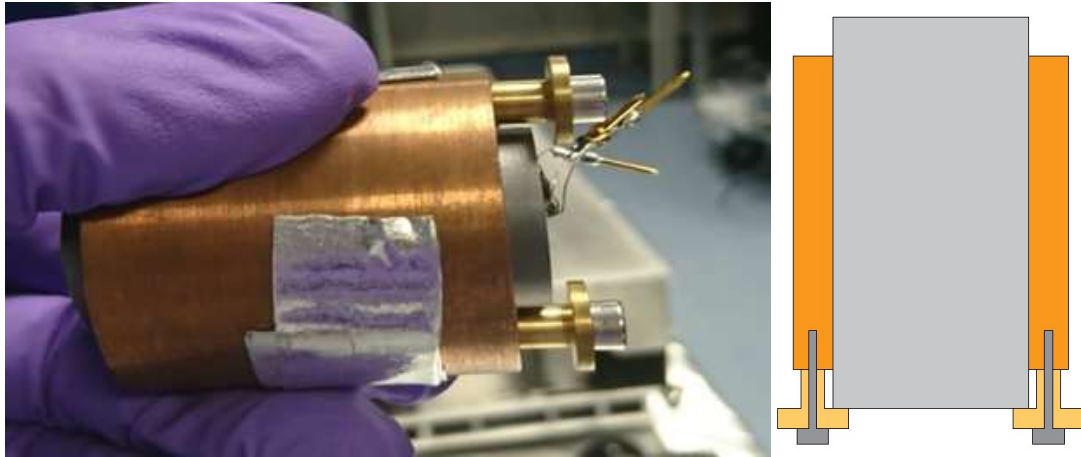


**Figure 1** Left: Cylindrical single crystal 111 Silicon in copper heat exchanger sleeve. Right: Cross-sectional diagram of silicon crystal in copper heat exchanger sleeve. Steel bolts hold brass stoppers in place to hold crystal in the heat exchanger.

The sleeve illustrated in Figure 1 featured a  $30\ \mu\text{m}$  room temperature gap between the crystal and sleeve at room temperature. The assembly was tested multiple times to ensure results were repeatable.



**Figure 2** Crystal assembly contained in vacuum vessel placed in view of mini-Fizeau interferometer. Liquid nitrogen receptacle for cold finger visible on the right side of the picture. Insert close up of crystal assembly

#### 4. Results

The crystal was measured at room temperature and atmospheric pressure. The crystal was found to have a saddle-shaped deformation with a maximum height difference of 850 nm, as shown in Figure 3 below.

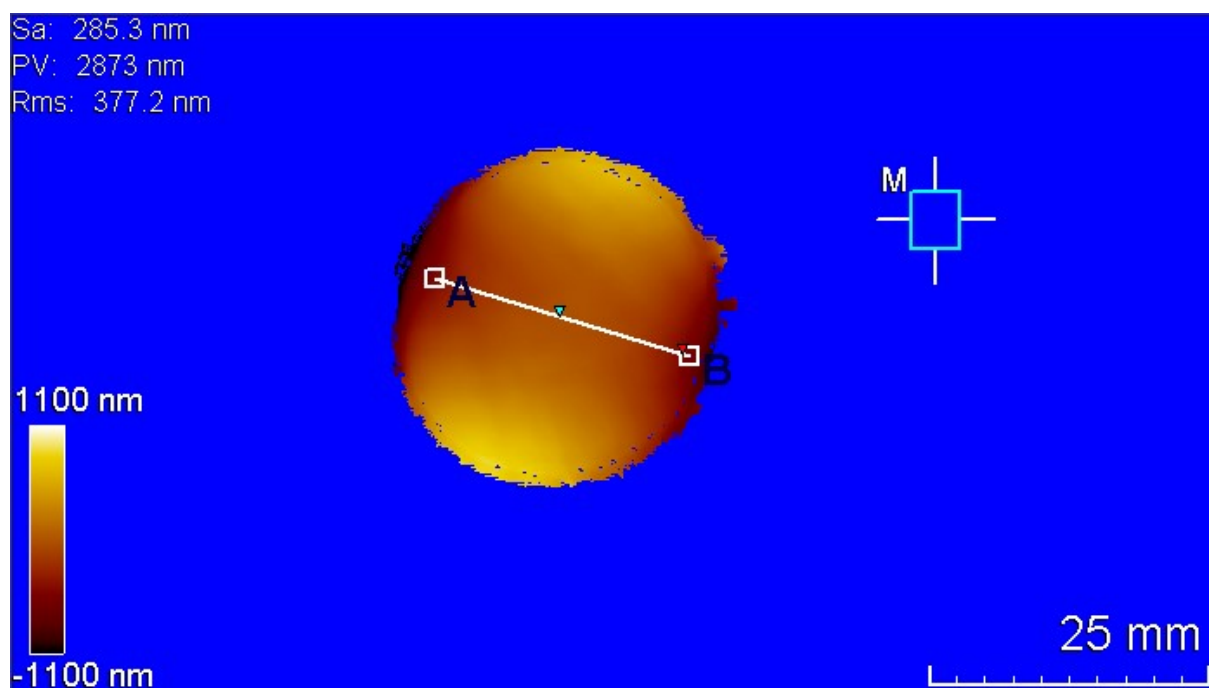
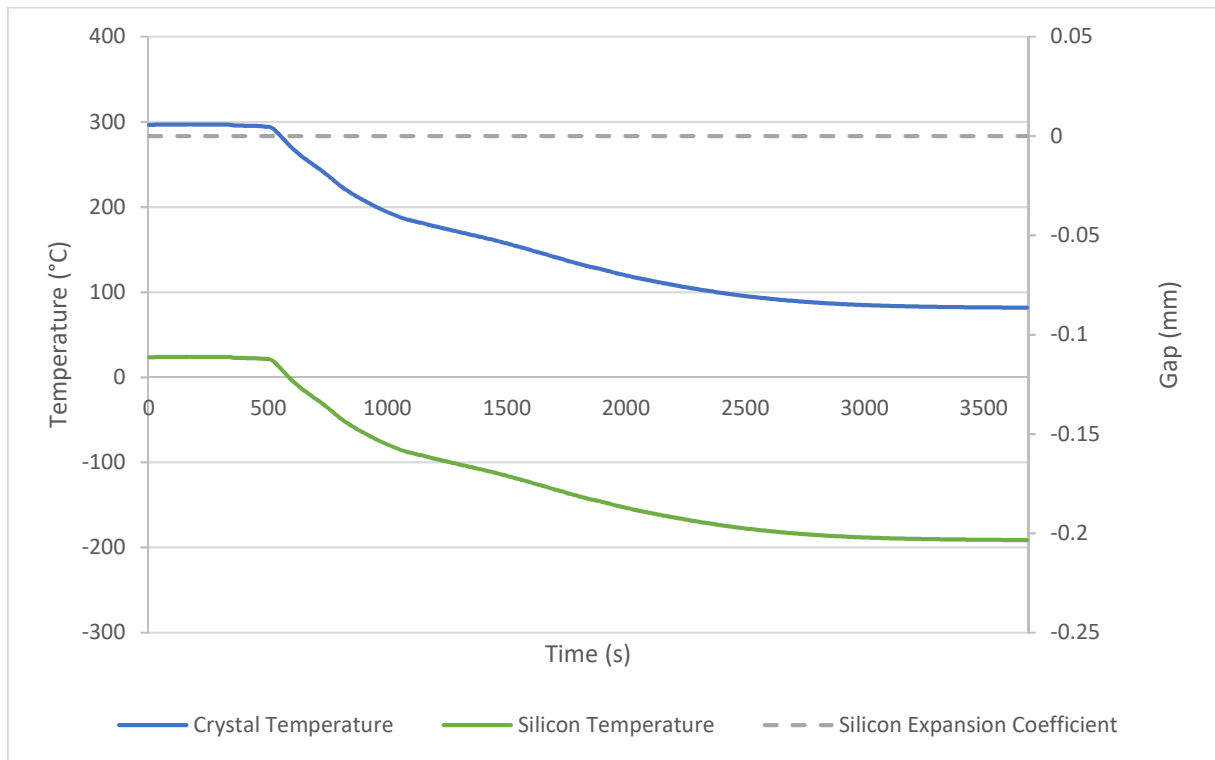


**Figure 3** Room temperature, atmospheric pressure surface profile of silicon crystal, showing a maximum difference of 850 nm.

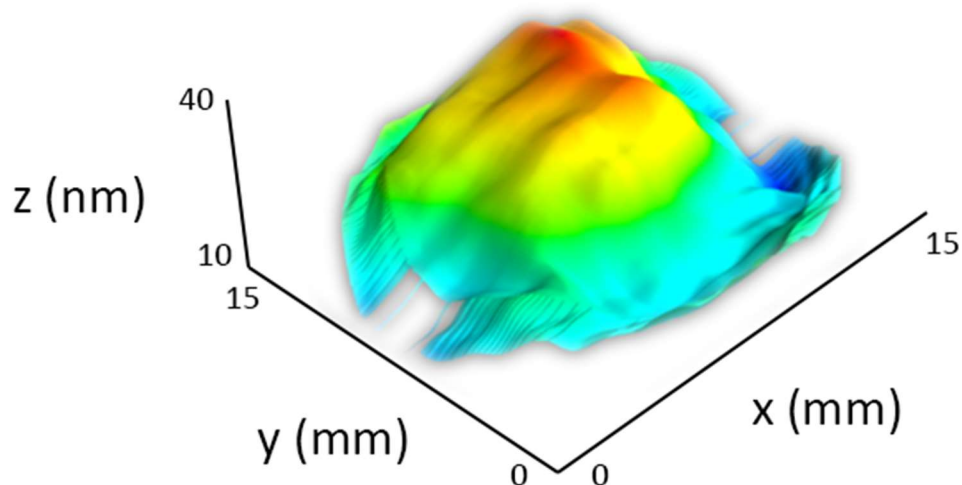
The vessel was pumped down to  $10^{-8}$  mbar and the crystal surface was imaged again; there was no significant difference in the crystal surface measurement between atmospheric pressure and under vacuum. Liquid nitrogen was then introduced to the cold finger, and the temperature of the crystal and sleeve was measured using PT100 temperature sensors until they reached equilibrium with the cold finger, around  $-190$  °C after an hour of cooling.

The temperatures of both the crystal and sleeve were measured as the system cooled, as shown in Figure 4 below. Figure 4 also shows the gap between the copper and the silicon calculated using the thermal expansion coefficient of each material integrated over the change in temperature, to compare the internal radius of the copper sleeve to the radius of the silicon crystal; once this line drops below 0, the two bodies are forced into an interference fit regime. There is a visible turning point in the temperature of the silicon crystal at 500 seconds; this is the point at which the copper shrank sufficiently to form good thermal contact with the silicon, approximately  $10$   $\mu\text{m}$ . The silicon continues to cool faster than the copper until the two are in ideal thermal contact at 800 seconds, which correlates to a shrinkage of  $60$   $\mu\text{m}$ , i.e. the two bodies coming into interference. Once cooled, the crystal surface was measured again. The room temperature scan was subtracted from the cryogenic temperature scan to find the deformation induced in the surface of the crystal due to cooling and

clamping. It is worth noting that we cannot separate cooling and clamping deformations by design, as cooling the sleeve is what causes it to clamp the crystal.

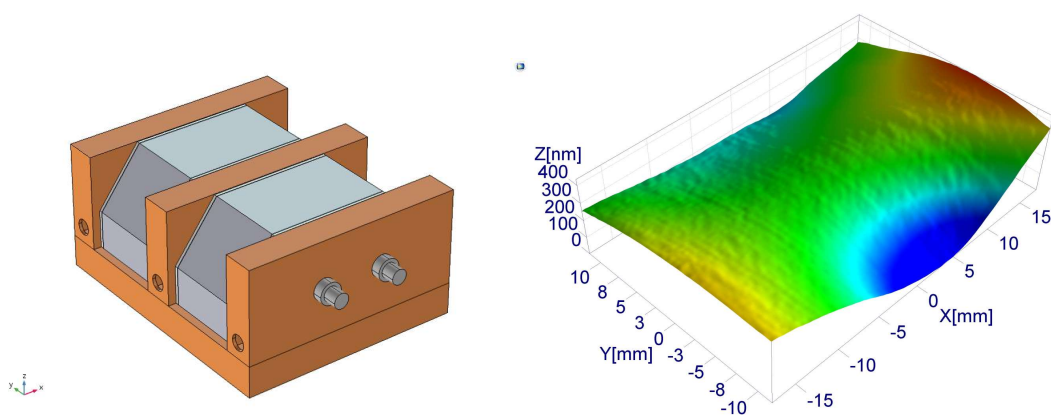


**Figure 4** On the left axis, temperature of silicon crystal and copper heat exchange as a function of time. On the right axis, calculated gap between copper and silicon as a function of time; a negative gap indicates the two materials are interfering.



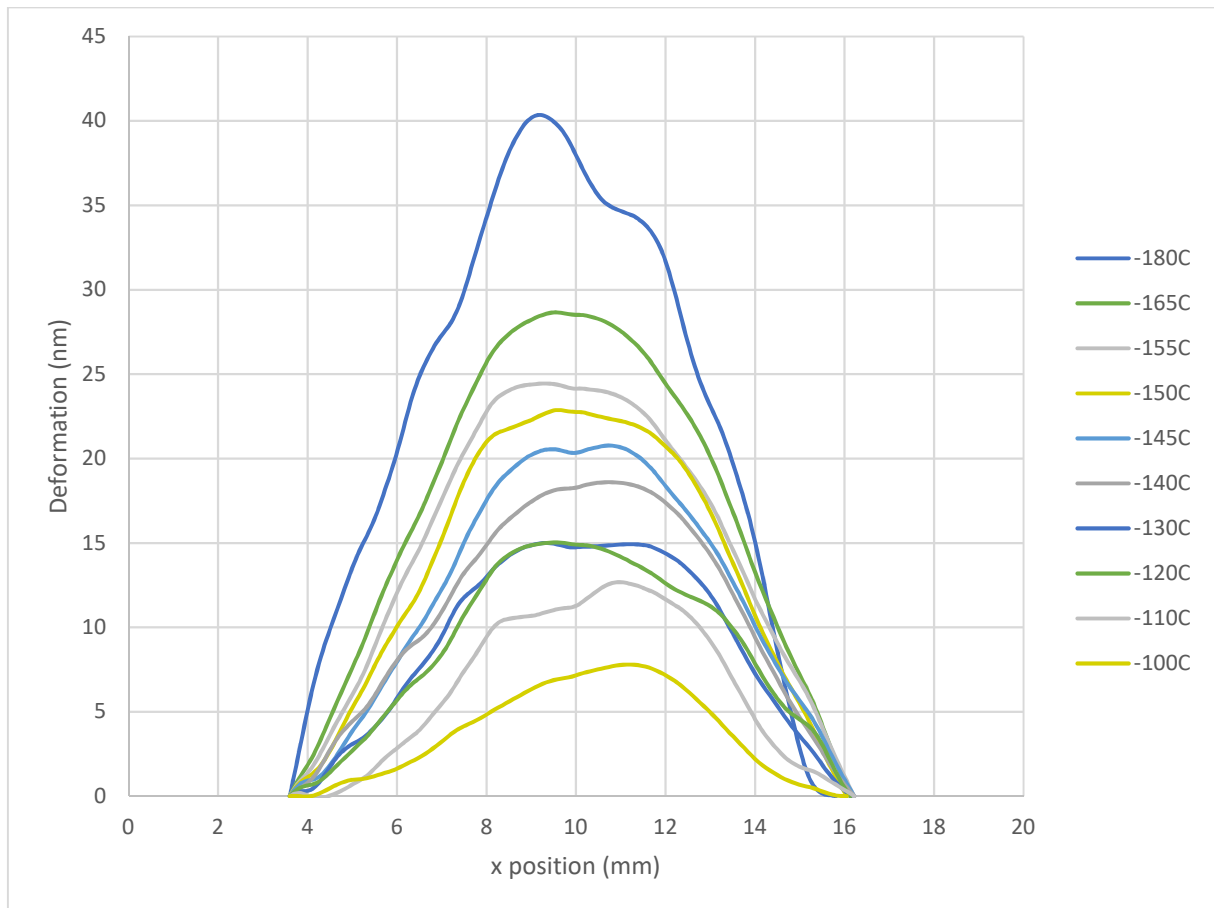
**Figure 5** The surface deformation caused in the crystal by cooling and clamping it. Image created by subtracting image of crystal at 27 °C from picture of crystal at -190 °C shows a 30 nm deformation across the diffracting area.

Figure 5 shows that the total deformation caused across the entire crystal surface is approximately 30 nm. In contrast, the conventional side clamped first monochromator crystal assembly used at the I20 beamline at the Diamond Light Source was measured in the same manner (Docker *et al.*, 2013), and deformation from cooling was found in some cases to be as high as 400 nm, an order of magnitude higher. See Figure 6. It should be noted that these earlier measurements were taken between a clamped room temperature assembly and a clamped cryogenic assembly, and so would not show the deforming effect of clamping. These earlier tests also relied on interfaces containing indium. It is important to note these tests also highlighted that the conventional assembly is not repeatable; multiple repetitions of the same assembly yielded remarkably different results highlighting the unreliability of such an approach.



**Figure 6** Left: The conventional side clamped first monochromator crystal assembly used at the I20 beamline at the Diamond Light Source. Right: The surface deformation caused in the crystal by cooling of standard assembly. Image created by subtracting image of crystal at 27 °C from picture of crystal at -190 °C shows a 400 nm deformation across the diffracting area.

The assembly was then allowed to return to room temperature and the procedure was repeated showing negligible difference between the results on each repetition. The crystal was also removed from the assembly, inspected for deformations or damage and returned and the procedure repeated once more resulting in another negligible difference. Finally the surface profile of the crystal was taken as the assembly warmed up from -200 to room temperature. Figure 7 below shows the surface profile of the crystal as it was warmed after cooling.



**Figure 7** Deformation observed in silicon diffracting surface as crystal warmed to room temperature. Significant deformation observed between -155 °C and -180 °C

There is a visible, dramatic increase in deformation below -155 °C; the maximum deformation grows from 0 nm at 27 °C to 25 nm at -155 °C, a difference of 25 nm over a range of 182 °C, while it grows to over 40 nm by -180 °C, a difference of 15 nm over just 25 °C. This is of interest as -155 °C correlates to 120 K, a temperature at which silicon shows a coefficient of thermal expansion of zero. This is the ‘ideal’ temperature to run a first crystal at in service. The cause of this sudden deformation is the thermal expansion coefficient of silicon, which dips below 0 at -150 °C. This suggests that at temperatures this low the silicon effectively grows as the temperature falls, creating further stress within the interference fit. This additional stress can be modelled using FEA software, though this has been left for future work at this stage.

## 5. Discussion

The low surface deformation caused by the new proposed clamping methodology presented in this paper demonstrates great promise. When compared with the side clamping regime it is proposing to replace, the interference fit design can offer an order of magnitude improvement in terms of the deformation of the diffracting surface for Bragg diffraction. In addition, the repetition demonstrated shows that the crystal can be a “set and forget” system, assembled once and losing no quality or efficiency over repeated cooling cycles. The design presented herein can also be assembled once and then maintained as such indefinitely, as the tapered crystal and brass stops prevent the crystal dislocating from the heat exchanger.

A very strong thermal contact was achieved, as shown by the temperature of the heat exchanger and the crystal rapidly reaching equilibrium over no longer than fifteen minutes, and maintaining a temperature difference less than 4 °C after the interference fit; this indicates a strong thermal contact, theoretically suitable for even higher heat loads than are currently utilised in synchrotron devices.

Taken together, these results indicate that the novel design suggested here of a cylindrical silicon crystal located within a sleeve-shaped copper heat exchanger such that an interference fit is created upon cooling to liquid nitrogen temperatures, is a revolutionary design when compared to the conventional monochromator assembly. Further work will focus on the introduction of x-ray beams and heaters to test the monochromator’s performance as a Bragg diffractor under various thermal loads, as well as modelling the stresses present within the crystal.

## 6. Bibliography

- Bilderback, D. H., Freund, a K., Knapp, G. S. & Mills, D. M. (2000). *J. Synchrotron Radiat.* 7, 53–60.
- Carpentier, P., Rossat, M., Charrault, P., Joly, J., Pirocchi, M., Ferrer, J. L., Kaïkati, O. & Roth, M. (2001). *Nucl. Instruments Methods Phys. Res. Sect. A Accel. Spectrometers, Detect. Assoc. Equip.* 456, 163–176.
- Docker, P., Alcock, S. & Nistea, I. (2013).
- Middelmann, T., Walkov, A., Bartl, G. & Schödel, R. (2015). *Phys. Rev. B.* 92, 174113.
- National Institute of Standards and Technology (NIST) (1992). *Monograph*, 270.
- Odier, P., Thoulet, S. & Ludwig, M. (2009).
- Petersen, K. E. (1982). *Proc. IEEE.* 70, 420–457.
- Shah, J. S. & Straumanis, M. E. (1972). *Solid State Commun.* 10, 159–162.
- Stimson, J., Docker, P., Ward, M., Kay, J., Chapon, L. & Diaz-Moreno, S. (2017). *IOP Conference Series: Materials Science and Engineering*, Vol. 278, p. 012055.
- Tipler, P. A. (1999). *Physics for scientists and engineers* W.H. Freeman/Worth Publishers.
- Wilson, E. J. N. (1996). *5th European Particle Accelerator Conference*, Vol. C960610, pp. 135–139. Spain.